LEABHARLANN CHOLÁISTE NA TRÍONÓIDE, BAILE ÁTHA CLIATH | TRINITY COLLEGE LIBRARY DUBLIN
Ollscoil Átha Cliath | The University of Dublin

Terms and Conditions of Use of Digitised Theses from Trinity College Library Dublin

Copyright statement

All material supplied by Trinity College Library is protected by copyright (under the Copyright and Related Rights Act, 2000 as amended) and other relevant Intellectual Property Rights. By accessing and using a Digitised Thesis from Trinity College Library you acknowledge that all Intellectual Property Rights in any Works supplied are the sole and exclusive property of the copyright and/or other IPR holder. Specific copyright holders may not be explicitly identified. Use of materials from other sources within a thesis should not be construed as a claim over them.

A non-exclusive, non-transferable licence is hereby granted to those using or reproducing, in whole or in part, the material for valid purposes, providing the copyright owners are acknowledged using the normal conventions. Where specific permission to use material is required, this is identified and such permission must be sought from the copyright holder or agency cited.

Liability statement

By using a Digitised Thesis, I accept that Trinity College Dublin bears no legal responsibility for the accuracy, legality or comprehensiveness of materials contained within the thesis, and that Trinity College Dublin accepts no liability for indirect, consequential, or incidental, damages or losses arising from use of the thesis for whatever reason. Information located in a thesis may be subject to specific use constraints, details of which may not be explicitly described. It is the responsibility of potential and actual users to be aware of such constraints and to abide by them. By making use of material from a digitised thesis, you accept these copyright and disclaimer provisions. Where it is brought to the attention of Trinity College Library that there may be a breach of copyright or other restraint, it is the policy to withdraw or take down access to a thesis while the issue is being resolved.

Access Agreement

By using a Digitised Thesis from Trinity College Library you are bound by the following Terms & Conditions. Please read them carefully.

I have read and I understand the following statement: All material supplied via a Digitised Thesis from Trinity College Library is protected by copyright and other intellectual property rights, and duplication or sale of all or part of any of a thesis is not permitted, except that material may be duplicated by you for your research use or for educational purposes in electronic or print form providing the copyright owners are acknowledged using the normal conventions. You must obtain permission for any other use. Electronic or print copies may not be offered, whether for sale or otherwise to anyone. This copy has been supplied on the understanding that it is copyright material and that no quotation from the thesis may be published without proper acknowledgement.

NOISE CONTROLLED SEMICONDUCTOR OPTICAL AMPLIFIERS

Robert Lennox

March 2012

A thesis submitted for a degree of
Doctor of Philosophy
to the University of Dublin

School of Physics
Trinity College
University of Dublin
Ireland

TRINITY COLLEGE
2 4 MAY 2013
LIBRARY DUBLIN

Thesis 9813

Summary

Semiconductor optical amplifiers (SOA) have been widely used in communications systems for decades, in a multitude of capacities. In their simplest form SOAs offer cost effective linear amplification at a variety of wavelengths, simultaneously covering a large gain bandwidth, with the added benefit of practical photonic integration. They are electrically pumped and have good thermal stability, all packaged within a very small volume. In addition to this, SOAs can be operated as non-linear entities under saturation, with the capability to perform all-optical functional duties over a range of configurations and data rates far beyond the realm of commercial high-speed electronics currently used for signal processing. These latter attributes are becoming ever more important as our appetite for digital information drives bandwidth consumption to greater heights.

Overshadowing these benefits however is an innately high noise figure (NF), compromising performance. On top of this, the saturation output power (P_{sat}) can be low, limiting the dynamic range of input powers over which signals can be amplified cleanly without distortion, inhibiting widespread adoption. This can have a significant penalty when the SOA is used as a multichannel amplifier due to the effects of channel crosstalk. Currently, the amplifier of choice in communications systems is the Erbium doped fibre amplifier (EDFA), with an inherently low NF and favourable carrier dynamics. For the SOA to gain the same level of ubiquity, both of these shortfalls must be addressed without undermining overall performance.

This thesis seeks to address both of these shortfalls. A concept of NF control is presented whereby the carrier density along the entirety of the gain length is tailored to either decrease the chip-NF, or alternatively, to increase P_{sat}, whilst having a limited effect on the maximum gain. Two novel designs will be presented via simulation and experiment to achieve this. The first incorporates a lateral laser within the SOA structure along a proportion of the active length, clamping the carrier density in this region upon reaching threshold. The second is more direct in its approach, using multiple contact electrodes to independently control the injected current. The level of control achievable via this technique was quantified and further developed through post-fabrication etching of the contact isolation slot, with very positive results. The effect of an asymmetric and variable carrier density on the interband & intraband gain dynamics will also be demonstrated experimentally through contra-propagation pump-probe studies. The implications of this on all-optical switching will be addressed.

DECLARATION

I declare that this thesis has not been submitted as an exercise for a degree at this or any other university and it is entirely my own work.

I agree to deposit this thesis in the University's open access institutional repository or allow the library to do so on my behalf, subject to Irish Copyright Legislation and Trinity College Library conditions of use and acknowledgement.

Publications

Peer Reviewed

1. K. Carney, **R. Lennox**, R. Maldonado-Basilo, S. Philippe, F. Surre, A. L. Bradley and P. Landais, "Control of noise figure and saturation power in multi-contact semicon- ductor optical amplifiers: Simulation and experiment," IEEE Journal of Quantum Electronics, Submitted.

2. **R. Lennox**, K. Carney, R. Maldonado-Basilio, S. Philippe, A.L. Bradley, P. Landais, "Impact of bias current distribution on the noise figure and power saturation of a multicontact semiconductor optical amplifier", *Optics Letters*, Vol. 36, No. 13, July 1, 2011.

3. K. Carney, **R. Lennox**, R. Maldonado-Basilio, S. Philippe, A.L. Bradley, P. Landais, "Novel noise controlled semiconductor optical amplifier based on lateral laser cavity", *Electronics Letters*, Vol. 46, No. 18, pp. 1288-1289, September 2, 2010.

Conference Contributions

1. **R. Lennox**, K. Carney, R. Maldonado-Basilio, S. Philippe, P. Landais, and A. L. Bradley, "Power saturation and noise figure control of a multi-electrode bulk semiconductor optical amplifier", *Photonics Ireland 2011*, September 7-9, 2011.

2. K. Carney, **R. Lennox**, R. Maldonado-Basilio, S. Philippe, A.L. Bradley, P. Landais, "Simulation of noise figure and saturation power control technique in multi-section semconductor optical amplifiers," *Photonics Ireland 2011*, September 2011.

3. K. Carney, **R. Lennox**, S. Latkowski, R. Maldonado-Basilio, A.L. Bradley, P. Landais, *12th International Conference on Transparent Optical Networks (ICTON), 2010*, pp. 1-4, June 2010.

4. **R. Lennox**, S.Philippe, P. Landais & A.L. Bradley, "Polarisation resolved gain dynamics in bulk semiconductor optical amplifiers", Oral presentation at Conference of Semiconductor Integrated Opto-Electronics (SIOE), University of Cardiff, Cardiff, Wales, April 2009.

5. K. Carney, **R. Lennox**, F. Surre, S. Philippe, A.L. Bradley, P. Landais, "Simulation of a noise controlled semiconductor optical amplifier", *Photonics Ireland 2009*, Kinsale, September 2009.

6. **R. Lennox**, K. Carney, P. Landais & A.L. Bradley, "First experimental demonstration of novel noise-controlled semiconductor optical amplifiers", *Photonics Ireland*, Kinsale, September 2009.

Acknowledgements

I would like to acknowledge the time, effort and patience that my supervisor, Dr. Louise Bradley, has put into this work over the last four years. Her guidance, advice and enthusiasm for research have been a constant driving force, and without it none of this would have been possible. Thanks for everything Louise! The project was a team effort, a collaboration with Dublin City University (DCU), and so I would like to extend my thanks to Dr. Pascal Landais, Dr. Ramon Maldonado-Basilio, Dr. Sev Philippe, Dr. Sylwester Latkowski, and my good friend Dr. Kev Carney.

A big thank you to the Photonics Group (members past and present) who have supported me without question and inspired me to keep going. I am privileged to have worked within such an impressive group. This is true of all the amazing people I have met through the School of Physics. Thanks to everyone in the admin. office, Marie, Ciara, Sam and Robbie; the technical boys Gordo, Pa(t), Ken, Al and; the main man himself JK. I also can't forget Tina and Joan, who kept me sane with endless chat in the evening time over the years. Getting to know all of you has been a pleasure and an important part of my life. I consider myself very lucky to be able to call you my friends.

I am also hugely indebted to Dr. Colm Faulkner of the Advanced Microscopy Lab (AML), who's expertise with the FIB and general discussions about life and experimental physics were both insightful and helpful. Colm took time out to come in on weekends, and stay late, always making sure that the SOAs were ready when we needed them.

I have been lucky to have had the understanding and unconditional love of my girlfriend Lauren, the greatest friends and my incredible family. You have always been there, not only to encourage, but to remind me when needed, that there is only ever this moment. Life exists outside of the confined world of a Ph.D. (such as football, Go BOX!!) and I look forward to being with you all in this magical place! It has been some time.

Finally, it would be remiss not to mention Trinity College. My eight years here have been wonderful and I will miss it.

Now, let's get...

Contents

Declaration ii

Publications iv

Acknowledgements v

1 Motivation **1**

References 5

2 Semiconductor Optical Amplifiers **7**

2.1 Optical Gain in Semiconductors 8

2.2 SOA Operation 14

2.3 Steady State Properties 21

2.4 Carrier Dynamics 26

2.5 The State of the Art 28

2.6 Conclusion 29

References 31

3 Control of Noise Figure & Saturation Power **37**

3.1 Noise Figure 38

3.2 Controlling the Noise Figure 47

3.3 Gain Saturation 51

3.4 Realisation of Noise Figure Control 54

3.5 Conclusion 55

References 57

4 Lateral Cavity SOA: Steady State Characterisation **63**

4.1 Design Concept 64

4.2 Steady State Modelling 67

4.3 Experimental Characterisation 74

4.4 Prototype Limitations 89

4.5 Conclusions 91

References 93

5 Multi Contact SOA: Steady-State Characterisation **97**

5.1 Design Concept 98

5.2 Steady State Modelling 100

5.3 Experimental Characterisation 109

5.4 Quasi-Continuous Wave Performance 125

5.5 Conclusions 131

References 135

6 Multi Contact SOA: Gain Dynamics **137**

6.1 Pump-Probe Studies 138

6.2 Noise Controlled Bias Configurations 143

6.3 Variation of Probe Facet Bias 151

6.4 Variation of Pump Facet Bias 163

6.5 Conclusions 170

References 173

7 Multi Contact SOA: Design Development **177**

7.1 Adjacent Carrier Leakage 178

7.2 Improving Carrier Density Control 179

7.3 Iterative Characterisation 187

7.4 Comparison 199

7.5 Conclusions 201

References 203

8 Conclusions & Future Work **205**

8.1 Lateral Cavity SOA 206

8.2 Multi Contact SOA 207

References 215

A Steady-State Multi-Section Program **217**

References 219

1

Motivation

Semiconductor optical amplifiers (SOA) have been heavily researched for decades. Originally, study stemmed from the seminal work on semiconductor laser diodes. Interest subsequently dwindled, until resurgence followed in the eighties and nineties as application became more widespread, simulations became more powerful and the future need for all-optical networking became evident. We are now at a point where SOA functionality has evolved to a multitude of areas.

The different duties which the SOA performs, access two distinct parts of the gain regimes of the device. This translates to use as a simple gain block for economical linear amplification, or increasingly, for functional duties such as all optical logic or 3R regeneration (re-amplifying, re-shaping, re-timing) [1]. The role of semiconductor optical amplifiers (SOA) within optical communications systems is ever increasing, moving in tandem with ascending network capacities to the high gigabit per second domain. Their capabilities are both straight forward, where amplification in the linear regime is required, and more dynamic, where opportunities as optically functional components become viable when operated in saturation.

Regarding linear functionality, a number of hurdles have existed historically, hindering mainstream adoption. Particularly, these include a modulated gain due to internal oscillation, high polarisation dependence, very fast gain recovery (but not fast enough), high coupling loss and a high noise figure (NF). Through advances made in both simulation and fabrication technologies the effects of these disadvantages have largely been mitigated, where complex structures have been coupled with exotic gain media such as quantum dots, leading to improved linear gain and more efficient input coupling. Much work has also been concerned with the extension of the linear operating regime, in an effort to accommodate a larger range of input powers. The specific improvements will be outlined in the relevant sections of the thesis.

Notably, one area which has yet to be improved upon significantly is noise figure (NF). SOAs

possess high NF values in the region of 6−9dB [2], offsetting the multitude of advantages that SOAs possess. The high NF stems directly from the amplified spontaneous emission produced in the gain material (ASE), which somewhat corrupts the signal being amplified [3]. The effects from a practical point of view can be detrimental and costly, requiring an increase in the number of repeater points along the fibre link. The build up of ASE can also lead to the premature saturation of amplifiers further down the chain. Currently, the amplifier of choice for linear amplification of signals is the Erbium doped fibre amplifier (EDFA). The EDFA benefits from a number of features unique to the physics underlying its operation, resulting in a low NF near the theoretical limit of 3dB. These advantages include low coupling loss and a three level system, both of which favour a low fibre-to-fibre NF. In addition, the carrier dynamics are much slower than current transmission rates, meaning a reduced patterning effect on the transmitted bit sequence. Be that as it may, the SOA maintains a significant number of advantages for linear amplification. The device is economical in fabrication, with many devices grown simultaneously per wafer, depending of course on the internal complexity involved. The SOA is electrically pumped, with a minute footprint. In addition, it possesses huge potential for integrated functionality.

The primary motivation of this thesis is to show that the NF of SOAs, although impossible to eliminate completely, can be reduced. In fact it will be shown that NF control is possible by directly modifying the longitudinal carrier density profile. For the SOA to realise true ubiquity, the noise figure (NF) performance must be improved, especially when compared with the more established EDFA. As such, minimizing this unavoidable characteristic is an attractive goal. In addition to this, it is believed that by proving the concept of NF control, that it can be shown that the saturation power may also be controlled directly using a similar approach, thereupon extending the linear operating regime.

In relation to the non-linear regime, over the course of recent years extensive research has been carried out for use as active switching elements for future high-speed optical communication networks [4]. This has coincided with a concerted effort to produce highly functional integrated photonic components for a multitude of promising applications. These have ranged from non-linear optical loop mirrors [5], to clock-recovery [6], pulse delay descriminators [7] and all optical logic elements [8]. Full integration with lasers, Mach Zhender Interferemoters (MZI), electro-absorber modulaters (EA) etc require specific knowledge of the SOA dynamic performance. Specifically, gain and phase recovery times limit the rate at which SOAs can perform high-speed operations. The speed of the band-filling process is ultimately what determines this limit. Many

experimental and theoretical investigations of the physics underpinning both the gain and phase dynamics of SOAs have been carried out [9, 10, 11, 12] but few have related the physics to the concepts proposed herein. The idea of noise figure control, on which this thesis is based, may modify this behaviour from the norm. Acquisition of the dynamic gain response then, under picosecond pulse injection, is pertinent. This acts as the second part of the motivation behind this work.

Thesis Overview

In **Chapter 2** the fundamental operation of the semiconductor optical amplifier (SOA) is outlined. Beginning with optical gain in semiconductors and the pin junction, introducing the SOA double heterostructure structure, which provides optical and carrier confinement necessary for efficient operation. The steady-state performance of the device is outlined briefly, including a brief discussion of the gain saturation and noise figure properties, as this is necessary for the characterisation of devices in later chapters. The carrier dynamics of the SOA are then addressed as a basis for dynamic characterisation in a later chapter.

Building on the foundations of Chapter 2, the proposed concept of noise figure and saturation control is given in **Chapter 3**. This is aided by simulation, and discussed in a general sense, before briefly proposing two unique design concepts to realise this concept in practical SOAs, known non-specifically as noise controlled semiconductor optical amplifiers (NCSOA).

Chapter 4 will then detail the first of the proposed designs, based on the introduction of a lateral cavity laser within the SOA (LCSOA). The function of the device is given initially, before describing the steady-state model used to describe the NCSOAs. This chapter will also take the opportunity to detail the experimental method used for all continuous wave data taken throughout the thesis. Finally experimental characterisation of the LCSOA is presented, and compared with a control device. The chapter closes with a discussion on the limitations of such a design.

Using many of the experimental details given in Chapter 4, the introduction of the second design is presented and characterised in **Chapter 5**. This design relies on a multi-contact bulk structure, which is explained, and information given in the context of a modified version of the model previously used. Experimental characterisation is then presented under conditions of non-injection and continuous wave injection. The chapter closes by progressing the steady-stage NF characterisation to a more practical figure of merit, the bit error ratio (BER). This represents a quasi-continuous wave performance.

After establishing a good understanding of the MCSOA steady-state performance, the gain dynamics are investigated in **Chapter 6**. Degenerate pump-probe studies are used to this end, looking first at the at the constant pump current operating conditions detailed in Chapter 5, and then the effect of varying the facet section currents on the recovery dynamics. Conclusions are drawn, and the implications for optical switching detailed.

An aspect of the development of the MCSOA design is treated in **Chapter 7**, whereby attempt is made at improving the level of isolation between adjacent contacts. This is carried out through Focused Ion Beam (FIB) etching, over a number of steps, of the localised region corresponding to the isolation slots between the p-electrodes. The procedure and the FIB technique are described, and the iterative CW characterisation after each step is presented.

Finally conclusions are drawn in **Chapter 8**, and the vast array of future work outlined.

References

[1] B. Lavigne, E. Balmefrezol, P. Brindel, B. Dagens, R. Brenot, L. Pierre, J. L. Moncelet, D. de la Grandiere, J. C. Remy, J. C. Bouley, B. Thed, O. Leclerc, "Low input power all-optical 3R regenerator based on SOA devices for 42.66Gbit/s ULH WDM RZ transmissions with 23dB span loss and all-EDFA amplification," *Optical Fibre Communications*, pp. 8–10, 2003.

[2] M. J. Connolly, *Semiconductor Optical Amplifiers*. Kluwer Academic Publishers, Boston, 2010.

[3] M. Premaratne, G. P. Agrawal, *Light Propagation in Gain Media: Optical Amplifiers*. Cambridge University Press, 2011.

[4] P. G. Eliseev, V. V. Luc, "Semiconductor optical amplifiers: Multifunctional possibilities, photoresponse and phase shift properties," *Pure Applied Opt.*, vol. 4, pp. 295–313, 1995.

[5] M. Eiselt, W. Pieper, and H. G. Weber, "SLALOM : Semiconductor laser amplifier in a loop mirror," *Journal of Lightwave Technology*, vol. 13, no. 10, pp. 2099–2112, 1995.

[6] E. Awad, C. Richardson, P. Cho, N. Moulton, and J. Goldhar, "Optical clock recovery using SOA for relative timing extraction between counterpropagating short picosecond pulses," *IEEE Photonics Technology Letters*, vol. 14, pp. 396–398, Mar. 2002.

[7] M. Premaratne, S. Member, A. J. Lowery, and S. Member, "Semiclassical analysis of the impact of noise in SOA-based optical pulse delay discriminator," *IEEE Journal of Selected Topics in Quantum Electronics*, vol. 12, no. 4, pp. 708–716, 2006.

[8] B. P. Ali Hamie, Amma Sharaiha, Mikael Guegan, "All-optical logic NOR gate using two-cascaded semiconductor optical amplifiers," *IEEE Photonics Technology Letters*, vol. 14, no. 10, pp. 1439–1441, 2002.

[9] J. Mø rk and T. W. Berg, "The Dynamics of Semiconductor Optical Amplifiers," *Optics & Photonics News*, pp. 42–48, 2003.

[10] A. Reale, A. Di Carlo, and P. Lugli, "Gain dynamics in traveling-wave semiconductor optical amplifiers," *IEEE Journal of Selected Topics in Quantum Electronics*, vol. 7, no. 2, pp. 293–299, 2001.

[11] L. Schares, S. Member, C. Schubert, C. Schmidt, H. G. Weber, L. Occhi, and G. Guekos, "Phase dynamics of semiconductor optical amplifiers at 1040GHz," *IEEE Journal of Quantum Electronics*, vol. 39, no. 11, pp. 1394–1408, 2003.

[12] P. Berger, M. Alouini, J. Bourderionnet, F. Bretenaker, and D. Dolfi, "Dynamic saturation in Semiconductor Optical Amplifiers: accurate model, role of carrier density, and slow light.," *Optics express*, vol. 18, pp. 685–93, Jan. 2010.

2

Semiconductor Optical Amplifiers

The semiconductor optical amplifier (SOA) is essentially a semiconductor laser operated under conditions of restricted cavity oscillation, whereby no lasing is allowed to occur. In this way an optical signal of appropriate frequency can be amplified upon injection through a single pass of the structure. This chapter will provide a succinct introduction to the SOA, starting from the premise of optical gain in semiconductor materials, and building on this to introduce the pin double heterojunction. The steady-state and dynamic operation of the device will be explained in the context of the structural state of the art.

2.1 Optical Gain in Semiconductors

The mechanisms responsible for optical gain in semiconductor materials can be derived from a two-level system - a simplification of the energy bands in a semiconductor crystal. To progress beyond this point an understanding of the energy which electrons can occupy in the chosen gain medium is necessary. Very detailed discussions of this can be found in Kittel [1]. For the purposes required here, Figure 2.1 provides a qualitative two band system for a semiconductor crystal, and its deviation from an isolated single atom [2, 3].

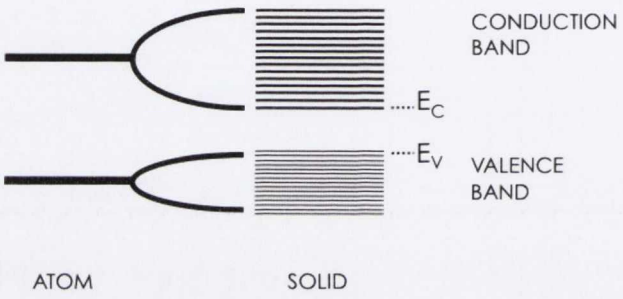

Figure 2.1: Atomic energy levels change to a band like energy distribution in a semicondcutor crystal

These levels are obtained through Schrodingers equation using the appropriate electronic potentials [3]. Due to the covalent nature of the III-V crystal, the uppermost energy levels of the constituent atoms broaden into bands of energy levels. Although this figure suggests that many conduction-valence band state pairs may interact with photons of energy E_g, due to momentum conservation the process is limited to a relatively small set of state pairs, for a given transition energy. This is illustrated by the simplified energy versus k-vector plot in Figure 2.2, for a direct bandgap bulk system [2, 4]. The bandgap energy is given by $E_C - E_V = E_g$.

The difference between the lowest and highest energies in the CB and VB respectively, represent the minimum energy required to induce a transition, called the bandgap, E_g. Since the momentum of the interacting photon is negligible, transitions between the bands have the same k-vector, allowing only direct (vertical) transitions. This bulk semiconductor example is therefore labelled a direct bandgap material, a property of the semiconductor alloy used, important for the efficient operation of semiconductor lasers and amplifiers.

Before deriving the optical transitions and their relative likelihood in the context of optical gain, the main processes, either radiative or non-radiative, are illustrated schematically in Figure 2.3. Although relating to the band structure introduced above, only transitions between a single level from each band are given for simplicity. The filled circles represent electrons (filled states) and

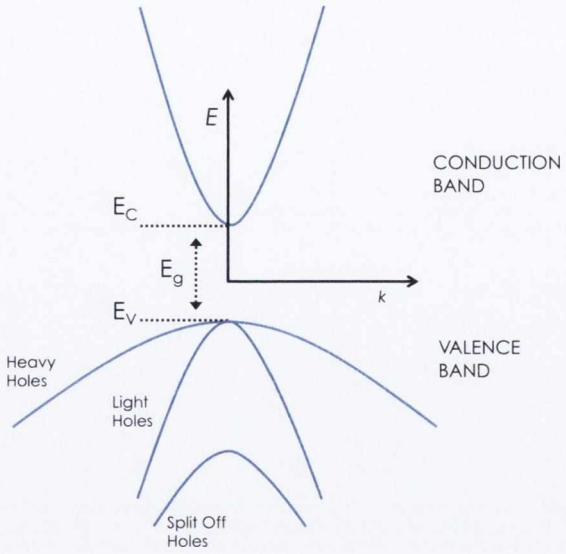

Figure 2.2: Simplified band structure of a direct gap bulk III-V Semiconductor crystal, showing the conduction band and the heavy-hole, light-hole and split-off components of the valence band

the empty circles holes (unfilled states) [2].

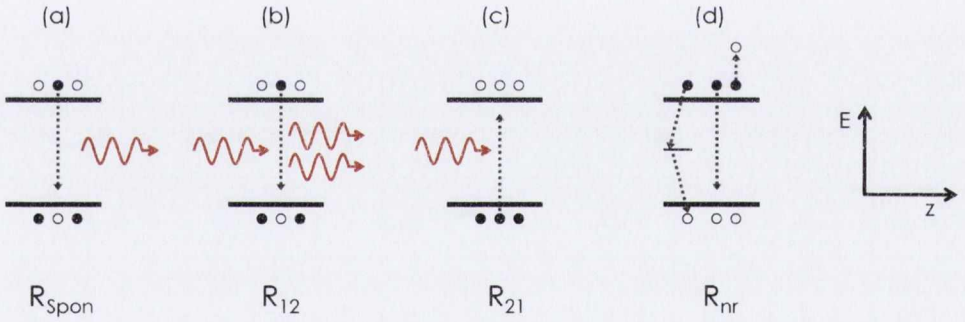

Figure 2.3: Radiative and non-radiative processes possible in a direct gap semiconductor

They are: (a) spontaneous emission via recombination; (b) stimulated emission through recombination; (c) stimulated generation via absorption and; (d) non-radiative recombination of carriers. Taking each of these in turn:

(a) *Spontaneous Emission*

There is a finite probability that an excited carrier in the conduction band will spontaneously drop to the valence band. This drop results in the emission of a photon of random phase, frequency, polarisation and direction. If the population density of the excited energy state is N_2

and the lower is N_1, the rate of this spontaneous decay is given by,

$$R_{21,spon} = \left[\frac{dN_2}{dt}\right]_{sp} = -\left[\frac{dN_1}{dt}\right]_{sp} = A_{21}N_2 \tag{2.1}$$

A_{21} is the spontaneous emission probability. The average time which the electron exists in the upper state before spontaneously recombining is defined as the spontaneous emission lifetime, $\tau_{21,spon}$, the inverse of A_{21}, $1/A_{21}$.

(b) *Stimulated Emission*

A photon of sufficient energy passing close to an excited carrier may interact causing stimulated emission before it would do so spontaneously. The excess photon energy has the same frequency, phase, direction and polarisation as the stimulating photon. Hence this amplification of an input signal is a coherent process. The stimulated emission rate is dependent on the incoming field as well as the population density to be stimulated. It is given by,

$$R_{21,stim} = \left[\frac{dN_2}{dt}\right]_{st} = -\left[\frac{dN_1}{dt}\right]_{st} = B_{21}N_2\rho(\nu) \tag{2.2}$$

Where $\rho(\nu)$ is the average spectral energy density per unit frequency for blackbody radiation, B_{21} is the stimulated emission probability per unit time per unit spectral density.

(c) *Stimulated Absorption*

After absorbing an incident photon an electron can be excited to the higher energy level as shown in (c). In the presence of a quasi-monochromatic radiation field of central frequency ν, the population level of the ground state is depleted at a rate proportional to both the population of that state and the radiation field density. This absorption rate is given by,

$$R_{12} = \left[\frac{dN_2}{dt}\right]_{abs} = -\left[\frac{dN_1}{dt}\right]_{abs} = B_{21}N_2\rho(\nu) \tag{2.3}$$

Where B_{12} is the absorption probability per unit time per unit mean intensity at a specific frequency. The input energy is accordingly decreased by an amount that was absorbed. At thermal equilibrium, the photon absorption rate must equal the sum of the spontaneous and stimulated emission rates.

An atomic system that is subject to all three of these radiative processes at once has a total decay rate given by,

$$R_{tot} = \left[\frac{dN_2}{dt}\right] = -\left[\frac{dN_1}{dt}\right] = -A_{21}N_2 + B_{12}N_1\rho(\nu) - B_{12}N_1\rho(\nu) \tag{2.4}$$

At equilibrium R_{tot}, and so the ratio of population densities, is,

$$\frac{N_2}{N_1} = \frac{B_{12}\rho(\nu)}{A_{21} + B_{21}\rho(\nu)} = \frac{g_2}{g_1}\exp(-E/kT) \tag{2.5}$$

The right most term in Equation 2.5 represents this ratio in terms of the Boltzmann distribution at thermal equilibrium, where $g_{1,2}$ relate to the degeneracy of the energy. The ratio N_2/N_1 is always less than unity when $E_2 > E_1$ and $T = 0$K. At thermal equilibrium for $T = 300$K, N_2 is 10^8 times less than N_1, implying that at this temperature at thermal equilibrium, optical amplification by stimulated emission is not possible. By equating the total decay rate with population density ratio, the spectral energy density can be obtained.

$$\rho(\nu) = \frac{A_{21}}{B_{21}}\left[\frac{g_1}{g_2}\frac{B_{12}}{B_{21}}\left[\exp(E/kT) - 1\right]\right]^{-1} = \frac{8\pi h\nu^3 n^3}{c^3\left[\exp(E/kT) - 1\right]} \tag{2.6}$$

The right most term in this case is the spectral energy density given by Plancks form [4], where n is the refractive index, c the speed of light and ν the optical frequency.

The terms in Equation 2.6 can be equal if, and only if,

$$\frac{B_{12}}{B_{21}} = \frac{g_2}{g_1} \qquad \text{and} \qquad A_{21} = \left[\frac{8\pi h\nu^3 n^3}{c^3}\right] B_{21} \tag{2.7}$$

From this point the optical material gain can be derived with the spatial dependence of the radiation field included. Starting by deconstructing $\rho(\nu)$ as a product of the transition lineshape function $l(\nu)$, and the energy density of the electromagnetic field inducing the transition ρ_ν, where $l(\nu)$ is normalised such that,

$$\int_{-\infty}^{\infty} l(\nu)\,\mathrm{d}\nu = 1 \tag{2.8}$$

the inducing field intensity (W/m^2) is,

$$I_\nu = \frac{c}{n}\rho_\nu \tag{2.9}$$

If a plane wave propagating along the z direction of the gain medium with area A and infinitesimal length dz is considered, the net power generated by a volume $A \cdot dz$ is simply a product of the transition energy, this volume and the difference in stimulated transition rates,

$$\frac{dP_\nu(z)}{dz} = (R_{21,stim} - R_{12}) \cdot h\nu A = g_m(\nu)P_\nu \tag{2.10}$$

where $g_m(\nu)$ is given by,

$$g_m(\nu) = \frac{A_{21}c^2 I(\nu)\,(N_2 - N_1)}{8\pi n^2 \nu^2} \tag{2.11}$$

$g_m(\nu)$ is defined as the material gain coefficient, and describes the fundamental ability of the material in question to provide gain, provided the condition of population inversion is adhered to ($N_2 \gg N_1$). This is the primary criteria for optical gain, stating that some external energy is required to invert the populations. It will be seen in the following sections that this is achieved in SOAs through the direct injection of carriers into an active gain region. $g_m(\nu)$ can also be derived in a more theoretically rigorous way [4, 3], yielding,

$$g_m(\nu) = \frac{c^2}{4\sqrt{2}\pi^{3/2}n^2\nu^2\tau_{rad}}\left[\frac{2m_c m_{hh}}{\hbar(m_c + m_{hh})}\right]^{3/2} \cdot [f_c(E_a) - f(E_h)]\sqrt{\nu - \frac{E_g}{h}} \tag{2.12}$$

where m_c, m_{hh} are the electron and heavy-hole masses and $f_c(E_a)$ and $f(E_h)$ are the occupations probabilities of electrons in the conduction band and holes in the valence band, respectively. All other symbols are as before. The occupation probabilities are given by,

$$f_c(E_a) = \frac{1}{1 + exp\left(\frac{E_b - E_{fc}}{kT}\right)} \tag{2.13}$$

$$f(E_h) = \frac{1}{1 + exp\left(\frac{E_b - E_{fv}}{kT}\right)} \tag{2.14}$$

where k is Boltzmann's constant and T is the temperature. The material gain is composed of a gain coefficient (g'_m) and an absorption coefficient (g''_m)

$$g_m = g'_m - g''_m \tag{2.15}$$

For positive gain to dominate the gain coefficient must be greater than the loss.

(d) *Non-Radiative Processes*

The non-radiative processes in (d) are given here again, and split up for clarity. It is important to ascertain the effect of each on the total carrier recombination process. Ideally their total sum would be zero, where all recombination is radiative, and higher levels of gain could be achieved.

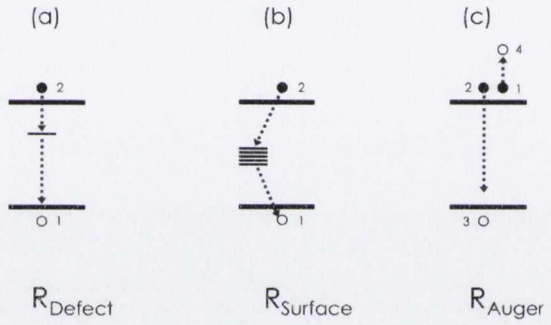

Figure 2.4: The (a) defect, (b) surface and (c) Auger related non-radiative recombination processes

The first non-radiative recombination concerns defect and impurity states (a). This results in mid-bandgap energy levels, which can trap electrons and holes. The rate is denoted by R_{defect}. Where this is particularly important is in the ageing of a device. As it goes through many thermal cycles the crystal lattice is put under stress leading to an increasing level of defect states throughout, increasing R_{defect}.

Figure 2.4 (b) denotes the non-radiative recombination of carriers due to surface states. In essence it is similar to defect or impurity states, but instead of being modelled as a two dimensional sheet density. The surface states generally arise from the termination of the lattice [2], leaving so called dangling bonds, in high density. These are likely to form mini bands as shown. Low quality surfaces also contribute greatly to this. As will be explored in Chapter 7 a resultant increase in the surface area, a by-product of post processing modifications to the SOA chips, can lead to an increased level of this type of recombination.

Finally, Figure 2.4 (c) illustrates the recombination due to Auger processes. They are shown in

Figure 2.5 in more detail [2]. The underlying component of this process is a collision between carriers (electrons or holes). A collision between 2 electrons can knock an electron to higher energies within the conduction band, which then settles back through an energy transfer to the lattice. Similarly a hole-hole collision will result in a hole dropping to a lower energy state from the heavy hole (HH) band to the split off (SO) or light hole (LH) bands. For intrinsic active regions, such as those of an SOA, all three are contributory processes[2].

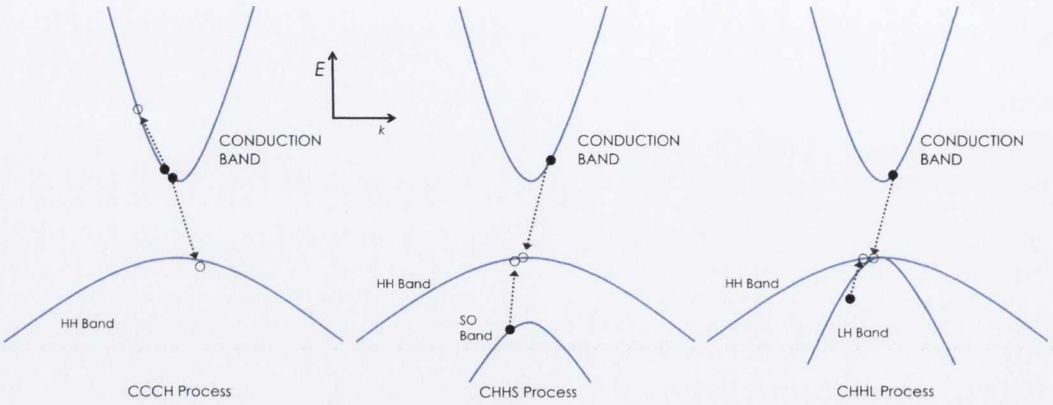

Figure 2.5: Quaternary related Auger processes (a) CCCH (b) CHHS and (c) CHHL. C is the conduction band and H,L and S the heavy hole(HH), light hole(LH) and split-off (SO) valence bands respectively

2.2 SOA Operation

With the gain processes in semiconductor materials understood, the SOA function is now described. This section will begin with a basic description of the pin heterostructure which constitute the SOA, and how this relates to the guiding of the optical mode and confinement of the injected carriers.

2.2.1 The PIN Junction

Having discussed the basis of optical gain in semiconductors, and the requirement for some external influence inducing a population inversion, we will now review the the structural solution of how to amplify a light signal practically. The fundamental structure behind the SOA is the pn junction which is well understood and detailed in [3, 5]. Briefly, a semiconducting layer which is p-doped with electron acceptor ions (an excess of holes), is joined with an n-type material, which is doped with an excess of electrons. The excess electron concentration begins to diffuse into the p-type material and vice versa. As this process continues an electric field begins to build up

at the junction. This electric field then causes a counteracting drift of charges, creating a space-charge free region, known as the depletion region. The criteria for population inversion is met through the introduction of an external forward bias greater than the barrier potential, across the structure, injecting carriers into the depletion region. The population inversion critera is met, where $N_2 > N_1$. It is here that carriers recombine via radiative and non-radiative processes. The main issue is that the dimension of the depletion region is driven by the mobility of the carriers and therefore is of the order of a few microns. By increasing this region it will be possible to increase the gain. A structure based on this operation, where population inversion is achieved when an external voltage is applied, but providing both optical and carrier confinement, is called the double heterostructure and is shown in Figure 2.6. This structure provides the basis for the SOA.

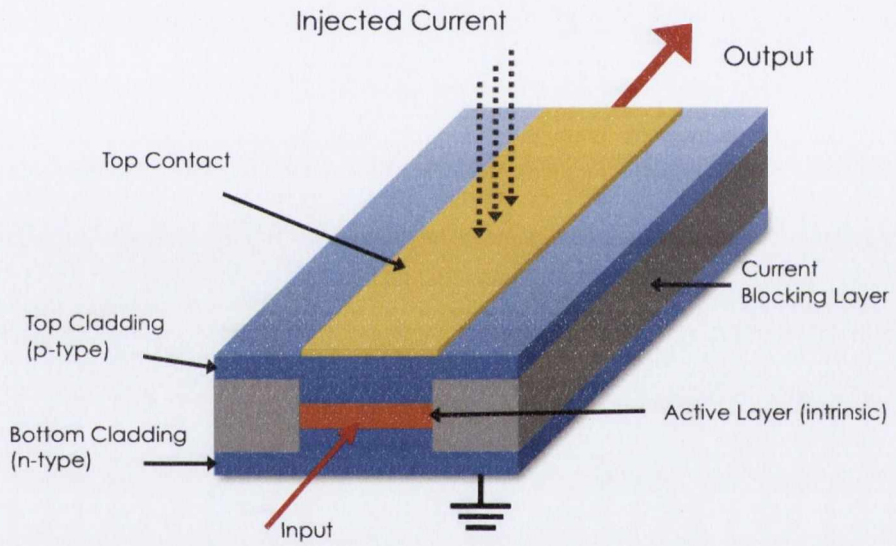

Figure 2.6: Schematic of a double heterostructure–the fundamental basis of the SOA. Shown is the layer structure:active and cladding layers;contacts for applying current, and current blocking layers

Practically, recombination must occur in a region of the device through which the optical input signal can propagate for efficient amplification. To this end the SOA consists of an optical waveguide (the intrinsic layer) in which the input signal is confined to a core of higher refractive index than the cladding. This is called the active region, where the recombining carriers contribute to useful gain. The cladding is comprised of p-type and n-type layers of the heterojunction. The active layer has a lower bandgap than the cladding, trapping injected carriers in a potential well for spatial overlap with the injected photons [6] These properties are shown in Figure 2.7. It should be noted that emission can occur at other points in the structure, due to defect and surface states. This does not contribute to the useful gain of the device.

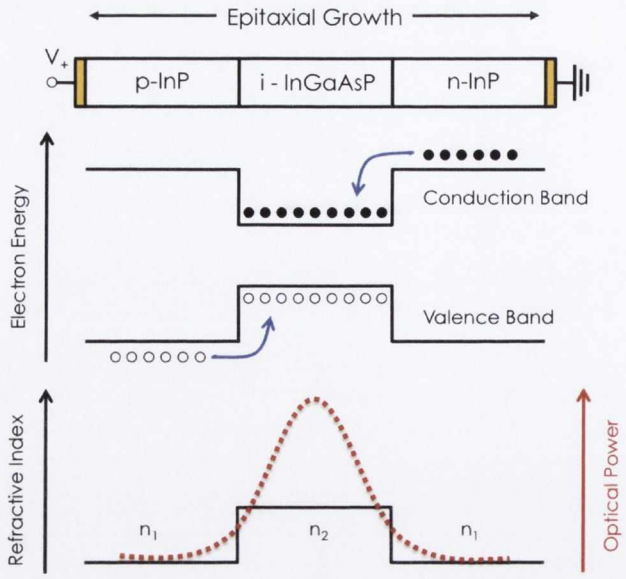

Figure 2.7: Qualitative illustrations of the epitaxial structure, consequent energy diagram and refractive index step, across the growth layers. The red line shows the resultant confinement of optical power.

The applied forward bias provides the necessary population inversion required. However not all of the injected current contributes to this process. The internal quantum efficiency (η_i), or simply conversion efficiency, is the fraction of the terminal current that generates carriers in the active region. This definition includes all carriers produced, not just those that contribute radiatively. The rate of injected carriers is,

$$G_{gen} = \frac{\eta_i I}{qV} \tag{2.16}$$

2.2.2 Confinement Factor

Detailed analysis of waveguiding in double heterostructures by taking a three slab approach is dealt with in [2, 5]. Briefly, starting from a single layer of Figure 2.8 and Maxwells equations, a wave equation of the form below is derived,

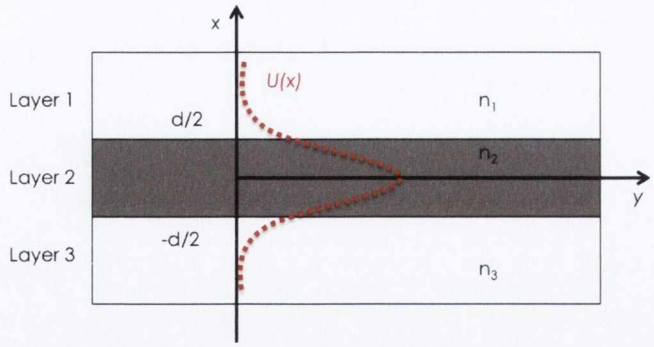

Figure 2.8: Three layer slab waveguide, with top p-layer, middle intrinsic layer of thickness d and third layer of cladding material. $U(x)$ is the normalised optical intensity per unit length

$$\nabla^2 E = \mu\epsilon \cdot \frac{\partial^2 E}{\partial t^2} \tag{2.17}$$

where ϵ is the dielectric constant, and μ the magnetic permeability. The imaginary part of ϵ includes the gain or loss that can occur in the medium. To solve this equation for a wave propagating along the z direction, the following solution is used,

$$E(x, y, z, t) = \hat{e} E_0 U(x, y) \cdot e^{j(\omega t - \tilde{\beta} z)} \tag{2.18}$$

The unit vector $\hat{e}$ accounts for the polarisation. $U(x, y)$ is the transverse amplitude function and has units of per unit length. Upon substituting this solution into Equation 2.17, it is found that the transverse amplitude function must satisfy,

$$\nabla^2 U(x, y) + \left[\tilde{n}^2 k_0^2 - \beta^2\right] U(x, y) = 0 \tag{2.19}$$

where $\tilde{n}^2$ is equal to the free space propagation constant, and $k_0^2 = \omega^2 \mu_0 \epsilon_0 = (2\pi/\lambda)^2$ To progress this to the three slab case, the above equation is solved for uniform n in each of the three regions and then matching the boundary conditions at the interfaces. It can be found from this that the solutions vary slightly for the TM mode, where the magnetic field is polarised along the x axis [2, 5].

The confinement factor is a quantifiable measure of the wave guiding process. It is defined as the fraction of optical energy that is contained in the active waveguide region (Layer 2), and is

given by,

$$\Gamma = \frac{\int_{-d/2}^{d/2} |U(x,y)|^2 \, dx}{\int_{-\infty}^{\infty} |U(x,y)|^2 \, dx} \tag{2.20}$$

This is a general form, and as will be discussed in a following subsection, is a polarisation dependent quantity.

2.2.3 Residual Reflection

The entirety of this work is based on travelling wave SOAs where a signal is amplified through a single pass of the device. In this way any residual or stray reflections within the waveguide cavity can have a detrimental effect on most device parameters. With the high index contrast at the active InGaAsP/air interface this can be of more concern. As was stated above, the facets have anti-reflection coatings (ARC), and the waveguide is angled, but in reality a proficient SOA will use a number of structural precautions to further diminish any facet reflections. Figure 2.9 shows some examples of these techniques.When a number of these methods are combined, extremely low levels of effective reflectivity of $2x10^{-6}$ have been attained [7].

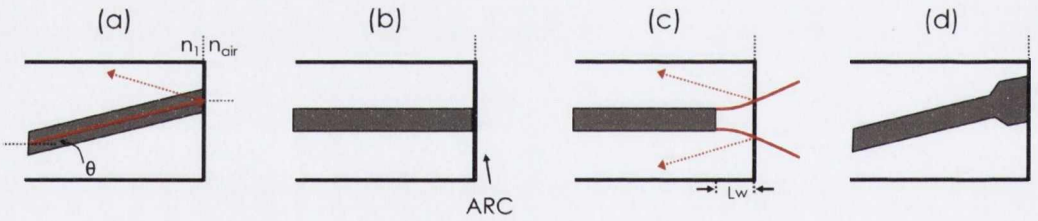

Figure 2.9: Top down view of SOA facets with different techniques of cavity effect suppression. (a) An angled waveguide (b) anti-reflection coatings (c) a window region and (d) an angled flared waveguide

If the facet is angled, as in (a), the waveguide is slanted away from the cleaved plane. The result is to reduce the effective reflection coefficient, where reflected light is directed into the cladding region. Angles in the range $7° - 12°$ range tend to act as a balanced trade off between successful reduction of reflections and the loss of coupling to an optical fibre, due to asymmetry introduced at the far field at higher angles. In addition, where this technique is usually used in conjunction with ARCs (b), higher angles increase the polarisation sensitivity of the coatings [8]. The ARCs are dielectric stacks of differing refractive index, designed such that destructive interference occurs among reflections at each interface [7, 8]. Polarisation sensitivity is in general

very low in modern ARCs at small angles of incidence. An additional technique now commonly used is the window region (c). The active waveguide is terminated tens of microns before the facet, allowing the modal field to diverge thereby providing poor coupling of the reflected light back into to the waveguide [7]. The final method is the angled flared waveguide (d). The reflectivity decreases as a function of waveguide width (w), however single mode operation must be maintained. To avoid the introduction of higher order modes, the active waveguide width can be increased near the facet region only, abiding both single mode operation and reduced reflection [7].

The effect of residual reflections is most evident in the form of resonant or anti-resonant amplification, depending on whether a whole number of wavelengths fit in the cavity. The effect is most readily observed in the amplified spontaneous emission (ASE), where ripples can be seen. Their depth is given by,

$$R_D = \frac{(1 + g \cdot r)^2}{(1 - g \cdot r)^2} \tag{2.21}$$

where g is the chip gain, and r is the effective reflectivity. If r is known, the ripples may be used to calculate the gain of the device by various techniques [9, 10, 11], the most prominent of which is the Hakki-Paoli Method [12]. This will be discussed in more detail when addressing the ASE.

2.2.4 Gain Media

With the operation of the SOA now understood in terms of a non-specific bulk active layer, and the consequent waveguiding, it is important to explain that the active layer discussed can be replaced by a number of alternate structures, each with their own benefits and drawbacks. In fact, beyond the growth of the different gain media, the structures may otherwise be identical.

1 *Bulk Material*

The most common and well developed material system is based on the bulk properties of InGaAsP/InP [13]. The choice of this material system is adequate to allow access to both $1.3\mu m$ and $1.5\mu m$ bands, both heavily used for communications. Bulk active regions will feature prominently in this thesis. For a bulk device the layer growth must be many times larger than the point at which quantum effects become apparent [14, 15]. The material gain coefficient derived in Equation 2.12 (g_m) is based on this structure, where a continuous density of states exists. A theoretical description of bulk InGaAsP can be read in [16]

2 *Quantum Well*

If the thickness of the active layer is sufficiently reduced to very small dimensions below the De Broglie wavelength, quantisation effects of the confined carriers will occur, forming a quantum well (QW) region. Several layers (including barrier layers in between) can be stacked to form multi QW (MQW) regions. This can result in both larger optical gain per electron-hole pair and lower injected current densities [17, 2]. The difference in band energies and density of states are shown in Figure 2.10. Specific advantages include: enhanced differential gain associated with reduced (2-D) density of states, which can in turn be applied to achieving a high modal differential gain and high direct-modulation bandwidth; reduced threshold current as a result of suppression of Auger recombination achieved via band-structure engineering; higher characteristic temperature [18].

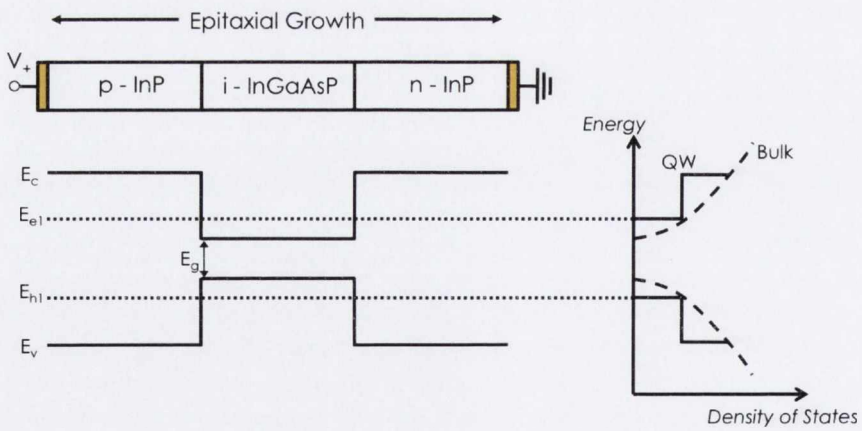

Figure 2.10: Qualitative comparison of the band energies and density of states of a bulk III-V SOA and a quantum well structure. The top layer schematic does not represent the difference in layer thickness to scale. Layer thickness is in general less than 10 nm [2, 5]

3 *Quantum Dot*

If carriers are further confined in all three dimensions a quantum dot (QD) is formed. In this case the emission wavelength is directly related to the dot size, and therefore tunable. If the density of states were shown on the above diagram it would consist of isolated lines at specific energies. In reality however a broad gain spectrum can be achieved by multiple layers of dots with varied size distributions. QD SOAs have very limited confinement, compensated for by very high polarisation-independent gain, requiring much longer chips. SOAs in excess of 3mm are not uncommon [19, 20, 21]. QDSOAs have been produced with ultra wideband operation and excellent polarisation sensitivity using isotropic stacks. Additionally, very promising carrier dynamics exist due to the wetting layer, a thin film of the QD material produced as a by-product of the formation process acting essential as a carrier reservoir. The result of this is pattern free linear amplification and interesting functional operation in the saturated regime [22, 23, 24]. Finally, the added effect of both low confinement and the quasi-three level system relating to the wetting layer, have produced demonstrations of low chip noise figures. This will be discussed further in Chapter 3.

2.3 Steady State Properties

2.3.1 Amplified Spontaneous Emission

An unavoidable consequence of establishing population inversion is the spontaneous recombination of carriers, producing photons of random phase, direction, polarisation and energy, as was described in section 2.1. This occurs both in the absence of an injected signal and under injection. In a laser cavity the effect is harnessed and a particular wavelength selected. In an SOA however, it acts as a source of noise. The ASE is plotted in Figure 2.11 (a), where the spectral dependence of the ASE is given for increasing pump current. The corresponding integrated ASE power as a function of applied current (LI curve) is shown in (b).

At low injected currents the device acts much like a light emitting diode (LED). However as the pumping is increased the spontaneously produced photons act to stimulate further transitions which are eventually guided, in turn inducing yet more transitions. As was seen by the formulation of the material gain coefficient, this is an inherent process and will always occur no matter what structure is used or how the device is pumped. Spontaneous emission occurs over a range

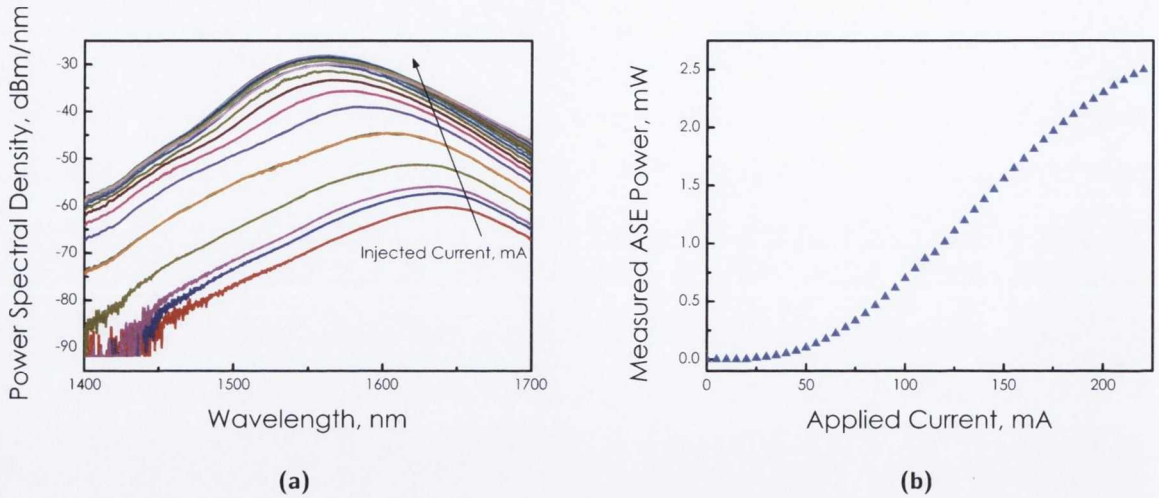

Figure 2.11: (a) Amplified Spontaneous Emission (ASE) spectra at high injected bias for an arbitrary bulk SOA. (b) Total ASE output power as a function of applied current

of wavelengths corresponding to the occupied states of the semiconductor energy bands, in all spatial directions. There are two main reasons for the bandwidth limited gain. Firstly, as described previously, the material gain itself is highly frequency dependent. The second relates to the wavelength dependent performance of the waveguiding structure, namely dispersive effects. More details of the frequency cut off of waveguides can be found in [4]

Although a negative attribute, much information can be garnered through analysis of these data including estimation of the polarisation dependent gain spectrum, threshold current and non-radiative processes [25]. The most common method uses the residual reflections which survive in the cavity in conjunction with the facet reflectivity values to determine the device gain [12]. Alternative non-injection based methods varying in complexity also exist [12, 9, 10, 11].

2.3.2 Gain

Frequently, the most important parameter of any optical amplifier is its ability to provide gain to an incoming signal. As previously described the process occurs via stimulated emission by the input light, where population inversion is achieved by electrically pumping the double heterostructure. The gain is defined as the ratio of the output to input signal powers and given (in dB) by,

$$G = Log\left(\frac{P_{out}}{P_{in}}\right) = e^{(\Gamma g_m - \alpha)} \tag{2.22}$$

where g_m is the material gain and α is a loss coefficient.These terms correspond to the total wavelength dependent gain from the chip, i.e accounting for losses. To characterise the gain in a practical scenario, including losses from the coupling optics, we refer to the fibre-to-fibre gain (G_{ff}), which represents the lower value of gain at this point. All gain values quoted in this work are chip gain, the gain experienced without any coupling losses.

There is a spectral dependence of the gain, where the useful range of frequencies is called the 3dB gain-bandwidth. These are the boundary wavelengths at which the gain has decreased by half. The same reasons that cause this effect with the ASE are at play here too. The experimental calculation of gain will be described in Chapter 4.

2.3.3 Gain Saturation

An optical amplifier has two distinct regimes of operation: The linear gain region and the saturated gain region. The point that marks the juncture between these is defined as the Saturation Power (P_{sat}). It represents the input or output power at which the gain has decreased by 3dB (a factor of two). It can be given in terms of input ($P_{sat,in}$) or output powers (P_{sat}), although the latter is more common [4, 6]. The saturation input and output powers are shown in Figure 2.12.

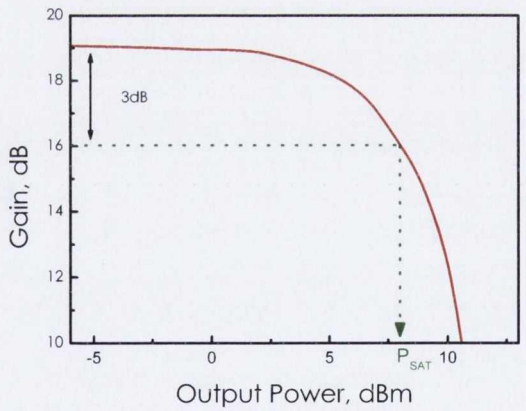

Figure 2.12: Plot of gain as a function of output power. The saturation point is shown on the x-axis

In the same way that an optical amplifier has wavelength dependent limits, so too can it only accommodate a limited input power. The origins of the gain saturation lie in the depletion of available carriers by stimulated emission. As the input power is increased, at some point the rate of carrier generation cannot accommodate the extra photons entering the active region. As carriers recombine the gain is reduced and at the same time the peak wavelength shifted

to lower energies. It should be noted that the input power refers to all incident light, including accumulated ASE from other amplifiers in a real network situation. Quantification of P_{sat} will be undertaken in Chapter 3, where it will be shown that control of this property is both desirable and possible.

At powers beyond this point, the gain behaves non-linearly, having a negative impact on incident optical signals if the intended operation is based on linear amplification. In a multi-channel system, this manifests as patterning, where the gain recovery time occurs over a time frame comparable to the bit rate of the signal. Be that as it may, if instead the intended use of the SOA is more functional, where optical switching is desired etc, these non-linear effects can be harnessed for positive uses [26]. This will be discussed in more detail below when describing gain dynamics, and in Chapter 6 where these effects are experimentally examined.

2.3.4 Noise Figure

Accompanying the amplified output is an additive noise power term, stemming directly from the production of amplified spontaneous emission in the active waveguide through g_m. All phase sensitive optical amplifiers exhibit this property [27, 6]. The output of the amplifier can be represented as,

$$P_{out} = G \cdot P_{in} + P_{ASE} \tag{2.23}$$

where G is the gain factor in linear units P_{out}, P_{in} and P_{ASE} are the absolute signal-output, signal-input and ASE powers, respectively.

The effect of the ASE power component on a propagating signal is quantified in the steady state by the noise figure, defined as the degradation of the signal-to-noise ratio (SNR) of the passing signal, i.e. the ratio of the SNR_{in} and SNR_{out} of the device given in dB,

$$NF = 10 \cdot log\left(\frac{SNR_{in}}{SNR_{out}}\right) \tag{2.24}$$

The extent to which ASE noise dominates has inhibited the widespread adoption of SOAs, and thus far has yet to produce a practical solution. Typical values accepted by modern communications systems are 7-9dB fibre-to-fibre. In contrast to this, the Erbium doped fibre amplifer

(EDFA), can operate with NFs of 4dB fibre-to-fibre [28]. The reason for this will be treated more comprehensively in the next chapter, where it will also be shown that, much like the saturation power, it is possible to reduce the NF through SOA design considerations. This thesis is concerned with the investigation of two possible techniques to reduce the noise figure and the effect of these modifications on other performance characteristics of the SOA.

2.3.5 Polarisation Sensitivity

Gain insensitivity to the input polarisation state is a fundamental requirement for SOAs, and has been intensively studied. In general, an SOA will not provide equal gain for all input polarisations. In a fiberised communications scenario the input signal will have an arbitrary polarisation state. If the SOA does not provide sufficient gain across all polarisations deleterious effects can manifest, reducing the practical situations for which the SOA can be used.

The gain media, comprised of III-V materials, are generally isotropic and therefore independent of polarisation. However when the entire structure of the SOA is taken into account, the orthogonal confinement factors deviate from each other, due to lattice strain between different growth layers and geometrical differences. In general this causes a reduced TM gain [29]. This leads to a natural definition of the polarisation dependent gain (PDG) under continuous wave injection, which is the difference in steady state gain between the transverse electric (TE) and transverse magnetic (TM) modes.

$$PDG(dB) = G_{TE}^{dB} - G_{TM}^{dB} \tag{2.25}$$

Where this condition equates to a value of less than 1dB, an SOA is by definition polarisation independent [6].

Gain anisotropy of less than 1dB is still significant and so much work has concentrated on minimising this dependence [15, 30, 31]. An impractical technique, but one which shows excellent results, is to produce a perfectly square waveguide, thus equalising the separate confinement factors [30]. This requires difficult growth and waveguide dimensions are quite limited so as to maintain single mode operation [30]. Furthermore great care is required to ensure a very high degree of lattice matching, minimising any residual strain [32, 33]

A more practical method is to introduce a small, but carefully calculated level of lattice mismatch

between the substrate and the active layer. This leads to an introduction of tensile strain, lifting the degeneracy of the valence band in such a way that the TE gain is reduced, and the TM gain favoured. This is accounted for by the fact that the two polarisations couple to different hole reservoirs [33, 29, 31, 34]. These correspond to the heavy-hole (HH) and light-hole (LH) valence bands seen in Figure 2.5 on page 14.

By careful tailoring of the lattice mismatch, effectively polarisation independent gain can be attained [35, 29]. It should be noted that although this is true for the continuous wave regime, it does not necessarily carry over when short optical pulses are injected into the device [33, 31].

2.4 Carrier Dynamics

The SOA gain and refractive index nonlinearities are governed by the free-carrier dynamics resulting from interband and intraband effects. The dynamics associated with the interband effects are induced by changes in the total free-carrier concentration inside the conduction and valence bands caused by stimulated emission, absorption, spontaneous emission, and nonradiative recombinations.

The carrier recovery time of SOAs can have a negative impact on the use of the device in linear amplification setups. In general, for bulk and QW structures the recovery times once the gain has been saturated are very fast, on the order of tens to hundreds of picoseconds [36, 37, 38]. Comparing this with the more common amplifier of choice, the Erbium Doped Fibre Amplifier (EDFA) which has a recovery time of a few milliseconds, it is clear that for an SOA to be practical in this way, the saturation must be very low, or the recovery time must be sufficiently different from the bit rate being amplified [39]. The electron dynamics are illustrated in Figure 2.13 under injection of a short optical pulse, saturating the gain.

Upon injection of the optical pulse depletion of carriers from the conduction band leads to a reduction in gain at a characteristic rate, given by the fall time, τ_{fall}. As a consequence of the reduction in the density of excited electrons the refractive index of the waveguide is also modified [40]. The gain and index subsequently recover by the temporal overlapping of the processes shown in Figure 2.13 and described below, each with their own unique timescales, depending on the conditions of the system. The fastest processes are generally intraband, where carriers recover to states within the same band.

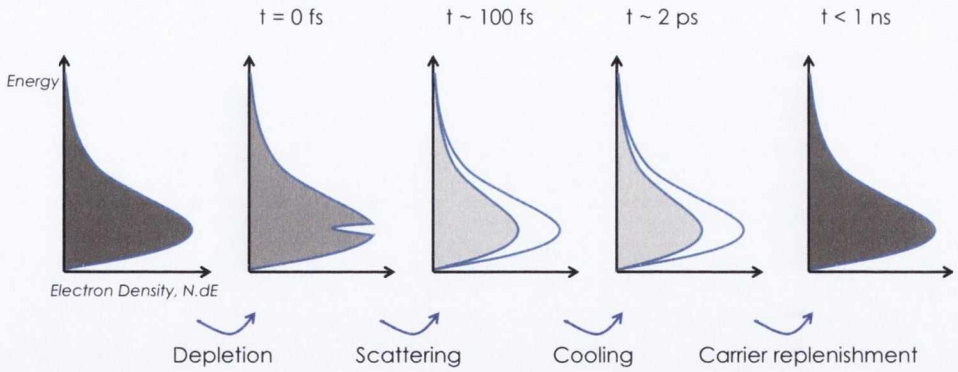

Figure 2.13: Qualitative evolution of the electron energy density ($N.dE$) as function of electron density (ρ). Under injection of a short optical pulse, carriers are depleted and the gain saturated. The subsequent steps illustrate the recovery of the carriers to the conduction band, through stages of scattering, temperature relaxation and finally, electrical pumping.

Immediately following gain compression, the carrier energy-density is characterised by a non-equilibrium distribution, governed by Spectral Hole Burning (SHB), the frequency-dependent gain saturation occurring at the transition energy, and other quasi-instantaneous non-linear effects, such as two photon absorption (TPA) and optical Kerr effects [41, 42, 43]. It has been suggested that the main contribution to the recovery of the electron energy-density to a quasi-Fermi-Dirac distribution are carrier-carrier scattering and heating, occurring over a timescale of 50−1000fs. The majority of this recovery will likely have occurred within less than a few hundred femtoseconds and is a material dependent property.

Following the main intraband processes of SHB and the subsequent recovery, carrier heating (CH) dominates, where transient heating of the electrons and holes occur. Injection of carriers into the gain structure contribute to this process, as well as free carrier absorption (holes in particular), and Auger related recombination. Finally the carrier density is fully restored over hundreds of Pico seconds via interband transitions through electrical pumping [41].

In Chapter 6, the carrier dynamics will be experimentally examined in a Multi Contact SOA using pump-probe studies, assessing the effect of longitudinal carrier density modification on the rise and fall times. To this end, more details will be provided at this point relating to the above processes and their characteristic times.

2.5 The State of the Art

The extensive research concentrated on semiconductor optical amplifiers for the last three decades has overcome many of the disadvantages originally associated with them. These have included high polarisation sensitivity as previously described, a gain recovery which induces patterning at high communication speeds, poor saturation and noise figure performance (the techniques established for this will be treated in detail in the next chapter) and low coupling efficiency. At the design and fabrication level structure has become technically advanced, playing a significant role in overcoming these negative attributes, where SOAs are now commonly grown with specific objectives in mind [44, 6, 3, 4].

By far the largest explosion in research in recent years, has focused on quantum well and quantum dot SOAs, for both linear and non-linear operation [45]. The latter in particular is developing at pace, where excellent performance has been demonstrated regarding high gain, high saturation power and low NF [19, 46, 47, 39]. The unique behaviour of QDSOAs and QWSOAs have been comprehensively studied through both numerical modelling and experimental characterisation [21], with a very comprehensive overview given by [19] and references therein. Both structures are readily available in both the 1300nm & 1550nm varieties for specific application [46]. For QDSOAs, the reasons for their improved performance over bulk materials, is in general related to a combination of a low modal gain, low differential gain, and the large energy separation between ground state (GS), excited state (ES), and wetting layer (WL). The latter results in a system which can in many respects be considered a three-level system similar to the EDFA. Indeed published data have shown properties which more closely resemble the properties of an EDFA than those of bulk and QW amplifier. In addition to their impressive linear operation, QDSOAs have shown exceptional dynamic recovery [23, 48, 49], with full gain recovery dominated by intraband processes, shown to be one and two orders of magnitude faster than their bulk counterpart. This points to very promising potential for ultrafast functional duties.

More recently, integrated and all optical functionality has been demonstrated. The majority of work has concentrated on the integration of SOAs with Mach-Zender Interferometers (MZI), lasers, array waveguides (AWG) and other SOAs in various combinations as part of functional photonic integrated circuits [50, 51, 52]. This has ranged from components for all optical logic, most recently the demonstration by Kang et al of all-optical "OR" operation with a hybrid MZI/SOA, to the combination of SOAs and phase modulators (PM) for the fabrication of coupled-ring filters at communications wavelengths [53], to the demonstration of an all-optical

square wave photonic clock [54]. A review by Lie et al [55] covers the progress to date in all optical signal processing in communications comprehensively.

Finally, an SOA structure which has received a lot of attention in the last decade is the reflective SOA (RSOA) [8, 56]. Unlike a travelling wave SOA, the RSOA presents the conflicting requirements of a high reflectivity coating at the back facet and a low reflectivity coating at the front facet. This requires a combination of a normal and an angled facet on the same device. RSOAs are generally used as functional elements. For example, they have recently been used in demonstration of all-optical modulation [57], and chirp reduction in directly modulated RSOAs [58]. RSOAs represent the newest in a long line of SOA structures, where a vast array of applications potentially exist.

2.6 Conclusion

After establishing the requirements for gain in bulk semiconductor materials, the operation of the SOA was described in the context of carrier and optical confinement for different gain media, where population inversion is achieved through electrical pumping. The steady state properties were then defined. Following this, the basic attributes of gain compression and subsequent recovery under dynamic injection were outlined. A brief state of the art was provided addressing the technical aspects of device design. The next chapter will provide greater detail regarding the noise figure and saturation behaviour of SOAs, where it will be shown that these parameters can be improved by controlling the carrier density along the length of the device.

References

[1] C. Kittel, *Introduction to Solid State Physics*. No. March, Wiley, 8th ed., 2004.

[2] L. A. Coldren, S. W. Corzine, *Diode Lasers and Photonic Integrated Circuits*.

[3] A. Yariv, *Photonics: Optical Electronics in Modern Communications*. No. March, Oxford University Press, 2007.

[4] H. Ghafouri-Shiraz, *The Principles of Semiconductor Laser Diodes and Amplifiers*. Imperial College Press.

[5] J. Buus, *Tunabe Laser Diodes & Related Optical Sources*.

[6] M. J. Connolly, *Semiconductor Optical Amplifiers*. Kluwer Academic Publishers, Boston, 2010.

[7] J. M. Wiesenfeld and L. H. Spiekman, "Semiconductor optical amplifiers," in *Handbook Of Optics*, pp. 1–42, 2010.

[8] A. E. Kelly, C. Michie, W. Zhong, S. Karagianopoulos, W. I. Madden, C. Tombling, and I. Andonovic, "High performance polarisation independent reflective semiconductor optical amplifiers in the S , C , and L Bands," *IEEE Journal of Selected Areas in Communications*, vol. 28, no. 6, pp. 943–948, 2010.

[9] P. Blood, G. M. Lewis, P. M. Smowton, H. Summers, J. Thomson, and J. Lutti, "Characterization of Semiconductor Laser Gain Media by the Segmented Contact Method," *IEEE Journal of Selected Topics in Quantum Electronics*, vol. 9, no. 5, pp. 1275–1282, 2003.

[10] D. T. Cassidy, "Technique for measurement of the gain spectra of semiconductor diode lasers," *J. Appl. Phys*, vol. 56, no. 11, pp. 3096–3099, 1984.

[11] W.-h. Guo, Q.-y. Lu, Y.-z. Huang, S. Member, and L.-j. Yu, "Measurement From Amplified Spontaneous Emission Spectra of Fabry Pérot Semiconductor Lasers," *IEEE Journal of Quantum Electronics*, vol. 40, no. 2, pp. 123–129, 2004.

[12] B. W. Hakki, T. L. Paoli, "Gain spectra in GaAs double-heterostructure injection lasers," *Joural of Applied Physics*, vol. 46, no. 3, pp. 1299–1306, 1975.

[13] K. Hara, K. Kojima, K. Mitsunaga, and K. Kyuma, "Gain and noise characteristics of a 1.5micron near travelling wave semiconductor laser amplifier," *Electronics Letters*, vol. 25, no. 7, pp. 434–436, 1989.

[14] Ch. Holtmann, P. A. Besse, T. Brenner, H. Melchior, "Polarization independent bulk active region semiconductor optical amplifiers for 1.3micron wavelengths," *IEEE Photonics Technology Letters*, vol. 8, no. 3, pp. 343–345, 1996.

[15] J. Emery, T. Ducellier, M. Bachmann, P. Doussiere, F. Pommereau, R. Ngo, F. Gaborit, L. Goldstein, G. Laube, and J. Barrau, "High performance 1.55 um polarisation-insensitive semiconductor optical amplifier based on low-tensile-strained bulk GaInAsP," *Electronics Letters*, vol. 33, no. 12, pp. 1083–1084, 1997.

[16] M. J. Connelly, "Wideband semiconductor optical amplifier steady-state numerical model," *IEEE Journal of Quantum Electronics*, vol. 37, no. 3, pp. 439–447, 2001.

[17] D. Tauber, R. Nagar, A. Livne, G. Eisenstein, U. Koren, G. Raybon, "A low noise figure 1550nm multiple-quantum well optical amplifier," *IEEE Photonics Technology Letters*, vol. 4, no. 3, pp. 238–240, 1992.

[18] G. Eisenstein, N. Tessler, U. Koren, J. M. Wiesenfeld, G. Raybon, C. A. Burrus, "Length dependence of the saturation characteristics in 1550nm multiple quantum well optical amplifiers," *IEEE Photonics Technology Letters*, vol. 2, no. 11, pp. 790–791, 1990.

[19] B. T. Akiyama, M. Sugawara, and Y. Arakawa, "Quantum-Dot Semiconductor Optical Amplifiers," *Proceedings of the IEEE*, vol. 95, no. 9, 2007.

[20] B. W. Tilma, M. S. Tahvili, J. Kotani, R. Nötzel, M. K. Smit, and E. a. J. M. Bente, "Measurement and analysis of optical gain spectra in 1.6 to 1.8 μm InAs/InP (100) quantum-dot amplifiers," *Opt. Quant. Electron.*, vol. 41, pp. 735–749, May 2009.

[21] M. Sugawara, H. Ebe, N. Hatori, M. Ishida, Y. Arakawa, T. Akiyama, K. Otsubo, and Y. Nakata, "Theory of optical signal amplification and processing by quantum dot semiconductor optical amplifiers," *Physical Review B*, vol. 69, pp. 1–39, June 2004.

[22] T. Berg, J. Mork, "Saturation and noise properties of quantum dot optical amplifiers," *IEEE Journal of Quantum Electronics*, vol. 40, no. 11, pp. 1527–1539, 2004.

[23] C. Meuer, C. Schmidt-Langhorst, R. Bonk, H. Schmeckebier, D. Arsenijević, G. Fiol, A. Galperin, J. Leuthold, C. Schubert, and D. Bimberg, "80 Gb/s wavelength conversion using a quantum-dot semiconductor optical amplifier and optical filtering.," *Optics express*, vol. 19, pp. 5134–42, Mar. 2011.

[24] J. Park, Y. D. Jang, J. S. Baek, N. J. Kim, K. J. Yee, H. Lee, D. Lee, S. H. Pyun, W. G. Jeong, and J. Kim, "Gain recovery in a quantum dot semiconductor optical amplifier and corresponding pattern effects in amplified optical signals at 1.5 μm.," *Optics express*, vol. 20, pp. 6215–24, Mar. 2012.

[25] B. F. Kennedy, P. Landais, S. Philippe, M. Martinez-Rosas, A. L. Bradley, "Temporal and spectral dependence on polarization of the input signal in a semiconductor optical amplifier," in *Integrated Photonics Research (IPR)*, 2004.

[26] W. Freude, R. Bonk, T. Vallaitis, A. Marculescu, A. Kapoor, E. K. Sharma, C. Meuer, D. Bimberg, R. Brenot, F. Lelarge, G.-h. Duan, C. Koos, and J. Leuthold, "Linear and nonlinear semiconductor optical amplifiers," in *International Conference of Transparent Optical Networks (ICTON)*, vol. 1, pp. 4–7, 2010.

[27] E. Desurvire, "On the physical origin of the 3-dB noise figure limit in laser and parametric optical amplifiers," *Optical Fiber Technology*, vol. 5, pp. 40–61, 1999.

[28] B. J. Ainslie, "Noise Figure for Erbium Doped Optical Fibre Amplifiers," *Electronics Letters*, vol. 24, no. 22, pp. 1363–1365, 1988.

[29] P. Koonath, S. Kim, W.-j. Cho, and A. Gopinath, "Polarisation-insentitive quantum-well semiconductor optical amplifier," *IEEE Journal of Quantum Electronics*, vol. 38, no. 9, pp. 1282–1290, 2002.

[30] C. Michie, a. E. Kelly, J. McGeough, I. Armstrong, I. Andonovic, and C. Tombling, "Polarization-Insensitive SOAs Using Strained Bulk Active Regions," *Journal of Lightwave Technology*, vol. 24, pp. 3920–3927, Nov. 2006.

[31] L. Huang, D. Huang, J. Chen, D. Liu, and X. Zhang, "Analysis of a semiconductor optical amplifier with polarization-insensitive gain and polarization-insensitive phase modulation," *Semiconductor Science and Technology*, vol. 21, pp. 1643–1650, Dec. 2006.

[32] T. Kakitsuka, Y. Shibata, M. Itoh, S. Member, Y. Kadota, Y. Tohmori, and Y. Yoshikuni, "Influence of buried structure on polarization sensitivity in strained bulk semiconductor," *IEEE Journal of Quantum Electronics*, vol. 38, no. 1, pp. 85–92, 2002.

[33] S. Philippe, A. L. Bradley, B. Kennedy, F. Surre, and P. Landais, "Experimental Investigation of Polarization Effects in Semiconductor Optical Amplifiers and Implications for All-Optical Switching," *Journal of Lightwave Technology*, vol. 26, no. 16, pp. 2977–2985, 2008.

[34] E. O'Reilly and A. Adams, "Band-structure engineering in strained semiconductor lasers," *IEEE Journal of Quantum Electronics*, vol. 30, no. 2, pp. 366–379, 1994.

[35] R. Lennox, K. Carney, R. Maldonado-Basilio, S. Philippe, a. L. Bradley, and P. Landais, "Impact of bias current distribution on the noise figure and power saturation of a multi-contact semiconductor optical amplifier," *Optics letters*, vol. 36, pp. 2521–3, July 2011.

[36] R. J. Manning, R. Giller, X. Yang, R. P. Webb, and D. Cotter, "SOAs for all-optical switching techniques for increasing the speed," in *International Conference of Transparent Optical Networks (ICTON)*, vol. 00, pp. 239–242, 2007.

[37] J. C. S. F. Ginovart, "Gain dynamics studies of a semiconductor optical amplifier," *J. Opt. A: Appl. Opt.*, vol. 4, pp. 283–287, 2002.

[38] R. Giller, R. J. Manning, G. Talli, R. P. Webb, and M. J. Adams, "Analysis of the dimensional dependence of semiconductor optical amplifier recovery speeds.," *Optics express*, vol. 15, pp. 1773–82, Feb. 2007.

[39] D. Bimberg, "Quantum dots for lasers, amplifiers and computing," *Journal of Physics D: Applied Physics*, vol. 38, pp. 2055–2058, July 2005.

[40] A. J. Zilkie, J. Meier, P. W. E. Smith, M. Mojahedi, J. S. Aitchison, P. J. Poole, C. N. Allen, P. Barrios, and D. Poitras, "Femtosecond gain and index dynamics in an InAs/InGaAsP quantum dot amplifier operating at 1550nm.," *Optics express*, vol. 14, pp. 11453–11459, Nov. 2006.

[41] J. Mø rk and T. W. Berg, "The Dynamics of Semiconductor Optical Amplifiers," *Optics & Photonics News*, pp. 42–48, 2003.

[42] X. Yang, D. Lenstra, H. D. Waardt, G. D. Khoe, T. Simoyama, H. Ishikawa, H. Kawashima, and T. Hasama, "Ultrafast refractive-index dynamics in a multi-quantum well semiconductor optical amplifier," *Lasers and Electro-Optics Society (LEOS)*, pp. 16–19, 2002.

[43] J. Mark and J. Mork, "Subpicosecond gain dynamics in InGaAsP optical amplifiers: Experiment and theory," *Applied Physics Letters*, vol. 61, no. 19, pp. 2281–2283, 1992.

[44] M. Premaratne, G. P. Agrawal, *Light Propagation in Gain Media: Optical Amplifiers*. Cambridge University Press, 2011.

[45] K. Morito, S. Tanaka, S. Tomabechi, and A. Kuramata, "A Broad-Band MQW Semiconductor Optical Amplifier With High Saturation Output Power and Low Noise Figure," *IEEE Photonics Technology Letters*, vol. 17, no. 5, pp. 974–976, 2005.

[46] Z. Bakonyi, G. Onishchukov, L. Lester, A. Gray, T. Newell, and A. Tunnermann, "High-gain quantum-dot semiconductor optical amplifier for 1300 nm," *IEEE Journal of Quantum Electronics*, vol. 39, pp. 1409–1414, Nov. 2003.

[47] T. Akiyama, M. Ekawa, M. Sugawara, K. Kawaguchi, H. Sudo, A. Kuramata, H. Ebe, and Y. Arakawa, "An Ultrawide-Band Semiconductor Optical Amplifier Having an Extremely High Penalty-Free Output Power of 23 dBm Achieved With Quantum Dots," *IEEE Photonics Technology Letters*, vol. 17, no. 8, pp. 1614–1616, 2005.

[48] V. Cesari, W. Langbein, P. Borri, M. Rossetti, A. Fiore, S. Mikhrin, I. Krestnikov, and A. Kovsh, "Ultrafast gain dynamics in 1.3 μm InAsGaAs quantum-dot optical amplifiers: The effect of p doping," *Applied Physics Letters*, vol. 90, no. 20, p. 201103, 2007.

[49] T. Vallaitis, C. Koos, R. Bonk, W. Freude, M. Laemmlin, C. Meuer, D. Bimberg, and J. Leuthold, "Slow and fast dynamics of gain and phase in a quantum dot semiconductor optical amplifier.," *Optics express*, vol. 16, pp. 170–8, Jan. 2008.

[50] P. R. a. Binetti, M. Lu, E. J. Norberg, R. S. Guzzon, J. S. Parker, A. Sivananthan, A. Bhardwaj, L. a. Johansson, M. J. Rodwell, and L. a. Coldren, "Indium phosphide photonic lintegrated circuits for coherent optical links," *IEEE Journal of Quantum Electronics*, vol. 48, pp. 279–291, Feb. 2012.

[51] J. W. Raring, "Advanced integration schemes for high-functionality/high-performance photonic integrated circuits," *Proceedings of SPIE*, vol. 6126, pp. 1–20, 2006.

[52] J. S. Barton, E. J. Skogen, M. L. Ma, S. P. Denbaars, and L. A. Coldren, "A widely tunable high speed transmitter using an integrated SGDBR laser semiconductor optical amplifier and Mach- Zehnder modulator," *IEEE Journal of Selected Topics in Quantum Electronics*, vol. 9, no. 5, pp. 1–8, 2003.

[53] T. Chattopadhyay, "All-optical programmable Boolean logic unit using semiconductor optical amplifiers on the MachZehnder interferometer arms switch," *IET Optoelectronics*, vol. 5, no. 6, p. 270, 2011.

[54] A. M. Kaplan, G. P. GhafouriShiraz, D. N. Maywar, "All-optical phase control of a square-wave photonic clock," *IEEE Photonics Technology Letters*, vol. 23, pp. 405–407, Apr. 2011.

[55] Y. Liu, L. Chen, T. Xu, J. Mao, S. Zhang, and Y. Liu, "All-optical signal processing based on semiconductor optical amplifiers," *Frontiers of Optoelectronics in China*, vol. 4, pp. 231–242, Aug. 2011.

[56] G De Valicourt, Chanclou, P and Brenot, R, "High gain (30 dB) and high saturation Power (11 dBm) RSOA devices as colorless ONU Sources in Long-Reach Hybrid WDM / TDM-PON Architecture," *IEEE Photonics Technology Letters*, vol. 22, no. 3, pp. 191–193, 2010.

[57] G. D. Valicourt, D. Maké, C. Fortin, A. Enard, F. V. Dijk, and R. Brenot, "10 Gbit/s modulation of Reflective SOA without any electronic processing," in *Optical FIbre Communications*, pp. 20–22, 2011.

[58] G. D. Valicourt, S. Member, F. Pommereau, F. Poingt, M. Lamponi, G. H. Duan, S. Member, P. Chanclou, M. A. Violas, and R. Brenot, "Chirp reduction in directly modulated multielectrode RSOA devices in passive optical networks," *IEEE Photonics Technology Letters*, vol. 22, no. 19, pp. 1425–1427, 2010.

3

Control of Noise Figure & Saturation Power

The sources of noise in an SOA will be discussed, along with an appreciation of how it manifests in a real network situation. The problem of noise quantification, an assessment of the noisiness of an element, will be addressed and defined. A formula for optical noise figure will then be derived for an SOA based entirely on experimentally obtainable parameters. This will then be used to describe the noise figure of a cascade of amplifiers in series. The concept of noise control is outlined with the aid of simulation. A consequent effect of this on saturation power is also described. Two designs are then proposed as a means of practical realisation.

3.1 Noise Figure

3.1.1 Definition of Noise Figure

As a signal propagates an optical network it picks up additive noise, an undesired but unavoidable consequence of spontaneous emission from the constituent amplifiers. The theoretical determination of optical noise and its origins have been dealt with in great detail semi-classically and quantum mechanically in [1, 2, 3, 4, 5, 6, 7] and references therein. In a general communications system scenario (optical or electrical), terminated signals are reduced in power and accompanied by a noise component. A simple assessment of this uses the signal-to-noise-ratio (SNR), but this proves inadequate when it comes to a more realistic active network, with receivers and amplifiers [5]

To address this shortcoming and to acquire information about how the noise of a network changes due to an individual component, a familiar measure used extensively is the noise factor (nf). In this case, the 'noisiness' of an individual amplifier, or any active or passive component, can be determined by considering two signal-to-noise ratios. The noise factor (in linear units) of an element N is defined as the ratio of the SNR_{in} and the SNR_{out}, i.e. a measure of the SNR degradation as it propagates through the element. A test element is shown in Figure 3.1.

Figure 3.1: Input and output SNR of a dual-port network element

$$nf = \frac{SNR_{in}}{SNR_{out}} \tag{3.1}$$

The noise figure (NF) is defined as the noise factor expressed in Decibels. It should be noted that by definition a lossy element has a NF equal to that loss. For example a 3dB attenuator has an SNR degradation of 3dB [5].

$$NF = 10\log_{10}(nf) = 10\log_{10}\frac{SNR_{in}}{SNR_{out}} \tag{3.2}$$

3.1.2 Noise in Optical Communications

The fundamental limits on current communication systems are governed in large part by the additive noise of the constituent components. As the ASE levels of each amplifier propagate with the signal, their effect is further augmented by additional amplifiers. Mitigation of individual amplifier noise is of critical importance, especially at the beginning of a particular amplifier stretch [8].

Noise can be considered an unwanted signal present in a communications system, tending to impede the reception of the designated signal. The resultant optical power fluctuations introduced cause transmission impairments and closure of the optical eye diagram on an optical sampling oscilloscope (OSO). Eye diagrams will be discussed further in Chapter 5. The effect of this noise on an intensity modulated signal is shown in Figure 3.2, where a clear degradation of the signal SNR can be seen.

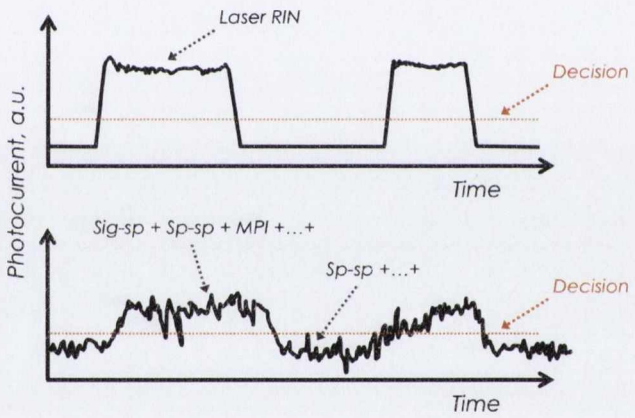

Figure 3.2: Manifestation of noise in an intensity modulated system. Top: An input signal with minimal noise. Bottom: The same signal after passing through a noisy element. The features present are a result of the signal-spontaneous beat noise (sig-sp); spontaneous-spontaneous beat noise (sp-sp) and; multipath interference (MPI).

As noise cannot be wholly eliminated its effect must be minimized, or alternatively, the signal-to-noise ratio (S/N) must be maximized as far as possible. As systems become more transparent, with evolution towards all optical operation, extended in situ optical monitoring will be required [9]. Optical add/drop multiplexers and optical cross-connects require monitoring to insure proper functionality at the component level. Large-scale use of such components in transparent networks will have consequences that drive the need for additional optical monitoring. In this case, minimizing the NF as much as possible for all amplifier components, and so the system as a whole, will be invaluable [10]. The individual noise components which constitute the overall

noise effects of an SOA, are given in the next section.

3.1.3 Semiconductor Optical Amplifier Noise

This thesis concerns the noise generated by a semiconductor optical amplifier and the potential control of this noise. The individual causes are now outlined, while a more rigorous derivation can be found in [6, 11, 12, 2]. Figure 3.3 plots the power spectral density for the individual sources of noise of an SOA. This data is measured using a photo detector and electrical spectrum analyser combination, where the optical signal passes through a filter of bandwidth B_0 before detection. Signal beating in this description occurs at the detector, however it will be shown that when deriving the optical noise figure from the electrical domain the individual terms are optically equivalent [5]

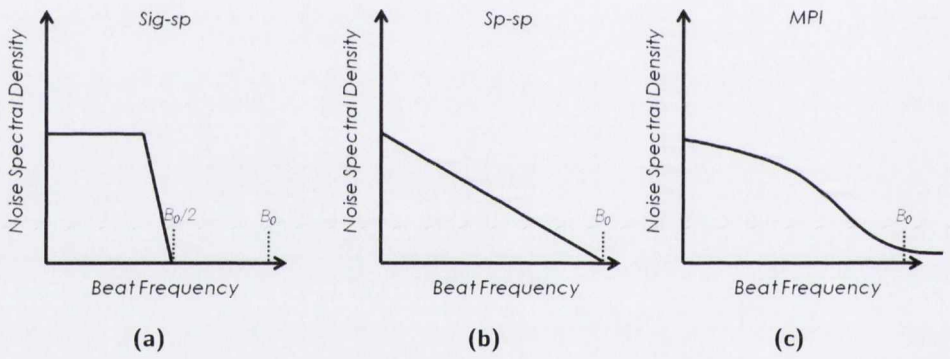

Figure 3.3: Noise Power spectal densities for three sources of noise in SOAs, as measured on an optical spectrum analyser (OSA)

(a) *The signal Spontaneous Beat Noise (sig-sp)*

The sig-sp beat noise power spectral density is given in Figure 3.3a. It results from the beating of the amplified signal photons and the spontaneous emission photons upon termination at the photo detector. This occurs within the bandwidth of the signal and where both components are of the same polarisation [13, 6]. It will be shown that sig-sp noise is the dominant contributor to the total NF of SOAs of appreciable gain. B_0 again is the optical bandwidth.

(b) *The Spontaneous beat Noise (sp-sp)*

The sp-sp beat noise follows similar mechanisms to sig-sp noise described. However in this case it is the interaction at the detector of spontaneous photons only, and the consequent components which originate from this process. The same polarisation and bandwidth criteria

apply. The measured power spectral density is illustrated in 3.3b.

(b) *Multipath Interference Noise (MPI)*

MPI represents the transference of phase and frequency noise to an intensity noise resulting from multiple reflections in the cavity of the amplifier. This occurs as a direct consequence of the small but finite reflection coefficient at the facets. Although this contributes negligibly to the NF in a travelling wave SOA, for completeness, it is included in all calculations that follow in Chapters 4 & 5. This is shown in 3.3c.

(d) *Shot Noise (shot)*

The shot noise is the fundamental limit of optical intensity noise in electrical or photonic circuits. This is a quantum noise effect related to the discrete nature of photons and electrons [6]. The input SNR described herein is shot-noise limited. This proves a useful input noise, and is widely used in the literature [5]

3.1.4 Optical Noise Figure

The NF defined in subsection 3.1.1 was given in terms of SNRs, where traditionally it was used as a figure of merit for an electrical signal [14]. In the discussion of the individual sources of semiconductor optical amplifier noise, the properties were described in relation to the detection of an optical signal and the subsequent analysis of the photocurrent. This section will derive an optically equivalent form of NF from this electrical analysis [5], in terms of experimentally obtainable optical parameters such as gain and ASE spectral density.

The SNR is defined in terms of the signal and noise levels of a photo detector placed in the optical path. The detected signal photocurrent is i_{sig} and the variance of this signal, the noise, is $\langle \Delta^2 i_n \rangle$. The noise variance is found by integrating the received intensity noise spectrum over the desired bandwidth. The resultant definition of SNR on which we base our noise figure definition, is given by,

$$SNR = \frac{\langle i_{sig} \rangle^2}{\langle \Delta^2 i_n \rangle} \tag{3.3}$$

The NF is a ratio of the SNR_{in} to the SNR_{out}, which are now defined. The input SNR (SNR_{in})

is shot-noise limited, and the measured quantity is given by [5],

$$SNR_{in} = \frac{\langle i_{sig} \rangle^2}{\langle \Delta^2 i_n \rangle} = \frac{R^2 P_{in}^2}{2qRP_{in}B_e} = \frac{\eta P_{in}}{2h\nu B_e} \tag{3.4}$$

where i_{sig} is the photocurrent generated by the optical signal of power P_{in}. $\langle i_{sig} \rangle^2$ is proportional to the signal power, and $\langle \Delta^2 i_n \rangle$ is the mean-square value of the single-sided noise power spectrum. B_e is the baseband bandwidth of the noise, and ν is the optical frequency R is the responsivity of the photodetector, given by,

$$R = \frac{\eta q}{h\nu} \tag{3.5}$$

where η is the quantum efficiency of the photo detector, h is Planck's constant and q is the electron charge. For an ideal receiver with negligible thermal noise, and a baseband frequency of 1Hz, Equation 3.4 reduces to,

$$SNR_{in} = \frac{P_{in}}{2h\nu} \tag{3.6}$$

The SNR_{out} requires the principle sources of SOA noise discussed, and is given by,

$$SNR_{out} = \frac{\langle i_{out} \rangle^2}{\langle \Delta^2 i_{out} \rangle} \tag{3.7}$$

where,

$$\langle i_{out} \rangle^2 = R^2 g^2 P_{in}^2 \tag{3.8}$$

where g is the gain, taken to be linear for the remainder of this chapter unless otherwise stated. The NF is also linear in the following sections, unless stated otherwise. $\langle \Delta^2 i_{out} \rangle$ can in turn be expressed as the sum of intensity noise power spectral densities of all the sources of noise,

$$SNR_{out} = \frac{R^2 g^2 P_{in}^2}{B_e R^2 \left[S_{sig-sp} + S_{sp-sp} + S_{MPI} + S_{pump} + \ldots + \eta^{-1} S_{shot} \right]} \tag{3.9}$$

g is the optical gain of the SOA, S_{sig-sp}, S_{sp-sp}, S_{MPI} are the noise power spectral densities described, and the other parameters have their previous meanings. The different contributions to noise are in general optical frequency (ν) and baseband frequency (f) dependent, and so are lumped together into a sum of an 'excess' noise term (S_e) and the shot noise term,

$$SNR_{out} = \frac{g^2 P_{in}^2}{B_e \left[S_e(\nu, f) + \eta^{-1} S_{shot} \right]} \tag{3.10}$$

Here $S_e(\nu, f)$ is the spectral density for all excess noise contributions. The total amplifier noise factor is given by the ratio of SNR_{in}/SNR_{out} as defined in Equation 3.1 giving,

$$nf(\nu, f) = \frac{\eta S_e(\nu, f)}{2h\nu g^2 P_{in}} + \frac{S_{shot}}{2h\nu g^2 P_{in}} = F_{excess} + F_{shot} \tag{3.11}$$

Equation 3.11 represents a general description of nf, providing a basis for measurement where $S_e(\nu, f)$ is found using electrical techniques at baseband frequencies, and all other parameters may be found optically. The nf can now be derived completely in terms of optically obtainable values. To do this it is necessary to further expand on $S_e(\nu, f)$, and the principle sources of noise. More specifically, the 'excess' noise term can be reduced to a form accounting for the beating between the ASE and the signal fields [5].

$$S_e(\nu, f) = S_{sig-sp} = 4\rho_{ASE} g P_{in} \tag{3.12}$$

and,

$$S_{shot} = 2h\nu g P_{in} \tag{3.13}$$

From Equation 3.11 then, we can obtain the optical equivalent nf formula,

$$nf(\nu, f) = F_{excess} + F_{shot} = \frac{2\eta\rho_{ASE}}{G\nu h} + \frac{1}{G} \tag{3.14}$$

This noise factor expression contains the terms for the dominant sources of noise in an optical amplifier element: the signal spontaneous beat noise and the shot noise. For an amplifier of appreciable gain the latter may be neglected, yielding a final NF expression of,

$$NF = 10\log_{10}(nf) = 10\log_{10}\left(\frac{2\eta\rho_{ASE}}{Gh\nu}\right) \tag{3.15}$$

Where the quantum efficiency term, η, is equal to one when accounted for using an optical spectrum analyser, as will be described in Section 4.3.4.

Equation 3.15 represents an accepted standardised all optical technique for characterising the NF of an optical amplifier, through experimentally realisable parameters [5].

3.1.5 Concatenated Noise Figure

The concatenated NF represents the total NF of a chain of n optical amplifiers. In this way ASE from the previous components is amplified, building with each successive amplification stage. This can have an added effect on the dynamic range of input powers of the higher order components of the chain, saturating their gain [5]. A chain of n optical amplifiers is shown in Figure 3.4. Each amplifier has its own unique gain (g_n), ASE (ASE_n) and noise factor (nf_n).

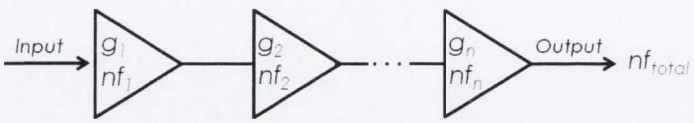

Figure 3.4: Chain of n optical amplifiers

the total nf of this system is found by the Friis Equation [15],

$$nf_{total} = nf_1 + \frac{nf_2 - 1}{g_1} + \ldots + \frac{nf_n - 1}{g_1 . g_2 \cdots g_{n-1}} \tag{3.16}$$

The overall noise factor of such a system is largely determined by the nf of the initial subsections. Each successive term in the equation is reduced in value compared with the last, due to the presence of an additional gain term at every stage. Thus the first few terms are the most important contribution to the overall value of nf_{total}.

The Friis equation can be progressed to a format more consistent with the optical NF formula, as follows, excluding the shot noise for $g \gg 1$ (linear). Figure 3.5 illustrates the accumulation of gain and noise, where the gain is increased in a multiplicative fashion, while the ASE depends on both a multiplicative and additive increase [5]. The corresponding ASE power after each amplifier is given by the appropriate colour.

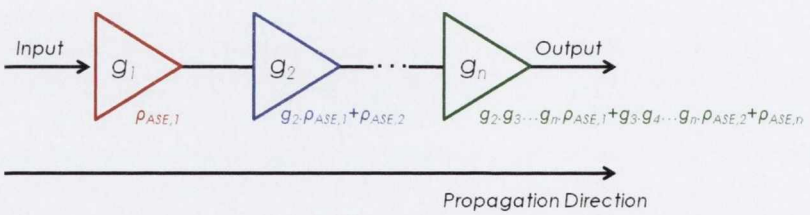

Figure 3.5: Chain of amplifiers, showing effect of additive ASE accumulation

The ASE from the first amplifier is multiplied by the gain of the second stage which in turn

adds additional ASE. This process continues to the n^{th} amplifier stage. The cumulative ASE density after the n^{th} component is,

$$\rho_{total} = \rho_{ASE,1} + g_1 \cdot \rho_{ASE,1} + \rho_{ASE,2} + g_2 \cdot g_3 \ldots g_n \cdot \rho_{ASE,1} + g_3 \cdot g_4 \ldots g_n \rho_{ASE,2} + \rho_{ASE,n} \quad (3.17)$$

The overall NF can then be given in terms of the optical noise figure formula of Equation 3.16 if we assume there is appreciable gain so that the main contributor to the total noise is the NF_{sig-sp}. Inserting Equation 3.17 into the NF formula, where the total gain is given by,

$$g_{total} + g_1 \cdot g_2 \cdot g_3 \ldots g_n \quad (3.18)$$

yields,

$$nf_{total} = \frac{2\rho_{total}}{h\nu g_{total}} = \frac{2\rho_1}{h\nu g_1} + \frac{2\rho_2}{h\nu g_1 g_2} + \ldots + \frac{2\rho_n}{h\nu g_1 g_2 \ldots g_n} \quad (3.19)$$

Finally expressing in terms of NF_n

$$nf_{total} = nf_1 + \frac{nf_2}{g_1} + \ldots + \frac{nf_n}{g_1 g_2 \ldots g_n} \quad (3.20)$$

Similar to the Friis equation, this formula too dictates that the total NF is largely dependent on the initial values. With an understanding of the NF of a chain of amplifiers in mind, we will come back to this as an analogy for noise figure reduction in a single optical amplifier, in section 3.2.2

3.1.6 Current Methods of Noise Reduction

With the optical NF defined and derived, it is a good opportunity to present current methods of NF reduction in SOAs from the literature. As one of the main disadvantage of SOAs, it has garnered a lot of interest as a research subject. The different techniques can be categorised as follows:

(a) *Holding Beam at Transparency*

By injecting a holding beam on the high energy side of the ASE at transparency Crottini et al. [16] have realised improvements in NF of 0.5dB at high chip-gains of 23dB, and 2.5dB improvement at a low pump current chip-gain of 13dB, for co-propagation injection. The effect is akin to carrier density modification along the length of the device, producing more favourable NF conditions. The disadvantages of this is a trade off in chip gain of almost 4dB, for modest improvements in NF, and the additional laser required to produce the holding beam, adding to the complexity of the system.

(b) *Exotic Gain Media*

The introduction of chapter 2 briefly mentioned the ability to replace a bulk active region with that of more exotic quantum confined materials. Quantum wells (QW) [17], quantum dots (QD) [18, 4] and more recently quantum dashes (QDash) [19, 20] have all been actively probed, where improvements in NF over their bulk counterparts were seen across the board.

Quantum wells have proven to produce low NF values due to their low confinement factor reducing the effect of ASE carrier depletion. Coupled with this is a density of states, which results in a much reduced threshold current and so better inversion at lower biases, whilst maintaining a high gain [21, 22]. Hasegawa et al have developed QWSOAs of varying ultra low confinement which produce chip NF values of 3.8dB, an excellent result [23]. However these low confinement QW structures are known to have poor input coupling coefficients, increasing the fibre-to-fibre NF significantly.

Quantum dots yield a beneficial NF performance due to both their low confinement and unique inversion properties. The fabrication of the QD layers require the growth of an initial thin layer of the dot material, known as the wetting layer [24, 18, 4]. This acts as a carrier reservoir to the active dots, and so as a quasi three level system [24], not dissimilar to the EDFA, producing more efficient electrical pumping than bulk materials. With similar properties to QDSOAs, InAs/InP Quantum Dash SOAs, have been demonstrated by Bilenca et al [19, 20], with unique very wideband (120nm) gain and NF performance.

(c) *Carrier Density Modification*

Saini et al [25] have produced a novel fabrication design, whereby introduction of non-uniform resistivity along the p-contact has the effect of altering the carrier density to an optimum profile for both low NF and high P_{sat} performance. This carrier profile dependence of NF will be

described in the next section, where it will be seen that the optimum profile is slightly different to that used by Saini.

(d) *Vertical Cavity SOA*

Investigation of the noise figure of a vertical cavity SOAs (VCSOA) was undertaken by Bjorlin et al [26]. The treatment of NF for VCSOA had not previously been examined in detail, and so initially a Fabry-Perot SOA based model had been adopted, where inversion factor (n_{sp}) is investigated as a function of the finite mirror reflectivity. In VCSOAs, the intrinsic NF is affected by MPI noise due to the mirror reflectivity, a negligible contributor concerning TWSOAs [27]. However VCSOAs produce a very low fibre-to-fibre NF based on the naturally high coupling efficiency of these structures, where the circular symmetric cross section of the optical mode is compatible with optical fibre. This occurs at the expense of substantial gain and gain bandwidth. Both are a direct consequence of the cavity mode [28].

(e) *Waveguide Termination & Confinement*

In chapter 2 methods of cavity suppression were detailed via differing structural solutions. While the reduction of residual reflections in the SOA will minimise the effect of MPI noise, a great effect on signal spontaneous beat noise can be achieved through the flared waveguide structure described [29]. By this method, backward travelling ASE is reduced, which would otherwise deplete carriers available for stimulated emission [30]. By altering the confinement in this way the level of ASE coupled back into the waveguide is thus reduced.

In addition to waveguide termination techniques, overall low confinement structures have shown an improved NF [31, 32, 33, 34]. In such a scenario, the above carrier density effect is achieved due to less interaction of the stimulated and spontaneous emissions. As this leads to a higher carrier density at the input of the device, the NF_{tot} parameter is optimised, as described in the chain of amplifier section.

3.2 Controlling the Noise Figure

3.2.1 Carrier Density Relationship

The NF is directly proportional to the inversion factor n_{sp}, which relates the relative carrier population of the conduction to valence band. Reduction of noise figure then relies heavily on

this parameter, defined as,

$$n_{sp} = \frac{N_2}{N_2 - N_1} \tag{3.21}$$

where N_1 and N_2 are the conduction and valance band carrier populations, respectively.

Now expressing the optical NF formula Equation 3.16 in terms of n_{sp}, this effect is seen more clearly. The equation for the additive noise power of an amplifier is given by,

$$P_{ASE} = n_{sp}(g-1)h\nu B_0 \tag{3.22}$$

where B_0 is the measurement bandwidth. As ρ_{ASE} is equal to the noise power per unit bandwidth Equation 3.22 cab be re-written as,

$$\rho_{ASE} = n_{sp}(g-1)h\nu \tag{3.23}$$

Replacing ρ_{ASE} in Equation 3.14 with Equation 3.23 yields an expression for the nf in terms of n_{sp} and gain, expressed in linear units,

$$nf = \frac{2n_{sp}(g-1)}{g} + \frac{1}{g} \tag{3.24}$$

In cases where $g \gg 1$, this expression reduces to $nf = 2n_{sp}$. In the case of total population inversion, where $n_{sp} = 1$, this leads to a quantum limit of noise figure of 3dB [35].

In Figure 3.6 the carrier density and the consequent population inversion are presented, illustrating the relation described. The details of this plot and the simulation used to produce it are given in the next chapter. The carrier density profile shows the effect of carrier depletion at the facets of the SOA due to ASE intensity being stronger at the extremities of the waveguide. This effect is increased in longer devices [36].

The net outcome of this is that to achieve a reduced NF, the highest level of population inversion achievable must be reached. However, as will be seen, this does not lend itself to an overall NF reduction technique, due to the carrier dependent nature of non-radiative processes and thermal effects in the SOA active region, coupled with ASE based carrier depletion.

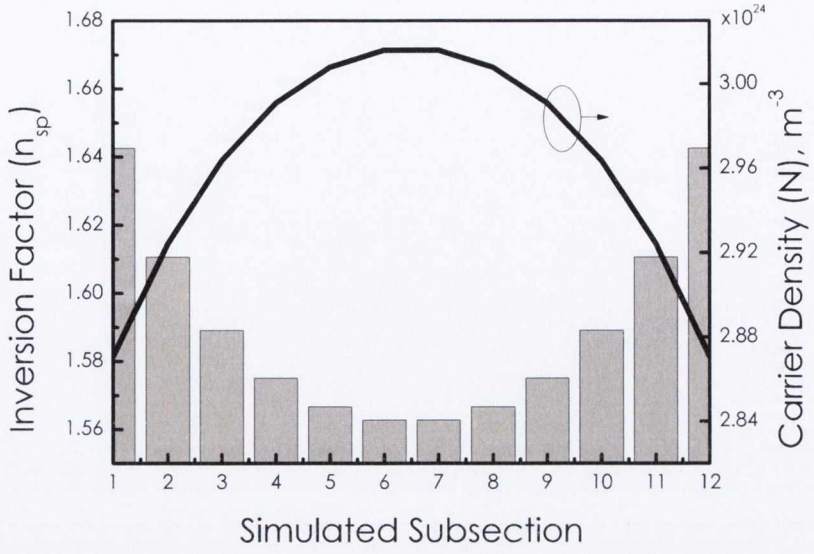

Figure 3.6: Simulated carrier density and inversion factor dependence for a standard single contact SOA at a bias of 150 mA, with a finite but very low injected signal

3.2.2 Longitudinal Carrier Density Profile

Reducing the NF cannot be achieved by simply pumping the device indefinitely, as the n_{sp} relationship would suggest. At higher biases two unavoidable problems reduce the rate of reduction: non-radiative recombination and amplified spontaneous emission.

The carrier density dependent non-radiative recombination rates were described in chapter 2, where three specific cases were explored. The most important of these are the Auger related processes which vary as N^3. At higher pump currents this acts to reduce the decrease in n_{sp}. Additionally, as N is increased, the rate of spontaneous emission increases. This includes ASE travelling towards the facet, and ASE reflected back to that same facet, which will further act to deplete carriers in this region.

Knowing this, and recalling the chain of amplifiers analogy, the concept of NF reduction can be presented. The SOA is thought of as a chain of n_{amp} sub-sections, each with their own carrier density and subsequent gain and nf. At this point we define a designated input facet. Like the cascade, the *nf* must be reduced at the beginning of the chain, and so a high level of pumping is required here. This increases the *gain* and reduces n_{sp}. The NF of the entire system is largely set by this initial condition. Not neglecting the ASE related carrier depletion, the carrier density along the length of the device is now reduced to some point above 0dB gain, reaching its minimum at the output facet. To clarify, this is for a total injected bias value, i_{tot}.

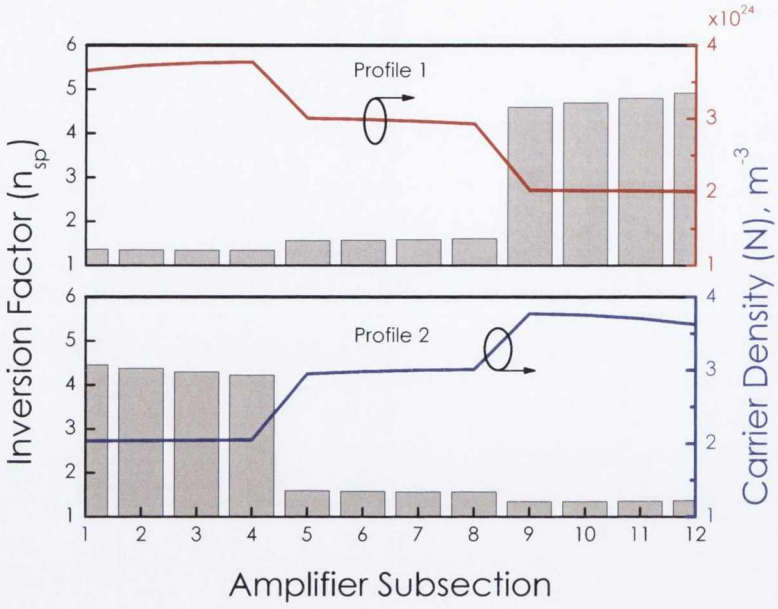

Figure 3.7: Simulated carrier density and inversion factor dependence along the length of the device, for both a proposed low noise scenario, and the corresponding reversal of this.

At this point it is important to define, from a proof of concept point of view, that the standard profile, Profile 1 and Profile 2 represent the conditions which illustrate the concept completely.

3.2.3 Optimum Profiles

However they are achieved in a practical device, the optimum profiles will be labelled as follows:

- The Standard Profile corresponds to a regular carrier density applied to an SOA.
- The Low Noise Profile described above, with a high carrier density at the input, and reduced carrier density at the output.
- The High P_{sat} Profile is the inverse of the Low Noise Profile, which will yield the largest deviation in NF illustrating the control achievable. The name suggests an added feature of improved saturation power. This will be described in the next section.

The methods of carrier density profiling in a real device will be described briefly at the end of this chapter, and given in much more details in the chapters relating directly to the individual techniques.

3.3 Gain Saturation

In the previous chapter the gain saturation was described as a cross over point between linear and non-linear operation, quantified by the saturation power P_{sat}. This section will derive the saturation power, and using these relationships explains the improvement in P_{sat} given by the reverse Low NF profile, the High P_{sat} profile .

3.3.1 Derivation of Saturation Intensity

The material gain coefficient at the saturating signal wavelength is assumed to be a linear function of carrier density such that,

$$g_m = a_1(N - N_0) \tag{3.25}$$

where,

$$a_1 = \frac{\mathrm{d}g_m}{\mathrm{d}N} = constant \tag{3.26}$$

Equation 3.26 is the differential material gain with respect to carrier density and N_0 is the carrier density at transparencey. This rate equation then can be described by,

$$\frac{\mathrm{d}N}{\mathrm{d}t} = \frac{i}{qd} - \frac{N}{\tau} - a_1(N - N_0)\left(\frac{I_{sig}}{h\nu}\right) \tag{3.27}$$

i is the injected current, q is the charge of the electron, τ is the carrier lifetime, N is the carrier density, N_0 is the carrier density at transparency, a_1 is the differential gain and I_{sig} is the travelling signal intensity. The propagation of I_{sig} along z is given by the rate equation,

$$\frac{\mathrm{d}I_{sig}}{\mathrm{d}z} = [\Gamma \cdot a_1(n - n_0) - \alpha]\, I_{sig} \tag{3.28}$$

Solving Equation 3.27 in the steady state gives,

$$n = \left[\frac{\tau i}{qd}\right]\left[1 + \frac{I_{sig}}{I_{sat}}\right]^{-1} + \frac{N_0 I_{sig}}{I_{sig} + Isat} \tag{3.29}$$

I_{sat} can be solved for, which thus gives the saturation power, P_{sat}

$$I_{sat} = \frac{h\nu}{a_1 \tau} \tag{3.30}$$

$$P_{sat} = \frac{A a_1 \tau}{\Gamma h\nu} \tag{3.31}$$

where A is the cross-sectional area of the waveguide. Combining Equation 3.29 and Equation 3.28 gives,

$$\frac{dI_{sig}}{dz} = \left[\frac{\Gamma g_0}{1 + I_{sig}/I_{sat}} - \alpha \right] I_{sig} \tag{3.32}$$

The material gain at transparency is given by,

$$g_0 = a_1 \left(\frac{\tau i}{qd} - N_0 \right) \tag{3.33}$$

Equation 3.32 has the solution

$$I_{sig,out} \left(\frac{I_{sig,out} - I_{sig,in}}{I_{sat}} \right) = I_{sig,in}^{(\Gamma g_0 L)} \tag{3.34}$$

From chapter 2, the gain (in linear units) is defined as,

$$G = \frac{P_{out}}{P_{in}} \tag{3.35}$$

Giving the gain in terms of the unsaturated gain (G_0) and combining to solve for the 3dB saturation output intensity yields,

$$I_{3dB} = \frac{\ln(2) G_0 I_{sat}}{G_0 - 2} \tag{3.36}$$

3.3.2 Carrier Density Dependence

In section 3.2 the reduction in NF as a consequence of modifications to the longitudinal carrier density profile was outlined. A reverse of this profile was put forward to act as an indicator of the realisable control. In this case, according to the concatenated NF formula and due to the low gain of the input section, the NF will be maximised. An additional consequence of this is to increase the saturation power of the device, for the same injected bias i_{tot}, hence the label High P_{sat} profile. This can be explained by using the equations derived above in the previous section, Equation 3.31.

It was found that the saturation power is directly proportional to the spontaneous carrier lifetime, the differential gain and the cross section area. Thus, increasing any of these will increase P_{sat}. For the purposes of this concept a_1 and A are constant. In addition to this, reducing the confinement of the active waveguide further tends to produce better linear operation. This has been shown by Brenot [33] in bulk volumes, as well as the QD, QW and QDash SOAs described previously. As such, it is the spontaneous carrier lifetime that increases along the propagation length, increasing the saturation power.

What this states is an interesting relationship between the ASE and each profile. In essence the detrimental effect of the ASE improves the dynamic range of input powers supported by the SOA, for i_{tot}. This is in stark contrast to the reason the low noise profile exists, which is to minimise the ASE noise.

3.3.3 Common Methods for Improving Linear Gain

For linear operation in a practical environment, such as simultaneous multi-wavelength amplification, an extended saturation point is desired. Upon saturation the fast dynamics produce negative effects, such as signal waveform distortion described in chapter 2. In order to improve the usefulness of SOAs for communications, especially with the inevitable evolution to higher capacity and denser wavelengths spacing [37], the saturation must be improved. Remembering Equation 3.31 P_{sat}, can be increased by influencing a number of device parameters. By modifying the total confinement factor for different length SOAs, but for a constant active volume Brenot et al [33] recorded substantial increases in P_{sat}. They examined confinements ranging from 5% to 80%, where the effect of ASE was reduced in low confinement structures.

Yoshino et al [38] reached an improvement in saturation power through the use of a pump beam.

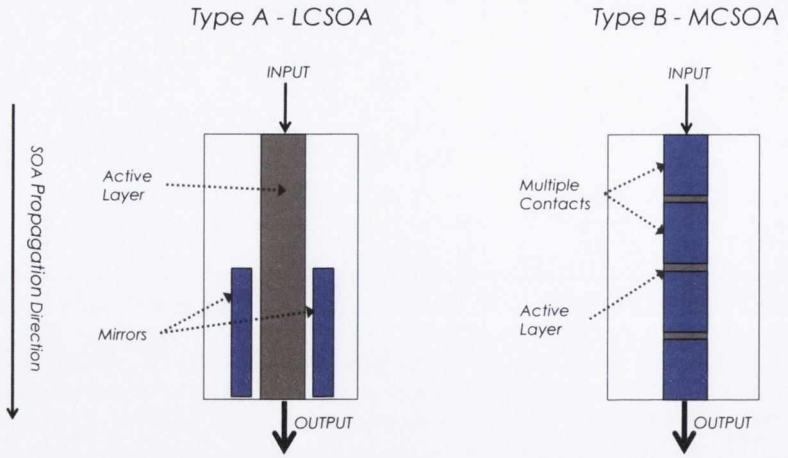

Figure 3.8: Top down schematic of two novel SOA designs providing the control of longitudinal carrier density. Type A - Lateral Cavity SOA (LCSOA) and Type B - multi-contact SOA (MCSOA).

By the introduction of an additional holding-beam at the blue edge of the gain spectrum, an improvement of 4.9dB was achieved for a bulk active region. The technique requires careful optimisation of the pump wavelength to counteract any decrease of unsaturated gain induced. From a practical point of view, the residual pump beam must be filtered out from the intended optical signal being amplified.

Finally, Linear SOAs (LOA) take advantage of gain clamping of the entire active length to increase the output saturation power. Doussiere et al. [39] produced bulk gain-clamped structures two decades ago which incorporated a Bragg grating with wavelength selective feedback. Based on the homogeneous broadening of the semiconductor gain, the overall bandwidth is clamped once the threshold oscillation is reached. Specifically the effect of this on the suppression of gain saturation induced crosstalk in WDM applications is reported. In this example the lasing occurs parallel with the signal field, however vertically lasing LOAs have also been realised [40], removing the effects of the additional signal.

3.4 Realisation of Noise Figure Control

The concept discussed to this point has not yet mentioned practical implementation in the lab. To this end this section will briefly describe two design options which achieve carrier density control through very different techniques. Much greater detail will be given when these designs are addressed individually in the later characterisation chapters.

3.4.1 Type A - Lateral Cavity SOA

Carrier density control is achieved in this design through the inclusion of a laterally lasing cavity perpendicular to the propagation axis of the SOA (LCSOA). A simplified schematic is shown on the left of Figure 3.8. As the injected bias is increased, the laterally generated ASE is coupled to this cavity. Lasing ensues, clamping the carrier density. By incorporating this structure along a particular percentage of the SOA output, the carriers in this region available for optical amplification of an input signal are clamped according to the threshold condition of the laser, thus achieving the required profiling of the carrier density [41].

3.4.2 Type B - Multi-Contact SOA

The second design is much more direct in its approach to carrier control, using multiple electrical contacts to individually pump different sections of the device [42]. It is clear then that in this way any carrier profile desired can be set, providing much versatility over the LCSOA. A schematic of this design is shown in Figure 3.8.

3.5 Conclusion

This chapter has defined the noise figure and derived the optical noise figure for an individual element, and a chain of optical amplifiers in series. The concept of NF reduction for a constant pump current was then introduced, whereby the SOA is considered as a chain of sub-amplifiers obeying the cascaded NF formula. From this, and taking into account ASE carrier depletion, an optimal carrier density profile was presented and labelled the Low Noise Profile. Progressing from this, the saturation power was more thoroughly defined and derived in terms of active waveguide parameters. Using this information the inverse Low Noise Profile was explained, and its high P_{sat} performance justified.

Finally, the practical realisation of direct carrier density control along the entirety of the gain length was briefly discussed, where two designs were proposed. This thesis will be based on the steady state and dynamic characterisation of these devices, and so each will be discussed in detail in subsequent chapters.

References

[1] Y. Yamamoto, S. Member, and K. Inoue, "Noise in amplifiers," *Journal of Lightwave Technology*, vol. 21, no. 11, pp. 2895–2915, 2003.

[2] P. Morel, A. Sharaiha, R. Brenot, and B. Thédrez, "Wideband gain and noise figure modelling in SOA," *Optical and Quantum Electronics*, vol. 38, pp. 231–236, Jan. 2006.

[3] E. Staffan Bjorlin and J. Bowers, "Noise figure of vertical-cavity semiconductor optical amplifiers," *IEEE Journal of Quantum Electronics*, vol. 38, no. 1, pp. 61–66, 2002.

[4] T. Berg, J. Mork, "Saturation and noise properties of quantum dot optical amplifiers," *IEEE Journal of Quantum Electronics*, vol. 40, no. 11, pp. 1527–1539, 2004.

[5] D. M. Baney, P. Gallion, and R. S. Tucker, "Theory and Measurement Techniques for the Noise Figure of Optical Amplifiers," *Optical Fiber Technology*, vol. 6, pp. 122–154, 2000.

[6] H. Haus, "The noise figure of optical amplifiers," *Photonics Technology Letters, IEEE*, vol. 10, no. 11, pp. 1602–1604, 1998.

[7] S. Donati and G. Giuliani, "Noise in an optical amplifier: formulation of a new semiclassical model," *IEEE Journal of Quantum Electronics*, vol. 33, no. 9, pp. 1481–1488, 1997.

[8] H. Ghafouri-Shiraz, *The Principles of Semiconductor Laser Diodes and Amplifiers*. Imperial College Press.

[9] D. C. Kilper and W. Weingartner, "Monitoring optical network performance degradation due to amplifier noise," *Journal of Lightwave Technology*, vol. 21, no. 5, pp. 1171–1178, 2003.

[10] D. C. Kilper, R. Bach, D. J. Blumenthal, D. Einstein, T. Landolsi, L. Ostar, M. Preiss, A. E. Willner, "Optical performance monitoring of QPSK data channels by use of neural networks trained with parameters derived from asynchronous constellation diagrams.," *Journal of Lightwave Technology*, vol. 22, pp. 4931–8, Mar. 2004.

[11] W. Loh, J. J. Plant, J. Klamkin, J. P. Donnelly, F. J. O. Donnell, R. J. Ram, and P. W. Juodawlkis, "Limitations of noise figure in InGaAsP quantum well semiconductor optical amplifiers," in *Conference on Lasers and Electro-Optics (CLEO)*, vol. 1580, pp. 5–6, 2010.

[12] A. Bilenca, S. Member, and G. Eisenstein, "On the noise properties of linear and nonlinear quantum dot semiconductor optical amplifiers : The impact of inhomogeneously broadened gain and fast carrier dynamics," *IEEE Journal of Quantum Electronics*, vol. 40, no. 6, pp. 690–702, 2004.

[13] T. Briant, P. Grangier, R. Tualle-brouri, A. Bellemain, R. Brenot, and B. Thédrez, "Accurate Determination of the Noise Figure of Polarization-Dependent Optical Amplifiers : Theory and Experiment," *Journal of Lightwave Technology*, vol. 24, no. 3, pp. 1499–1503, 2006.

[14] N. Olsson, "Lightwave systems with optical amplifiers," *Journal of Lightwave Technology*, vol. 7, pp. 1071–1082, July 1989.

[15] H. T. Friis, "Noise figures of radio receivers," in *Proceedings of the I.R.E.*, pp. 419–422, 1944.

[16] A. Crottini, F. Salleras, P. Moreno, M.-a. Dupertuis, B. Deveaud, and R. Brenot, "Noise figure improvement in semiconductor optical amplifiers by holding beam at transparency scheme," *Photonics Technology Letters, IEEE*, vol. 17, no. 5, pp. 977–979, 2005.

[17] D. Tauber, R. Nagar, A. Livne, G. Eisenstein, U. Koren, G. Raybon, "A low noise figure 1550nm multiple-quantum well optical amplifier," *IEEE Photonics Technology Letters*, vol. 4, no. 3, pp. 238–240, 1992.

[18] B. T. Akiyama, M. Sugawara, and Y. Arakawa, "Quantum-Dot Semiconductor Optical Amplifiers," *Proceedings of the IEEE*, vol. 95, no. 9, 2007.

[19] A. Bilenca, D. Hadass, R. Alizon, H. Dery, V. Mikhelashvili, G. Eisenstein, T. Physik, and U. Wurzburg, "Gain and noise properties of InAs/InP quantum dash semiconductor optical amplifiers," *Proceedings of SPIE*, vol. 6014, pp. 1–12, 2005.

[20] M. N. Ngo, G. Girault, M. Gay, L. Bramerie, J.-C. Simon, R. Brenot, F. Lelarge, and G.-H. Duan, "Suppression of slow gain recovery in ultralong quantum-dash semiconductor optical amplifier emitting at 1.55μm," *Optics Communications*, vol. 284, pp. 4910–4913, Sept. 2011.

[21] K. Morito, S. Tanaka, S. Tomabechi, and A. Kuramata, "A Broad-Band MQW Semiconductor Optical Amplifier With High Saturation Output Power and Low Noise Figure," *IEEE Photonics Technology Letters*, vol. 17, no. 5, pp. 974–976, 2005.

[22] K. Morito and S. Tanaka, "Record high saturation power (+22dBm) and low noise figure (5.7dB) polarisation insensitive SOA module," *IEEE Photonics Technology Letters*, vol. 17, no. 6, pp. 1298–1300, 2005.

[23] H. Hasegawa, M. Funabashi, N. Yokouchi, K. Kiyota, and K. Maruyama, "Design and fabrication of semiconductor optical amplifier with low noise figure," in *OptoeElectronics and Communications Conference (OECC)*, no. July, pp. 204–205, IEEE, 2010.

[24] J. J. Owens, C. P. Poole, *Introduction to Nanotechnology*. John Wiley & Sons Ltd., 2003.

[25] S. S. Saini, J. Bowser, R. Enck, V. Luciani, P. J. S. Heim, M. Dagenais, "A Semiconductor Optical Amplifier with high saturation power, low noise figure and low polarization dependent gain over the C-band," in *Lasers and Electro-Optics Society (LEOS)*, pp. 102–103, 2004.

[26] E. S. Björlin, S. Member, and J. E. Bowers, "Noise Figure of Vertical-Cavity Semiconductor Optical Amplifiers," *IEEE Journal of Quantum Electronicsu*, vol. 38, no. 1, pp. 61–66, 2002.

[27] C. Tombling, T. Saitoh, and T. Mukai, "Performance predictions for vertical-cavity semiconductor laser amplifiers," *IEEE Journal of Quantum Electronics*, vol. 30, no. 11, pp. 2491–2499, 1994.

[28] P. Wen, M. Sanchez, M. Gross, S. C. Esener, "Noise and noise figure of vertical-cavity semiconductor optical amplifiers (VCSOAs) operated in reflection mode," *Journal of the Optical Society of America. A, Optics, image science, and vision*, vol. 5111, Nov. 2003.

[29] G. Bendelli, K. Komori, S. Arai, and Y. Suematsu, "A new structure for high-power TW-SLA," *IEEE Photonics Technology Letters*, vol. 3, no. 1, pp. 42–44, 1991.

[30] M. J. Connolly, *Semiconductor Optical Amplifiers*. Kluwer Academic Publishers, Boston, 2010.

[31] J. Klamkin, J. J. Plant, M. Sheehan, W. Loh, S. M. Madison, and P. W. Juodawlkis, "High-output saturation power variable confinement slab coupled optical waveguide amplifier," in *Optical FIbre Communications*, vol. 1, pp. 10–12, 2011.

[32] T. D. Visser, H. Blok, B. Demeulenaere, and D. Lenstra, "Confinement Factors and Gain in Optical Amplifiers," *IEEE Journal of Quantum Electronics*, vol. 33, no. 10, pp. 1763–1766,

1997.

[33] R. Brenot, F. Pommereau, O. Le Gouez, J. Landreau, F. Poingt, L. Le Gouezigou, B. Rousseau, F. Lelarge, F. Martin, and G. Duan, "Experimental study of the impact of optical confinement on saturation effects in SOA," *OFC/NFOEC Technical Digest. Optical Fiber Communication Conference, 2005.*, p. 3 pp. Vol. 1, 2005.

[34] F. Pommereau, R. Brenot, J. Landreau, L. L. Gouczigou, O. L. Gouezigou, F. Lelarge, F. Martin, F. Poingt, B. Rousseau, G. H. Duan, B. Thkdrez, R. D. Nozay, and F. Marcoussis, "Realisation of semiconductor optical amplifiers with homogenous carrier density and low noise factor," in *International Conference on Indium Phosphide and Related Materials*, pp. 102–105, 2005.

[35] E. Desurvire, "On the physical origin of the 3-dB noise figure limit in laser and parametric optical amplifiers," *Optical Fiber Technology*, vol. 5, pp. 40–61, 1999.

[36] M. J. Connelly, "Wideband semiconductor optical amplifier steady-state numerical model," *IEEE Journal of Quantum Electronics*, vol. 37, no. 3, pp. 439–447, 2001.

[37] A. Yariv, *Photonics: Optical Electronics in Modern Communications*. No. March, Oxford University Press, 2007.

[38] M. Yoshino and K. Inoue, "Improvement of saturation output power in a semiconductor laser amplifier through pumping light injection," *IEEE Photonics Technology Letters*, vol. 8, no. 1, pp. 58–59, 1996.

[39] M. K. P Doussiere, P. Garabedian, C. Graver, D. Bonnevie, T. Fillion, E. Derouin, M. Monnot, J. G. Provost, D. Leclerc, "1.55um Polarisation independent semiconductor optical amplifier with 25dB fiber to fiber gain," *Technology*, vol. 6, no. 2, pp. 170–172, 1994.

[40] D. A. Francis, S. P. Dijaili, and J. D. Walker, "A single chip linear optical amplifier," in *Optical FIbre Communications (OFC)*, no. 510, pp. 8–10, 2001.

[41] K. Carney, R. Lennox, R. Maldonado-Basilio, S. Philippe, L. Bradley, and P. Landais, "Noise controlled semiconductor optical amplifier based on lateral cavity laser," *Electronics Letters*, vol. 46, no. 18, p. 1288, 2010.

[42] R. Lennox, K. Carney, R. Maldonado-Basilio, S. Philippe, a. L. Bradley, and P. Landais, "Impact of bias current distribution on the noise figure and power saturation of a multi-

contact semiconductor optical amplifier," *Optics letters*, vol. 36, pp. 2521–3, July 2011.

4

Lateral Cavity SOA: Steady State Characterisation

The foundations for noise reduction were presented in Chapter 3, where two possible SOA designs were proposed for practical implementation. In this chapter the first of these prototypes will be described with the aid of simulation, before presenting the experimental characterisation of a number of chips of varying specifications. The optical characterisation technique employed is described, as well as the treatment of the data, and ultimate calculation of the gain and noise figure. Initial characterisation will compare the behaviour of these devices under the conditions where no signal is injected. Based on this the CW performance is then attained. Finally, the limitations of the prototype are detailed.

4.1 Design Concept

4.1.1 Longitudinal Carrier Density Control

To control the NF, the Lateral Cavity SOA (LCSOA) achieves carrier density modification through the strategic placement of a mirror on each side of the active region. The mirrors form a resonant cavity lateral to the principle propagation axis. Whereas a Linear-SOA (LOA), or other gain clamped SOAs, provide a transverse cavity along the complete gain length of the waveguide [1, 2, 3], the LCSOA requires the transverse cavity to be of an optimum length, thus modifying the carrier density non-uniformly. It functions as follows: Current is applied by a single contact. As the current is increased, ASE production is in turn increased, emitting light in all directions, consuming carriers both longitudinally and laterally. The LCSOA harnesses this effect, where lateral ASE is coupled to this resonant cavity. At the threshold condition, at which point the gain is equal to the loss, lasing occurs. This clamps the carrier density in the mirror region, designated the output side. As the input portion of the LCSOA has no cavity in place, the carrier density in this region increases with injected bias as normal. The sum effect of this is to establish a carrier density profile akin to the low noise profile detailed in chapter 3. A top down device schematic is given in Figure 4.1.

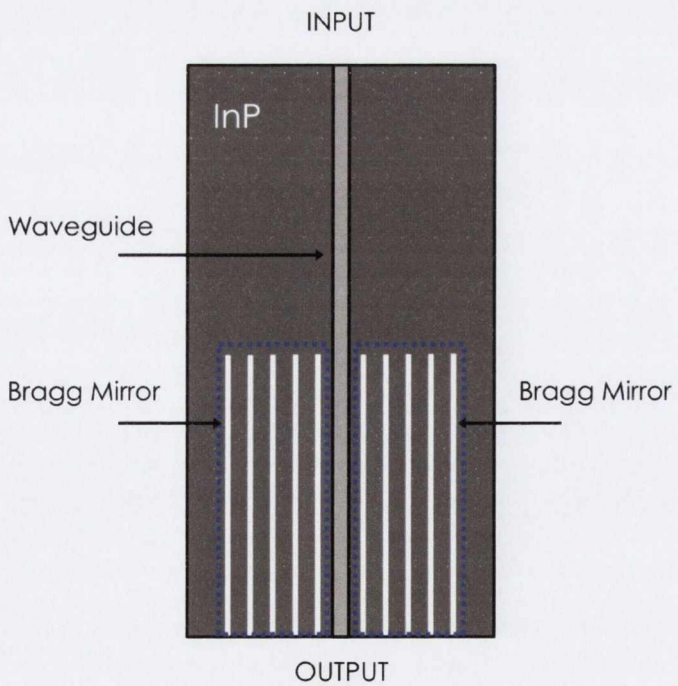

Figure 4.1: Top down illustration of LCSOA showing lateral cavity embracing the active region, over a proportion of the device. This is located at the output of the device.

4.1.2 Lateral Mirror Design

The mirrors used to supply feedback in the lateral cavity, are Distributed Bragg Reflectors (DBR). DBRs comprise alternating layers of high (n_h) and low (n_l) refractive indices, where each layer (i) is of thickness d_i. When an incident signal of appropriate wavelength (λ_B) is normally incident on the DBR the phase shift due to propagation builds up. It is important to note that the phase shift referred to in this case is the phase of a signal relative to the phase of the incident signal. Propagation through each of the layers results in a phase accumulation. Each bi-layer represents the period of the structure (Λ). In general, symmetric DBRs are used [4], where each optical layer thickness corresponds to $\lambda_b/4$ of the wavelength for which the mirror is designed. In this instance, the index contrast can be low, requiring many mirror pairs to achieve high reflectivity coefficients [4, 5]. These structures are grown layer by layer from the bottom up, and high quality mirrors with reflectivity >99% are commercially available. However, growth of vertical layers in this way is technically difficult and not used in this work. Instead, asymmetric DBRs are used, where the layers are not of equal optical thickness. In an asymmetric DBR, the formulas describing symmetric DBRs prove redundant in defining the wavelength characteristics. However, they can be simply modeled using the Transfer Matrix Method or equivalent technique. For example the symmetric DBR formulas are just a special case of the general multilayer case.

The asymmetric DBRs embracing the active region of the LCSOA are formed by dry etching [6] parallel slots into the InP cladding material parallel to the direction of propagation. This is shown face on in Figure 4.2. Each air trench and the adjacent InP layer correspond to one mirror period. A number of these periodic pairs in series constitute the DBR stack. In Figure 4.2, Λ denotes the mirror period, d_1 and d_{air} the thickness of the air and InP layers in nm, and n_1 and n_{air} are the corresponding refractive indices. The distance between the mirrors is the cavity length, L_{cav}. For a DBR based cavity an effective length may be used to describe the cavity length, however the front of each mirror proves sufficient, particularly for few mirror pairs of high contrast [7].

Air trenches are etched vertically into the InP cladding either side of the active waveguide. The process begins at the surface removing material with sufficient depth to extend beyond the active layer. The large index contrast offered by the air-gap/semiconductor interfaces result in mirrors of high reflectivity [8, 9]. A further consequence of the large index contrast is that the number of layer pairs needed is reduced compared to the symmetric DBR. Reflectivity in excess of 90%

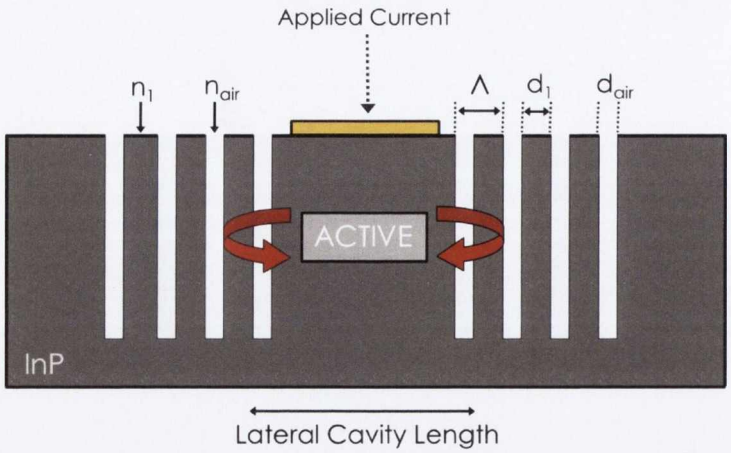

Figure 4.2: Face on slice of Bragg cavity schematic showing the mirror period (Λ), material indices (n_i) and cavity width.

using air/InP asymmetric DBRs have been demonstrated in Vertical Cavity Surface Emitting Lasers (VCSEL) using just four pairs [8, 10, 9, 10].

When modelling the effect of the lateral cavity on the longitudinal carrier density, it is not necessary to simulate the mirrors as DBRs. Instead they are modelled as simple mirrors with reflectivity coefficients $R_1 = R_2 = R_{las}$. This proves sufficient in quantifying the effect of the cavity on the carrier density in this region. However, the structure of the mirror becomes important when trying to analyse the effect of the lateral cavity in the context of its specific performance. This last point is beyond the scope of this thesis, however it is addressed in the discussion section at the end of this chapter and earmarked for future work.

Due to the short cavity length, and the resulting low cavity life time, the mirror reflectivity required to reach the lasing threshold is very high [5]. In addition, large longitudinal mode spacing results as a consequence of the short cavity lengths in these structures. This will be discussed in the context of the experimental data in the discussion at the end of the chapter in Section 4.4. The behaviour is reminiscent of the VCSEL, which due to short cavity lengths operates with true single mode operation [5]. Due to the wavelength dependent nature of the DBR, the cavity length must be chosen carefully to fall within the stopband of the DBR, and the material gain bandwidth of the active layer. Two mirror designs are utilized in this work:

Type A has a period Λ=288nm, with alternating air/InP layers. The InP layer is 248nm, with a refractive index of n_2=3.15, and the air gap is 40nm, with an index of n_{air}=1. The number of pairs has not been specified by the vendor, but, as was discussed for such a large index step, very few layer pairs are required to achieve high reflectivity (low transmission) coefficients, and

so the value is likely limited to five or less. The total width (the length it takes up along the principle axis of the SOA) of the Bragg Cavity is $W_{cav} = 500\mu$m.

Type B has the same optical period of Λ=288nm, but an InP layer thickness of 208nm, where the air gap is increased to 80nm. The total width of the Bragg cavity is $W_{cav} = 450\mu$m.

Both mirror types are fabricated by the same process under the same conditions. Good surface morphology is critically important. The sidewalls must maintain a high surface uniformity, and be as close to parallel as possible, with each layer within the same DBR, and with those of the other DBR. A small change in angle of any of the layers may impact the mirror bandwidth and reflectivity of the mirror [10]. The asymmetric DBR cavity in these structures has a broad reflectivity spectrum due to the index contrast, allowing for the difficult mode selectivity of such a narrow cavity. The actual cavity length is not known for these structures but it is at least 1.6μm (the active width), and unlikely to be larger than a few microns.

4.2 Steady State Modelling

4.2.1 Fundamentals of Numerical Model

Device modeling was undertaken in collaboration with Dublin City University. The simulations have been developed based on a travelling wave models by Durhuus and Connollly [11, 12], representing a deterministic model. The gain and NF performance generated represents relative differences. The SOA is modeled in n subsections, each electrically isolated from the neighbouring sections. The carrier density is set at an initial value and is updated from the determined values of the ASE and signal fields. This process continues over a defined number of iterations, until a steady-state is reached. Values for carrier density as well as ASE and signal fields are used as initial conditions for the next iteration. An overview of the concept of the simulation is shown schematically in Figure 4.3, which depicts the sectioning of the SOA from subsection 1 to subsection n. The levels of carrier density and the forward and backward traveling spontaneous emission fields are depicted as a function of the subsection, m. The carrier density is not uniform but peaked at the center of the SOA where the cumulative intensity of the forward and backward ASE is minimal.

The ASE intensity and the signal intensity travelling along the waveguide are calculated as a function of angular frequency (ω) by slowly varying envelope functions, and calculated using the

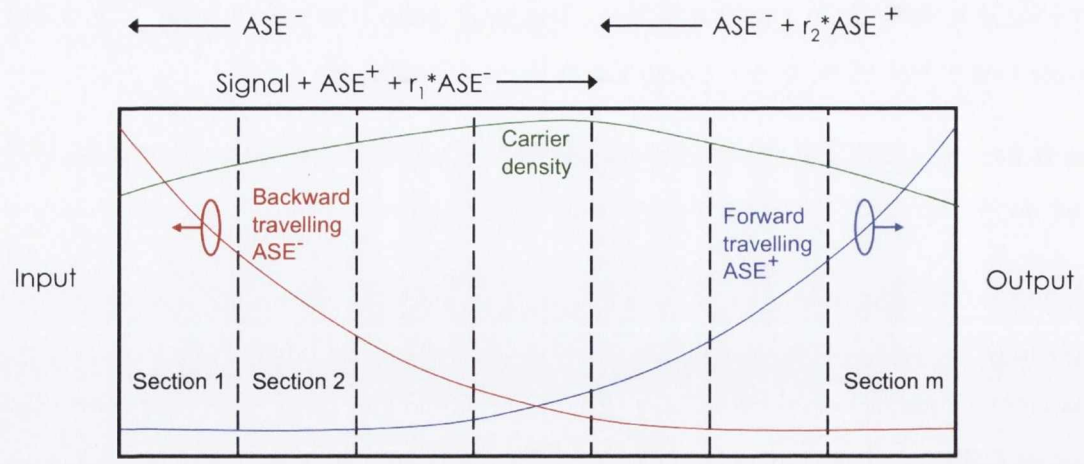

Figure 4.3: Schematic of simulated SOA, indicating carrier density (green), forward (blue) and backward (red) travelling spontaneous emission photon density, for the case of no injected signal.

set initial value of the carrier density and the material gain. The material gain is determined from the physical properties of the SOA specified in the simulation. The values of the ASE intensity I_m, for each successive subsection are determined by the values in the previous subsection according to the boundary conditions. These boundary conditions govern how the facet reflectivity affects the signal and the ASE, and are defined by,

$$\begin{aligned}
I^+_{m,sp}(\omega, z^-_m) &= I^+_{m-1,sp}(\omega, z^+_{m-1}), && m \neq 1 \\
I^-_{m,sp}(\omega, z^+_m) &= I^-_{m+1,sp}(\omega, z^-_{m+1}), && m \neq n \\
I^+_{1,sp}(\omega, z^-_1) &= r_1^2 I^-_{1,sp}(\omega, z^-_1), && m = 1 \\
I^-_{n,sp}(\omega, z^+_n) &= r_2^2 I^+_{n,sp}(\omega, z^+_n), && m = n
\end{aligned} \tag{4.1}$$

where m indicates subsection number. The relations above determine the behaviour of the ASE intensity travelling in the positive ($I^+_{m,sp}$) and negative ($I^-_{m,sp}$) directions at the subsection boundaries and the facets, where r_1 and r_2 are the reflectivity of facet 1 (input) and 2 (output). A similar equation set determines the behaviour of the signal intensity, also in the positive $F^+_{k,m}(t, z_m)$ and negative $F^-_{k,m}(t, z_m)$ directions, with respect to time (t) and position (z) along the propagation axis. The boundary conditions for the signal envelope functions are,

$$\begin{aligned}
F^+_{k,m}(t, z^-_m) &= F^+_{k,m-1}(t, z^+_{m-1}), && m \neq 1 \\
F^-_{k,m}(t, z^+_m) &= F^-_{k,m+1}(t, z^-_{m+1}), && m \neq n \\
F^+_{k,1}(t, z^-_1) &= r_1 F^-_{k,1}(t, z^-_1) + F^{in}_k(t) e^{i(\omega_{po} - \omega_{ko})t}, && m = 1 \\
F^-_{k,n}(t, z^+_n) &= r_2 F^+_{k,n}(t, z^+_n), && m = n
\end{aligned} \tag{4.2}$$

where ω_{po} and ω_{ko} are the gain peak angular frequency and signal angular frequency respectively. Using the values for the ASE envelope function, modified by the boundary conditions above, the spontaneous emission photon density is obtained,

$$S_{m,spon} = \frac{4\pi n_{g,o}}{\hbar\omega_{po}c}\left[\left(I^{+}_{m,sp}(z^{-}_{m}) + I^{-}_{m,sp}(z^{+}_{m}) + \frac{\beta R_r(N_m)\hbar\omega_{po}}{2\pi(\Gamma\cdots g(\omega_{po},N_m)-\alpha_i)}\right)\cdot\frac{G_m-1}{ln(G_m)}\right] - \frac{2\beta R_r(N_m)n_{g,o}}{(\Gamma g(\omega_{po},N_m)-\alpha_i)c} \quad (4.3)$$

where N_m is the carrier density in subsection m, G_m is the single pass gain (expressed in linear scale) in subsection m calculated from the carrier density and material gain, $R_r(N_m)$ is the radiative recombination rate, α is the internal loss coefficient and β the effective spontaneous emission factor, a measure of the spontaneous emission coupled to the travelling mode. The photon density for the signal is also obtained in a similar way using the signal envelope function,

$$S_{m,sig} = \frac{G_m-1}{ln(G_m)}\frac{\pi n_{g,o}}{c\xi}\times\left(\left|\sum_{k=1}\frac{1}{\sqrt{\hbar\omega_k}}F^{+}_{k,m}(t,z^{-}_{m})\right|^2 + \left|\sum_{k=1}\frac{1}{\sqrt{\hbar\omega_k}}F^{-}_{k,m}(t,z^{+}_{m})\right|^2\right) \quad (4.4)$$

The values for the spontaneous emission photon density and the signal photon density are then used to solve the carrier density rate equation. The program algorithm attempts to find a solution for carrier density N_m such that the time derivative is equal to zero,

$$\frac{dN_m}{dt} = \frac{i_m}{qV} - R(N_m) - \nu_g\left[g(\omega_{sig},N_m)S_{m,sig} + g(\omega_{spon},N_m)S_{m,spon}\right] \quad (4.5)$$

i_m is the bias current injected into an individual subsection m, q is the charge of the carriers, V is the volume of the active region in subsection m, $R(N_m)$ represents the recombination rate, given by,

$$R(N_m) = AN_m + BN_m^2 + CN_m^3 \quad (4.6)$$

where A is the non-radiative recombination coefficient, B is the radiative recombination coefficient, and C is the Auger recombination coefficient.

Equation 4.5 then needs to be modified to take account of the lateral cavity effect on carrier density upon intialisation of lasing. This is achieved by defining the lateral cavity photon density S_{las}, the time dependence given by,

$$\frac{dS_{las}}{dt} = \nu_g \Gamma_L [g(\omega_{las}, N_m) - \gamma_l] S_{m,las} + \Gamma_L R_{sp}(N_m) \tag{4.7}$$

where Γ_L is the optical confinement factor of the lateral laser cavity, γ_l is the photon lifetime, ω_{las} is the angular frequency of the transverse laser and R_{sp} the spontaneous emission rate coupled to the lasing mode. The consequent reduction in total carrier number as a result of transverse lasing is then attained by subtracting the lateral laser component from Equation 4.5.

This entire process comprises a single iteration of the model. The solved value of the carrier density is used to calculate the ASE and signal fields for the next iteration. Once convergence is reached, the gain and the noise figure for each subsection are then obtained. Further details of the simulation can be found in [13]. A flow diagram of the simulation is given in Appendix A. It must be noted at this point that the in-band nature of this model does not accurately account for the wideband nature of the spontaneous emission and its deleterious effect. However, for the intended purpose, i.e. to show that the carrier density control scheme modifies the NF and Saturation properties, the analysis is valid. For instance, the significance of the NF control lies in the reduction of the amplified spontaneous emission. As the ASE is homogeneously broadened any effect that the simulation produces on the in-band ASE will act as a good approximation of the broadband response, even though it is not explicitly modelled. Future work in this regard will be based on a truly wideband simulation.

4.2.2 Cavity Effect on Carrier Density

The carrier density of an SOA with and without a lateral cavity switched on at the output of the device is given in Figure 4.4, showing the direct effect on the longitudinal carrier density profile. The aim being to establish the low noise profile described in the previous chapter. The applied bias is the same for each of these cases.

The carrier density along the length of the simulated SOA when the lasing action is switched off corresponds to that of an unmodified SOA, given by the red data [14]. The maximum occurs in the centre of the device as the cumulative ASE at this point is at its minimum. As ASE propagates towards the facets carriers are depleted, the result of which is the strongest

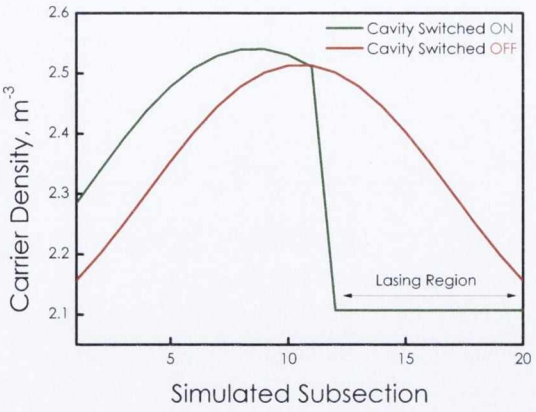

Figure 4.4: Simulated steady state carrier density with no injected signal, for both the lateral laser switched on (green) and switched off (red). The applied bias is equal in both cases, at 200mA.

ASE power occurring at the output facet, corresponding to a carrier density minimum at this point. This is compared with the green trend, where the simulated transverse lasing is initiated over a proportion of the output of the device. When the lateral cavity is switched on a direct change in carrier density is observed in the region of the transverse field. Two main features are present: The first is that the carrier density is dramatically reduced at the output according to the threshold condition of the lateral cavity. This provides the low carrier density required by the NF reduction criteria. The second feature is an increased carrier density at the input of the device due to the reduced level of reverse propagating ASE. This results in a higher gain and lower NF at the input of the device, setting the NF for the entire system to a lower value than the control situation, by the Friis equation, given by Equation 3.16.

4.2.3 Evidence for Lasing

The fabricated LCSOAs characterised in a later section do not have a direct window for measurement of the internal laser function, due to the design of the laterally transverse cavity. In other gain clamped SOAs the cavity mirrors are placed perpendicular to the propagating signal [3, 15] or as in the LOA, parallel with the propagation axis but for vertical lasing [16, 1, 2, 3]. In this way the clamping signal can be measured as an additional output component, or through the top of the structure. The present LCSOA chips, as a result of their cavity location, do not permit this. Etching a side-window is possible post fabrication but difficult to execute without damaging the SOA. As such, the only way to observe if the laser has switched on in the expected way is to note changes in the output LI data upon reaching the lasing criteria. A simulated light

output curve is plotted in Figure 4.5, plotting the total spontaneous photon density at the output as a function of increased bias to the device.

Figure 4.5: Simulated spontaneous photon density as a function of total injected bias, when the lateral cavity is switched on (green) and when it is off (red). A deviation in output power is seen at the output due to the clamping of carriers in this region.

The red data presents the linear increase of ASE power above threshold for a lateral cavity SOA where the simulated transverse laser is switched off, and no modification to the carrier density occurs. The green trend represents the switched on laser. At 30mA, the cavity condition is reached, and the carriers are clamped inducing a 'kink' (change in slope) in the generated ASE power. After this, due to the reduced carrier density at the output, the spontaneous power is reduced. The LI characterisation of the fabricated LCSOAs will be examined for evidence of such a kink, and a subsequent change in slope of the optical power. It should be reiterated that the value of lasing threshold does not necessarily coincide with the value recorded for a real device, although the best approximations for all material parameters are used.

4.2.4 Gain & Noise Figure

The program calculates the linear single pass gain (g_m) of each modeled section directly from the ratio of the input to output intensities to that section. The nf is calculated for each section by Equation 4.8, using g_m and the calculated inversion factor ($n_{sp,m}$) of that modelled section. The nf for this entire system can then be found by applying the concatenated nf formula of

Equation 3.20 to the total system. The data is then given in Decibels.

$$nf_m = \frac{2n_{sp,m}(g_m - 1)}{g_m} + \frac{1}{g_m} \tag{4.8}$$

This method takes into account the shot noise of the signal, the second term on the right hand side of the equation, however the value is found to contribute marginally in practice.

In order to obtain the best conditions for NF control, and the consequent reduction in gain induced by carrier clamping, the length of the lateral cavity relative to the total gain length should be examined. For this, a small non-saturating signal is injected into the simulated LCSOA with a wavelength in the peak gain region, for varying cavity lengths. The laser is operating above threshold, in the gain clamped regime, thus reducing the carrier density at the output. The gain and NF dependence of the relative lateral cavity length is plotted in Figure 4.6. The injected signal is -20dBm at the peak gain wavelength, at a drive current of 250mA.

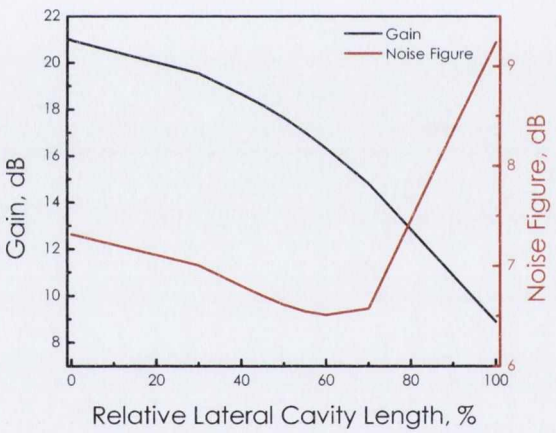

Figure 4.6: Simulated small-signal gain & NF as a function of the percentage of the total active length that the lateral cavity extends. The -20dBm injected signal is at the peak gain wavelength.

As described in Chapter 3, there is a sacrifice made to the total gain as a result of carrier clamping [17]. The gain and NF of this simulation when no lateral cavity is present are 21dB and 7.3dB, respectively. As the lateral cavity is introduced relative to the output facet, the gain and NF both start to decrease due to modification of the carrier density at the output. As the cavity length is increased to 60%, the NF drops to its minimum of 6.5dB with a corresponding 4.7dB decrease in gain to 16.3dB. This illustrates the trade off required to limit the NF by directly controlling the ASE by partial gain clamping, as the two are inherently linked. However, the relative benefit of NF control cannot be undermined as an important step, as the technique

does show direct control of this parameter. For the practical chips, cavities widths of 56% & 62% were investigated.

4.3 Experimental Characterisation

Methods of gain and noise figure measurement exist that are based on both electrical and optical techniques [18, 19]. For this work, an optical approach is taken, in line with the optical derivation of NF from chapter 2. All gain and NF values quoted herein, unless otherwise stated, refer to chip values. This provides a more meaningful evaluation of the output parameters from a comparison point of view, as all effects are device inherent. The experimental acquisition of raw data, the necessary treatment of these spectra and the subsequent calculation details are now given, for a variety of LCSOA.

4.3.1 Device Under Test

The devices investigated in this chapter are ridge waveguide InGasAsP/InP multi-quantum well (MQW) SOAs. The active region is 1.6μm wide, grown on an InP substrate. The length of the chips are 1000μm, including 100μm tapers at each end. The SOAs are angled and anti-reflection coated to reduce cavity effects. The chips comprise a single contact, pumped by a DC current supply. All chips are from the same wafer. The feature differences between them relating to mirror type, length and position, are given in Figure 4.7, where y is the distance from the beginning of the output taper, and W_{cav} the cavity width along the propagation axis.

Among this sample set, is an SOA with no laser cavity. This device is from the same wafer, having identical waveguide and layer structure and so acts as the ideal control case, and labelled SOA-C. An optical image of an LCSOA bonded to its submount is shown in Figure 4.8. Visible is the position of the waveguide, including angled tapers, and the bonding wires. The lateral structure is too small to resolve optically.

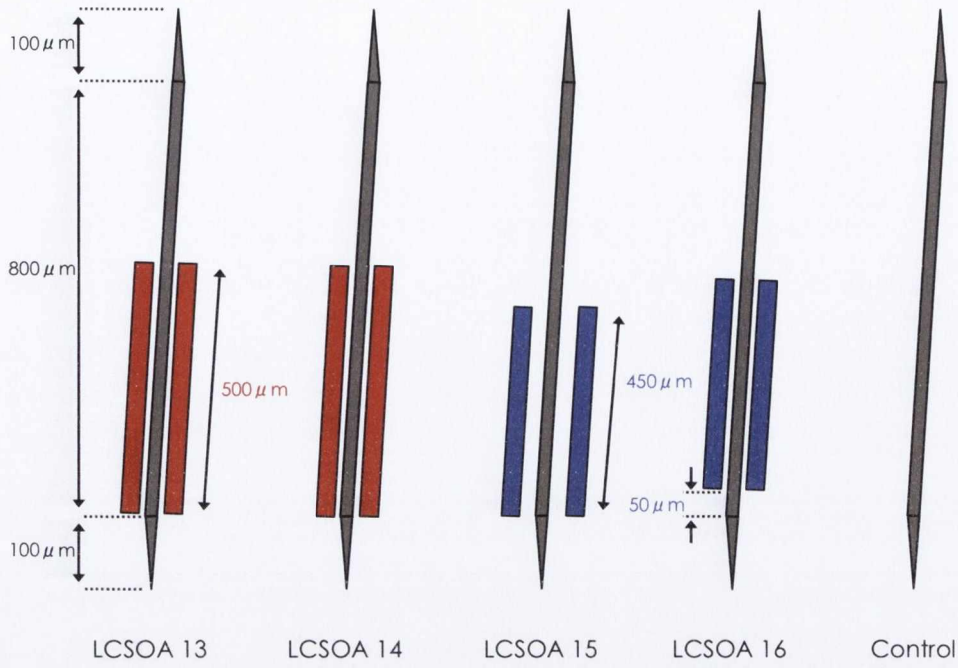

Figure 4.7: LCSOAs examined in this work. The red and blue mirrors represent different mirror designs, red being 'Type A', blue being 'Type B'. In all cases the lateral cavities are placed near the output facet. The control device is also shown, and contains no lateral cavity.

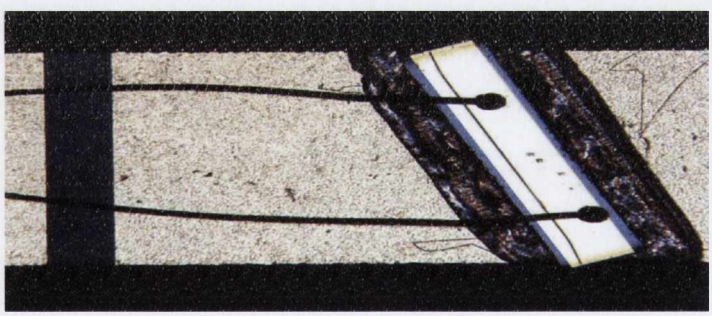

Figure 4.8: Optical image of an LCSOA chip, showing fillet bonded to the submount, and ball bonded wires.

The devices described in Figure 4.7, which provided specific details relating to relative position, length and type of mirrors, were selected after an initial probe station based LIV characterization. The devices represent the best candidates from the batch that produced any light output of appreciable magnitude. The remaining devices were not viable. This was attributed to damage that may have occurred during the implementation of the lateral cavity, as the etching takes place very close to the waveguide. This will be returned to in the discussion at the end of the chapter.

4.3.2 Experimental Setup

The optical steady-sstate setup is shown in Figure 4.9. The set up consists of a tunable external cavity laser (ECL), with continuous wave (CW) output, with a coupled-power range of 26dB from -20dBm to 6dBm, and a wavelength range of 1480nm - 1580nm. This passes through a fiberised polarisation controller to set the state of polarization of the injected signal. The light is coupled to free space, where it is incident on two separate mirrors to optimise the injection angle. The polarisation state is measured after the final mirror using a polarimeter, to offset any slight rotation effects or loss of linearity [20, 21]. The light is then coupled to, and collected from, the SOA using two 0.68 NA moulded aspheric, anti-reflection (AR) coated lenses. The SOA output signal is then collected on an optical spectrum analyser (OSA), with a minimum resolution bandwidth of 0.06nm. The NF and gain calculation are polarization dependent, and so the percentage of co-polarised ASE along a particular mode is also measured. This is done by measuring the TE and TM polarised ASE using an integrating sphere power meter and polarisor combination.

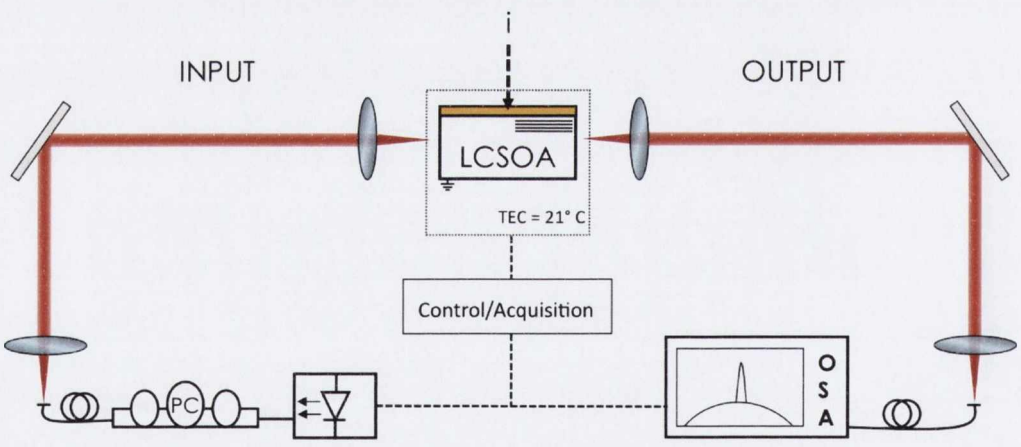

Figure 4.9: Steady state characterisation set up. Shown is the tunable external cavity laser (ECL) source, polarisation controller (PC), the MCSOA under test and an optical Spectrum analyser (OSA).

All chips are fillet bonded to a submount, which is further fixed to a larger insulated aluminium mount. The entire structure is temperature regulated at 21°C by a peltier and thermistor feedback loop. The pump current is supplied by a DC current supply. The pump current (i) is applied using a circuit board arrangement which is wedge bonded to the SOA chips directly.

4.3.3 Systemic Losses

The calculated chip gain and NF are highly sensitive to losses throughout the measurement system, and so must be corrected for this. As such accurate determination of the losses is vitally important. The losses can be catagorised as either input or output in origin.

Input Losses

The largest contribution to input loss arises from the mismatch between the circular mode of optical fibre and that of the elliptical SOA waveguide mode. This is estimated by measuring the output power after the SOA coupling lens and again after optimising the coupling of this light to the optical fibre. A modal mismatch of approximately 3dB is generally used in the literature, depending on the structure specifics [14]. Here, this is not the case, and accurate values are used. In the case of the LCSOAs this is increased substantially to approximately 7dB, even with the aid of the integrated tapers. Lens, fibre loss, mirror loss and coupling from the ECL source are also estimated and applied to the calculated gain and NF values.

Output Losses

The output losses have a less significant affect on the NF, but greatly affect the gain. The modal mismatch is again the primary portion of total output losses, but again lens, fibre, mirror losses and the coupling of light to the optical spectrum analyser (OSA) are determined too. These are all calculated in the same way and applied as necessary. An additional source of loss at the output side of the setup is due to the placement of a polarisor in the optical path to measure the percentage of co-polarised ASE.

4.3.4 Treatment of Raw Spectra

As no electrical signal analysis is undertaken after termination of the output signal at a photodiode, all data is calculated from raw spectra directly recorded by the OSA. The gain and NF are generated as a function of wavelength, power and injected bias, where all raw data is treated in the same way in each case. A representative output spectrum is shown in Figure 4.10.

Measurement attributes are calculated using the entire set of trace points of the spectra in order to provide more repeatable results, where this is particularly useful for devices that exhibit significant levels of fluctuation in the distribution of optical energy. All spectra are acquired over a 1nm span and must be corrected for the measurement resolution bandwidth (R_{bw}), which

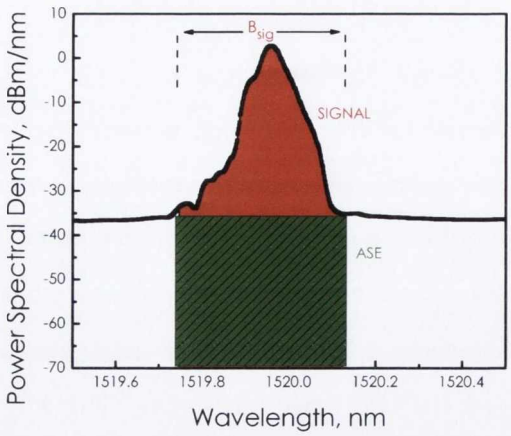

Figure 4.10: Representative raw spectrum, with a 1nm span centred on 1520nm, used to calculate a single gain/NF point. Shown in red is the integrated signal power (P_{sig}), and in green the ASE power (P_{ASE}) calculated by the program.

is 0.06nm. A Matlab program identifies the signal peak, then summing under this curve for a particular bandwidth (B_{sig}) the total power (P_{tot}) is found. The total power represents the summation of the power at each trace point, normalised by the ratio of the trace point spacing and the resolution bandwidth, and includes both the signal and the ASE together. It is given by,

$$P_{tot} = P_{sig} + P_{ASE} = \sum_{i=1}^{n} p_i \left(\frac{\text{trace point spacing}}{R_{bw}} \right) \tag{4.9}$$

where p_i is the trace point, i is the number of the trace point, R_{bw} is the resolution bandwidth of the measurement.

In order to isolate the level of ASE in this signal bandwidth, a line is extrapolated across the base of the signal trace over B_{sig}, and integrated under it. This area then accounts for the total ASE power (P_{ASE}) in B_{sig}. At this point the power spectral density necessitated by the optical NF formula must be found using B_{sig},

$$\rho_{ASE} = \frac{X P_{ASE}}{B_{sig}} \tag{4.10}$$

where ρ_{ASE} is the ASE power spectral density, X is the percentage of ASE co-polarised with the signal, P_{ASE} is the measured ASE power, and B_{sig} is the signal bandwidth.

Once ρ_{ASE} has been obtained, the gain and NF can be generated as a function of wavelength, bias or power using the equations established in chapter 2 & chapter 3, which are repeated

below. The chip gain is given by the ratio between the input and output powers, whilst the NF is calculated by the optical NF formula. It should be noted that the quantum efficiency, η, is set equal to unity as the effect is taken into account internally by the OSA. This is true for all NF and gain calculations.

$$G(dB) = 10\mathrm{Log}_{10}\left(\frac{P_{sig}}{P_{in}}\right) \tag{4.11}$$

$$NF(dB) = 10\log_{10}\left(\frac{2\eta\rho_{ASE}}{Gh\nu}\right) \tag{3.15}$$

4.3.5 Light-Current Characteristics

The ASE power output of each chip is collected using an integrating sphere power meter directly after the coupling lens. The power is measured from both sides of the device. The control device, SOA-C, is shown in Figure 4.11.

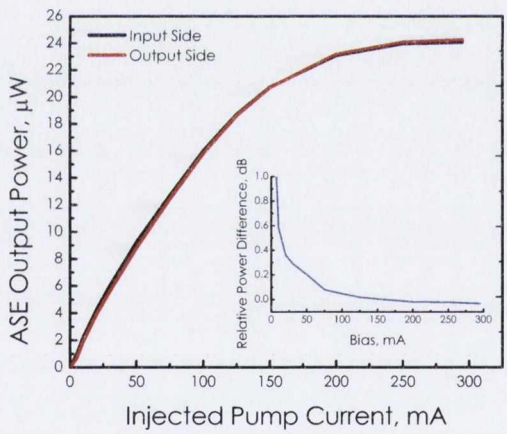

Figure 4.11: ASE power output measured at the input/output as a function of pump current for SOA-C, where no lateral cavity function exists. Inset: Relative power difference (dB) measured from the input and output of the SOA.

With no lateral mirrors present a symmetrical ASE output is expected. This is due to the equal carrier density in the facet regions of the SOA-C where no gain clamping occurs in the absence of transverse lasing. This not only illustrates the effect of the cavity on the level of ASE produced when explored in the following plots, but so too the condition of the tapers and facets. In this case the fact that the powers are identical would suggest that the tapers and AR coatings are functioning as designed. The peak power levels off at approximately 250mA, to 24μW.

This is an extremely low ASE power level, and may be an indication of the low confinement nature of the quantum well waveguide, which may still provide a reasonable gain in the absence of appreciable ASE levels. Inset is a plot of the relative power difference between each facet, which for SOA-C is negligible at higher biases.

Figure 4.12 presents two of the four viable LCSOA devices that will be reported on in this thesis. These data are plotted side by side as the LCSOAs share an identical design in terms of mirror type (Type A) and position relative to the output facet (y = 0μm). Inset in both cases is the relative power difference measured between the designated input and output.

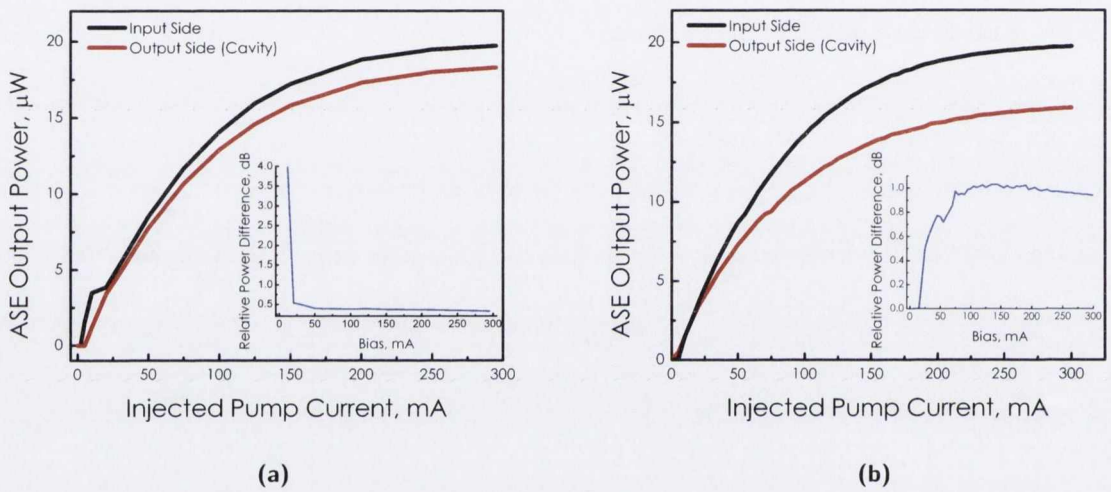

Figure 4.12: ASE power output as a function of pump current for (a) LC SOA 13 and (b) LCSOA 14. These devices are identical in design, using mirror Type A. Inset: Relative power difference (dB) when measured at the input and output facet.

The prominent feature of these plots is the difference in ASE power between the measurement at each facet. The lower ASE power collected from the section with the lateral cavity present is consistent with the reduced carrier density expected of this portion of the waveguide. The same is true of light collected from the input side, where a higher carrier density exists by function of the carrier clamping at the output. In this way, carriers which would otherwise be consumed by reverse propagating ASE from the output section are instead available for signal gain. Measuring the LI data for the LCSOA serves as an indicator of any carrier density modification. However, it should be noted that it is difficult to state with certainty if the lateral cavity has reached threshold. In fact, the only way to unambiguously examine this, is to collect the light emitted from the side of the device as stated previously. With such low powers emitted along the main propagation axis of these SOAs, it is likely that only through the etching of a small window

region in the side of the chip (in line with the waveguide) that this is plausible, an option not practical for this work.

There is some evidence that transverse lasing occurs beyond the difference in power emitted from the input and output facets. As was proposed through simulation a 'kink' should manifest at the point of laser oscillation. In Figure 4.12 (a) a change is observable in the measured power of LCSOA 13 at 10mA when measured from the input side of the device. Low thresholds of 7mA have been demonstrated in VCSELs [22], however at this very low bias it is unlikely that the lateral cavity has begun to lase. This assertion is justified by the fact that the powers converge once more as seen in the inset, and the relative difference remains low. It is possible that this is occurring not due to gain clamping in this region, but an increased level of loss.

LCSOA 14, given in Figure 4.12, (b) demonstrates a greater divergence of spontaneous power at an injected current of 15mA. Onset of a small feature manifests at 55mA when measured on the input side, and 73mA measured on the output side. The maximum relative difference is 1dB at an injected bias of 117mA, before slowly starting to converge. Remembering that these chips are from the same wafer, and of identical design, indicates a level of unreliability in the processing. Mirror Type-A is comprised of the more technically demanding 40nm trenches, leading in this case to a higher likelihood of failure of the lateral cavity function initializing.

Figure 4.13 presents LCSOA-15 and LCSOA-16, both of which use mirror Type-B. LCSOA-15 has a mirror position of y= 0μm, and a longer lateral cavity length than all other chips (i.e. the mirrors are placed further from the active region), the length of which is not known. LCSOA-16 is given in Figure 4.13 (b), having the same cavity length of LCSOA-15, but a mirror position of y=50μm.

Looking at Figure 4.13 (a), ASE power divergence occurs from 10mA to the strongest level of ASE power of all the LCSOAs, including the control. The highest value attained on the input side, for the same reasons discussed previously, is 40μW. Of all the devices tested, the property unique to this one is the lateral cavity length. Although this does not explain the difference in the ASE production relative to SOA-C, it may be an indication that the cavity length is too short in the other LCSOAs, inducing losses. The highest power measured at the output is 33.7μW, representing a relative power difference of 0.75dB over the input side. Regions corresponding to a small change in power on the LI curves are again visible as small peaks in the relative power difference, inset. The first region peak occurs at approximately 50mA. The second region has peaks at 99mA and 130mA. The change in power is very small and is at first easily attributable

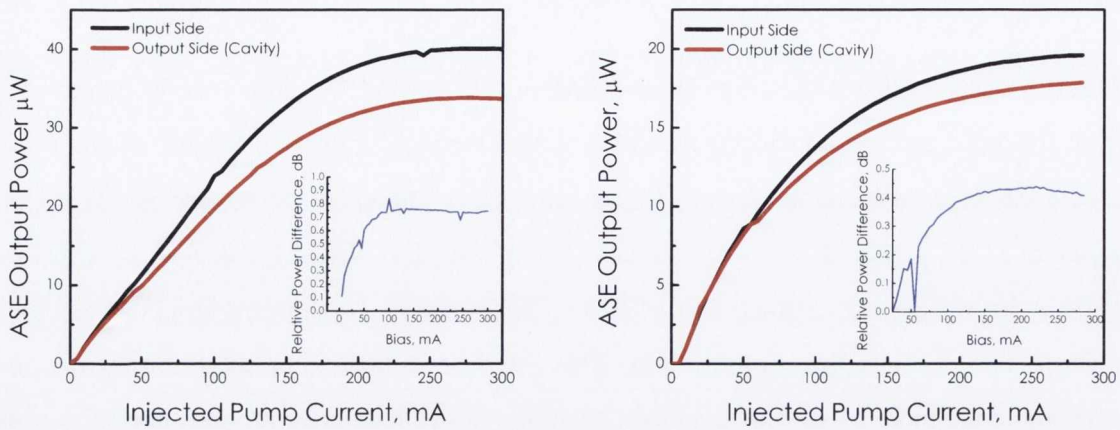

Figure 4.13: ASE power output as a function of pump current for (a) LCSOA 15 and (b) LCSOA 16. These devices are not identical in design. Both use mirror Type B, however have differing mirror positions and cavity lengths. Inset: Relative power difference for each device in dB.

to error, however the data is measured on each side independently, and the kinks occur in pairs, suggesting significance.

The most distinct observation of these kinks are plotted in Figure 4.13 (b) for LCSOA-16. The powers emitted are equal from each facet until 35mA at which point they begin to diverge. It is not until approximately 50mA that a significant onset in ASE power divergence occurs . This occurs first when measured from the input side and then the output, constituting a kink. After this point the powers begin to diverge at a greater rate. Inset, the relative power difference exhibits this kink, however it is a low value, with a maximum shift of 0.2dB. The total output power from this chip is comparable to the devices in Figure 4.12, at 19.5μW and 17.7μW when measured on the input and output sides, respectively. LCSOA-15 produces 20μW more on the input side, double that of SOA-C.

In summary, the LI data provides a significant indication of how the LCSOAs will operate under CW injection. The higher output of LCSOA-15 suggests a better gain performance, while still maintaining a good level of carrier density control, seen by the 1dB ASE power difference. That LCSOA-15 is the most promising device based on this data, possibly related to the longer lateral cavity length, coupled with the mirror Type B, with 80nm Air trenches. Before describing the CW characterization, the ASE spectra are presented.

4.3.6 ASE Spectral Response

The ASE of SOA-C and LCSOA-14, measured using an OSA with a 1nm resolution bandwidth is given in Figure 4.14. The left side of the figure is the ASE collected from the input facet, the right hand side is collected from the output facet. The top row is the control, SOA-C, and the bottom row is LCSOA-14. The data is collected for increasing bias from 0-300mA.

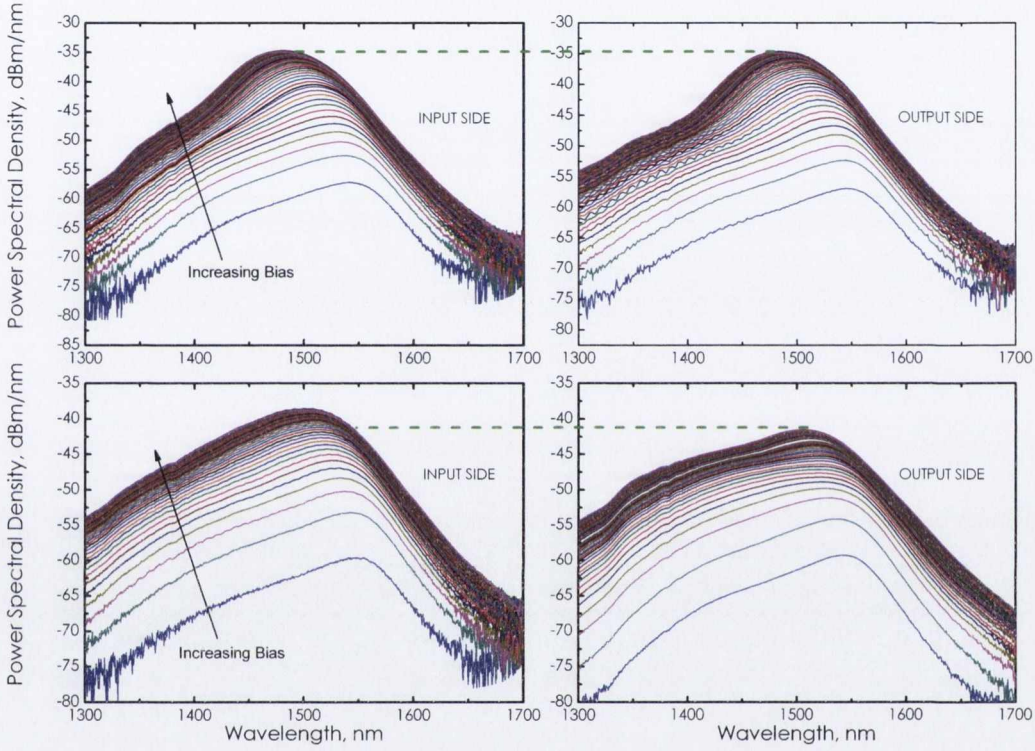

Figure 4.14: Measured ASE for SOA-C and LCSOA-14, collected at the input (left) and output (right), for increasing injected current. The top row is SOA-C, with no lateral cavity. The bottom row is LCSOA 14, which does have a cavity as previously described.

As the LI data of Figure 4.11 confirmed, the control SOA should have a symmetric output, in the absence of any carrier density modification. This is mirrored by the spectral data collected from both sides of the SOA being of the same peak power for each drive current. The only feature difference that exists is a negligible reduction of power density in the 1400nm region, possibly a result of the wavelength dependent nature of the waveguide termination [23, 14]. The blue shifting of this data is due to band filling. As the bias is increased transitions tend to occur from higher energy states. The bottom row of this plot again reflects well the LI data, previously shown in Figure 4.12, where a reduction in ASE power is seen at the output side, highlighted by the dashed line. There is no spectral evidence of lasing present in either plot for LCSOA-14. The reason for this is the homogenous gain broadening of the amplifying medium

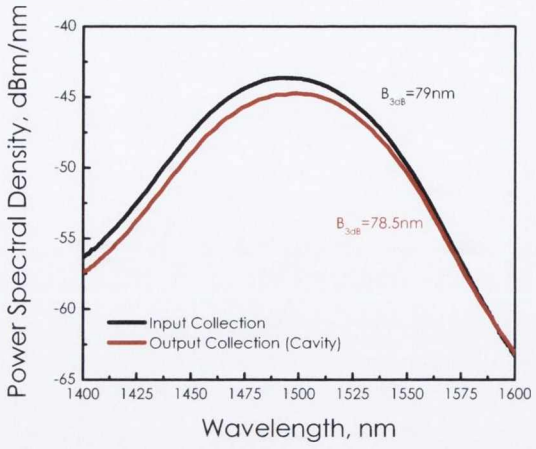

Figure 4.15: Measured ASE at a 250mA drive current, collected at the input (black) and output (red), for LCSOA-15. The data shows the effect of the lateral laser on the carrier density at the output of the structure with its reduced ASE spectrum.

[14, 24].

Figure 4.15, depicts a plot of the ASE for LCSOA-15 at a high drive current, measured at the input and output facet. This device displayed the most promising LI data in terms of higher levels of ASE likely connected to higher levels of gain. In addition small kinks observable, potentially related to the transverse lasing function, were also visible. Although evidence for lasing in LCSOA-15 is not definitive, the device directly controlled the ASE collected from the input and output facets, and at the highest powers. In addition to this it was the only chip with Bragg mirrors etched quite far from the active layer, which is a possible reason for the superior performance as will be seen later, as data showing gain and NF control is presented in the next section. There is a clear wavelength dependence of the realisable control, with a greater effect seen at higher energies. Finally, there is negligible residual ripple seen in the device.

4.3.7 Continuous Wave Injection

The continuous wave performance of LCSOA-15 and SOA-C are now presented. From an initial characterization of all five prototype chips, and from the LI data discussed, the remaining LCSOAs proved non-viable, with very low gains (negative gain) over a very small bandwidth. The consequent NF was thus extremely large, with the devices largely acting as lossy elements. It is important to reiterate at this point that LCSOA-15 and SOA-C are difficult to compare directly, as they have different ASE output powers and therefore a difference in gain. The reasons for this difference are unknown, however a number of explanations are addressed at the

end of the chapter. However, they are from the same wafer and in that sense are well suited for comparison. The term 'Forward' injection will relate injection of the optical signal into the designated input of the device. 'Reverse' injection will be into the output. For SOA-C these are equivalent, and so only one will be shown. The importance of forward and reverse injection, is the consequent carrier density profile that the input signal 'sees' i.e. Low Noise Figure versus High P_{sat}.

Wavelength Dependence

The CW wavelength dependent gain is shown in Figure 4.16. The applied bias is 250mA, in the high gain regime, the injected power is -18dBm after input losses, TE polarized. The peak gain in the control case is 4.5dB at 1488nm, at a 3dB gain bandwidth of 66nm. This compares with a LCSOA-15 forward injection gain of 8.46dB at 1494nm and a reverse injection gain of 6.6dB at 1495nm. If the control and LCOSA devices were identical, this result would directly contradict Figure 4.6, which demonstrated the simulated sacrifice to gain induced by the carrier clamping mechanism. The difference between forward and reverse injection is 1.86dB. This result was not expected and will be returned to in the discussion section. An additional point of interest relates to the gain bandwidth, which corroborate the ASE spectra. Specifically the gain peak for the SOA-C is 1488nm, blue shifted by 7nm from the LCSOA peak of 1495nm. The lower gain performance of SOA-C was predicted by the LI data, however it is still unclear why this occurs. The symmetric output of the ASE suggests no problems with the facets or tapers. It was seen that the overall yield of the growth was low, with very few functioning devices. It could be argued then that a poor growth process is responsible, but to what end remains unknown.

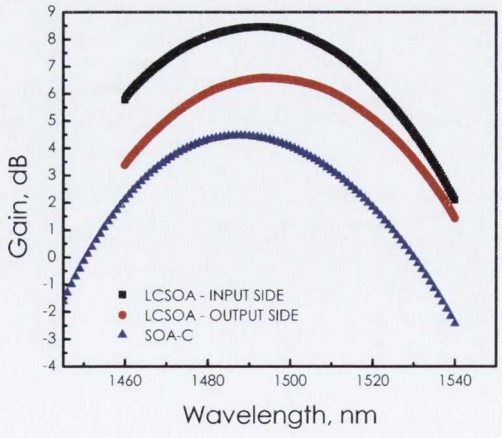

Figure 4.16: Experimentally obtained gain as a function of wavelength under forward and reverse injection for LCSOA-15, and SOA-C, for a small injected signal of -18dBm, TE polarized, at a pump current of 250mA.

The corresponding NF data is plotted in Figure 4.17. The worst NF performance is produced by SOA-C, with a minimum of 11.55dB at 1482nm, expected due to the low gain of this device. This is blue shifted from the LCSOA again predicted by the ASE and gain spectra for this device. The forward injection of the LCSOA yields a NF of 8.2dB at 1499nm, compared with the reverse value of 10.75dB. These values demonstrate directly the effect of longitudinal carrier density profiling on the chip NF, and provide conceptual corroboration of the noise figure reduction technique. However, the values themselves are poor, due to the low level of gain provided by the chips.

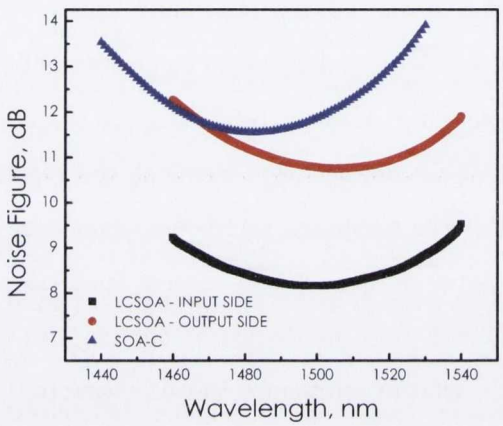

Figure 4.17: Experimentally measured NF as a function of wavelength under forward and reverse injection for LCSOA-15, and SOA-C, for a small injected signal of -18dBm, TE polarized, at a pump current of 250mA.

Like the gain, the reasons for this are unclear, and a variety of possible reasons exist. Furthermore, a difference in NF would manifest due to the gain difference experienced as a function of signal propagation. However this does not sufficiently account for a NF difference of 2.55dB between forward and reverse injection, again suggesting a definite influence of carrier density modification.

Injected Current Dependence

Figure 4.18 plots the gain as a function of applied bias. The injected wavelength is 1500nm, and TE polarized, and the current is varied from 0-300mA. The low level of gain reached at 250mA is 8.1dB & 6.4dB, in forward and reverse injection, respectively. However, it is not until the bias passes 78mA for injection into the input facet, and 88mA for injection into the output facet, that the device imparts a positive gain to the small injected signal. Before this point the device acts as an absorbing element, clearly a negative in terms of performance. The fact that

it requires such high applied currents to induce gain, would yet be another indicator that the device is not operating properly. This ties in with the very low level of ASE produced, where a large proportion is likely absorbed by the device.

The corresponding NF data is given by Figure 4.19. As a result of the negative gain at low biases the NF is extremely high as expected as it is directly proportional to the level of loss [19]. The minimum value measured is 8.3dB at 230mA, but the change is this over the 20mA to 250mA is very small. The minimum in reverse propagation configuration is 10.9dB. This value and those of the gain as a function of bias, differ within error to those previously given due to heating effects of the bias scan. Above transparency the NF decreases rapidly with bias in agreement with the gain performance.

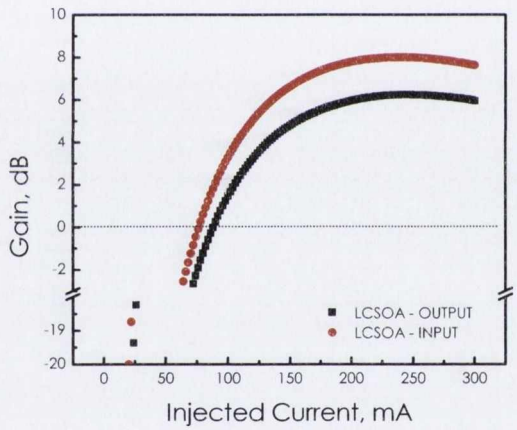

Figure 4.18: Experimentally measured gain as a function of applied bias under forward and reverse injection for the noise controlled SOA, LCSOA-15, under a small injected signal of -13dBm, TE polarized, at 1500nm.

Saturation Dependence on Injection Direction

The effect of longitudinal carrier density modification on the saturation performance of the device is now discussed for LCSOA-15. The gain is given as a function of both output and input power in Figure 4.20.

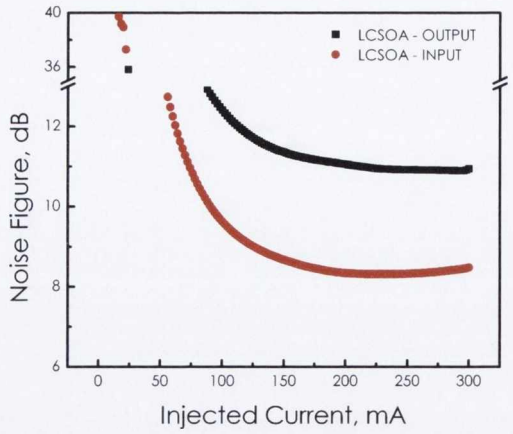

Figure 4.19: Experimentally measured NF as a function of applied bias under forward and reverse injection for the noise controlled SOA, LCSOA-15, under a small injected signal of -13dBm, TE polarized, at 1500nm.

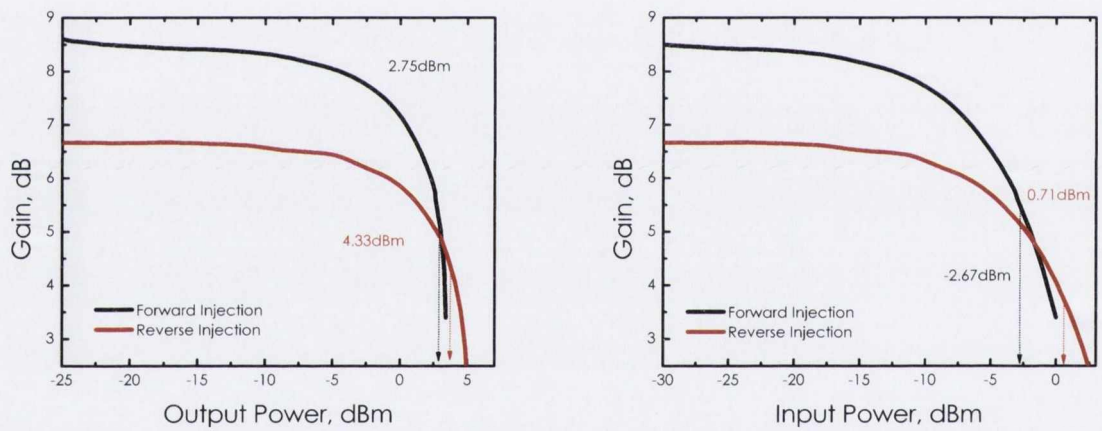

(a) **(b)**

Figure 4.20: Gain as a function of (a) output power and (b) input power, for LCSOA-15. The injected wavelength is 1500nm, and injected in both forward and reverse propagation.

Again, the striking difference in gain is present. The data was taken in the small signal range to assess the linear performance of the LCSOA. It is the extent of this region that is of importance in a practical situation [14]. As was shown in chapter 3, the reverse injection profile should lead to an increase in the saturation performance, seen in the figure above. The 3dB saturation output power for forward injection is 2.75dBm, and 4.33dBm for reverse injection, representing the High P_{sat} carrier density profile. This is an improvement in saturation power of 1.58dB, significant when compared with other methods [25, 26, 27]. However in this case it comes at

a sacrifice to gain, although it is the High P_{sat} configuration that experiences the lower small signal gain. On the other hand this will improve with future generations of the LCSOA, where the gain discrepancy has been addressed.

This effect is further illustrated by looking at the saturation input power Figure 4.20 (b). The difference in P_{sat},in between forward and reverse propagation is 3.38dB, marking a extensive additional range of input powers accommodated before saturation of the gain becomes important. The relative performance difference compares favourably with the holding beam and staggered resistance methods of Crottini and Saini, respectively [28, 29].

4.4 Prototype Limitations

As this is a 1^{st} generation prototype device, requiring a complex internal structure to function as designed, some complications are inevitable. This section will discuss some potentially problematic areas. Three significant features endure throughout the characterization of the LCSOA chips. The first is the low level of gain (and so ASE power). The second is confirmation of carrier density clamping, or, confirmation of lasing in the transverse direction. The third is the difference in gain with propagation direction. These will be now be addressed.

The most striking feature of all gain plots is the discrepancy between forward and reverse propagation. It will be seen in the next chapter that as the total density of free carriers is the same, the small signal gain should be the equal, regardless of propagation direction. The reason for the gain discrepancy is unclear, and due to the equally low ASE power produced across the entire range of devices, it is difficult to attribute it to any specific feature. One possibility is that the presence of the lateral cavity may reduce the local refractive index around the active region, increasing the confinement factor in this region. This could then introduce a direction dependent injection loss. On top of this, the device which provides the largest gain, including the control device, is a lateral cavity device (LCSOA-15), where gain clamping should produce a reduction in gain. This makes it difficult to specifically identify the implementation of the lateral cavity as the main cause. More likely, it is the fabrication that is the cause, as the entire chipset is affected.

The function of the lateral cavity was described in section 4.1, where the lasing condition was described, i.e. lasing is initiated when the gain is equal to the cavity loss, clamping the carrier density at this threshold value [7]. As pump current is further applied, the lasing intensity is

increased. However, the onset of lasing requires a number of additional criteria to be met. Firstly, setting aside the mirror structure and reducing them to simple broadband reflective elements, the transverse laser can be modeled as a simple Fabry-Perot cavity, with a cavity length of L_{cav}. This dimension is not known exactly for these chips, but is thought to be in the region of 1.6 - 3.2μm. The net effect of such a short cavity length is single longitudinal mode operation with a large free spectral range (FSR). The FSR for such a cavity can be enlarged by as much as two orders of magnitude compared with that of a conventional edge-emitting laser diode (with cavity lengths of hundreds of microns) [7]. As such, good spectral overlap with the material gain spectrum of the active region and the reflectivity spectrum of the mirrors is required for lasing, as well as high reflectivity to compensate for the low single-pass gain of such a short active region [30].

This description of the lateral cavity neglects the mirror structure. When taking the Distributed Bragg Reflectors into account, the system becomes more complex. The DBRs which comprise the lateral cavity are required to have very high reflectivity as was stated. This is achieved in the LCSOA by the use of air/InP asymmetric DBRs, with a very high theoretical reflectivity per layer-pair. This is possible due the high index contrast of the air/InP interfaces. However, due to the layer dimensions required, particularly the air trenches, very precise and difficult processing results. This may lead to unpredictable trench morphology, at localized points or along the entire width of the mirror. If this occurs and angles or poor surface smoothness are introduced, the reflectivity as a function of the longitudinal position along the mirror may vary dramatically, which is difficult to measure. During the metalisation process, gold may also permeate the mirror structure which would also affect the reflectivity spectrum. The net result of a combination of one or more of these scenarios, could be a non-ideal laser function, or a more localized lasing (meaning a shorter region of clamping than desired), or perhaps staggered lasing along the mirror region.

Finally, another potential issue related directly to the mirror structure is an increase in active region temperature. It has been shown in VCSELs and similar structures which rely on DBR that heat dissipation can be a problem [31]. If the temperature in the region of the cavity builds significantly it may produce a reduction of quantum efficiency in this region directly. However, the control chip has no such cavities and displays an even lesser gain, meaning that if there is a temperature effect it is likely not contributing to the low gain values, but may affect the threshold condition of the lateral laser [32, 7]. This would be particularly relevant where air gaps are used in place of a more typical material, with the added effect of also increasing surface

related non-radiative recombination in this region.

4.5 Conclusions

The concept of noise figure control by longitudinal carrier density modification was modeled and experimentally demonstrated. Specifically, the incorporation of a lasing cavity in the output portion of the SOA, laterally transverse to the propagation axis, clamps the localised carrier density in this region at a particular value of laser threshold. The input carrier density is free to vary with pump-current, establishing the Low NF carrier profile detailed in chapter 3. Local gain clamping occurs at the expense of gain variability in this region, in that the value is fixed at a point chosen at the design level. In addition, injecting into the output side (reverse propagation), produces the High P_{sat} carrier profile previously described, which allowed for the demonstration of the control of this parameter.

It was shown through simulation that the optimum percentage of the SOA length that the lateral cavity should cover is approximately 55%, the value used in the most promising LCSOA realised. Of the batch fabricated after initial probe characterization five were suitable for full characterisation. Of these five, two proved viable (produced gain): the control SOA (SOA-C) with no cavity implemented, and a single Lateral Cavity SOA (LCSOA-15), which as well as being the only device to function properly, also featured a unique lateral cavity length, larger than the other LCSOAs, providing valuable information for future iterations of the design.

Under non-injection conditions, the ASE power of LCSOA-15 was measured, producing an asymmetrical dependency when collected from both the input and output facets, demonstrating the effect of carrier control. The relative difference achieved was 1dB between the input and output facets at 250mA. This control was also evident in the ASE spectra, which also illustrated the wavelength dependence. Under the injection of a low power CW beam, the LCSOA provided linear-gain values of 8.5dB and 6.6dB, in the forward and reverse propagation schemes, respectively. The corresponding NF values were measured to be 8.2dB & 10.75dB at approximately the same bandwidth. This shows direct control of the NF as a consequence of the carrier density profile, proving the concept described in Chapter 3. Accompanying this result is a difference in gain experienced by the signal, dependant on the injection direction. This discrepancy is counter to expectation, and the reason for it is not known presently. However, it is possible that it is related to either, difficulties encountered during fabrication, or the lateral laser not operating as

expected. SOA-C, which contains no lateral cavity effect, yielded a symmetric ASE output as expected, where no modification of the carrier profile takes place. The experimentally measured gain and NF were 4.5dB and 11.55dB, in both directions of injection. The lower value of ASE and gain produced by this device possibly reveal a potential problem during fabrication of the chips. The LCSOA should have less total chip gain, as a consequence of the gain clamping mechanism.

In addition to direct control of NF, the gain was measured as a function of input and output power. This provided the opportunity to assess the level of control obtainable over the saturation point in terms of both input and output powers, $P_{sat,in}$ and P_{sat}. In forward propagation the values measured are P_{sat} = 2.75dBm and $P_{sat,in}$ = -2.67dBm. In contrast to this, the reverse propagation values were recorded as P_{sat} = 4.33dBm and $P_{sat,in}$ = 0.71dBm. This equates to a total level of control, dependent on the carrier density profile, of $\Delta P_{sat,in}$ = 3.38dB and ΔP_{sat} = 1.58dB. The potential practical implementation of this control, of both NF and P_{sat}, is the use of the SOA for two distinct scenarios, both in the linear regime. The first is as a booster amplifier, and relies on having a high saturation power. The second is as a pre-amplifier, where the main criteria is minimum NF. Both of these practical implementations are achievable with a single device, using this method.

The techniques used to experimentally compare the LI, gain and NF characteristics will be progressed in the next chapter, which will continue the steady state investigation of NF and saturation control through the second proposed design of a noise controlled SOA.

References

[1] D. A. Francis, S. P. Dijaili, and J. D. Walker, "A single chip linear optical amplifier," in *Optical Flbre Communications (OFC)*, no. 510, pp. 8–10, 2001.

[2] C.-y. Jin, Y.-z. Huang, S. Member, L.-j. Yu, and S.-l. Deng, "Detailed model and investigation of gain saturation and carrier spatial hole burning for a semiconductor optical amplifier with gain clamping by a vertical laser field," *IEEE Journal of Quantum Electronics*, vol. 40, no. 5, pp. 513–518, 2004.

[3] M. K. P Doussiere, P. Garabedian, C. Graver, D. Bonnevie, T. Fillion, E. Derouin, M. Monnot, J. G. Provost, D. Leclerc, "1.55um Polarisation independent semiconductor optical amplifier with 25dB fiber to fiber gain," *Technology*, vol. 6, no. 2, pp. 170–172, 1994.

[4] D. Sridharan and E. Waks, "All-optical switch using quantum dot saturable absorbers in a DBR microcavity," *IEEE Journal of Quantum Electronics*, vol. 47, no. 1, pp. 31–39, 2011.

[5] C. Tombling, T. Saitoh, and T. Mukai, "Performance predictions for vertical-cavity semiconductor laser amplifiers," *IEEE Journal of Quantum Electronics*, vol. 30, no. 11, pp. 2491–2499, 1994.

[6] S. Thomas, S. W. Pang, "Dry etching of horizontal distributed Bragg reflector mirrors for waveguide lasers," *J. Vac. Sci. Technol. B*, vol. 14, no. 6, pp. 4119–4123, 1996.

[7] L. A. Coldren, S. W. Corzine, *Diode Lasers and Photonic Integrated Circuits*.

[8] A. Altoukhov, J. Levrat, E. Feltin, J.-F. Carlin, A. Castiglia, R. Butte, and N. Grandjean, "High reflectivity airgap distributed Bragg reflectors realized by wet etching of AlInN sacrificial layers," *Applied Physics Letters*, vol. 95, no. 19, p. 191102, 2009.

[9] K. Streubel, S. Rapp, and N. Chitica, "Fabrication of InP/air-gap distributed microcavities," in *Materials Science & Engineering B44*, vol. 5107, 1997.

[10] R. Sharma, E. D. Haberer, C. Meier, E. L. Hu, and S. Nakamura, "Vertically oriented GaN-based air-gap distributed Bragg reflector structure fabricated using band-gap-selective photoelectrochemical etching," *Applied Physics Letters*, vol. 87, no. 5, p. 051107, 2005.

[11] T. Durhuus, B. Mikkelsen, and K. Stubkjaer, "Detailed dynamic model for semiconductor optical amplifiers and their crosstalk and intermodulation distortion," *Journal of Lightwave Technology*, vol. 10, no. 8, pp. 1056–1065, 1992.

[12] M. J. Connelly, "Wideband semiconductor optical amplifier steady-state numerical model," *IEEE Journal of Quantum Electronics*, vol. 37, no. 3, pp. 439–447, 2001.

[13] K. Carney, R. Lennox, R. Maldonado-Basilo, S. Philippe, F. Surre, A. L. Bradley, P. Landais, "Control of noise figure and saturation power in multi-contact semiconductor optical amplifiers: Simulation and experiment," *IEEE Journal of Quantum Electronics*.

[14] M. J. Connolly, *Semiconductor Optical Amplifiers*. Kluwer Academic Publishers, Boston, 2010.

[15] J. Park, X. Li, and W.-p. Huang, "Performance Simulation and Design Optimization of Gain-Clamped Semiconductor Optical Amplifiers Based on Distributed Bragg Reflectors," *IEEE Journal of Quantum Electronics*, vol. 39, no. 11, pp. 1415–1423, 2003.

[16] X. Song and E. A. Avrutin, "Analysis of high bit rate operation of a vertically gain-clamped semiconductor laser amplifier," in *IET Optoelectron.*, no. 1, pp. 34– 41, 2008.

[17] G. Giuliani and D. D'Alessandro, "Noise analysis of conventional and gain-clamped semiconductor optical amplifiers," *Journal of lightwave technology*, vol. 18, no. 9, p. 1256, 2000.

[18] E. S. Björlin, S. Member, and J. E. Bowers, "Noise Figure of Vertical-Cavity Semiconductor Optical Amplifiers," *IEEE Journal of Quantum Electronicsu*, vol. 38, no. 1, pp. 61–66, 2002.

[19] D. M. Baney, P. Gallion, and R. S. Tucker, "Theory and Measurement Techniques for the Noise Figure of Optical Amplifiers," *Optical Fiber Technology*, vol. 6, pp. 122–154, 2000.

[20] B. F. Kennedy, P. Landais, S. Philippe, M. Martinez-Rosas, A. L. Bradley, "Temporal and spectral dependence on polarization of the input signal in a semiconductor optical amplifier," in *Integrated Photonics Research (IPR)*, 2004.

[21] H. Soto, D. Erasme, and G. Guekos, "Cross-polarization modulation in semiconductor optical amplifiers," *IEEE Photonics Technology Letters*, vol. 11, no. 8, pp. 970–972, 1999.

[22] M. Linnik, "Effects of Bragg mirror interface grading and layer thickness variations on VCSEL performance at 1.55 μm," *Proceedings of SPIE*, vol. 4286, pp. 162–171, 2001.

[23] A. Vukovic, P. Sewell, T. M. Benson, and P. C. Kendall, "Advances in facet design for buried lasers and amplifiers," *IEEE Journal of Selected Topics in Quantum Electronics*, vol. 6, no. 1, pp. 175–184, 2000.

[24] M. Premaratne, G. P. Agrawal, *Light Propagation in Gain Media: Optical Amplifiers*. Cambridge University Press, 2011.

[25] J. Klamkin, J. J. Plant, M. Sheehan, W. Loh, S. M. Madison, and P. W. Juodawlkis, "High-output saturation power variable confinement slab coupled optical waveguide amplifier," in *Optical FIbre Communications*, vol. 1, pp. 10–12, 2011.

[26] M. Yoshino and K. Inoue, "Improvement of saturation output power in a semiconductor laser amplifier through pumping light injection," *IEEE Photonics Technology Letters*, vol. 8, no. 1, pp. 58–59, 1996.

[27] R. Brenot, F. Pommereau, O. Le Gouez, J. Landreau, F. Poingt, L. Le Gouezigou, B. Rousseau, F. Lelarge, F. Martin, and G. Duan, "Experimental study of the impact of optical confinement on saturation effects in SOA," *OFC/NFOEC Technical Digest. Optical Fiber Communication Conference, 2005.*, p. 3 pp. Vol. 1, 2005.

[28] A. Crottini, F. Salleras, P. Moreno, M.-a. Dupertuis, B. Deveaud, and R. Brenot, "Noise figure improvement in semiconductor optical amplifiers by holding beam at transparency scheme," *Photonics Technology Letters, IEEE*, vol. 17, no. 5, pp. 977–979, 2005.

[29] S. S. Saini, J. Bowser, R. Enck, V. Luciani, P. J. S. Heim, M. Dagenais, "A Semiconductor Optical Amplifier with high saturation power, low noise figure and low polarization dependent gain over the C-band," in *Lasers and Electro-Optics Society (LEOS)*, pp. 102–103, 2004.

[30] K. Iga, *Vertical-Cavity Surface-Emitting Laser Devices*. No. March, Springer, 2004.

[31] J. Shin, B. Yoo, W. Han, O. Kwon, Y. Ju, and J. Lee, "CW operation and threshold characteristics of all-monolithic InAlGaAs 1550nm VCSELs grown by MOCVD," *IEEE Photonics Technology Letters*, vol. 14, no. 8, pp. 1031–1033, 2002.

[32] J. Buus, *Tunabe Laser Diodes & Related Optical Sources*.

5

Multi Contact SOA: Steady-State Characterisation

The first of two designs for NF control was discussed in the previous chapter, where the control of the carrier density profile relied on gain clamping in the output portion of the device. This chapter will explore the steady state performance of a multi-contact SOA, where the modification of carrier density is more direct and versatile. The gain and NF characteristics are determined as a function of varying pump current profile, initially through simulation and then experimentally. Finally, the NF will be related to a more practical figure of merit, the bit error ratio, by demonstration of 10GBits/s inline amplification.

5.1 Design Concept

This section will provide structural and conceptual details of a Multi Contact SOA (MCSOA). The concept of reducing the NF via tailoring the longitudinal carrier density profile to an optimum distribution was treated comprehensively in chapter 3. The implementation of this will be given in relation to the MCSOA.

5.1.1 Longitudinal Carrier Density Control

Traditionally SOAs comprise a single contact on the p-side of the structure (with one or two bonding wires). The concept of NF reduction proposed, necessitates multiple isolated contacts and is shown in Figure 5.1

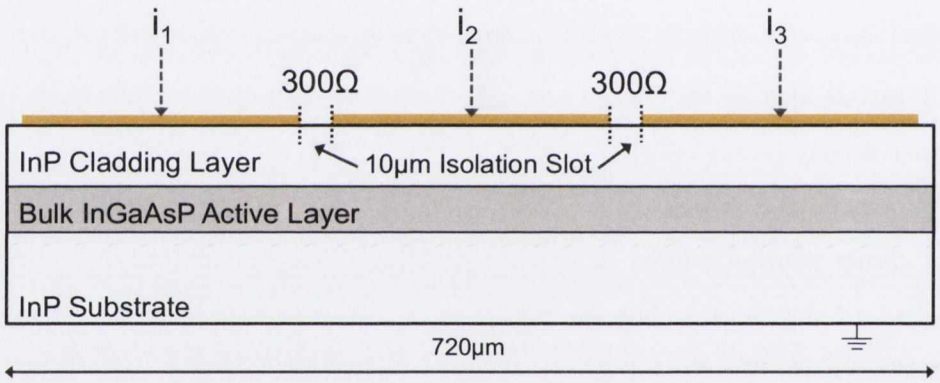

Figure 5.1: Multi-Contact SOA Schematic (side slice). Three seperate contacts are shown, sharing a common ground.

In this way, either by pumping each section independently, or by employing a single source in conjunction with a resistor network, the injected bias profile can be modified as required. For this work individual section pumping is used exclusively. This is designated by the label i_n, where n is the contact number. In this schematic three contacts are shown where, for a device of this length, the number is limited only by practical considerations. If the fabricated chips were longer in length, further sectioning could be warranted.

The fabrication technology is almost identical to that of a conventional single contact SOA, the difference being the chosen method for isolating the top p-type contacts from one another. This can be achieved via two distinct courses of action. The technique employed in the fabrication of the present chips benefits from the simplicity of dividing the contacts in the final stages of metallisation [1]. The advantage of this method is simplicity, and the precise command of slot

width, albeit at the expense of slot depth. Finding the balance between these two parameters is dependent on the waveguide confinement, the thickness of the top p-layer, and the ability of injected carriers to tunnel between contacts. Increasing the slot depth too far can lead to interaction with the travelling mode, inducing reflections and increasing waveguide loss, the effect of which is explored with more detail in Chapter 7. By simply splitting the contacts, as was done here, slot depth is limited to the contact thickness of 200nm.

An alternative avenue is to modify the top p-layer directly, i.e. to go beyond the depth of the contact. The two most common methods used in achieving this are: (a) ion implantation and (b) the localised removal of InP in the region between contacts. These are both, in general, post processing actions. Ion implantation offers greater control of depth and lateral implantation area. It also has the added advantage that deep implantation is possible before appreciable modification of the mode, as the induced refractive index contrast is less than the case where etching material introduces a sharp refractive index step (InP/air) [2].

The ultimate objective is to achieve the maximum control of the amplified spontaneous emission (ASE), directly affecting the gain (G), noise figure (NF) and saturation output power (P_{sat}). In Chapter 7, repeated etching of the isolation slots to improve the level of control over the carrier density profile will be explored.

5.1.2 Device Details

The MCSOA studied is a buried bulk-active waveguide with separate confinement heterostructure (SCH), based on the InGaAsP/InP III-V material system at 1550nm. The MCSOA is shown schematically in Figure 5.1. An optical image is given in Figure 5.2a. The chip is 720μm in length and has three individual top-electrodes. The lengths are 236μm, 254μm and 210μm, with respect to the designated input side labelled in the image. Also visible are two isolation slots, 10μm in width. These slots provide an electrical isolation of 300Ω, measured directly between the contacts using an ohmmeter. The waveguide terminates with a flared output, the benefits of which were discussed in chapter 2. The top cladding layer is approximately 4μm thick, and sits on top of a 500nm thick SCH, and shown in Figure 5.2b. The SCH is comprised of 3 layers: two outer layers of 200nm thickness encompassing a 100nm bulk active layer. The bottom InP n-type electrode is common to all sections. The maximum recommended injected current into any one section is limited to 90mA, the total maximum device current is 280mA.

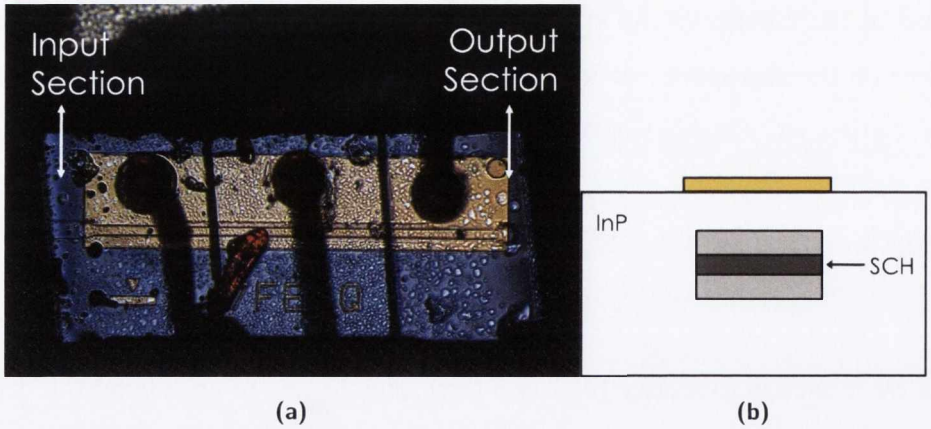

Figure 5.2: (a)Optical microscopy image of the MCSOA from above showing a flared waveguide termination. (b) In plane schematic illustration of the buried SCH structure

5.2 Steady State Modelling

Modelling the MCSOA requires three important changes to the lateral cavity simulation used in the previous chapter. The first is that the lateral cavity is simply switched off by removing the cavity component from the carrier density rate equation (setting it to zero). The result of this is that no gain clamping takes place.

The second distinction provides the introduction of multiple current sources. All pump current combinations are given with respect to the designated input contact, and labeled i_n, where n is the p-electrode number. For this three contact device the current combinations will be given by i_1, i_2, i_3 mA, where i_1 is the input contact. For example, an injected bias of 90,50,10mA, represents 90mA into the first section (i_1), 50mA into the second section (i_2) and 10mA into the final facet section (i_3). This is achieved by dividing the number of computational segments by the number of contacts to be simulated. For example, for a three section device we may choose 12 computational sections, divided into three groups of 4 computational sections. If then, the desired pump current is i_1=100mA, the bias would be further subdivided into four 25mA sources. This division is shown qualitatively in Figure 5.3 for clarity. It should be noted that the number of computational sections, as was the case with the LCSOA simulations, can be increased, but is limited by computational time. 24 sections proved a sufficient balance between accuracy and computational time. The isolation slots described in the real device are not present in the simulation. In this way perfect isolation is assumed, where no carrier leakage is possible between sections.

The conditions of injected bias can be divided into two categories: Those where the total input

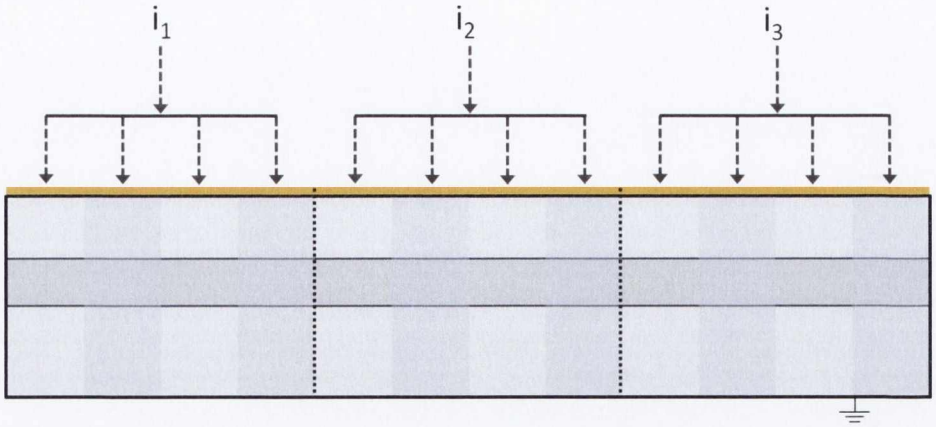

Figure 5.3: Multi Contact SOA schematic (side slice), showing how the program deals with bias injection by summing together the appropriate number of computational section, in this case 12. Note the simulations used herein model 24 subsections

bias (i_{tot}) can take any value within the restrictions set by the manufacturer (the Unlimited Bias Case) and secondly; where the different bias profiles all have the same i_{tot} value (the Limited Bias Case). In the former the fundamental performance of the device is acquired. For the latter, the goal is to compare the level of control of NF and P_{sat} relative to a control case at the same i_{tot} injection that a single contact SOA would experience.

The third change necessary accounts for the different geometry of this device. As before, polarisation dependence is not accounted for, in that only one fundamental mode is probed. Alloy ratios are also tweaked owing to differences between the LCSOA and MCSOA material gain coefficients.

5.2.1 Control of Gain & Noise Figure

Unlimited Injected Bias

Initially, the extent to which the chip gain and noise figure can be varied by this technique is investigated to ascertain the optimum current profiles for reduced NF, when i_{tot} is allowed to vary. The power is chosen to be sufficiently small so as to lie well below the input saturation power. The injected wavelength is 1565nm, near the material gain peak of the structure. Optimum NF values require a high carrier density at the input. In accordance with this, Low NF criteria are applied, where a high injected current is applied to the input contact of i_1=80mA. The middle and output contacts are then varied such that $i_2 = i_3$ = 0-90mA, in steps of 1mA. The simulated gain and NF colour maps are shown in Figure 5.4.

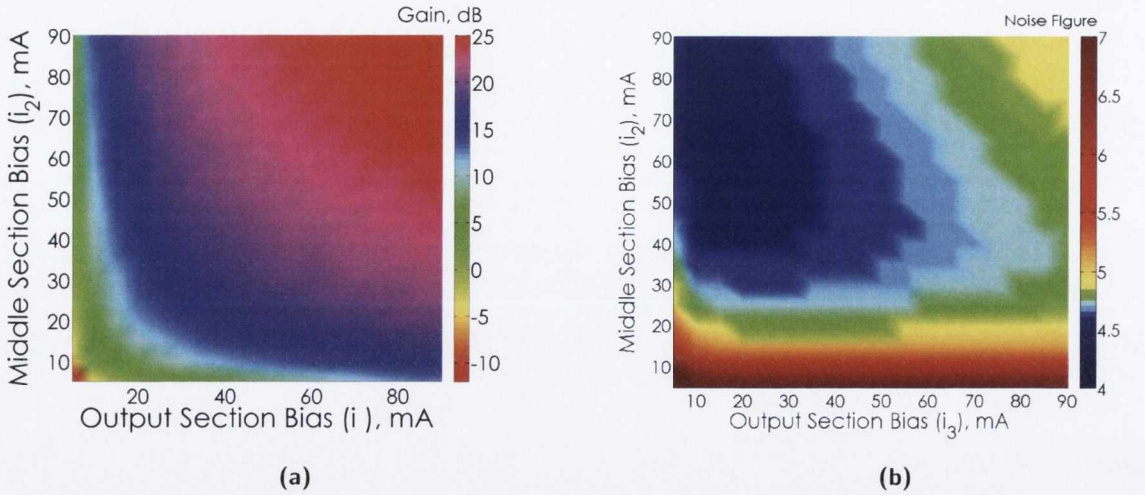

Figure 5.4: Simulated gain (a) and NF (b) colour maps for the ideal low noise condition of i_1=90 (its maximum value) while i_2 & i_3 = 0-90mA.

With a high bias injected into the first simulated contact there is a progression of the NF reduction as the middle contact is increased and the output bias held constant below 30mA. As predicted previously the NF is expected to decrease from its maximum value, at low middle and output bias, to its minimum for a carrier profile approaching that of the Low Noise profile. However, as the output pumping is increased beyond this the NF begins to increase again. This effect is due to increased backward-travelling ASE depleting the carrier density near the input facet, increasing the NF. This shows not only that there is a general range of profiles that leads to a reduction in the NF but also that increasing the bias indefinitely does not lead to further NF reduction [3]. The corresponding gain is shown in Figure 5.4 (b), where it increases with i_{tot} as expected [4].

Isolating i_2 values from Figure 5.4 for a variation in i_3, under the same simulated optical injection, is shown in Figure 5.5 and Figure 5.6 below. This allows for a more intuitive exploration of the overall control of NF as a change in gain occurs over the same bias range.

The gain increases rapidly before levelling off as a function of increasing i_{tot} current, for each i_2 value. Thus the maximum gain reached is for a current combination of i_1=80mA, i_2=90mA and i_3=90mA at a value of 24.75dB. Inset, is a plot of the gain as function of i_2, for i_3=60mA. The change in gain as the output contact current is varied, contributes less than the variation of the output contact above 20mA. For i_2 values in the range of 40mA to 80mA there is less than a 3dB change in gain, where the values level off due to an increase in the non-radiative term of the total recombination processes at high carrier density. This is because the non-radiative

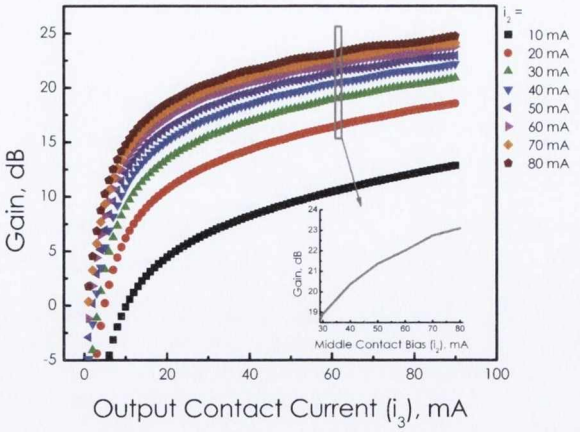

Figure 5.5: Simulated gain for an injected signal of -15dBm at 1565nm. Each plot represents a different middle contact bias (i_2), as the output (i_3) is varied from 0-90mA. The input contact is maintained at 80mA, for optimum NF performance. Inset: Change in gain as a function of i_2, for an isolated i_3 value of 60mA.

recombination scales with the cube of the carrier density, so at higher values becomes more significant. The result is a small sacrifice in gain when choosing an i_2 value for the best noise controlled profile. There will always be a trade off between total gain and overall reduction in NF, however the output contact is the predominant source of reduced ASE travelling towards the input facet.

The corresponding NF control under the same conditions is given in Figure 5.6. As expected the minimum NF for each i_2 value occurs for low injected i_3 biases, except in the case if $i_2 = 10mA$, which is below the transparency point of the model meaning the effect of increasing i_3 is to counter act the loss. For the remaining cases the clearest visible effect is a reduction in NF as i_2 is increased from 10-90mA. This is a direct result of the increase in gain, as the carrier density is increased. As was the case with the gain the effect begins to level off as the rate of non-radiative recombination becomes more significant. The close proximity of NF values for i_2=50-90mA is explained by the gain inset (Figure 5.5), where the change in gain due to Auger recombination is low over this range, and so to the consequent change in NF. This acts to push the NF minimum to lower i_3 biases for increasing i_2. The lowest NF occurs for 80,80,15mA, however the change in NF with i_2 is less than 0.1dB, and this simulation does not realistically predict the effect of temperature on the rate of stimulated and spontaneous emission. This total bias in this case is also quite high, producing a lower NF at such a high bias than the experimental device is likely to reproduce.

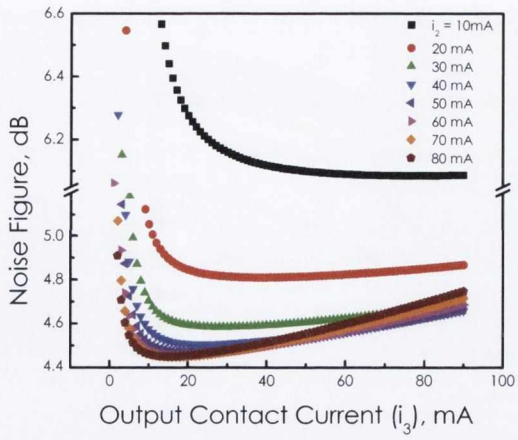

Figure 5.6: Simulated NF for an injected signal of -15dBm at 1565nm. Each plot represents a different middle contact bias (i_2), as the output (i_3) is varied from 0-90mA. The input contact is maintained at 80mA, for optimum NF performance.

Figure 5.7 below, show the gain and NF as a function of output section current for a single i_2=50mA bias, a magnitude which satisfies the low NF profile criteria, with a minimum reduction to the gain of that section. At very low injected currents, the output section acts as an absorber and so the NF is proportionally higher at this point. When i_3 is in excess of 2mA the level of NF control achievable, from its maximum to its minimum value is 5.7dB to 4.5dB. This minima occurs at 22.5mA. However the change in NF at higher gain values is extremely small. The corresponding gain at 20.5mA is 16.85dB.

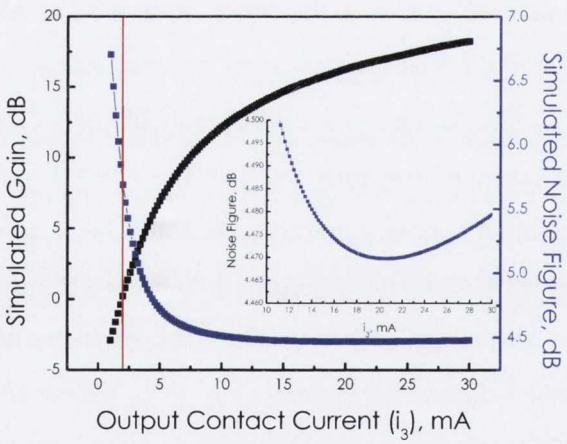

Figure 5.7: Simulated gain & NF for an injected signal of -15dBm at 1565nm, for i_1=80mA, i_2=50mA and i_3 is varied from 0-30mA. Inset: The minimum NF achieved for this arrangement, occurring at 20.5mA.

Limited Total Injected Bias

The above analysis determined the optimum injected current profile for NF reduction for a non-constant i_{tot}. The data excludes the improvement in NF over a standard SOA carrier density profile, at a constant i_{tot}. This section will look at the wavelength dependent gain and NF as a function of overall bias configuration for a total input current, i_{tot}=150mA. The Low Noise profile is taken from the above data given by 80,50,20mA . In addition the reverse is examined, 20,50,80mA, acting as a proof of concept. The standard configuration is 50,50,50mA. The wavelength dependent gain and NF are shown in Figure 5.8 and Figure 5.9, respectively.

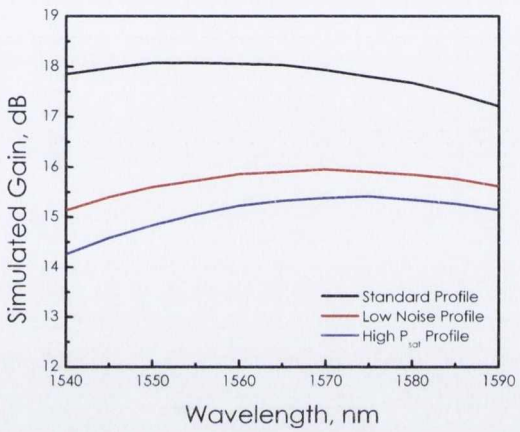

Figure 5.8: Simulated gain for an injected signal of -15dBm with a wavelength range of 1540-1590nm.The simulation is shown for the three current profiles: The Standard profile, the Low Noise profile and a High P_{sat} profile, where i_{tot} is constant.

The three bias profiles exhibit differing levels of gain over the full wavelength range simulated. The maximum value occurs for the standard profile, with a peak value of 18.07dB at 1550nm. The gain drops to 16dB at 1570nm and 15.45dB at 1572nm, for the low noise and high P_{sat} cases, respectively. The gain discrepancy of 0.55dB for the noise controlled cases can be explained by the non-uniform section size as the program mirrors those of the real MCSOA. Also of note is the shift to higher wavelengths for the standard case at its peak gain, compared with peak gains in the longer wavelength region for the noise controlled cases. This is an effect of band filling, whereby lower energy states are not filled due to the regions of reduced injected bias. The corresponding NF for these simulations is given by Figure 5.9.

Of prime importance is the trend of reduced NF via the low noise profile relative to the single contact SOA. The minimum values demonstrated are 4.47dB at 1570nm, an improvement of 0.6dB, extended over the 50nm span. The gap opens up slightly at lower energies to 0.7dB, as

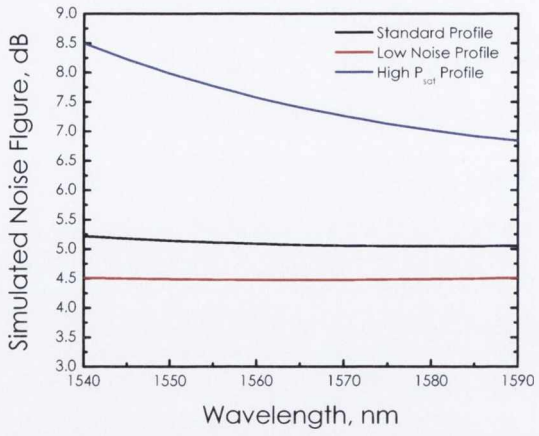

Figure 5.9: Simulated noise figure for an injected signal of -15dBm with a wavelength range of 1540-1590nm. The simulation data is shown for the three current profiles, where i_{tot} is constant.

a result of the gain peak shift, seen in the previous plot. The purpose of the reverse profile is to prove the concept of NF control, whereby providing poor conditions at the start of the amplifier chain would result in a higher NF [5, 6]. The NF for the high P_{sat} is 2.3dB higher at 1590nm, increasing to 4dB at lower wavelengths, showing substantial control by this technique. It should be noted here that the gain discrepancy detailed in the previous figure has little effect on the NF. The resultant improvement in the saturation power, given at the expense of NF with the High P_{sat} profile, is now presented.

5.2.2 Control of Saturation Properties

The bias profile dependent saturation effects are now simulated. The input power is varied from -30dBm to 8dBm, covering a significant range to simulate the linear and saturated regions. The injected wavelength is the peak gain wavelength for the standard case, as the NF varies little over the peak gain bandwidth. The gain as a function of output power is given in Figure 5.10, and the NF as a function of input power is shown in Figure 5.11. Although a plot of gain as a function of saturation input power is not given, the extracted $P_{sat,in}$ values are shown in Figure 5.11.

The data demonstrates the reverse of the noise figure technique, and indeed yields a much improved saturation point for the High P_{sat} carrier density of 12.6dBm. This represents a 1.6dB improvement over the control case and a 4.45dB increase relative to the low noise profile. This substantial level of control is a direct consequence of the increased carrier lifetime

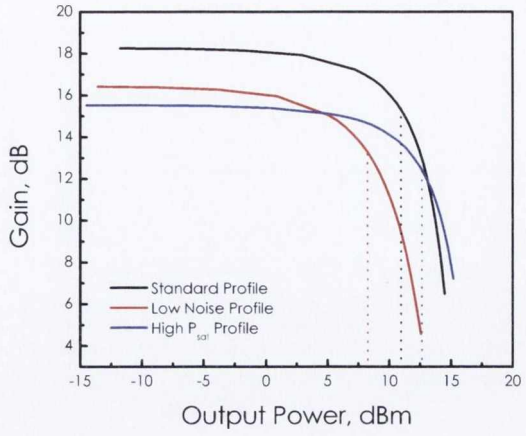

Figure 5.10: Simulated gain as a function of output power for the low noise, high P_{sat} and standard current profiles. The wavelength of the injected signal is 1570nm.

and differential gain induced by the high output carrier density at the output. This capacity to accommodate a larger range of input powers occurs at the expense of the small-signal gain for this configuration. This is nearly 3dB less than the standard bias injection, and may prove important in power amplification at repeater sites.

The NF concept becomes meaningless beyond the saturation point, but the extended linearity for the High P_{sat} configuration is clear in Figure 5.11. However, although the NF is constant for a greater range of input powers the value is high as expected. The NF for the low noise profile is improved over the standard case with a 1.2dB input power penalty.

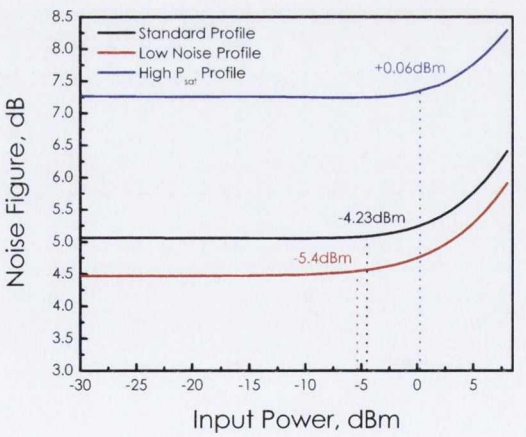

Figure 5.11: Simulated NF as a function of input power for the low noise, high P_{sat} and standard current profiles. The wavelength of the injected signal is 1570nm.

Finally, the gain, NF and saturation output powers are plotted as a function of injected bias

profile, for a constant i_{tot}, in Figure 5.12. The initial condition is a Low NF profile, where i_1 and i_3 are then varied in 5mA steps, passing through the Standard profile, and finishing with the High P_{sat} conditions. The middle contact bias is maintained at 50mA.

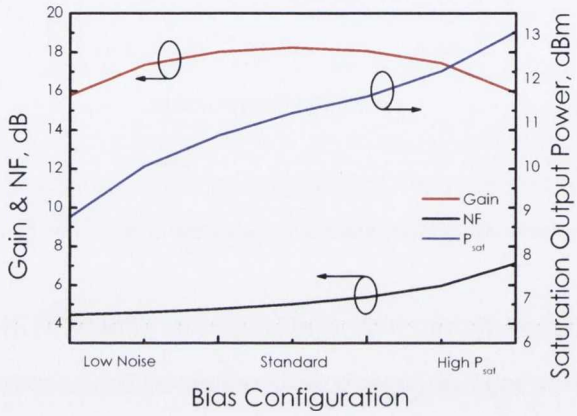

Figure 5.12: Simulated gain, NF and saturation power for an injected signal of -15dBm with a wavelength range of 1570nm as a function of changing pump profile.

This plot summarises the variation possible relative to a single contact scenario for a constant injected bias. The largest advantage, as was seen, is in the ability to vary the saturation power by a very substantial 4.2dB, for a constant i_{tot}. Over the same range of bias variation the NF is modified by 2.62dB, from its lowest value in the Low NF bias configuration, to its highest for the High P_{sat} profile. The gain profile changes almost symmetrically (taking the non-uniformity in contact size into account), where the reason for the decrease in gain is believed to be related to localised saturation in the low bias regions.

This section has demonstrated through simulation the ability to control important output parameters of the MCSOA, by variation of a single parameter: the longitudinal carrier density profile. By moving between particular non-uniform carrier densities at a constant total injected bias, the NF and saturation of the MCSOA can be modified as desired. In the next section the ability of a real device to achieve this will be demonstrated experimentally.

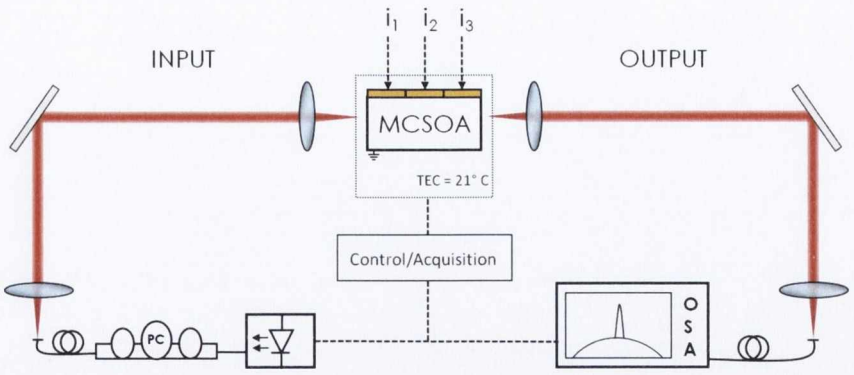

Figure 5.13: Steady state characterisation set up. Shown is the tunable continuous wave, external cavity laser (ECL) source, polarisation controller (PC), the MCSOA under test and an optical spectrum analyser (OSA).

5.3 Experimental Characterisation

5.3.1 Experimental Considerations

The acquisition of the gain and the NF data are undertaken using continuous wave injection. An identical technique is used for this purpose, basing all calculations on the formulas and techniques established in Chapters 2, 3 & 4. The injected signal of a modulated data stream was also investigated via bit error ratio measurements taken for a 10GBits/s pseudo random bit sequence (PRBS) modulated input.

Pumping Configurations

The set up for CW injection is given below in Figure 5.13, where the LCSOA has been replaced by the MCSOA. Experimentally a significant difference exists between this and the previous chapter: the DC pumping configurations necessitated by the multi-contact structure. As the premise of noise figure reduction here is related to the carrier density profile, the pumping arrangement is clarified.

The pump-current is provided by three independent DC current supplies. As before all pump current combinations are given with respect to the designated input contact, and labelled i_n, where n is the p-electrode number. For this three contact device, the current combinations will be given by i_1, i_2, i_3 mA, where i_1 is regarded as the input contact. Similarly to simulation, current combinations are divided into two categories: Firstly, the total input bias (i_{tot}) can take any value within the restrictions set by the manufacturer (the unlimited bias case); secondly,

i_{tot} is held constant (the limited bias case). The bias values used experimentally differ slightly from the simulated data, due to a difference in threshold current between the two, but i_{tot} remains at 150mA. The Low Noise profile will be given by 90, 50,10mA, the High P_{sat} profile by 10,50,90mA and the Standard profile by 50,50,50mA.

Systemic Losses

The effect of system losses on the calculation of the generated gain and NF data were described in Chapter 4, where it was shown that the NF in particular is directly proportional, by definition, to the input loss. Both the input and output losses determine the calculated chip-gain values. The same conditions, and therefore sources of power loss, exist in the characterisation of the MCSOA, and the same rigorous approach is taken. As before, the modal loss contributes the greatest effect to the input losses, although in the case of this bulk structure to a lesser extent than the QW LCSOA. The input modal loss is 3dB, with the total input loss given by 4.5dB. The output loss is approximately 5dB. All measured gain and NF data are the chip values, as this leads to a more meaningful comparison with other devices.

5.3.2 Light-Current-Voltage (LIV) Characteristics

As was the case with the LCSOA, the LI and ASE spectral data can provide insight into the fundamental operation of the SOA pertinent to the specific design principles [7]. The power of non-injection technique is illustrated by the subsequent choice of operating parameters for the continuous wave and dynamic characterisation of this and the next chapter.

Figure 5.14 depicts a plot of the light output as a function of drive current, measured using an integrating sphere power meter. For this data the same current is applied to all three contacts, such that i_1=i_2=i_3=0-90mA. The mode of injected bias is continuous. It is known that pulsed operation is advantageous when considering thermal effects in the diodes under test, however this was not possible with the sources used [8]

The plot presents a typical LI response for an InGaAsP device, with a quasi-linear trend to its maximum output power of 157μW, at an i_{tot} value of 125mA. The low total power achieved is indicative of the waveguide structure, where the incorporated flares and short length act to reduce the overall ASE transmitted. The substantial decrease in optical power to 60μW at a final i_{tot}=270mA, is related to temperature effects. As will be shown later the thermal

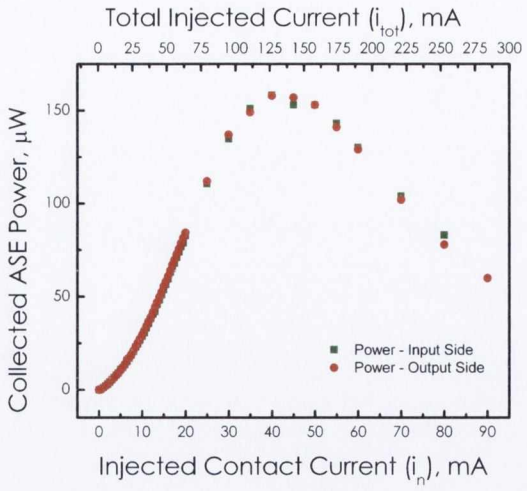

Figure 5.14: Collected ASE power as a function of pump current. The same value is maintained across all contacts for each data point, given by the bottom x-axis. The top x-axis gives the total bias value.

conductivity between the chip and its sub mount is low due to poor bonding. This results in an air gap under large portions of the SOA chip, where under normal circumstances close contact with the heat sink is required. As a consequence heating of the device occurs above 130mA, where adequate cooling by the temperature control system becomes ineffective. This in turn decreases the quantum efficiency significantly, reducing light output. It is reasonable to presume that similar behaviour will arise under injection, i.e. that above 130mA the gain will decrease, increasing the NF and decreasing the saturation power. The corresponding IV curves under the same conditions are given by Figure 5.15.

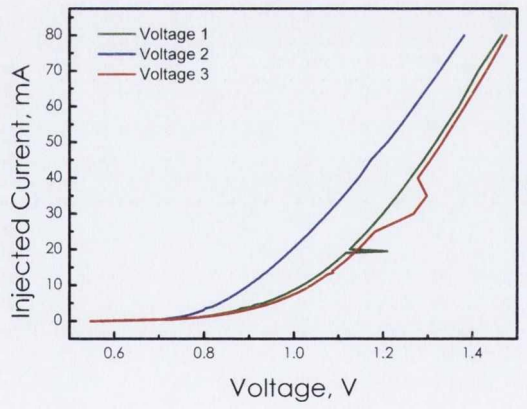

Figure 5.15: Corresponding Voltage curves as a function of pump current, for each of the three contacts

The linear intercept of the voltage above barrier potential corresponds with the bandgap of the junction [9, 10], and should be equal for the set of isolated diodes. For V_1 and V_3 (the facet sections) the knee of the curves are equal at approximately 0.9V, and the slight increase in the

forward-voltages above this point are as expected for a non-ideal diode. The plot shows that this is not the case in the MCSOA. The middle contact has a slightly reduced value of 0.8V, and a lower voltage response at higher currents. This suggests a fundamental difference between the middle section and the facet sections. A simplified electrical model of the MCSOA is illustrated by Figure 5.16

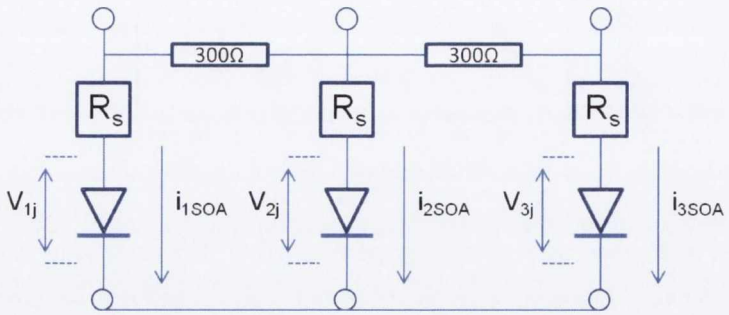

Figure 5.16: Simplified electrical model of the MCSOA.

It is unlikely that the junction voltage is different for the three structures for material reasons, as the sections all share the same material structure. Instead the small difference in voltage between the middle and facets sections is likely due to a combination of contact area non-uniformity and temperature accumulation in the middle section, which was seen in the LI data at higher biases. The middle section is more susceptible to this. To assess this further the emission of light from individual sections is measured. This will help to understand the level of symmetry obtainable with regards to ASE production. The light output for these cases can reveal some of the idiosyncrasies of the device, be they material or structural in nature.

The LI data for each individual section are shown in Figure 5.17. This is given in linear units in Figure 5.17 (a) and log scale in Figure 5.17 (b). The sections are represented by i_1=Green, i_2=Blue and i_3=Red, and when one is being measured the remaining two are switched off.

If varying i_2 the power should be equal when measured at both the input and output side, if the facet sections are identical. Similarly, if i_1 and i_3 are varied the power emitted on the input side (L_1) for i_1, should equal that collected on the output side (L_2) for i_3, and vice versa. This data is shown in 5.17c.

In quantifying the relative power difference, it is very difficult to attribute with certainty an underlying cause to any asymmetries. There are a multitude of sources inherent to the chip. The difference is not systemic as the lenses used for coupling were previously characterised and produce a negligible effect. The most obvious initial analysis is based on the facets: both the

AR coatings and the flare of the waveguide. An additional possibility is the slight variation in contact sizes, meaning a different level of localised gain.

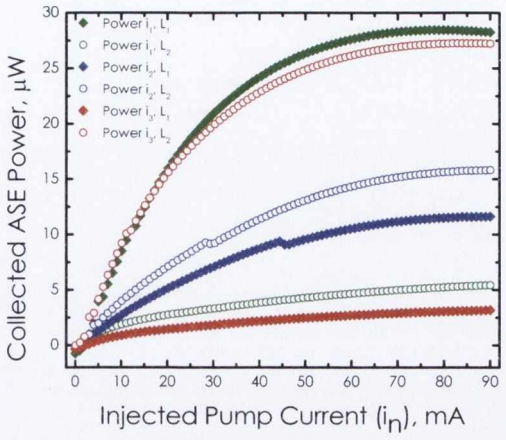

(a)

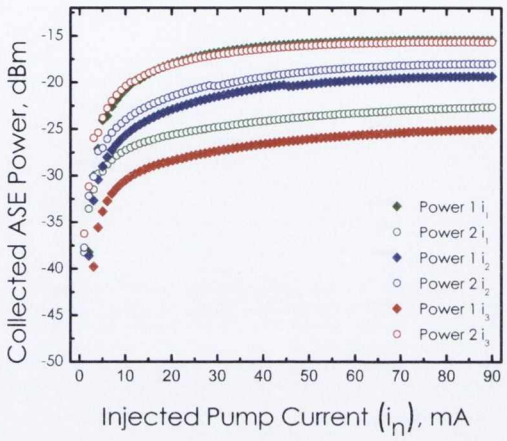

(b)

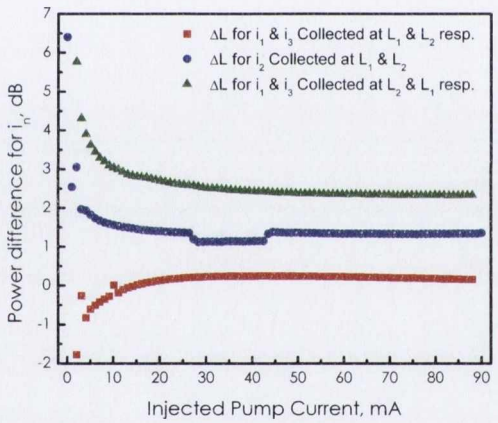

(c)

Figure 5.17: (a) Collected ASE Power as a function of i_n, for each individual section switched on in isolation and varied from 0-90mA. The power is collected from both the input side (L_1) & output side (L_2). (b) Collected ASE Power (decibel) for each individual section switched on in isolation, and varied from 0-90mA. The power is collected from both the input side (L_1) & output side (L_2).(c) Difference in measured ASE Power for situations where the particular sections should have the same output power when measured from the pertinent side.

The fact that the power for i_1 and i_3 is almost equal when measured at the input and output sides respectively, would suggest that the facets are working as intended (neglecting any spectral differences). Assuming this, and exploring the idea of size non-uniformity: The difference in i_2 collected from both sides, is quite large, and even though i_1 and i_3 are close, this is because they

are less reliant on another section to determine their values, where i_2 must pass through these regions to be measured. They are not transparent, and some absorption will occur. This would signify from (a) that section 1 is slightly larger (which it is) as less light passes through, and section 2 is further from the input facet. It would seem then, that the slight level of asymmetry in the ASE output, is probably reliant on slight variations in section size, much like the voltage across section 2. The kink observed in the linear i_2 data in (a) would seem to corroborate this. For the light collected on the output side (L_2), the kink occurs at 35mA, and for measurement on the input side (L_1) at 45mA. Either way, the device operates reasonably as predicted, and as was seen in Figure 5.13, the output when all sections are turned on is almost completely symmetrical in the linear gain region up to i_{tot}=130mA. Although the discrepancy is small, it will be shown to have a finite effect on the gain under CW injection, experimentally, as it did when simulated.

LI Colour Maps

To benefit from the nature of a multi contact device, as relating to the NF and P_{sat} control, we then need to progress the basic LI information to the variation of all section pump currents. This will help develop an understanding of the device in this region much like the 2D plots above, but with the NF and P_{sat} in mind. These data progress the basic 2D LI plots to account for the multi-contact nature of the carrier injection, and how this may affect the NF and Gain. Figure 5.18 to Figure 5.20 shows the colour maps of the absolute ASE power collected after the coupling lens from both the input (L_1) and output (L_2), for three scenarios: i_1=10mA, 50mA & 90mA; where in all cases i_2=0-90mA and i_3=0-90mA.

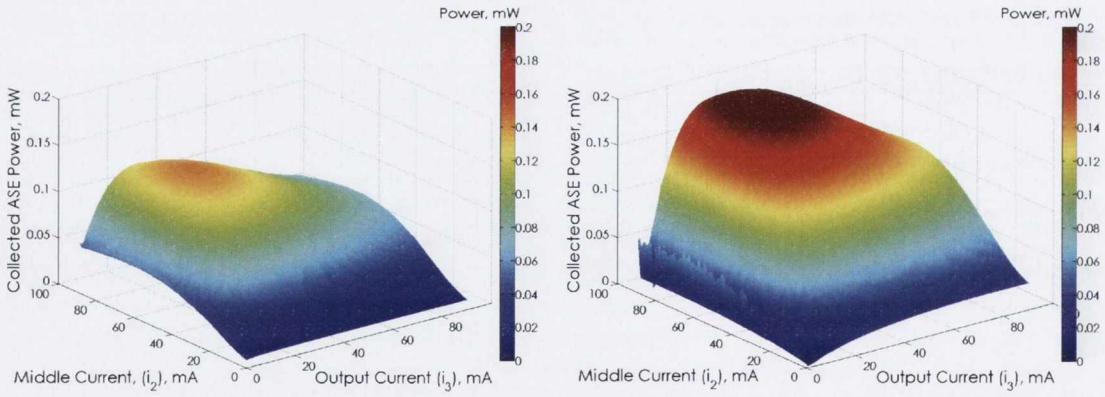

Figure 5.18: Total ASE power collected at (a) the input facet (L_1) and (b) the output facet (L_2), where i_1=10mA and i_2=i_3=0-90mA.

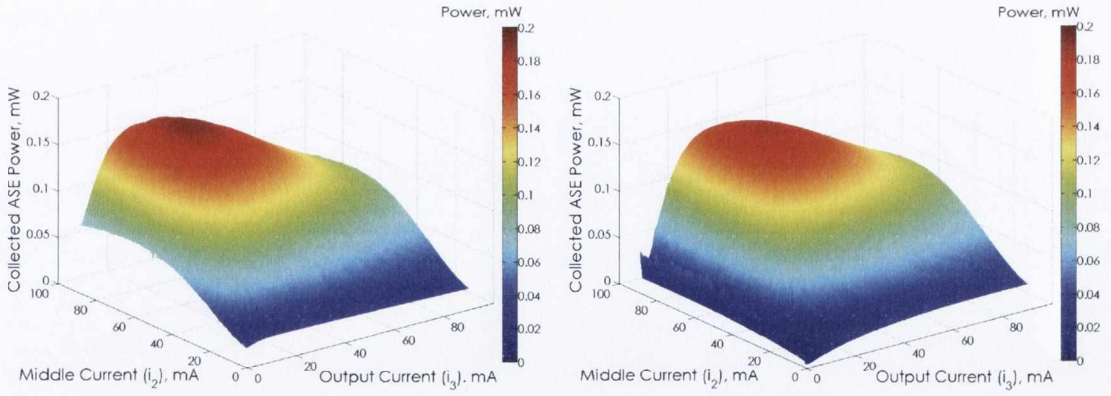

Figure 5.19: Total ASE power collected at (a) the input facet (L_1) and (b) the output facet (L_2) where i_1=50mA and i_2=i_3=0-90mA

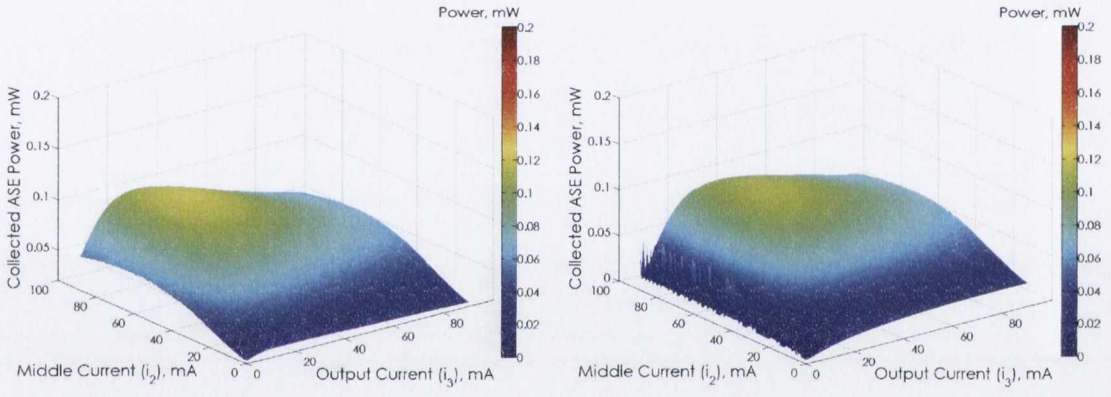

Figure 5.20: (a) Total ASE power collected at (a) the input facet (L_1) and (b) the output facet (L_2), where i_1=90mA and i_2=i_3=0-90mA.

The important distinction to make between the measured output in each of these scenarios, is that the i_{tot} value each time is increased, and it is specific regions that need to be compared. When looking at reverse combinations, below i_{tot}=150mA, we see a good correspondence between the curves. These data reiterate the problems of poor thermal related diminished output power above 130mA affecting the internal quantum efficiency [10, 11]. It is especially evident in Figure 5.18, where total power is quite reduced as expected. However when comparing points of equal interest, for instance the Low Noise Profile sections, and its reverse, in Figure 5.18 and Figure 5.20 the values for L_1 and L_2 are equal, showing direct control of the ASE as a function of applied bias across all sections.

Amplified Spontaneous Emission Spectral Response

5.21a plots the ASE spectra measured on the OSA from the device output as a variation of drive current, where each section is connected to an independent source, and varied as $i_1 = i_2 = i_3 = 0 - 90mA$. The measurement resolution bandwidth is 2nm. The 3dB bandwidth of the chip as a function of bias current and the shift in peak wavelength, are given in 5.21b.

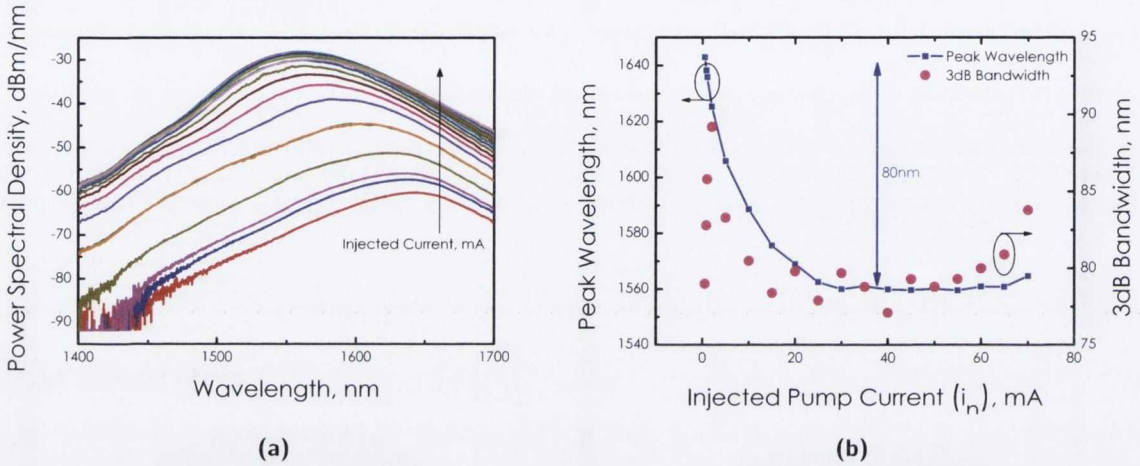

Figure 5.21: (a) ASE spectra corresponding to LI curve in Figure 5.6 (a), where $i_1 = i_2 = i_3$, from 0-90mA. (b) Peak wavelength & and 3dB bandwidth as a function of increasing pump current.

A blue shift of 80nm is observed as the pump current is increased from zero towards an i_{tot} value of 150mA and beyond. It is interesting to note that the bandwidth beyond this point is stable, and so is not affected by the same mechanism involved in decreasing the ASE. As expected the power spectral density does decrease in line with the LI data of Figure 5.14. The 3dB bandwith is shown in Figure 5.21 (b), and a similar trend exists. The bandwidth increases rapidly as the bias passes through the region where ASE production is rapidly increasing, before decreasing and levelling off at approximately 80nm, a similar trend to that observed with increasing device length. At i_n=50mA (i_{tot}=150mA) however the bandwidth begins to slowly increase again. This does not affect CW generated data in the case where i_{tot} is kept below 150mA.

After establishing a good understanding on the limits of performance it is important to then isolate the profiles which will show a reduction in ASE, relative to a standard profile. The ASE spectra are given in Figure 5.22. They are collected at the input of the device for the three bias distributions that will be qualified in the CW section below.

The Standard configuration yields the largest ASE, followed in peak magnitude by the Low Noise and High P_{sat}, respectively. This provides evidence for the control of the carrier distribution along

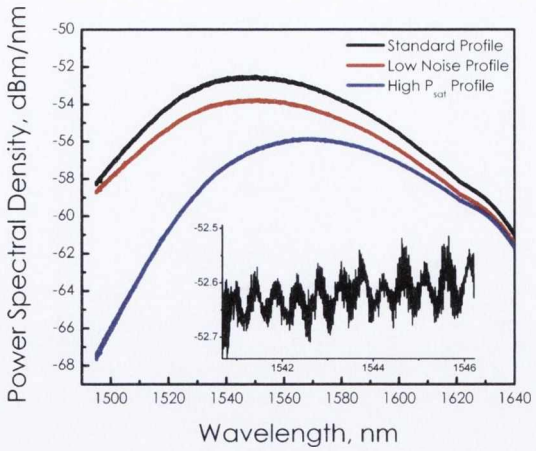

Figure 5.22: ASE Spectra for the three main profiles examined at i_{tot}=150mA. Inset: Short wavelength span showing the residual ASE ripple.

the device and based on the discussion of NF reduction in Chapter 3, it would be expected that the configuration showing the lower ASE should correspond to a lower noise figure performance. It is important to clarify at this point, that although the High P_{sat} configuration displays the minimum ASE power, it is expected to have the highest NF under investigation. This is simply a direct consequence of the side of collection. The level of control achievable is also seen to be limited at lower energies near the band edge. Also of note are the red shifted peak by 20 nm to 1575 nm and the broader ASE of the high P_{sat} case due to band filling resulting from a higher number of carriers in the output section. Finally, inset is a short wavelength span, illustrating the residual ripple effect for this SOA. The modulation depth is very small, signifying good single pass performance. This will result in negligible gain ripple when light is injected into the device. The ripple depth is constant across all pump configurations at approximately 0.15dB.

5.3.3 Continuous Wave Injection

Unlimited Injected Bias

With the foresight gained from the LI and ASE data, it is understood that beyond an injected current of i_{tot}=130mA thermal effects result in diminished gain. This i_{tot} value will be increased by 20mA for CW injection as the gain was not found to decrease until after this point. In addition to this, the maximum suggested current injected into any one contact by the manufacturer is 90mA. The Low NF profile requires the highest gain/lowest NF possible at the input of the device, and is limited to a profile given by 90, x, y mA, where $x + y \leq 60$mA.

The data for a -18dBm injected signal polarised along the TE mode is shown in Figure 5.23. The data is given in combination pairs: a low noise profile, and its opposite. The i_{tot} limited standard configuration of 50,50,50mA, the standard profile, is also shown for comparison. The gain and NF data are acquired using the optical NF formula (Equation 3.16), where the level of co-polarised ASE is measured using a linear polariser. Further details can be found in [12, 6].

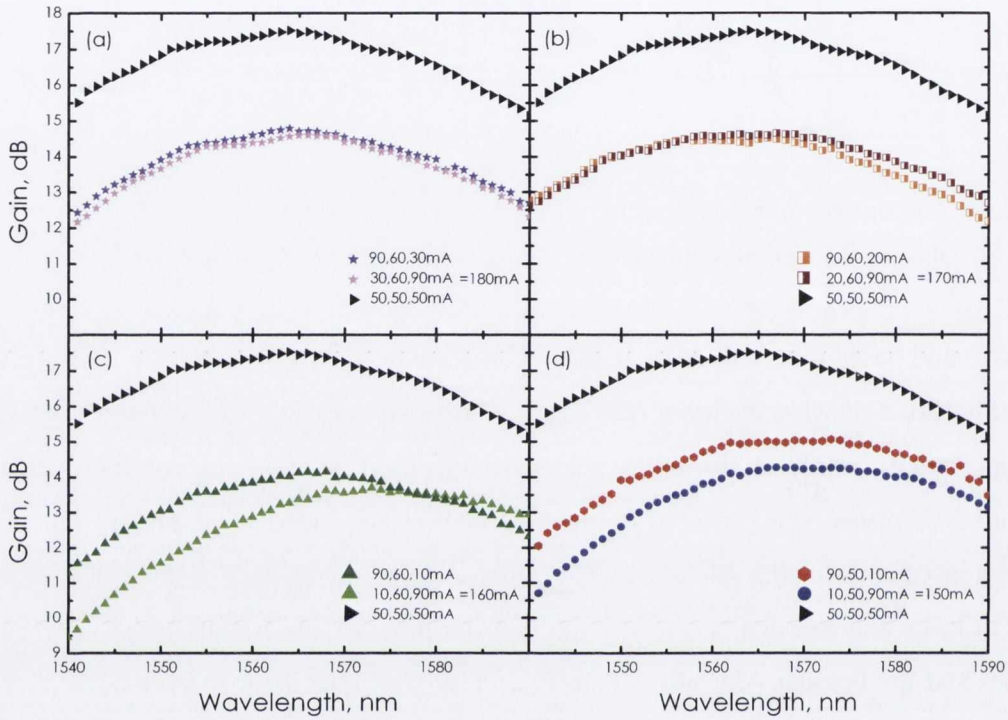

Figure 5.23: Chip-gain as a function of wavelength for four values of total injected current: i_{tot}=180mA, 170mA, 160mA and 150mA. The data correspond to pairs of potential Low Noise pump configurations and their reverse profile. A standard applied current density is also shown in each case.

The standard profile experiences the largest gain of 17.4dB at 1565nm, as expected from the LI, ASE and simulated data. For this reason, we justify the standard profile as the control case, and choose this peak wavelength for all injected steady-state plots. There is a difference in gain between all noise controlled pairs and the standard case. In Figure 5.23 (a), (b) & (c) i_{tot} >150mA and so a lower gain results, with peak values of 14.8dB. The largest gain occurring for the i_{tot}=150mA configuration of 90,50,10mA. The greatest gain level after this occurs at a slightly shifted wavelength of 1570nm, with a value of 15dB for the combination 90, 50,10mA. The reciprocal of this pump profile, 10,50,90mA, has a peak gain of just under 0.7dB less. Also of note is the blue shift of the gain peak at higher biases, reflecting the ASE behavior. Finally, as predicted there is a small level of gain ripple as a result of cavity reflection suppression, corroborating the previous ASE data well. This ripple cannot be well resolved. The

corresponding NF data for these device parameters are given in Figure 5.25.

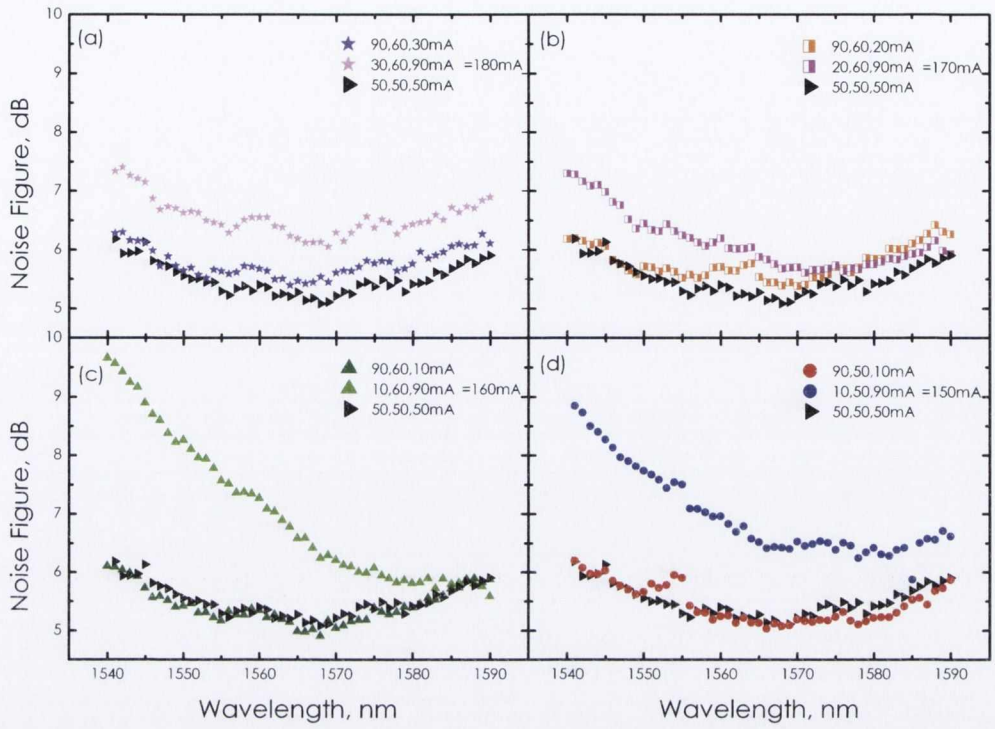

Figure 5.24: NF as a function of wavelength, for the four cases of Figure 5.23 where i_{tot}=180mA, 170mA, 160mA and 150mA.

Although the injected bias is larger in Figure 5.24 (a) and (b), the NF is the highest in these two cases due to the reduced gain at these biases. Furthermore, the level of control achievable in Figure 5.24 (a) and (b) is less than in Figure 5.24 (c) and (d), as evidenced by the smaller difference in NF between the Low NF and High P_{sat} profiles. Looking at (c) and (d), The Low NF approaches the value attained by the Standard profile of approximately 5dB, at 1565nm. The purpose of this section is to qualify the ideal scenario of the simulations at an i_{tot} of 150mA, and with this in mind Figure 5.24 (d) yields the closest properties to the optimum conditions of characterisation.

Based on simulations a -18dBm (after losses) TE signal is injected into the SOA at the peak gain wavelength, for isolated i_2 values and a variation of i_3 from 0-90mA. The purpose of this is to narrow down the best possible conditions, and compare with those found the same way through simulation. The data are shown in Figure 5.24.

This data illustrates some limitations of this prototype device, when compared with simulation. Looking first at Figure 5.25a, we plot the gain for these scenarios as a function of output current. For i_2=10mA, the device is mostly absorbing, for nearly all values of i_3, bar a 40mA

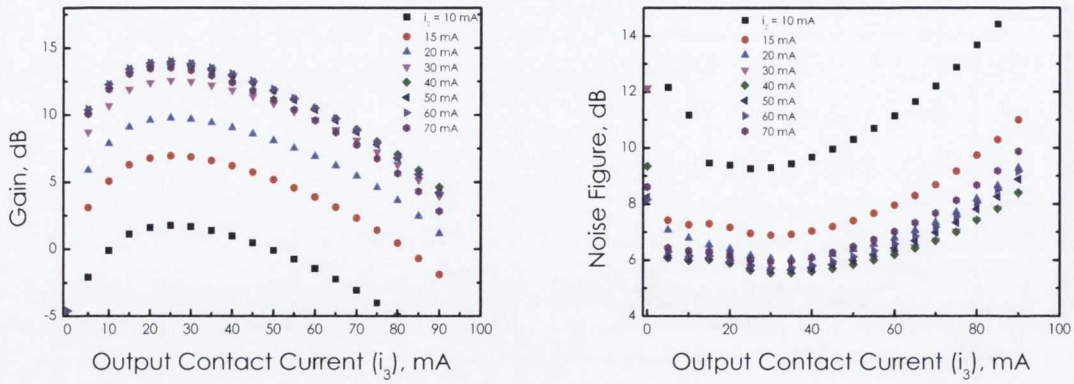

Figure 5.25: a) Gain vs output contact pump current (i_3) for i_1=90mA, and i_2=10 - 70mA. For a small injected signal of -18dBm, polarised along the TE eigenmode. (b) NF vs output contact pump current under the same conditions

range between i_3=10mA and i_3=50mA. Of course the i_{tot} value after this point in this case is above 150mA. As i_2 is increased with each step, a familiar gain-bias trend appears, with the increase in gain decreasing as i_2 approaches 50mA. The gain maximum occurs at approximately 50mA, although the difference is smaller than the error of 0.2dB. Moving to 5.25b, a plot of the corresponding NF as a function of i_3, it is seen that the NF data is much more convergent than the gain. The variation of the NF above i_3=5mA is approximately 4dB, although this is mostly in the wrong direction towards higher values. In fact the minimum range of NF values among this data occurs over the range of i_3=5mA−35mA, for an i_2=40,50mA. It is hard to distinguish between them, although we will choose i_2=50mA, based only on the collective information gathered so far. This includes the LI and spectral data, as well as the temperature related effects at higher applied currents.

The next stage is to use the values of i_1 & i_2, and to now search for the optimum i_3 arrangement. Figure 5.26 is a plot of NF versus i_3, in 0.2mA steps from 0-20mA, where i_1=90 and i_2=50mA. The injected light remains at 1565nm, with a signal power of -18dBm, TE polarised. The data is split into 3 regions. The green represents the decrease in NF as the device movies out of the absorption regime and towards gain; the red data depicts the region of minimum achievable NF; and the blue region the increasing NF. The insets of Figure 5.26 highlight these first two regions. The first shows the level of NF variation as the device becomes useful as an amplifier, with increased output section pumping. Although the variation above the 10mA range shown is low at 0.1dB, it is nonetheless the peak of operation for this configuration, and so 10mA is the

chosen i_3 value. It must be noted that this data, although technically similar in acquisition to Figure 5.25, when probing this single value of i_2, the temperature stability of this specific scan was significantly better due to a more stabilised set up.

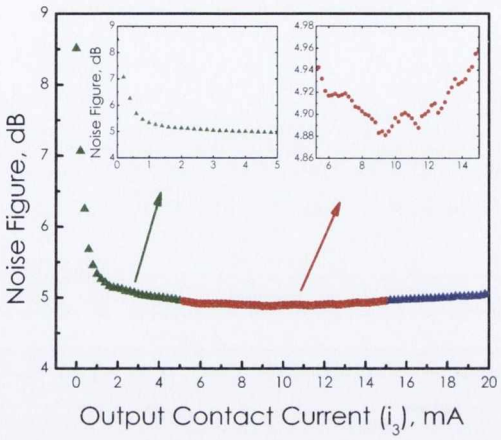

Figure 5.26: NF vs output contact pump current (i_3) for i_1=90mA, and i_2=50mA. For a small injected signal of 18dBm, for a TE polarisation.

The current profiles are redefined below. They correspond to a total injected current across the device of 150mA, representing the maximum gain achievable for the MCSOA. The Standard Profile is given by 50, 50, 50mA, the Low Noise, given by 90,50,10mA. The reverse of the Low Noise Profile is investigated as it should lead to a large deviation in NF, and labelled High P_{sat}, as was seen with the LCSOA.

Limited Total Injected Bias

Figure 5.27 plots the spectral characterisation of gain and NF for the three profiles. In this instance, the injected power is -18dBm, in the small-signal regime, and aligned along the TE eigenmode. The wavelength is isolated over the 3dB gain bandwidth.

The minimum NF observed for the experimental data is 5dB at a wavelength of 1568nm, measured for the low noise bias configuration. The maximum gain is again observed in the standard bias configuration and is measured as 17.5dB at a wavelength of 1565nm. A maximum gain of 15 dB is observed at 1565 nm for the Low Noise bias condition. A slightly lower peak gain of 14.3 dB is observed at the same wavelength for the High P_{sat} case. This is due to the larger value of ASE as shown in Figure 5.13, which reduces the fraction of carriers contributing to the amplification. The 3dB gain bandwidth is more than 50nm for both carrier distributions, where the measurement on the high wavelength side was limited by the tuning range of the

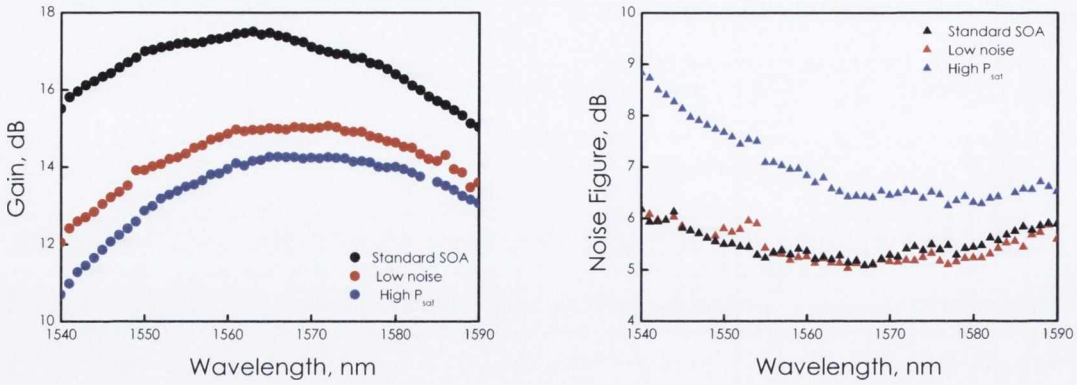

(a) (b)

Figure 5.27: (a) Gain and (b) noise figure as a function of wavelength for a small injected signal of -18dBm, polarised along the TE axis.

external cavity laser (ECL). The gain difference of 0.8dB observed between the Low Noise and High P_{sat} cases in the simulated data is also present here. This discrepancy is explained by a slight difference in the size of the individual sections of the SOA. The minimum NF achieved for the Low Noise configuration is at best marginally better than the Standard profile, with a reduction in the NF of approximately 0.2dB between the Low Noise configuration and the standard configuration at longer wavelengths, where the error in the measurement is estimated to be 0.2dB. At the peak wavelength the difference is minimal, even though the sacrifice to gain between the Standard and Low Noise is large.

The difference in NF of the high saturation power case over the low noise case is approximately 2dB, showing directly the clear effect due to the bias current distribution, but 0.75dB less than in simulation. However, it is possible that with this experimental device that carrier leakage across the sections occurs, therefore broadening the carrier profile. By improving the resistance between adjacent contacts it is expected that the experimental results will converge to a better extent towards the simulated data. This will be examined in Chapter 7.

The gain as a function of output power is presented in Figure 5.28, for a range of input powers at the standard profile peak gain wavelength 1565nm. Shown in (b) is the same gain data as a function of input power.

The experimental data follows the same trends set by the simulation well. The saturation output powers (P_{sat}) are marked by the corresponding arrows on both plots. The saturation power of the standard case, is 7.8dBm, 1.5dB greater than the low noise scenario. The High

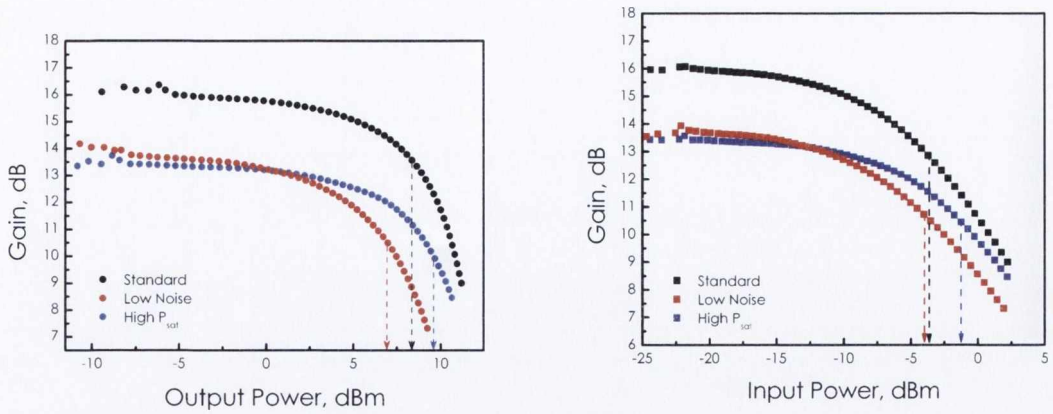

Figure 5.28: Gain versus (a) output power and (b) input power for a TE signal injected at 1565nm, for the three bias conditions

P_{sat} configuration on the other hand, has a value of 9.3dBm, a gap of 3dB from the low noise case. Whereas a high current density at the input of the device leads to a lower noise figure, increasing the injected current along the length of the waveguide towards the output facet increases the saturation power of the device, allowing it to operate as a linear amplifier for a wider range of input powers.

The corresponding saturation input powers ($P_{sat,in}$) are given in Figure 5.28b. As previously discussed the Low Noise pumping configuration saturates at lower input powers than the Standard and High P_{sat} cases. The input power at which this occurs is -3.90dBm, only 0.2dBm lower than the standard case, and the High P_{sat} case at -1.05dBm. While the quantitative values differ from the simulation, the trends are in agreement. The relative margin-less behavior between the input saturation powers of the Standard and Low Noise cases and the difference in saturation output power is explained by the much greater gain available to the standard case of over 2dB.

Finally, the total variation in all three output parameters measured experimentally is plotted in Figure 5.29. This is the equivalent plot of Figure 5.12, shown earlier. The bias profile is varied from the Low NF profile through the Standard control case, to High P_{sat} in steps of 5mA (maintaining a middle contact bias of i_2=50mA). The input signal is -18dBm at 1565nm for the gain and NF curves, while the P_{sat} curve is obtained using different powers depending on the bias configuration. The magnitude of the gain decreases as the carrier density profile becomes less symmetric, matching simulation, where the overall magnitude differs. As expected, the NF

is observed to decrease as the bias condition approaches that of the low noise profile, and the saturation power increases for the opposite bias distribution.

The NF is varied over a range of 2.8dB experimentally and 2.72dB through simulation, with a continuing upward trend of NF as the carrier density profile approaches the conditions of reduced gain at the input. Also of note is the continued lack of improvement between the Standard profile and the Low Noise profile, where the values are approximately equal within error. As mentioned, this is potentially due to carrier leakage between adjacent sections. The saturation output power has a range of approximately 3dB experimentally, compared to the simulation of 4.21dB. The peak gain value for the standard configuration is 16.1dB, 1.4dB less than the simulated value, and previous experimental values. This change is due to both device degradation (expected after hundreds of hours of operation [13]), and temperature problems. This plot highlights the adaptability of the MCSOA when pumped at a constant total bias, whilst also detailing the sacrifices made in one or more parameters as the other is optimized. For instance, the higher saturation powers capable with the High P_{sat} profile come with a sacrifice in NF and gain, whilst the lowest NF performance (using the Low NF profile) produces a dramatic decrease in the saturation point.

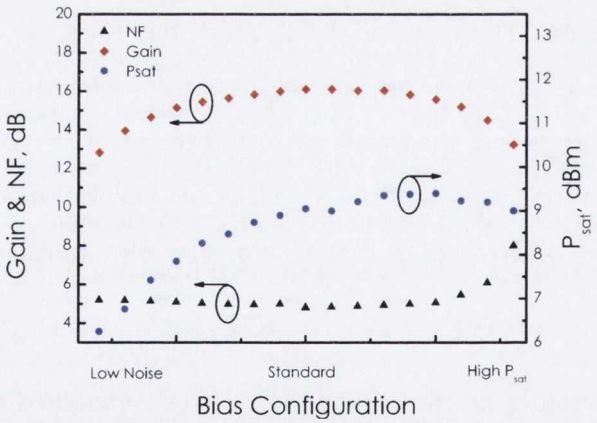

Figure 5.29: The dependence of Gain, NF & P_{sat} on the current combination applied, as it varies from Low Noise through the Standard Profile to High P_{sat}. The injected wavelength is 1565nm, at a power of -18dBm along the TE eigen mode. i_1 and i_3 are varied in steps of 5mA.

5.4 Quasi-Continuous Wave Performance

5.4.1 Bit Error Ratio Testing

To this point control and characterisation of the 'noisiness' of a signal has been discussed in terms of the NF, defined in the CW regime. This section will investigate the impact of NF control, via variation of the carrier density profile, on the detection of a known 10GBits/s data signal after propagation through the MCSOA. This constitutes a bit error test [14].

The bit error ratio (BER) is a fundamental measure of overall transmission quality: every system (and every part of it) has an intrinsic BER, in which the number of bits received correctly, are counted against the total number generated. In a real test system the BER is unknown and must be measured. For this purpose a bit error ratio tester (BERT) is used. This comprises of a pattern generator (PG) which modulates and injects a known data stream into a transmission system (the MCSOA). The received bits are then compared to the expected bit pattern. The bit error ratio is calculated by dividing the number of erroneous bits by the number of compared bits,

$$BER_m = \frac{N_{err}}{N_{bits}} \tag{5.1}$$

where BER_m is the measured bit erro ratio, and N_{err} and N_{bits} are the average number of errors and the number of transmitted bits, respectively.

For a 10Gbps system, the accepted BER corresponding to almost complete error free transmission is $\sim 10^{-9}$ [14]. However as higher data rates are approached, the conditions for error free transmission become tighter, and a BER of $\sim 10^{-12}$ is required. From a measurement point of view the difference between observing a 10 & 40Gbps stream is significant. For a 10Gbps source, an error will occur every 10 seconds. For a 40Gbps modulation, this will increase to 100 seconds, potentially leading to impractical measurement times in the lab [14].

5.4.2 Experimental Setup

The full setup for measuring the BER of the MCSOA, including the BERT, is given in Figure 5.30. It uses the same CW source as before, passed through a polarisation controller (PC) and Mach-Zender Interferometer (MZI). This modulates the CW signal with a 9.95 Gbits/s amplitude shift keyed (ASK), non-return-to-zero (NRZ) pseudo random bit sequence (PRBS),

with a pattern length of $2^7 - 1$. The data signal is amplified and filtered ($FWHM = 5nm$) to remove as much of the EDFAs ASE as possible. The modulated beam is coupled to free space and then the MCSOA under test, using identical coupling optics as those previously described. The output of the SOA data stream is then collected, passed through a final fibre amplifier, filtered ($FWHM = 2nm$) and terminated at the detection system.

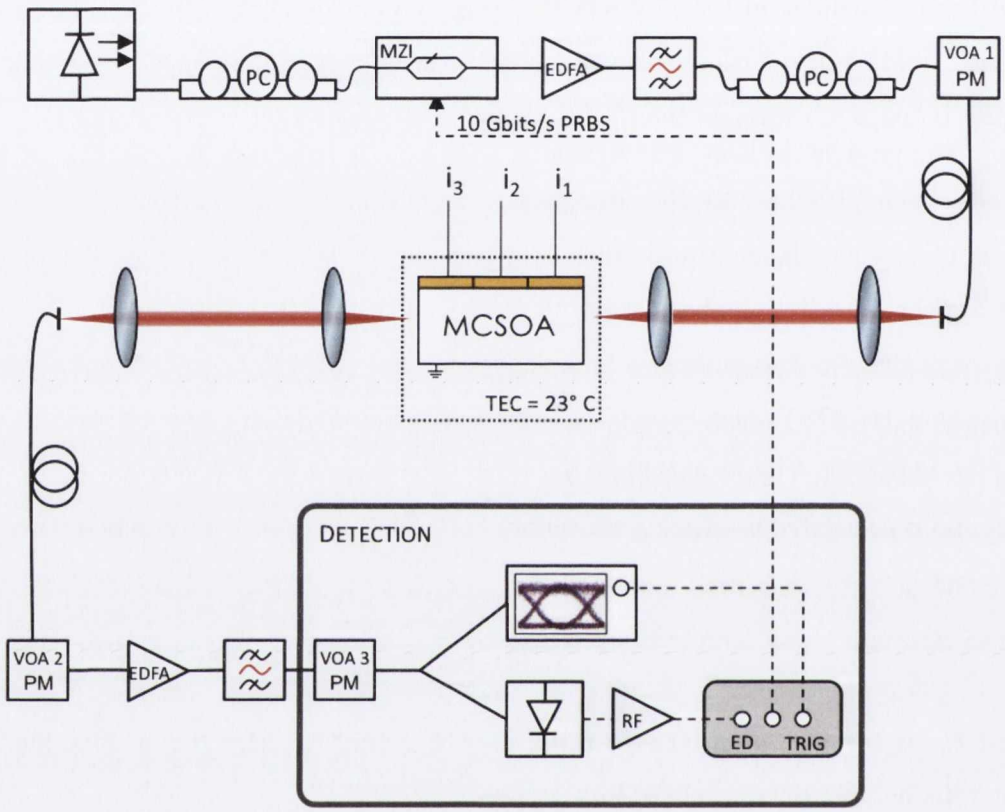

Figure 5.30: Bit error ratio (BER) measurement set upShown: External cavity laser (ECL); Polarisation controller (PC); Mach-Zhender Interfermoter (MZ); Erbium-doped fibre amplifier (EDFA); Variable optical attenuator and power meter combination (VOA/PM); RF Amplifier (RF). The BERT is shown after the RF amplifier in the detection segment, and is comprised of an error detector (ED) and Trigger (TRIG).

The detection contains a 10GHz optical sampling oscilloscope for acquiring the signal waveforms, and a photodiode/RF amplifier combination input directly to the BERT error detector (ED). The final VOA-3/PM-3 is placed before the detection to maintain a constant average power onto the detector. The scope is triggered externally from the BERT, whilst the error detector is internally clocked. The BERT has the facility to tune the reference receiver decision threshold and sample delay offsets to arbitrary levels, to alter the sensitivity of the system. Figure 5.31 relates these parameters to a standard eye diagram (measured on the sampling optical oscilloscope), which provides a means of observing the actual shape of the waveform.

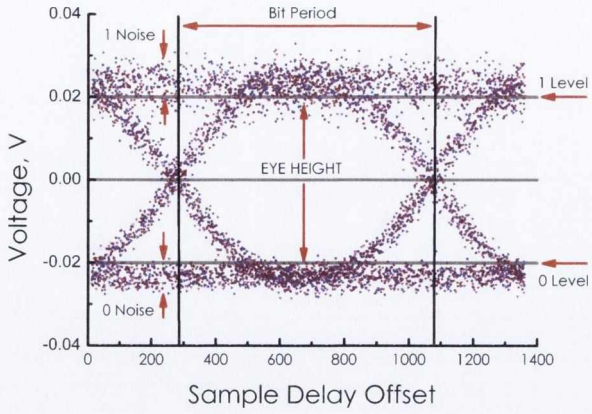

Figure 5.31: NRZ waveforms for linear gain region collected on an optical scope. Shown are the eye height, sampling point, the 0 & 1 levels and the bit period.

The appearance of the eye diagram and the quantity of information that can be gleaned from it depend on the sampling architecture used in the oscilloscope, either real-time sampling or equivalent-time sampling. In general however, the key parameters, shown in Figure 5.31, are the $One - Level$ and $Zero - Level$ which represent the mean logic 1 and 0 binary values; the associated noise-spread of these levels; the bit period or bit length and; the eye diagram height, which is qualitatively linked to the extinction ratio. More specifically, the eye height can be defined as the separation of the upper and lower 3σ points, where σ is the standard deviation, or spread, in the 1 and 0 levels due to intensity noise.

5.4.3 10Gbits/s Inline Amplification Performance

The BER and waveform measurements are taken, at both low and high input powers to probe the linear and saturated gain as a function of carrier density profile. Firstly, at the minimum NF wavelength of 1565nm, and secondly at 1550nm where the difference in NF between the Low Noise profile and the High P_{sat} profile is greater, as determined by the CW characterisation. The injected polarisation is set along the TE eigen mode. The BER measurements are taken over a 90 second scan period. This provides ample time to acquire a meaningful count [14].

Initially, BER data is taken for the system in the absence of a test element, known as a $back - to - back$ configuration, as a means of comparison to assess any improvement in sensitivity achieved. This is done through by-passing the MCSOA with optical fibre, removing the entire free-space section from the test. The measured back-to-back BER is given in Figure 5.32, while a representative waveform for this data (measured on the optical sampling scope) is inset. The

input power is varied over 4dB from -28dBm to -24dBm, measured at VOA-1 in the setup. This covers the transition of the BER from acceptable levels (10^9) where transmission is error free, to unacceptable levels (10^4), where the error rate is poor. This low power range is chosen as real telecom systems require the ability to operate at powers as low as -26dBm, however any power accessible in the linear regime of the SOA could be chosen.

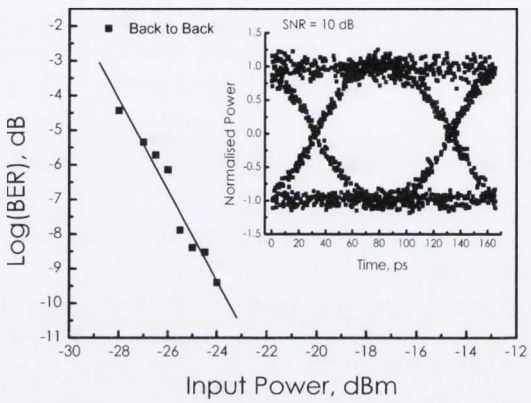

Figure 5.32: Back-to-back BER data at low injected power. Inset: Signal waveform measured with optical sampling oscilloscope at -26dBm input power, including SNR value at this power.

Small-Signal Gain BER Data

To ascertain the change in measured sensitivity by the SOA in the linear gain regime, low input powers were examined, where the amplified SOA output is maintained at 60μW (-12.2dBm) by the EDFA-2/VOA-3 combination at the detector. The measured eye diagrams for the Low Noise and High P_{sat} combinations are shown in Figure 5.33, for a small injected signal of -26dBm (accounting for losses) at 1550nm. This data is shown to illustrate both the closing of the eye diagram (the value has decreased by 0.84dB for the High P_{sat} case) and the measured difference in SNR: 7.87dB and 7.03dB for the Low Noise and High P_{sat} cases, respectively. The SNR provides a good indication of the noise characteristics but does not compare in accuracy to the BER measurements. Furthermore, in this work although the degradation in the SNR for the Low NF and High P_{sat} cases is not reduced by the CW NF previously calculated, this is because these values are being compared with the back-to-back measurement, and not the standard case. The SNR measurement for the Standard configuration is, in fact, higher than the back-to-back case and correlates well with the CW NF. The main point of the comparison is to show the relative difference between the Low NF and P_{sat} cases. This does not affect the BER data.

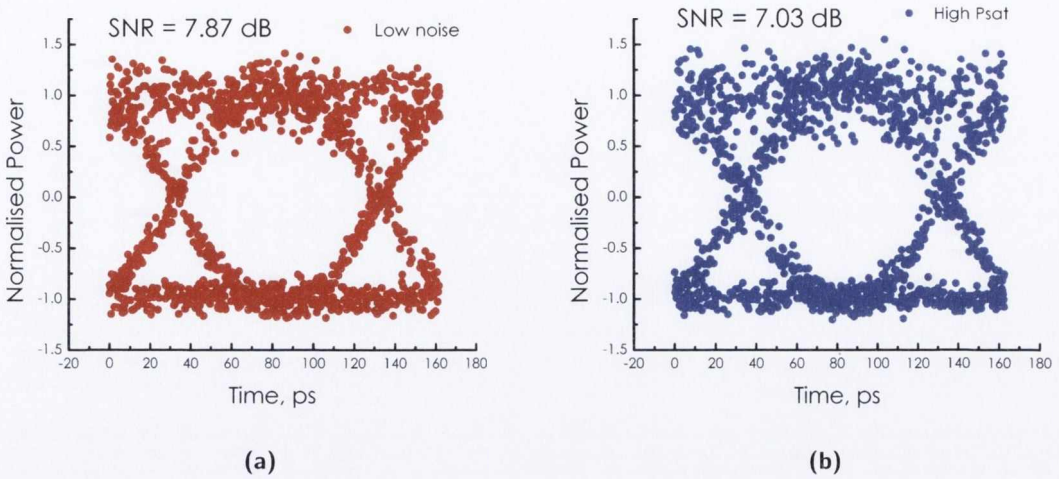

(a) (b)

Figure 5.33: Collected eye diagrams for the (a) Low Noise & (b) High P_{sat} current profiles, in the small-signal regime. Seen is the closure in the eye due to higher SNR in High P_{sat} case.

The full BER dataset from which these waveforms are taken are given in Figure 5.34 at 1565nm, shown in (a), and 1550nm, shown in (b). The data is taken for the Standard, Low Noise and the High P_{sat} bias configurations. The detector power is held constant at 60μW. The back to back data is present for comparison, and the black line represents the 10^{-9} level.

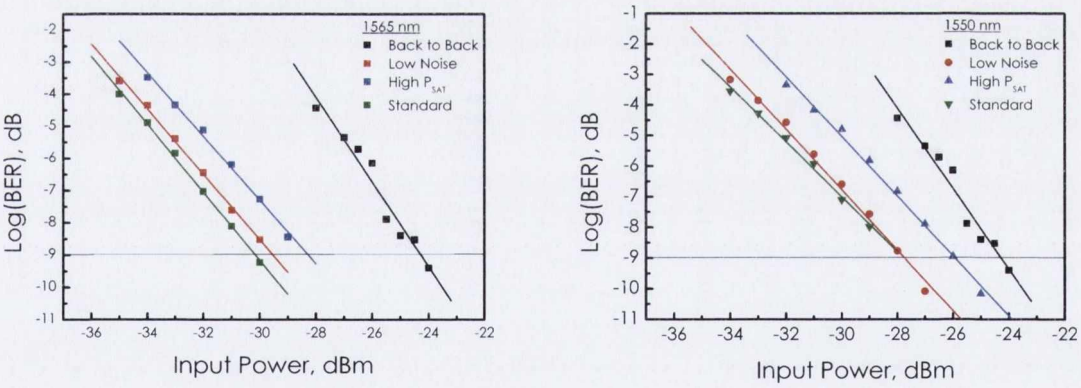

(a) (b)

Figure 5.34: BER in the small-signal regime for the Standard, Low Noise and P_{sat} pumping schemes, for an injected wavelength of (a) 1565 nm and (b) 1550 nm. Also shown is the back-to-back data with no test device present. The black line represents the minimum BER value for error free detection.

Firstly, the data taken for an injected wavelength of 1565nm, representing the wavelength of lowest NF_{TE} from the CW analysis, will be discussed. The low noise configuration clearly produces a better sensitivity over the high P_{sat} as expected, with a power penalty of 1.21dB for the High P_{sat} relative to this case. The low noise profile in turn concedes a small power penalty

over the standard configuration of 0.64dB. The 'power penalty' here relates to the difference in power required to reach an equivalent BER. Very little work has related NF control to BER measurements, although some naturally low NF devices have been studied, such as quantum dot SOAs by Akiyama et al [15]. However, the analysis above ties in well with the CW characteristics of the device.

The same analysis can be applied to data at 1550nm Figure 5.34 (b), where a larger power penalty between the noise controlled configurations is expected. The standard and low noise profiles experience a BER of 9dB at -27.78dBm, while the high P_{sat} data reaches an equivalent BER at -25.97dBm, resulting in a power penalty of 1.81dB. It was found under continuous wave injection that even though a decrease in ASE is achieved relative to the standard case, a corresponding reduction in gain meant that the overall NF improvement was minimal. This is echoed here by a Log(BER) that is only marginally different. Also of note concerning both plots of Figure 5.34 (a) & (b), is the relative BER performance to the back-to-back data. Based on the higher CW NF of 1550nm compared to 1565nm, a greater improvement over the back-to-back case is expected for the 1565nm data, and this is what occurs. Overall, this probing of the BER under the linear operating regime corroborates well the CW NF, where the level of control is based on carrier density engineering.

Saturated Gain BER Data

The concept of NF breaks down under saturation. The waveforms plotted in Figure 5.35 correspond to the low noise configuration under 6dBm injection (accounting for losses), at 1550nm. The extreme SNR degradation in the saturated regime can be seen as a consequence of closure of the eye diagram, with a value of 3.68dB after propagation through the MCSOA, significantly reduced from that of the back-to-back value of 10dB. This is a clear manifestation of gain saturation on an input signal.

The corresponding BER measurements are shown in Figure 5.36. The carrier density dependent improvement under these injected conditions corresponds to the high P_{sat} case, as the saturation has greater influence over the BER under saturation. As a consequence of this, and again reflecting the CW data in trend, the lower BER results at higher injected powers for the high P_{sat} bias configuration illustrating its extended linear operation over the low noise configuration.

It is the standard bias configuration that correlates with the worst BER performance. This is unexpected as the saturation output power of this profile falls between that of the low noise

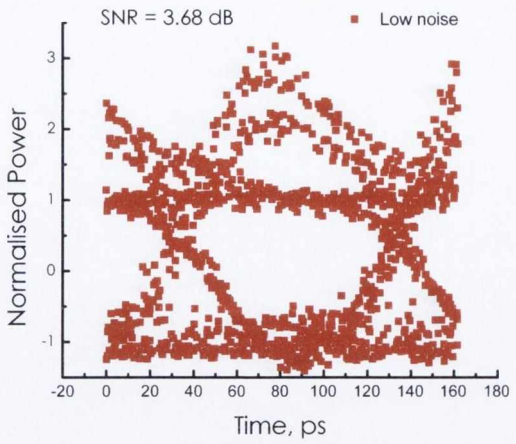

Figure 5.35: Measured waveform for the Low Noise current combination, for a high injected power, saturating the gain.

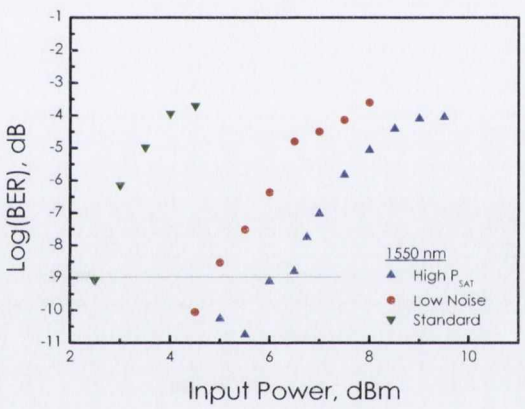

Figure 5.36: BER in the saturated regime for the Standard, Low Noise and P_{sat} pumping schemes, for an injected wavelength of 1550nm, and an input power of 6dB. The black line represents the minimum BER value for error free detection.

and high P_{sat}. A possible explanation is related to a lower saturation input power for this configuration, and the higher level of gain. As the compression in this case is larger than the noise controlled cases, it will have a more detrimental effect on the input signal.

5.5 Conclusions

The concept of noise figure reduction proposed in Chapter 3 was unequivocally confirmed by the second of two design strategies. Specifically, control of the noise figure of a Multi Contact SOA was demonstrated through simulation and experiment by direct modification of the carrier

density profile.

The simulation used was a modified version of the Lateral Cavity SOA numerical simulation discussed in Chapter 4. Initially, the total injected bias was not limited, determining the ultimate gain and NF performance. The applied conditions adhered to the main criteria for a low NF, with a high applied input current density. The middle and output sections were then varied accordingly. The resultant colour map illustrated firstly the potential versatility of the multi contact nature of the device, but so too that there are numerous profiles which exist that provide the lowest NF. All of these profiles exhibit a large step in applied bias between one or more sections, demonstrating the importance of the carrier density profile.

Upon assessment of the degree of NF control for the unlimited applied bias case, the steady-state characterisation was undertaken when comparing the simulated NF reduction over the equivalent standard SOA scenario. For this the total applied bias was held constant, and three current profiles were probed under continuous wave injection, in the linear regime. The minimum NF achieved corresponded to the simulated Low Noise configuration at 4.47dB, an improvement of 0.6dB over the equivalent standard SOA under the same injected conditions. The profile corresponding to a reverse of the Low Noise bias distribution, and effectively acting as a proof of concept, produced a further increase in NF from the standard profile of 1.8dB at higher wavelengths, increasing to 3.2dB at lower wavelengths. In addition to the increased NF, the High P_{sat} profile of course provides an extension of the linear amplification regime. To explore this, the same three profiles were tested, at the peak gain wavelength of the standard profile, as a function of input and output injected powers. An increase in the saturation output power of 1.6dB and 4.45dB relative to the Standard SOA and the Low Noise bias distribution, respectively, was found. To reiterate: the total carrier density is constant for each profile, meaning that the effects observed are directly a result of the non-uniform profiles injected.

The fabricated 3 section MCSOA was then experimentally characterised. The carrier density modification effect was evidenced through measurement of the amplified spontaneous emission. A direct observation of a reduced output and increased input carrier density could be seen in the relative spectral power difference. Under CW injection, this manifested in a NF variation at the peak wavelength of 1.5dB for a total injected current of i_{tot}=150mA, between the Low Noise and High P_{sat} current profile, illustrating the level of control achievable. The reduction of NF relative to a Standard profile was found to be negligible, however it is hoped that through further iterations of the concept at the design level this can be improved upon, as the trade off between ASE reduction and gain reduction can be optimised. For instance, the introduction of a

quantum dot based gain media in conjunction with carrier profile dependent operation may produce favourable results. This would require longer devices, and consequently a possible increase in the number of sections. To further this idea, Chapter 7 will look at the effect of modifying the MCSOA structure through a post-processing etching technique based on focused ion beam (FIB) etching. This work will attempt to assess if improving the isolation between adjacent sections can improve the level of accuracy in carrier profiling. The leakage across the section boundaries is thought to be an area where improvement is required for better performance. Future modelling efforts will take this carrier leakage into account.

References

[1] P. Tian, L. Huang, W. Hong, and D. Huang, "Pattern effect reduction in all-optical wavelength conversion using a two-electrode semiconductor optical amplifier," *Applied Optics*, vol. 49, no. 26, pp. 5005–5012, 2010.

[2] F. P. D Byrne, Q Lu, WH Guo, J. F. Donegan, B. Corbett, B. Roycroft, P. Lambkin, JP. Engelstaedter, "A facetless laser suitable for monolithic integration," *Lasers and Electro-Optics Society (LEOS)*, pp. 1–2, 2008.

[3] R. Lennox, K. Carney, R. Maldonado-Basilio, S. Philippe, a. L. Bradley, and P. Landais, "Impact of bias current distribution on the noise figure and power saturation of a multi-contact semiconductor optical amplifier," *Optics letters*, vol. 36, pp. 2521–3, July 2011.

[4] M. J. Connolly, *Semiconductor Optical Amplifiers*. Kluwer Academic Publishers, Boston, 2010.

[5] K. Carney, R. Lennox, R. Maldonado-Basilo, S. Philippe, F. Surre, A. L. Bradley, P. Landais, "Control of noise figure and saturation power in multi-contact semiconductor optical amplifiers: Simulation and experiment," *IEEE Journal of Quantum Electronics*.

[6] D. M. Baney, P. Gallion, and R. S. Tucker, "Theory and Measurement Techniques for the Noise Figure of Optical Amplifiers," *Optical Fiber Technology*, vol. 6, pp. 122–154, 2000.

[7] B. F. Kennedy, P. Landais, S. Philippe, M. Martinez-Rosas, A. L. Bradley, "Temporal and spectral dependence on polarization of the input signal in a semiconductor optical amplifier," in *Integrated Photonics Research (IPR)*, 2004.

[8] P. Meyer, "Pulse Testing of Laser Diodes," in *Keithley Instruments Manuals*, vol. 7, Keithley Instruments, Inc.

[9] T. Floyd, *Electronic Devices (Electron Flow Version)*. Pearson, 8th ed., 2007.

[10] A. Yariv, *Photonics: Optical Electronics in Modern Communications*. No. March, Oxford University Press, 2007.

[11] L. A. Coldren, S. W. Corzine, *Diode Lasers and Photonic Integrated Circuits*.

[12] K. Carney, R. Lennox, R. Maldonado-Basilio, S. Philippe, L. Bradley, and P. Landais, "Noise controlled semiconductor optical amplifier based on lateral cavity laser," *Electronics Letters*, vol. 46, no. 18, p. 1288, 2010.

[13] M. Wieckowski, M. Margala, M. H. Hu, and H. K. Nguyen, "Differential Resistance Testing for InP-Based Semiconductor Optical Amplifiers," *Journal of Lightwave Technology*, vol. 27, pp. 893–900, Apr. 2009.

[14] D. Derickson, *Digital Communications Test and Measurement: High-Speed Physical Layer Characterization*. No. March, 2007.

[15] T. Akiyama, M. Ekawa, M. Sugawara, K. Kawaguchi, H. Sudo, A. Kuramata, H. Ebe, and Y. Arakawa, "An Ultrawide-Band Semiconductor Optical Amplifier Having an Extremely High Penalty-Free Output Power of 23 dBm Achieved With Quantum Dots," *IEEE Photonics Technology Letters*, vol. 17, no. 8, pp. 1614–1616, 2005.

6

Multi Contact SOA: Gain Dynamics

The CW characterisation of the carrier-density-profile dependent noise figure and saturation power for a multi-contact SOA, was presented in the previous chapter. The study of ultrafast carrier dynamics in the semiconductor active region is important in understanding the ultimate limitations on the modulation speed of semiconductor amplifiers as well as for the tailoring of devices with specific application. This chapter will explore the dynamic effects of the ability to vary the carrier density of the MCSOA non-uniformly. Firstly, the Low Noise, High P_{sat} and Standard current profiles from the previous chapter are measured. Following this, the variation of the applied bias to each of the facet sections in turn is undertaken. This second experiment will aim to discover the impact of varying the carrier density, on the gain dynamics. Specifically, how this influences the relative importance of the interband and intraband gain compression. Potential application based on these findings will be addressed.

6.1 Pump-Probe Studies

6.1.1 Pump-Probe Technique

In general, the carrier dynamics of SOAs occur over time scales that are too fast to resolve directly by simply using a photodiode in conjunction with an optical sampling oscilloscope. Working at the state of the art allows the study of the slower processes involved, associated with the pumping of carriers back to the conduction band [1, 2, 3]. However this does not provide a complete observation of the complex array of processes which take place. The pump probe technique is capable of observing the fine structure of the ultrafast gain compression and recovery [4, 5]. The principle of a pump probe scheme relies on two signals: a pump and a probe. The injected pump signal induces a measureable change in the SOA. The effect of this on a probe beam then acts as a measurement of that change. The probe can be collected as either a transmitted or reflected quantity, depending on the type of property been investigated and the set up used [6, 5].

In a more specific sense relating to this work, two pulses of light, the pump and probe, are coupled to the MCSOA sample. The pump saturates the gain, and the probe samples this change as a function of time delay, making it possible to measure the decay and subsequent recovery of the excitation, resulting from both interband and intraband processes. The temporal resolution of the experiment is theoretically limited only by the pulse width, meaning a laser source with short optical pulses is desired, whilst not compromising the analysis with a broader spectral range [6].

The centre wavelengths of the pump and probe beam need not be identical. A so-called two-colour non-degenerate pump probe measurement, based on two synchronized sources of short pulses (e.g. a laser and an optical parametric oscillator, or two parametric oscillators pumped with the same laser) has additional capabilities in ultrafast spectroscopy [7, 6]. It is vital in such cases to ensure tight synchronization of the different laser sources with a very low relative timing jitter. Failure to do this may reduce the temporal resolution of the experiment.

6.1.2 Propagation Configuration

The relative direction of the pump and probe beams as they pass through the sample influences the effects observed. Two distinct transmission based detection configurations may be utilised: collinear propagation and contra propagation. These are now discussed separately:

Collinear Propagation

The pump and probe beams are in collinear formation when they travel along the same axis, in the same direction. In such an arrangement material dynamics can be acquired to a high temporal resolution. In this way the pulses overlap at a single delay, and do so for the entire journey through the device. As the delay in a collinear arrangement modifies the probe overlap with the pump as it propagates, purer effects can be resolved. Isolating the two pulses of the same wavelength efficiently can be difficult, requiring complex heterodyne techniques [8, 9, 4], or cross polarising the pulses. This leads to problems when assessing optically functional process for switching and influences transitions that can be studied, since they cannot be co-polarised and degenerate [10].

Contra Propagation

A contra propagation set up is used in this work, where the pump and probe travel towards each other through the SOA. In this way the probe experiences the induced changes by the pump at different points in and outside of the SOA according to the time delay. The pump and probe overlap at every delay by virtue of their opposite paths. The main disadvantage of this configuration is a longer fall time. In contra-propagation the pulse overlap occurs at different positions inside the device and is strongly dependent on the length of the SOA. The analysis and modelling of the experimental data is not as straightforward since the probe experiences different regimes as it travels. For one pump-probe delay, part of the SOA could be saturated by the pump signal while another section could have recovered already [11]. Finally, a contra-propagation configuration also results in an extension of the range of relevant delays to twice the value for a collinear arrangement.

6.1.3 Temporal Resolution

The timescales which can be resolved by pump probe measurements are directly linked with the temporal width of the optical pulses. Phenomena which occur over shorter time scales than the pulse width cannot be resolved, and so the shortest possible pulses are desired. However, as the temporal pulse-width is decreased the spectral width increases, leading to impracticalities in probing the relatively narrow gain bandwidth of an SOA [6]. In this way femtosecond pump probe studies have been carried out, but over relatively large bandwidth and requiring different filtering schemes [12]. In addition to this, for investigations relating to optical communications femto-

second behaviour is dominated by intraband effects, particularly spectral hole burning (SHB) and two photon absorption (TPA), speeds that represent impractical behaviour at present [13]. With this in mind low picoseconds pulses are used in this work, which have a temporal FWHM of approximately 2.5ps upon injection into the MCSOA. At this resolution intraband and interband processes are both resolvable, but not the individual contribution of ultrafast phenomena such SHB or TPA.

6.1.4 Free Space

FIberising a pump probe set up has some advantages, mostly regarding the dramatic simplification of alignment and data acquisition. However, polarisation is unpreserved and temporal broadening can be significant and variable. A free space set up on the other hand both preserves the state of polarisation and pulsewidth, allowing for more consistent measurement. The level of control over experimental conditions comes at a cost, where alignment procedures are complex and time consuming.

6.1.5 Set up

The free space, counter propagating, pump-probe setup used to obtain the carrier profile dependent gain dynamics is given by Figure 6.1. The configuration is similar to that used by Phillipe et al. [11].

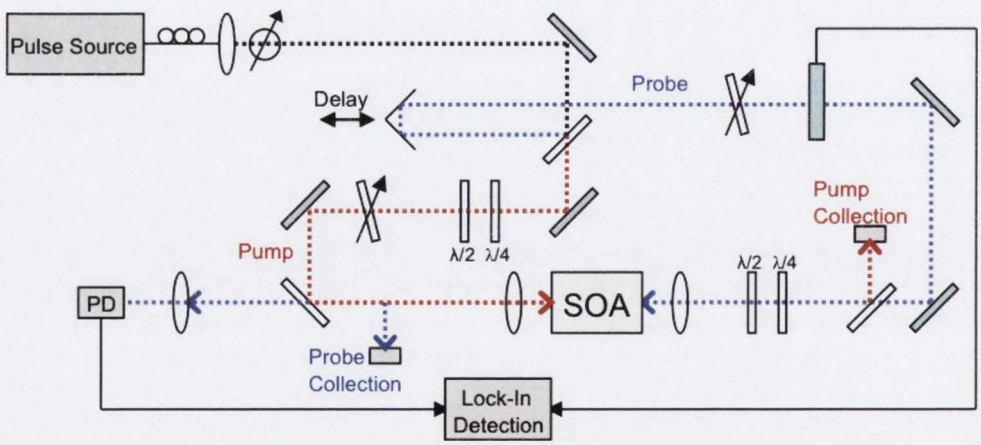

Figure 6.1: Free space, contra-propagation pump probe set up used for acquisition of carrier profile dependent gain dynamics. Shown is the femtosecond pulsed source; delay line; variable optical attenuator (VOA); polarisation optics, signal mechanical chopper; MCSOA and acquisition photodiode (PD).

The source used is a Menlo Systems 150 femtosecond pulsed laser, with a $sech^2$ intensity profile and a repetition rate of 82MHz, ensuring that the device has fully recovered before the next pulse has arrived. The wavelength is tuned to the appropriate wavelength by a fiberised diffraction grating filter, of 1nm spectral width, after which the pulses have a temporal FWHM of approximately 2.5ps $\pm$ 0.1 ps. The pulses are coherent and one is delayed with respect to the other by means of a variable delay line, automated through a Labview VI. The relevant pump and pulse powers are varied with variable optical attenuators (VOA), the values of which are given in the specific experimental sections.

The polarisation of the pump and probe beams is set using a half-wave and quarter-wave plate on each arm, just prior to injection into the SOA. All of the gain dynamics acquired in this chapter are co-polarised. That is, where pump and probe are both aligned along the TE eigenmode, corresponding to the mode of maximum gain. The output of each beam is monitored by two collection points that terminate at an optical spectrum analyser (OSA). The coupling optics are identical to the CW characterisation of this same MCSOA. Finally, a 10nm filter centred on the probe wavelength is used to isolate the pertinent signal from that of the broader ASE of the amplifier. This was placed just before a photodiode, where lock-in amplifier detection is used for probe acquisition. As a final note, we refer to the input (probe) facet of the device (i_1), as the input facet. The output is given by the pump input facet (i_3). This is shown in Figure 6.2b, in the next section.

6.1.6 Extracted Parameters

Compressions

Insight into the gain dynamics, including the relative importance of the interband and intraband effects, comes from the extraction of a number of parameters directly from the acquired probe transmission. The measured probe transmission is plotted as a function of time delay in Figure 6.2a, representing a typical decay plot for a contra prorogation set-up. As the lock-in output is proportional to the probe intensity, the raw data is normalised by the probe signal level to yield the transmission data, given here in decibels. This is directly proportional to the device gain. When plotted against the delay it represents the temporal evolution of the free carriers through the gain depletion and recovery. The zero delay point is artificially set to the decay minimum (described below).

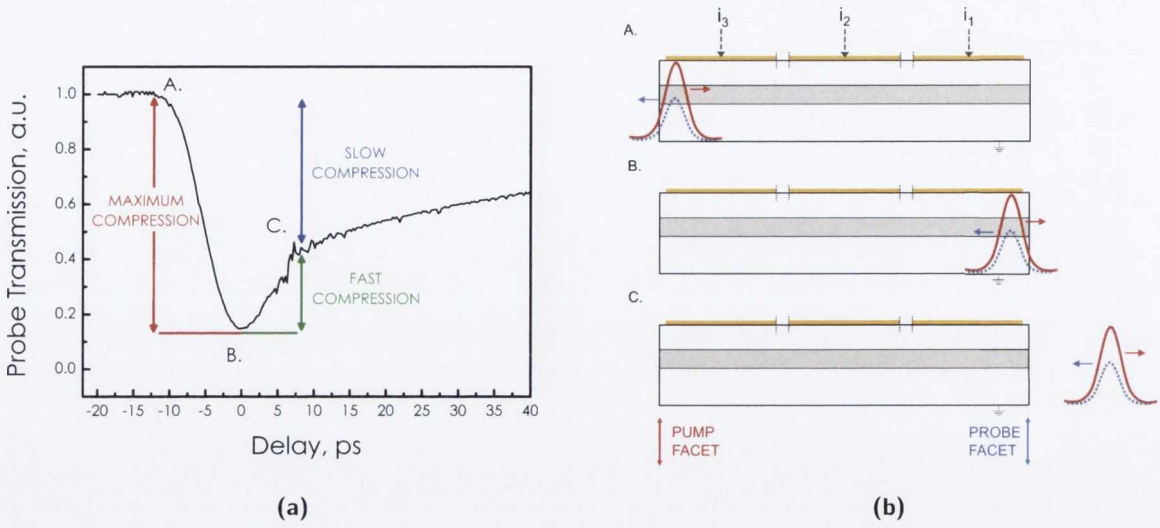

Figure 6.2: (a) Representative decay curve measured at high pump energy. Labelled are the various extracted paramaters: Maximum gain compression (red); the fast gain compression due to intraband processes (green); and the remaining slow recovery by external pumping (blue). (b) illustration of the pulse overlap at different points in the device (different delays) resulting in the various compressions.

The normalised unsaturated gain is represented by the baseline at negative delays. At this point the pump and probe overlap after the output facet (i_3), before 'A' in Figure 6.2b. In this way the probe leaves the SOA before entry of the pump and undergoes no modification. At some negative time delay the pump and probe will overlap at the pump facet, initiating the gain compression (red). This is the dominant feature at negative delay and is quantified by the Maximum Gain Compression (dB). At point 'B' the pulses overlap at the probe input facet, representing the largest effect of the pump pulse on the probe gain. Following this, point 'C' marks the overlap of the pulses after the pump has left the device. In this way all delays after this represent the gain recovery which the probe experiences. This will manifest as two distinct stages: A fast gain compression (green), a direct result of ultrafast intraband processes and a residual slow gain compression (blue), where carriers are pumped between bands by the externally applied bias. The specifics of these processes were described in chapter 2.

Timescales

The timescales over which these effects happen, and the technique of obtaining them, are described using Figure 6.3. The technique used to measure the time scales is based on the method used by Girardin, and later Occhi [2, 4]. It relies on calculating the 10-90% magnitude of the maxmum level and the decay minimum, for the relevant compression. The time delay is

then measured between these points, and is shown in the figure. It is not possible to use this technique for the interband recovery. For this, a double exponential fit is used and by convention the time constant of the secondary component is plotted [11].

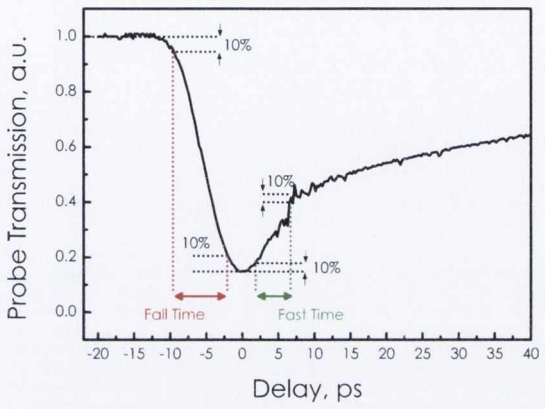

Figure 6.3: 10-90% technique for extracting time scales associated with the maximum gain compression and fast recovery.

With this in mind, the fall time associated with the maximum compression is measured between the 10-90% markers shown in red. Following this, the gain begins a fast recovery, due to a variety of intraband effects, notably carrier heating at this resolution (green). Faster effects such as spectral hole burning (SHB) or two photon absorption (TPA) also occur, however the pulse width is not short enough to resolve these. Following this, the gain is slowly restored to its unsaturated value by electrical pumping. This corresponds to the interband recovery of the device.

6.2 Noise Controlled Bias Configurations

6.2.1 Experimental Considerations

The gain dynamics are obtained for the same MCSOA characterised in the steady state in chapter 5, where the same pumping scheme and notation is used. In the first of the dynamic experiments, the current profiles previously used are repeated, assessing any difference in dynamic behaviour produced by the Low Noise, High P_{sat} and Standard profiles. These are given by 90,50,10mA, 10,50,90mA and 50,50,50mA, respectively. Injection of the pump and probe signals into the MCSOA chip is shown relative to the input (i_1) and output (i_3) facets in Figure 6.4.

The pump and probe are both polarised along the TE eigenmode of the MCSOA, and so will have experienced negligible rotation upon exiting the device [14, 15, 10]. The data will be given in terms of pump pulse energy (fJ), equal to the average power divided by the repetition rate. The average pulse energy of the probe signal after modulation is 6fJ, low enough not to perturb the state of the amplifier. The pump is varied from 24fJ - 878fJ.

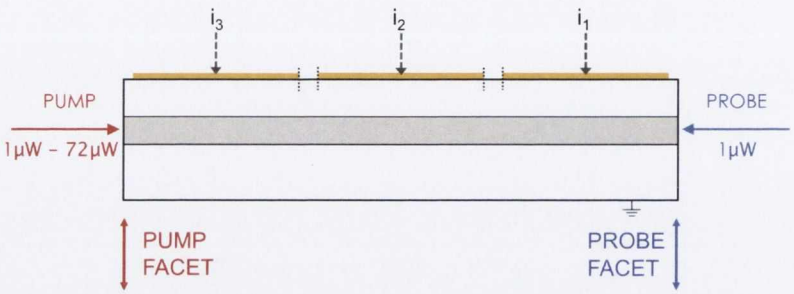

Figure 6.4: MCSOA under pump and probe injection. The probe is injected into the input side (i_1), pump is injected into the designated output (i_3). The current profiles used are the same as those from chapter 5, for a total injected current of i_{tot}=150mA: the Standard, Low NF and High P_{sat} Profiles.

6.2.2 Normalised Decays

Figure 6.5 shows the normalised probe transmission as a function of time delay, for (a) the Standard, (b) Low Noise and (c) High P_{sat} profiles, respectively. The raw lock-in response is not shown, instead the data is normalised to the unbleached gain baseline. It should be noted that the relative gain difference at negative delays matches that from the small signal gain measured in the previous chapter, attesting to good alignment of the pump-probe setup. In this case the Standard profile achieves the highest gain, with the Low NF and High P_{sat} reduced from this. Tied to this higher gain are more pronounced interference patterns at -13ps and +7ps delays, corresponding to the coupling optics, compared with the noise controlled cases. Furthering this to the noise profiles, the reflection is more evident on the side that is pumped at 90mA. It is from this data that the maximum gain compression and fall time, and the two recovery regions and their associated times are extracted. These are given in the next subsection.

6.2.3 Gain Compressions & Timescales

In a single contact SOA the carrier profile is essentially a parabola under no injection, reduced at the facets due to ASE carrier depletion. The extent of this depletion is largely related to the gain length of the structure [16]. There has been very little dynamic work undertaken where

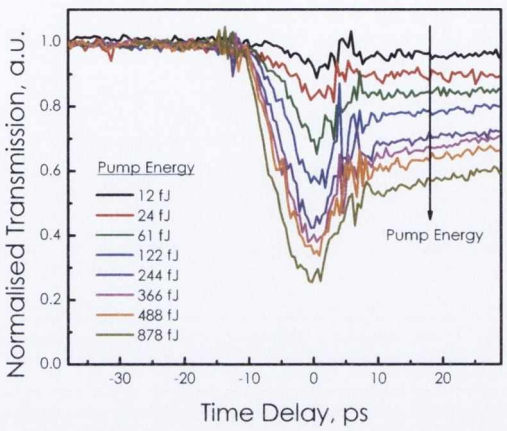

(a)

Figure 6.5: (a) Normalised probe transmission as a function of time delay, for the Standard bias combination, for a range of pump pulse energies

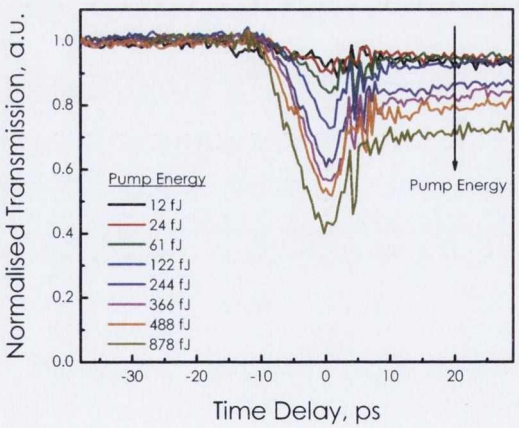

(b)

Figure 6.5: (b) Normalised probe transmission as a function of time delay, for the Low Noise bias combination, for a range of pump pulse energies.

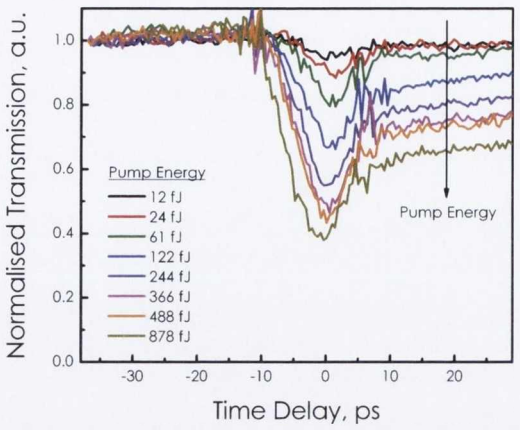

(c)

Figure 6.5: (c) Normalised probe transmission as a function of time delay, for the High P_{sat} bias combination, for a range of pump pulse energies.

the carrier density profile is artificially modified to arbitrary non-uniform configurations. Analysis must take the local carrier density into account relative to the pump and probe overlap in the structure (i.e. the delay). The purpose of this section is to determine how the compressions and time scales differ in relation to these non-uniform carrier density profiles.

Maximum Gain Compression & Fall Time

Figure 6.6 aggregates the maximum gain compressions induced as a function of pump pulse energy and corresponding fall times, for the three bias configurations.

The trend of increased gain compression as higher pump energies are injected into the MCSOA, is indicative of carrier depletion effects with higher injected powers [11]. Based on the higher continuous wave small signal gain, it is expected that the largest compression occurs for the Standard bias configuration, with a maximum value of 6.0 dB reached at a pump energy of 878 fJ. The Low Noise and High P_{sat} configurations are closer in behaviour at lower pump energy. Effects of gain bleaching relating to carrier density profile, are less evident at lower pump energies. However, as the pump energy is increased to its maximum value of 878 fJ, there is a clearer divergence of the Standard case and the noise controlled profiles. In fact, the maximum gain compression is still increasing at its maximum pump energy, whereas the High P_{sat} has levelled off, and converged with the Low Noise configuration. The smaller compressions associated with the Low Noise profile are a due to the low carrier density in the output-section for this profile. As the gain is largely set by the input section, it decreases with propagation

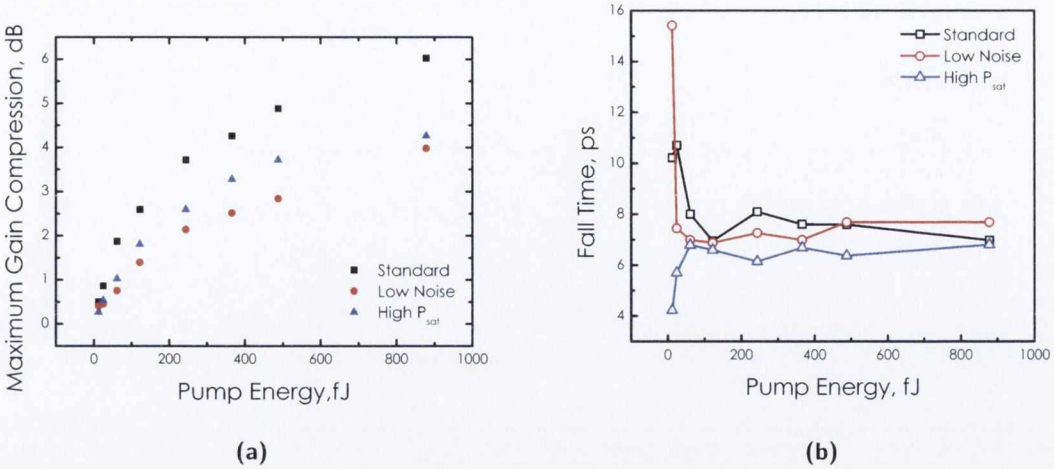

Figure 6.6: Maximum gain compression as a function of pump energy and (b) Associated fall time as a function of pump energy, for all three bias combinations.

length. The pump then has less of a bleaching effect. Contrary to this, the effect of the pump pulse on the High P_{sat} case can be explained in a similar way. In this case the gain increases with probe propagation, as the carrier density is increasing along the length of the MCSOA, and so the gain compression is higher.

In general, the fall time is limited to the transit time through the SOA at appreciable pump energies [16]. However, at low pump energies shorter fall times can be resolved as a consequence of the longitudinal carrier density, a feature unique to the MCSOA. The fall time is plotted in Figure 6.6b. The effects of the variation in applied current are seen at lower pump powers. This is likely due to the greater influence of the pump at higher energies, depleting carriers over a larger length at the input of the device. It should also be noted of this analysis at lower powers that the extraction error is larger due to system noise, including lens reflection, delay line jumps and the signal SNR. The range of fall times encompassing all three profiles at 12fJ, where the pump is only twice the energy of the probe, is 11.2ps. Remembering that the carrier profile is given with respect to the probe injection, the higher fall time of the LN configuration can be explained, relative to the other two profiles. As the pump enters the 10mA section it has little effect on the probe gain at this point, due to the reduced carrier density. In this way it takes longer for the effect of saturation to be seen. The probe has already reached its maximum gain level at this point, with the final section having little more effect in this regard. The function of this section is to reduce backward travelling ASE and so the pump has little effect on the gain saturation. As the pump pulse propagates, and the two overlap in a high gain region, the effect of the pump is greater, and it begins to saturate the total gain. In doubling the pump power

again this effect is washed out and the fall time levels off.

Taking the opposite case to this, the High P_{sat} configuration, we see an opposing trend for similar reasons. In this case the onset of compression occurs in the 90mA section, where the pump is saturating the point at which the probe is being amplified the most. In this way the fall time is at its minimum for lower pump energies of 12fJ and 24fJ before again levelling off. At higher pump energies the carrier density profile becomes less significant. The Standard profile falls in between the two, with the added feature of a higher level of ASE. This contributes to the fall time in a similar fashion to artificially setting a low carrier density at the input, as the higher ASE has depleted carriers in this region. This positional analysis can be further corroborated by a shift in the decay minima corresponding to absolute positions within the waveguide. This is described in more detail in section 6.3.

Fast Gain Compression & Recovery Time

The gain compression associated with intraband recovery and the corresponding recovery times are given in Figure 6.7.

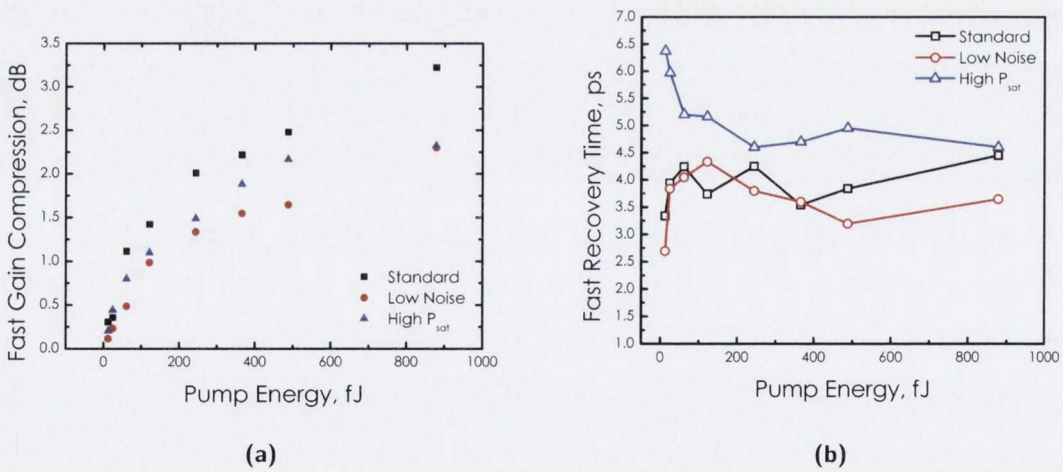

Figure 6.7: Fast gain compression as a function of pump energy, for the all bias combinations (b) Fast recovery times of intraband compression as a function of pump energy, for all three bias combinations

Again, the dominant compression occurs for the Standard profile with a quasi uniform carrier density. At high pump energy the difference is at its most extreme, with a fast compression maximum at 878fJ of 3.25dB, 1.1dB larger than the noise controlled cases. The fast gain compressions are still seen to be increasing at the highest pump energies however, whereas the other two cases have begun to level off. There is a dramatic increase in the Low Noise profile

at the highest pump energy, for an unknown reason.

The intraband recovery time is explained in a similar way as the fall times, based on the local carrier density at the pump input facet. Again, the low pump powers suggest the greatest effect of the carrier profile applied. After this, the trend is relatively flat within error, with fast recovery times between 4 & 5ps, corresponding to the low level of fast compression acquired. As a component of the total recovery time, the largest possible fast gain compression is desired for applications in optical processing [1, 17, 18, 19].

Slow Gain Compression & Recovery Time

The final stage of gain recovery to its baseline value is given by the slow gain compressions and its associated time constant, given by Figure 6.8.

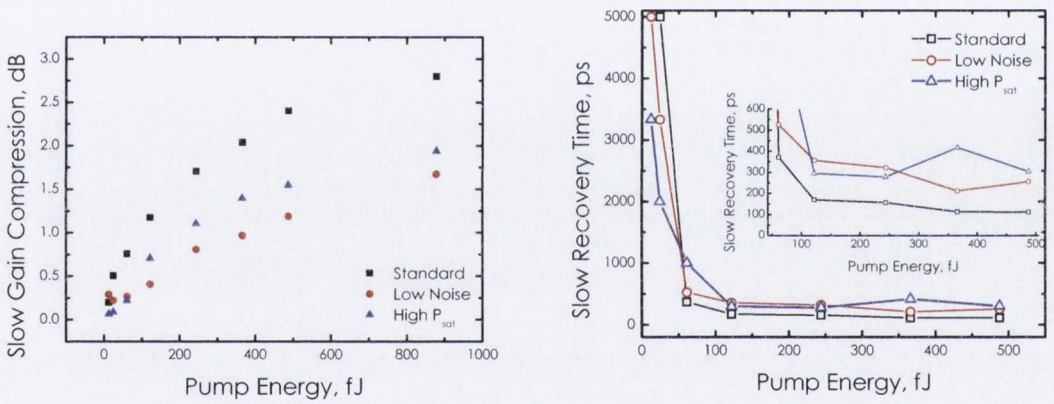

(a) **(b)**

Figure 6.8: (a) Slow gain compression as a function of pump energy, for the all bias combinations. (b) Slow recovery times of interband compressions due to electrical pumping as a function of pump energy, for all bias combinations

The slow gain compressions continue the trend associated with increasing the pump energy, as the free carrier density is reduced due to increasing stimulated emission. Typically, as the level of total compression is increased, the slow compression increases in turn. The maximum slow gain compression is reached for the Standard profile, with a value of 2.8dB. The noise controlled profiles never increase beyond 2dB, with maxima at 1.9dB and 1.7dB for the High P_{sat} and Low NF, respectively. The time constant plotted in Figure 6.8 (b) illustrates an important characteristic of the noise control technique. Due to the reduced level of ASE for the noise controlled profiles, the interband time constant is larger. Above pump energies of 100fJ, the

Standard profile is over 100ps quicker, relating to the excess ASE. ASE is a dominant contributor to the speed of the gain recovery, acting in a similar way to a holding beam [20, 21] reducing the equilibrium carrier density to which the device must recover and thus reducing the time constant of this recovery [16]. In the MCSOA, the overall level of ASE produced is lessened for both the Low NF and High P_{sat} carrier profiles.

6.2.4 Discussion

In the experimental pump probe work on SOAs to date, the component has comprised of a single contact, and not assessed the dynamics for a non-uniformly applied current profile. In some publications, an additional signal has been implemented when investigating optical speed up at transparency [20], or in some cases non-degenerate beams are injected to probe different parts of the gain spectrum [7]. However, to this point there has been only one simulation based paper performed on non-uniform current injection gain dynamics by the same technique [18]. In their work, the device has two electrodes, where the Cross Gain Modulation (XGM) on a CW probe is examined when the total carrier density is allowed to vary. The significant difference with this work is the choice of beam propagation modelled. A collinear XGM configuration is used, where the probe beam is non-degenerate. Those results predict a slight suppression of the slow compression for particular current densities to the output. However, this work is done at much lower resolution (~10ps) and at a non-constant injected current density. The overall performance is more closely linked with the next section of this chapter.

The effect of the non-uniform carrier density of the Noise Controlled profiles from an application point of view, is that at appreciable pump powers there is little sacrifice in the dynamic performance for the reduced noise or increased saturation behaviour, with the exception of the slow recovery. As this is the ultimate limiting factor, the sacrifice in recovery time shown relative to the Standard profile may impact on performance. In an addition, from an optically functional point of view the noise controlled profiles produce a slight reduction in gain compression, and so extinction ratio. In the next two sections, it will be shown, that by working at a variable injection current, and effectively treating the multi-contact SOA as either an Absorber-SOA combination (section 6.3) or the reverse of this (section 6.4) the gain recovery can be improved significantly.

6.3 Variation of Probe Facet Bias

6.3.1 Experimental Considerations

In the previous section the total current density was held constant at i_{tot}=150mA, much like the continuous wave characterisation. The pump-probe decays given below are for the non-limited i_{tot} configurations of i_2=i_3=50mA where i_1=0-90mA (0-90, 50, 50mA) and in section 6.4 the reverse of this, where i_1=i_2=50mA, and i_3 = 0-90mA (50, 50, 0-90mA). In this way the facet sections pass from absorption through transparency to gain. This bias arrangement is illustrated in Figure 6.9 with the pump and probe entry shown for clarity. The probe pulse energy in this case is 61fJ, 5 times higher than in the previous data, to reduce the level of noise. The average pump pulse energy is varied from 61 - 1220fJ.

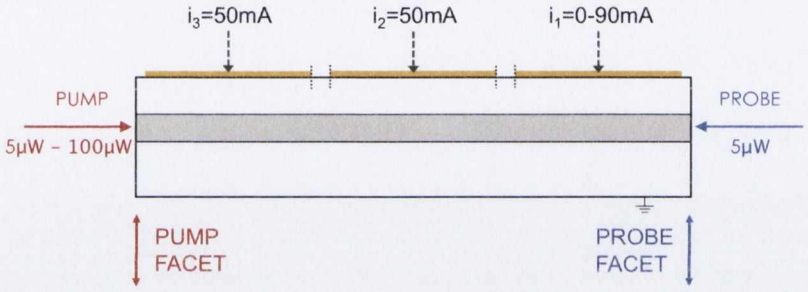

Figure 6.9: Bias configuration for the facet dependent gain dynamics acquisition. The middle and output contacts are held constant at i_2=i_3=50mA. The input (probe) facet is varied from 0 - 90mA.

6.3.2 Normalised Decays

The as-measured probe signal response given by the lock-in amplifier, after detection at the photodiode, is given by Figure 6.10. This data is plotted for both a minimum pump pulse energy of 61fJ and a pump energy 8 times this of 488fJ, respectively. The importance of the measured probe transmission decays is to provide context for the relative compressions and time scales extracted from the normalised data over the course of this section. From an optical processing point of view, the fundamental limiting factor is the slow recovery of the device[22, 13]. Where this is reduced with a large intraband component and subsequent ultrafast recovery, it is important to consult the raw data to ascertain the relative level of gain achieved.

The plots also illustrate well the impact of a high energy pump pulse with respect to carrier depletion in the SOA, where the unsaturated gain is bleached to a much greater degree than

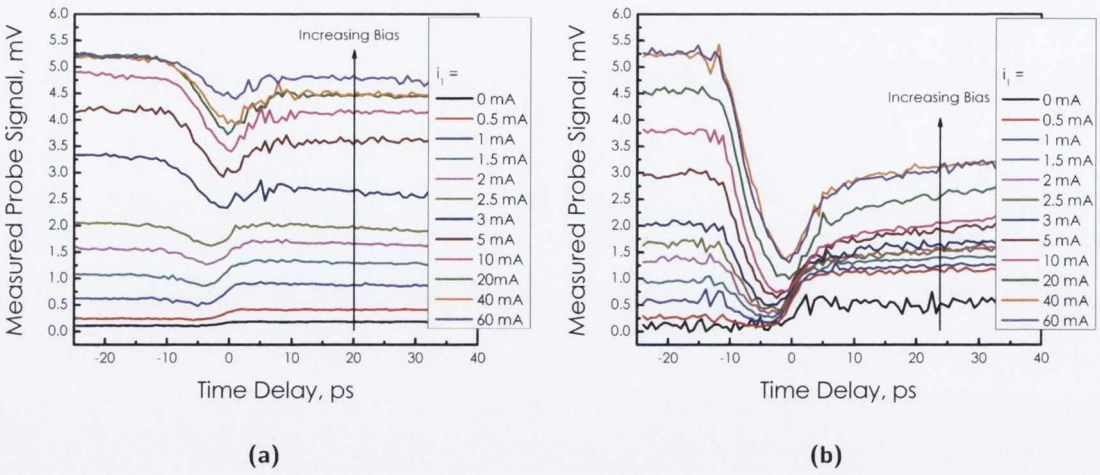

Figure 6.10: Measured probe signal response as a function of time delay for a variety of applied input contact current (i_1) for a pump energy of (a) a 61fJ and (b) a 488fJ.

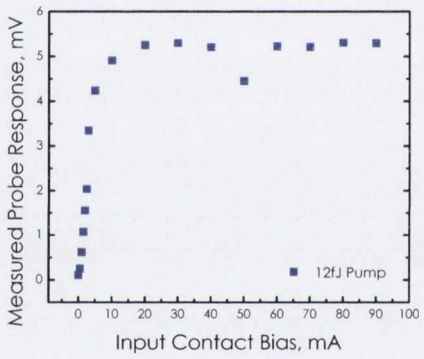

Figure 6.11: Unsaturated probe signal, measured at the lock-in as a function of time delay, for a 12fJ pump energy.

the low pump energy case. In addition, the increased pump energy leads to a greater level of absorption at low probe-facet biases. The specific features of these decays are detailed based on the normalised data. The raw unsaturated gain levels are plotted as a function of the applied input bias current in Figure 6.11, following a typical gain versus bias curve. Finally, the time delay is set to 0ps at the point at which the gain compression minimum occurs at a bias of i_1=40mA. This constitutes an i_1=40mA value below 140mA (minimising any temperature related effects), whilst corresponding to a regular decay curve, with no additional features.

Normalised Data

The raw decays are normalised to their respective unsaturated gain, highlighting the relative difference in the effects induced by the pump pulse. Representative plots are shown in Figure 6.12

for two pump powers. The data is split into two distinct regimes: in Figure 6.12 (a) and (c) very low input facet currents are applied, corresponding to the absorption regime; Figure 6.12 (b) and (d) represent currents above transparency where gain is the dominant factor, and a more typical evolution of the gain decay and recovery is witnessed, as per section 6.2. For this latter reason, the extracted parameters will be concentrated at lower applied bias, however, sample points above transparency will be described to provide context.

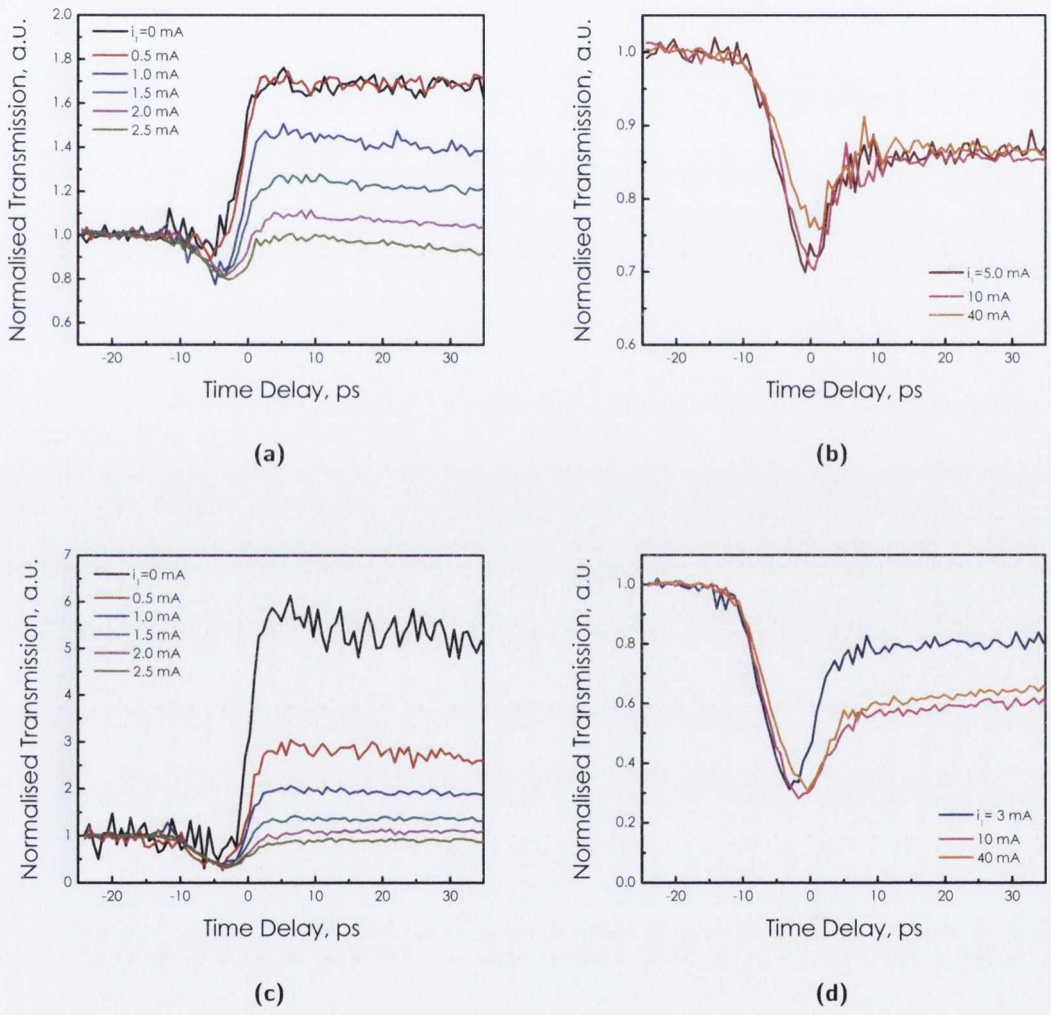

Figure 6.12: Normalised probe transmission for a 61 fJ pump pulse energy for (a) an input-probe-facet bias of i_1=0-2.5 mA (below transparency), and (b) an input-probe-facet bias of i_1=5, 10, 40 mA (above transparency), where i_2=i_3=50 mA in all cases. Normalised probe transmission for a 488 fJ pump pulse energy for (c) an input-probe-facet bias of i_1=0-2.5 mA (below transparency), and (d) an input-probe-facet bias of i_1=3.0, 10, 40 mA (above transparency), where i_2 = i_3=50 mA in all cases.

Looking first at the low bias regime of Figure 6.12 (a) & (c), higher pump pulse energy provides

pronounced evidence of bias dependent carrier absorption. Note the difference y-axis scale for both cases. To explain the specific behaviour above and below transparency, recall Figure 6.2, which relates the time delay to the individual transients. The onset of compression occurs at negative delay, where the pump and probe pulses first overlap in the device, at the output (pump) facet. As the input section is in the absorption regime, the gain compression which occurs when the pulses first overlap at the output, affects the small gain imparted to the residual probe that is transmitted through the first section plus any ASE travelling towards the output. As a consequence of this, the compression minimum corresponds to the effective gain length, or in other words the middle and output section length, approximately 500μm. In the gain region, the fall time corresponds with the transit time through the entire device. In this way then, the fall time (to the compression minimum) is reduced to the shorter values corresponding to a shorter device. This is followed by a rapid increase in the probe gain as a direct result of the pump beam optically promoting free carriers to the conduction band. The probe pulse then experiences gain at the point at which the pump and probe overlap in the input section. The gain the probe experiences at the higher pump energy is significantly higher than for the low pump case. Upon reaching this maximum value, the probe response then begins to relax back to the unsaturated level. Much like the slow recovery in previous decays this is not fully accessible by the delay length used.

As the bias in the probe input section is increased, the effect of the pump in this region is reduced, seen most clearly in Figure 6.12 (c). In fact, this transition brings about an interesting situation where the recovery of the device is almost entirely dominated by intraband processes, notably at this resolution is carrier heating [23, 12, 24]. This absence of interband compression (slow recovery) opens up the possibility of fast optical processing [25]. However to elaborate on this further at present the unsaturated gain levels from Figure 6.10 must be consulted. When these data are accounted for, it is clear that the gain is substantially lower than the case at higher input contact current. This could be remedied by improving the gain (by media, pumping or length) of the output sections and thus using the input section around transparency to benefit from this speed up of recovery and suppression of slow compression. The input section would then act as a recovery controller. This would prove vastly simpler in implementation that many other methods which investigate the dynamics of optical speed up of the gain at transparency. Previously, holding beams have been shown to significantly improve the complete recovery of the device, in much the same was as increased ASE does. Tailli et al. have furthered this by injecting near the transparency wavelength, minimising the effect on the peak gain region. However, it is difficult to implement this in practice as the transparency point changes along

the length of the device, under different conditions [26]. The Turbo-Switch, proposed and demonstrated by Manning et al. [27, 28, 7], offers very promising results, however requires the added complexity of two similar SOAs in series, separated by a filter. The advantage of this technique is a compression and recovery occurring within 20ps, without degrading the SNR. This will be discussed further in a later section.

As i_1 is further increased, where all three sections are operating in the gain region, the trend reverts to a typical decay, with a fall time that represents the full physical length of the device, followed by a two stage (resolvable) recovery process. As these data present little new information over what was given in Section 6.2, they will not be presented in full. Furthermore, above i_1=50mA, i_{tot} >150mA and so problems associated with increased device temperature, as previously observed, begin to affect the data.

Figure 6.13 plots the time delay at which maximum compression occurs as a function of bias at a pump pulse energy of 1220 fJ. In this case only, the zero delay point has been changed to the onset of gain compression. The effect of the pump on the gain compression minima can then be mapped specifically onto the delays which correspond to the transit time through the gain sections. This does not represent the fall time, which is calculated using the 10-90% method. Figure 6.13 illustrates the movement of the decay minima and does not equate exactly to the Fall Time but is linked to it. The fall time is presented at the end of this section.

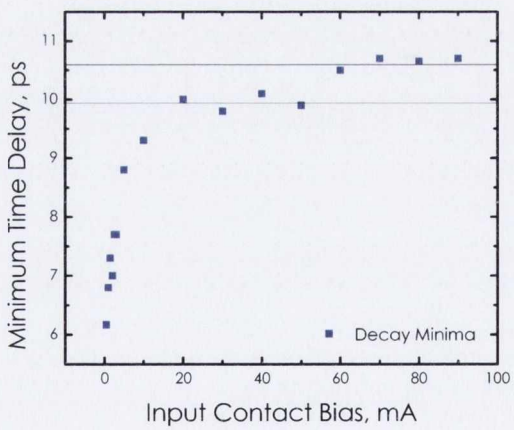

Figure 6.13: Time delay of maximum compression point as a function of input bias contact (i_1). (this data was taken with zero set artificially at the onset of compression, and does not replicate the true fall time extracted using the 10-90% method. It is to show the shift in decay minima).

Figure 6.13 can be explained as follows. Beginning at i_1=0.0mA, the probe is mostly absorbed in this section. The remnant of this transmitted to the final two sections is amplified as normal,

corresponding to the compression induced by the pump at negative delays. However, the pump usually induces its maximum effect (minimum compression) at the probe input constituting a fall time related to the full transit time. This is not the case here. The bias effect on the gain compression in this scenario can be mapped specifically onto the delays corresponding to the maximum compression delay time. At very low biases the gain compression, occurs over the final two sections, however upon reaching the input section, which does not provide gain, the pump induces the maximum absorption. The pump essentially compresses the gain of an effective length of the MCSOA. The initial section then partially accounts for the dramatic increase in probe response. As the bias to this contact is increased beyond i_1=10mA this behaviour begins to change and approaches that of a traditional SOA where the fall time corresponds to a compression induced along the entire gain length. This is evident in the movement in decay minima as a function of i_1 current, where at low biases the pump effect on saturation is reduced to an effective length, and at higher values corresponds to the full transit time. This effect is shown more quantitatively through the extracted compressions and timescales given in the next section. Finally, the increase to a higher plateau above 60mA is likely brought about by the temperature dependent effects discussed in Chapter 5 which occur above i_{tot}=150mA.

6.3.3 Gain Compressions & Timescales

Compressions

The extracted gain compressions are now given as both a function of pump energy and input section bias (i_1).Figure 6.14 quantifies the first feature at low bias of the previous decays. Where the injected input contact bias is below 2.5mA, the decays produce regions of high induced gain on the probe pulse. This is a result of the pump beam compensating for the lack of sufficient electrical pumping to achieve population inversion. The dominant effect here is stimulated absorption. The maximum level of gain achieved by the probe is quantified by the Maximum Absorption given in decibels relative to the unsaturated level to which the data is normalised. As can be seen in Figure 6.14 (a) the increase in probe gain relative to the unsaturated level is substantial, particularly at higher pump energies, where a greater number of carriers are optically promoted to the conduction band. The effect is clearly more dominant at lower biases where the competition by the electrically induced intraband process is weak. At i_1=0.0mA, the maximum value measured is 7.4dB above the unsaturated level at 488fJ. When the bias is increased by 0.5mA, the Max absorption decreases to 4.9dB at the same pump power.

As the bias is increased it compensates for this optical effect, which now begins to dominate the maximum gain bleaching. Indeed as the bias is increased further there is no overshoot of the gain upon recovery due to the absence of excess carriers. After this point, the normal processes dominate. This latter effect is exemplified by the data in Figure 6.14 (b) where the maximum absorption decreases and converge towards transparency at 0dB (the baseline). If this graph were to plot the data at higher biases those values would be representative of the slow gain recovery.

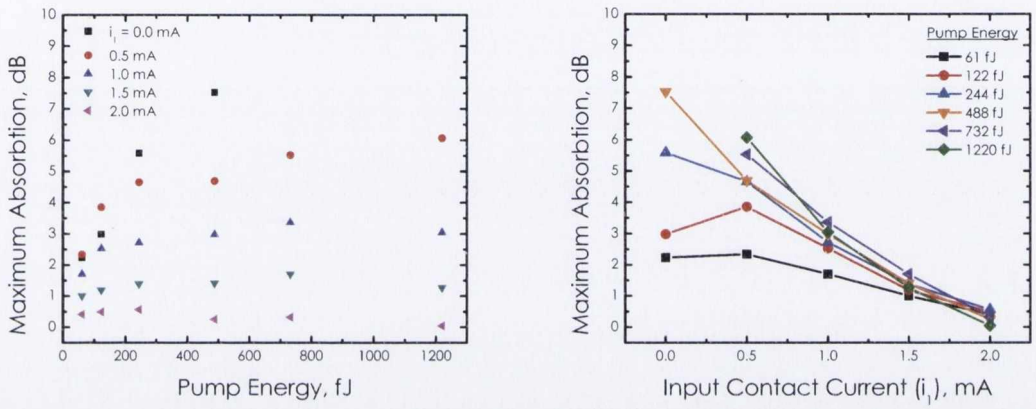

(a) **(b)**

Figure 6.14: Maximum absorption reached as a function of (a) pump pulse energy, for a variation in i_1 from 0-90mA, and (b) the input (probe) contact from 0-90mA, for pump energies of 61, 122, 244, 488 & 1220 fJ.

In Figure 6.15 the maximum induced compressions are plotted versus increasing pump energy for a range of injected biases (a) and as a function of i_1 current for a range of pump powers (b). For biases above the transparency point (inset) the compressions increase steadily in a similar trend seen in section 6.2, indicative of carrier depletion by the pump pulse. The maximum values reached occur for the highest energy pump as predicted, with 7.1dB for 10,50,50mA. At lower injected currents, the compressions increase steadily to slightly lower value. It is important to note, that the maximum compression is given relative to the normalised baseline. Therefore the gain compression might be of the same relative strength, but the total gain much lower. Also at very low bias values, the unsaturated gain level is low enough that it adds a degree of difficulty in extracting the parameters accurately. The 10-90% extraction technique employed for all parameters aids in acquiring consistent data, however the error is larger in these low bias conditions. For switching purposes a large gain compression is required.

Looking at the maximum compression with respect to the input contact current (b), the trend is clear across all powers. There is a sharp increase in maximum compression with bias, where the maximum is reached in each case between 10 & 20mA.

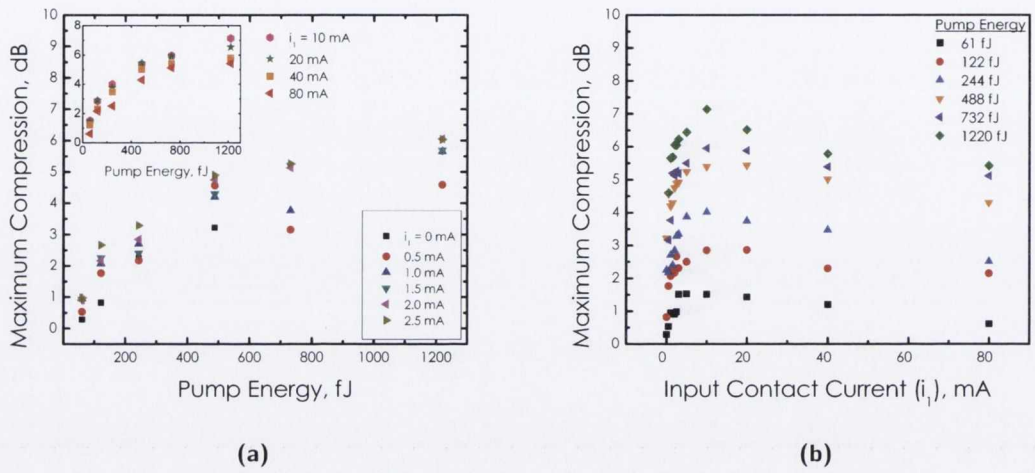

Figure 6.15: The extracted Maximum compression as a function (a) of pump pulse energy, for a variation in i_1 from 0-90mA, and, (b) of the input (probe) contact from 0-80mA, for pump energies of 61, 122, 244, 488 & 1220 fJ. Inset: Maximum compressions for four currents above transparency (10, 20, 40, 80 mA).

The residual slow compression due to electrical pumping is plotted in Figure 6.16 as a function of pump pulse energy (a) and input contact bias (b). Due to the transition between negative and positive gain in the input sections the slow recovery is only present for bias currents of 2.5mA and greater. As expected the contribution of interband recovery increases as a function of pump pulse energy, as seen in (a), however the values reached are not very high. Of particular note in (a) is the reduction, even at higher pump powers, for i_1=2.5 & 3.0mA.

In addition the maximum extent to which the slow recovery dominates is dependent on the injected bias, reaching its maximum values for the highest injected current of 10mA. The reason the maximum level is not seen at 20, 40 or 80mA current, is related to the total injected bias, i_{tot}. As was seen in chapter 5 that above i_{tot}=150mA, the gain begins to reduce with the increased effect of non-radiative transitions. The result is a slow compression at 1220 fJ pump pulse energy 0.5dB lower than the 10mA case maximum of 3.4dB.

The data presented in Figure 6.16 (b) shows the steep increase in the relative magnitude of the slow recovery as the bias is increased in the front contact. As can be seen, the effect of the slow recovery can be reduced, which is desirable for applications in optical processing. The maximum slow compression occurs for i_1=10mA, with the maximum value of 3.3 dB occurring

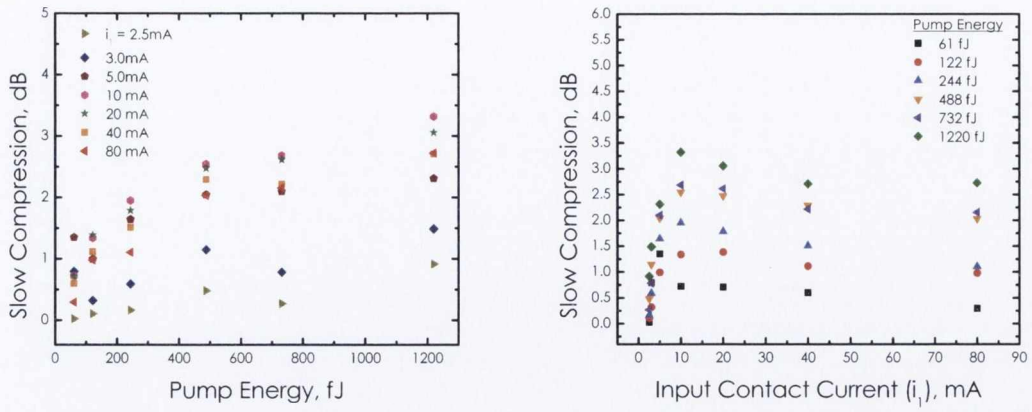

(a) **(b)**

Figure 6.16: Slow compressions as a function of (a) pump pulse energy, for a variation in i_{tot} from 0-90mA, and (b) as a function of the input (probe) contact from 0-90mA, for pump energies of 61, 122, 244, 488 & 1220 fJ.

with a pump pulse energy of 1220 fJ, and a minimum of 0.1dB for the probe matching pump pulse energy of 61fJ. It is this property, the ability of the input section to suppress the slow compressions, which yields the most interesting results regarding optical switching.

The gain compression due to intraband depletion is given by the fast gain compressions in Figure 6.17, again, as a function of pump pulse energy (a) and applied input contact current (b). The trend as a function of pump energy (a) is as expected from section 6.2, with an increase in the depletion of carriers within the band as pump energy in increased. This levels off at higher powers. However, also evident from this plot is the importance of bias especially from an optical switching point of view. The highest compressions achieved of 5dB from 732−1220 fJ pump energies occur for i_1=2.5mA, corresponding to the only recovery mechanism. The intraband gain compression is only extractable after the point at which the input section is not optically pumped by the pump pulse, and are plotted from 2.5−80mA. For an ideal optical switch the switched pulse would undergo a large compression, followed by an equally large fast component, where the residual slow compression would be as reduced as possible. As was shown in the decay plot of Figure 6.12, the MCSOA can create these conditions, by varying the bias around the transparency point of the input section, thus reducing the slow component. The larger values at 2.5mA are a result of this effect. The trade off is a reduced gain. In Figure 6.17 (b) the effect of the bias is shown more explicitly, with a rapid reduction in the fast gain compression as a function of the applied bias illustrating this point. The largest fast compression values occur at low biases, after which it begins to decrease as the interband compressions dominate.

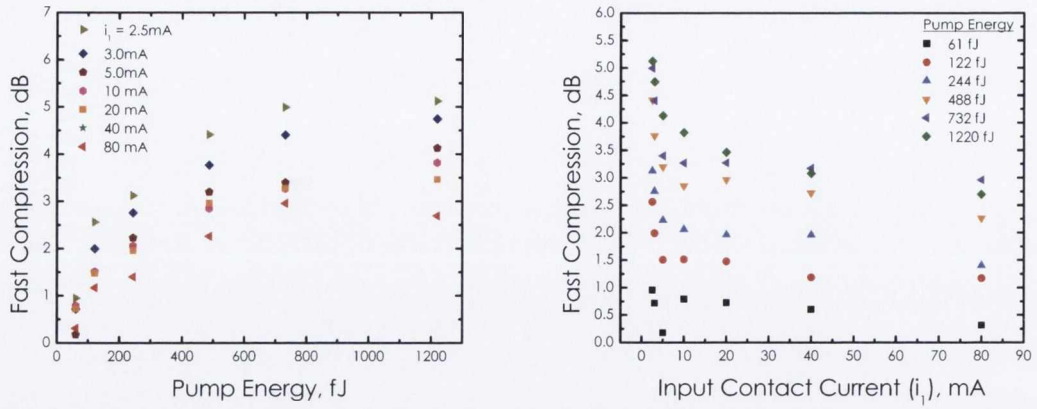

(a) **(b)**

Figure 6.17: Fast compressions as a function of (a) pump pulse energy, for a variation in i_1 = from 2.5−90mA, and (b) input (probe) contact from 0-90mA, for pump energies of 61, 122, 244, 488, 732 & 1220 fJ.

Timescales

The associated timescales of the above features are now given. They were extracted using the same 10-90% technique of the previous section. The fall time is presented in Figure 6.18 (a) as a function of pump pulse energy and in Figure 6.18 (b) as a function of input contact current.

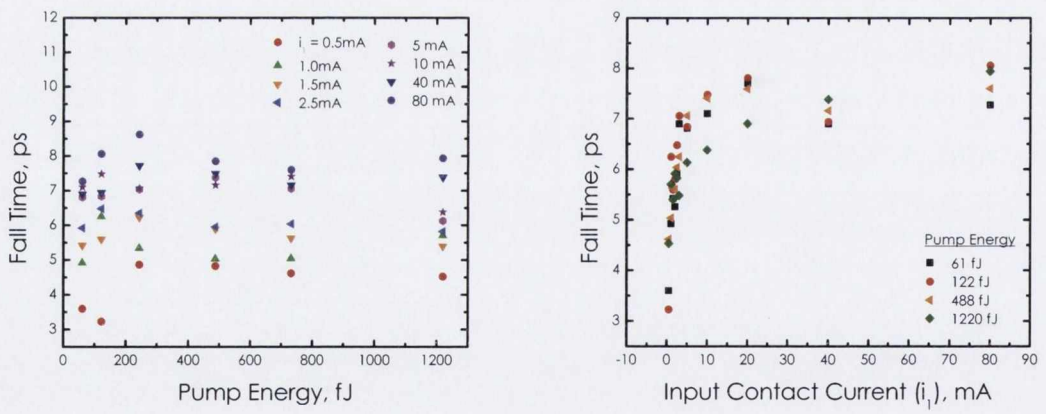

(a) **(b)**

Figure 6.18: Fall time as (a) a function of pump pulse energy, for a variation in i_1 from 0-90mA, and (b) function of the input (probe) contact from 0-90mA, for pump energies of 61, 122, 488 & 1220 fJ.

The strongest manifestation of the multi-contact nature of the device dynamics is an artificial

change in the effective gain length of the device, experienced by the probe as the bias is varied. This was shown above through the change in time delay of the compression minima, but is shown more accurately in terms of the fall time here. Looking at Figure 6.18 (a) for pump powers above 244fJ the fall times are reasonably level. Taking i_1=0.5mA as a starting point, it reaches an average value of $\sim$ 5ps, corresponding to the transit time of two sections. Comparing this to the higher i_1 bias (which have all levelled off in roughly the same region) to a fall time of 7.5ps, corresponding to the transit time through all three sections. This corresponds well with the effective lengthening of the device discussed. It can be seen however that this is not a sudden change, but a gradual one. As the bias is increased, and the input section gradually begins to impart gain, the fall time increases too.

The effect of increasing the bias from i_1=0−10mA illustrates this well and is shown in Figure 6.18 (b) for two low and two high pump powers. Taking the low pump energies (blue and red in figure) a very rapid increase in the fall time is witnessed. At lower current values the fall time increases from its minimum corresponding directly to the length of the final two sections, and transitioning towards the constant value of 7.5ps.

The fast recovery time is plotted in Figure 6.19, for biases above transparency, i.e. where a slow recovery component also exists.

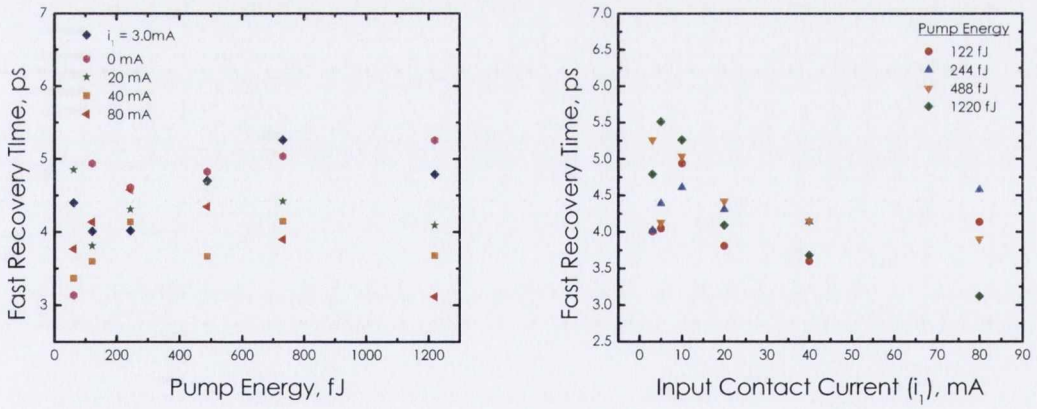

Figure 6.19: Fast recovery as a function of (a) pump pulse energy, for a variation in i_1 from 3-90mA and (b) the input (probe) contact current from 0-90mA, for pump energies of 122, 244, 488 & 1220 fJ.

The fast times increase slightly with pump power for the bias sample shown. Values are within a very close range of less than 1.5ps at lower pump powers, which extends to a 2.7ps range at 1220fJ pump pulse energy. The fast recovery in this case does not vary with bias in the same

way as the interband processes. The timescales observed here are almost exclusively related to carrier cooling effects within the band, as the ultra fast processes taking place such as TPA and SHB (which are intensity dependent) are not resolvable. The main contribution of the bias in this case of course, as was seen in the compression data above, is to increase the magnitude of the slow gain compression. However, as was seen in the decays themselves, the input section can be used as a control of this, where around transparency, the recovery is dominated by fast processes only. These data are given below in Figure 6.20, and labelled Rise Time.

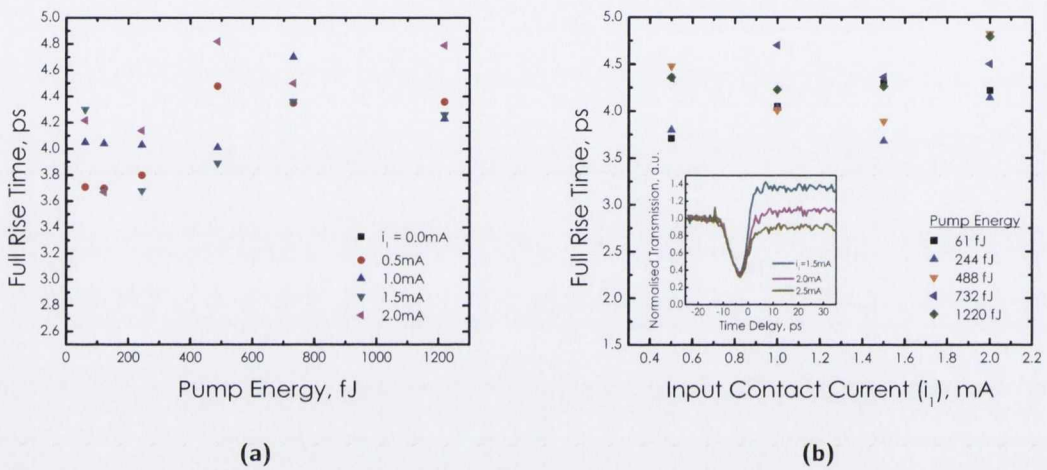

Figure 6.20: (Full rise time as a function of (a) pump pulse energy, for a variation in i_1 from 0-2mA and (b) Maximum gain compressions as a function of the input (probe) contact from 0-2mA, for pump energies of 61, 122, 244, 488, 732 & 1220 fJ. Inset: Decay curves for i_1=1.5, 2.0, 2.5mA, showing the reduction in slow gain compression.

As can be seen in the figure, again the rise time itself has little dependence on the bias or pump power. The unique cases here are for i_1=1.5, 2.0 & 2.5mA, where there is no overshoot, and negligible slow compression (decays are shown inset). A value of i_1=2.0mA acts as the optimum level of pumping to achieve a compression followed by a fast recovery. However, as is shown by Manning [27], a small gain overshoot can be effective in reducing patterning effects, by compensation of the gain.

6.3.4 Discussion

The MCSOA gain dynamics present a seemingly similar performance to that achieved by the Turbo-Switch [27], but with a single SOA. Manning *et al.* have demonstrated excellent gain compression and recovery, with the total process occurring in under 20ps. As described, the concept requires a pair of similar SOAs and a broadband filter. As shown, a single MCSOA may potentially be used functionally, by modifying the input bias to accommodate the suppression of the slow recovery, the ultimate limitation on speedy performance, and so achieving quicker speeds than the Turbo-Switch.

For the situation where the input contact is held at i_1=2.0mA, there is a complete suppression of the interband recovery component. This leads to a compression and complete fast recovery back to the baseline of ~11ps (the fall time + the rise time). However, this comes at a cost to the total gain, but could be a comprise worth making for application. As it stands this represents preliminary work, requiring further study. It is not yet understood if this is a realistic opportunity for very fast processing in a bulk SOA, as for comparison, the Turbo-Switch operates with no degradation of the SNR, and is operated under high gain in both SOAs. Future work in this regard will require a complimentary systems-based approach, examining high data rate wavelength conversion for instance. The effect of varying the output facet, which should result in higher levels of gain, are explored in the next section, to examine if similar suppression of the interband compression can occur.

6.4 Variation of Pump Facet Bias

This section assesses the gain dynamics as the output (pump) facet is varied from i_3=0-90mA, when i_1=i_2=50mA. As this arrangement results in slightly different decay features these will be discussed. The carrier dynamics for the cases of appreciable i_3 current are not given as they do not deviate from previous data. Instead, only the low bias properties are probed. The measured probe transmission, measured at the lock-in, is given in Figure 6.21, for a selection of bias values at (a) a low pump energy of 61fJ and (b) a high pump energy of 488fJ.

The raw decays of this figure illustrate the change in baseline gain associated with the increase in i_{tot}, as well as the significant effect of varying the output contact compared with the input contact of the previous section. This presents a different situation to the raw decays of section 6.3 where the probe facet was varied. The higher unsaturated level is related to the increased

output power resulting from the same level of gain, but imparted to a higher probe power. In the previous case, the gain achieved by the probe at low biases was attributed to the very low remnant signal that was transmitted through section one. The gain in this case was the same, but the amplified probe power (measured voltage) was lower. In this experiment, as it is the pump contact that is varied, the entire probe signal is immediately amplified, reaching high powers by the time it arrives at the final section. As the bias to this section is kept low, and the level of stimulated absorption of the pump therefore high, the signal increases rapidly to levels much higher than previously attained. Once the final section is above transparency, the decays settle to their usual form, and the same unsaturated levels as before, as expected. Figure 6.22 below plots the normalised decays, at a low and high pump power, for a selection of bias currents. These normalised plots are used to explain and extract the pertinent parameters, as before.

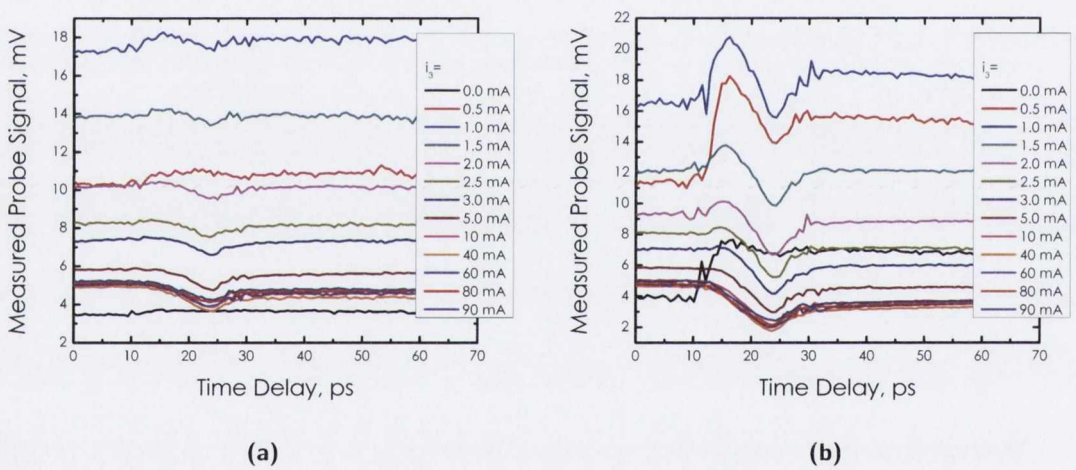

Figure 6.21: Measured probe signal response as a function of time delay for a variety of applied output contact currents (i_3) for a pump energy of (a) 61fJ and (b) 488fJ.

As mentioned the variation of the pump facet bias compared with the probe facet bias, yields different decay features at low biases. At higher current normal decays ensue and will not be restated. Looking at 6.22c, under low bias conditions a number of features are present. The pump and probe first overlap at the output of the device, meaning that at low biases (below transparency) the high energy pump pulse, optically promotes carriers to the CB, defined by the Maximum Absorption (dB). Upon passing this point, the gain seen by the probe proceeds as normal, and is compressed by the pump. This is followed by the usual fast recovery, and a slow decay to the original unsaturated level.

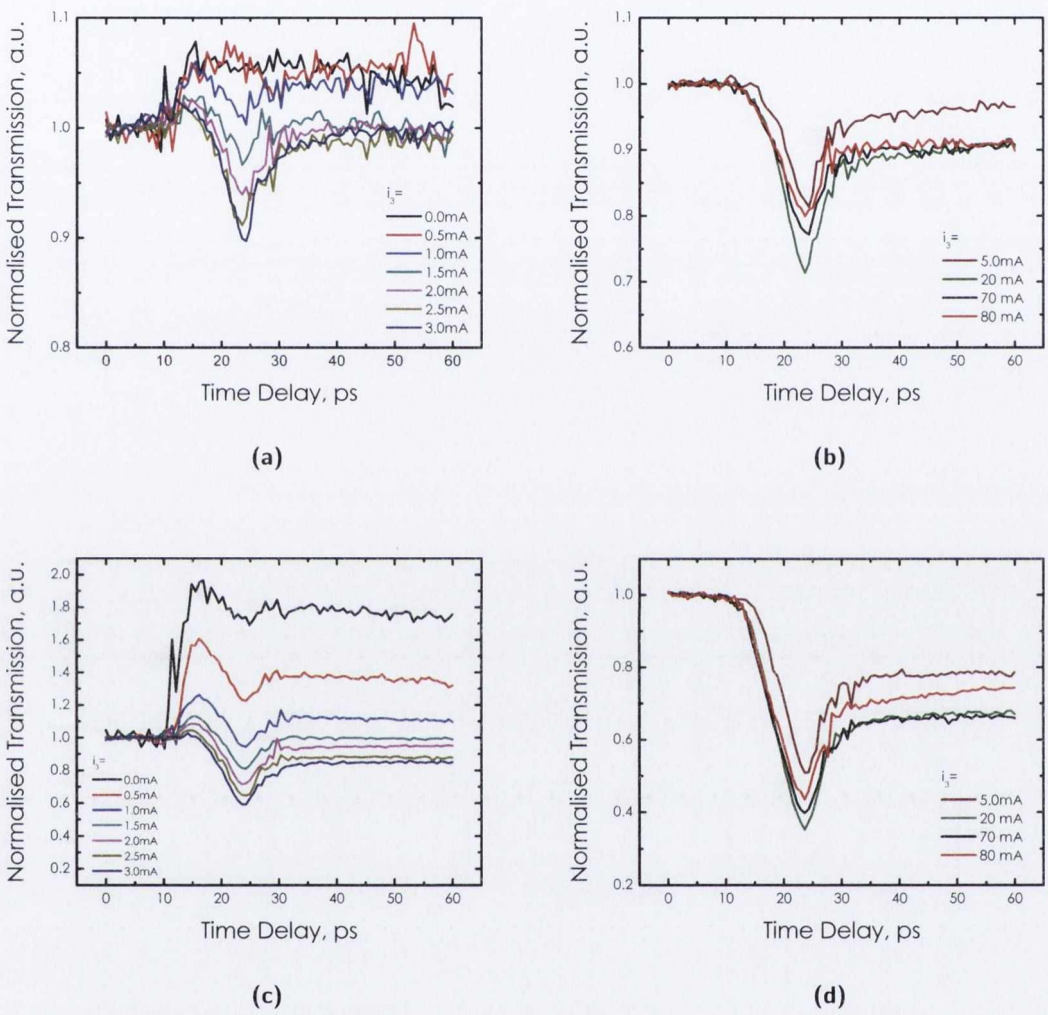

Figure 6.22: Normalised probe transmission for a 61 fJ pump pulse energy for (a) an output facet bias of i_3=0-3.0mA (below transparency), and (b) an output facet bias of i_3=5, 20, 70, 80mA (above transparency), where i_1=i_2=50mA in all cases. Normalised probe transmission for a 488 fJ pump pulse energy for (c) an output facet bias of i_3=0-3.0mA, and (d) an output facet bias of i_3=5, 20, 70, 80mA (above transparency), where i_1=i_2=50mA in all cases.

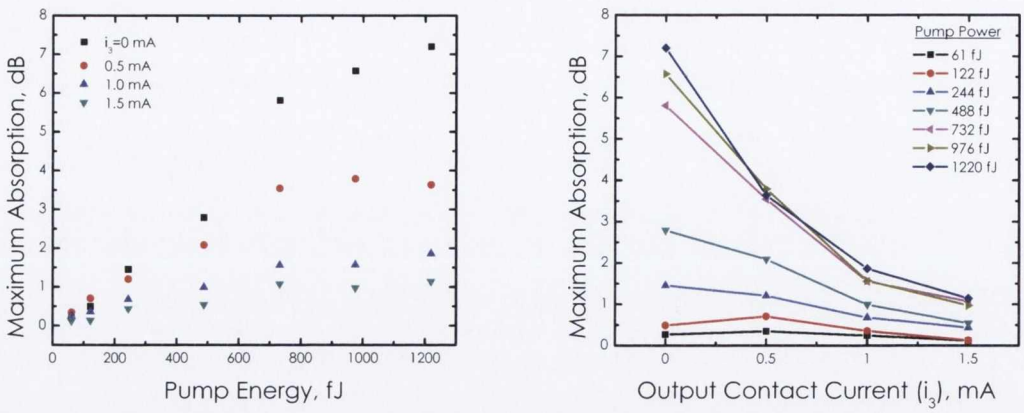

Figure 6.23: Maximum absorption reached as a function of (a) pump pulse energy, for a variation in i_3 from 0-1.5mA, and (b) output (pump) contact from 0-1.5 mA, for pump energies of 61, 122, 244, 488, 732, 976 & 1220 fJ.

6.4.1 Gain Compressions & Timescales

The more interesting compressions are plotted below, beginning with the Maximum Absorption in Figure 6.23, which occurs at low applied currents.

The Maximum Absorption increases rapidly as a function of pump energy at reduced i_3 values. This effect decreases as the conduction band is filled through electrical pumping at higher biases (approaching transparency). The maximum value reached when zero bias is applied to the output section, is increased over the baseline by over 7dB at 1220fJ pump energy. As the bias reaches higher values it begins to level off at 732fJ, as lower pump energies are required to completely fill the CB. The magnitude of absorption above i_3=1.5mA is not given as the effect approaches 0dB. In Figure 6.23 (b), the relative magnitude of the absorption is given as a function of pump current (i_3). This illustrates clearly the rapid decrease with applied bias of the level of absorption by the output section, as expected. At low pump energies between 1 and 5 times the probe power, the Maximum Absorption is low converging to values less than 1dB at 1.5mA. After this maximum gain is reached, it undergoes saturation by the pump of the gain already achieved by the probe to this point. To quantify the compression relative to this maximum point, the Total Compression is used. This is plotted in Figure 6.24.

The total gain compression corresponds to the peak absorption value from the unsaturated level to the minimum value, relative to the saturation level. If the total compression can be

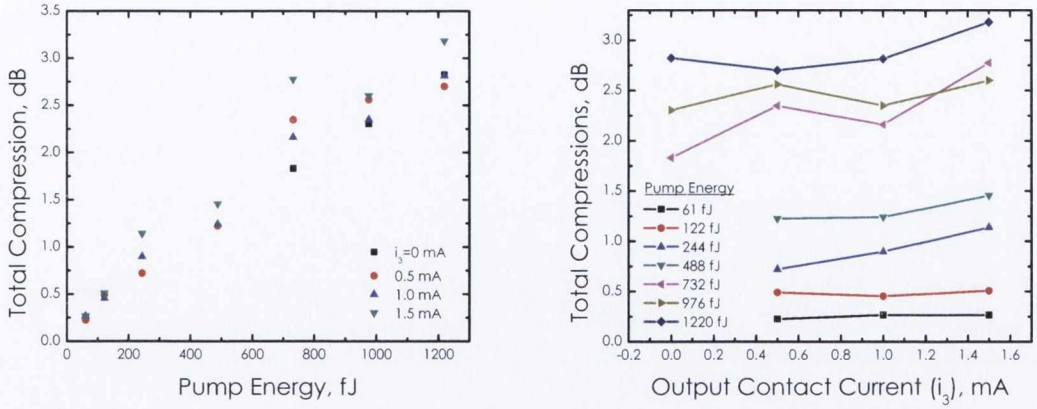

(a) **(b)**

Figure 6.24: Total gain compression from optically pumped value to saturated minimum, as a function of (a) pump energy and (b) applied current. The pump energies are 61, 122, 244, 488, 732, 976 & 1220 fJ

utilised in this way, it may offer greater extinction ratios. The maximum value achieved are moderate in this case however, approaching 3dB at the highest pump power of 1220fJ. The trend for all bias values is a steady increase with pump energy, with little deviation. When plotted against the applied current, the slight variation is seen more closely. This makes sense: As the absorption decreases with increasing bias, the corresponding total compression stays the same, as the maximum gain compression begins to take over. This means that at low biases the total compression may be useful in application, as it occurs and recovers over intraband timescales as will be shown. The characteristic timescales are now presented beginning with the Rise Time of the absorption in Figure 6.25.

The rise time of this absorption peak occurs within a range of times across all parameters of about 1.5ps, however the data is quite erratic. When looking at it as a function of current, the trend is clearer, with a decrease associated with a diminished maximum absorption at higher biases. This effect is more evident at higher pulse energies, however it should be noted that at lower pump energies the error is higher due to the poorer SNR. The total fall time corresponding to total compression following this, is given by Figure 6.26.

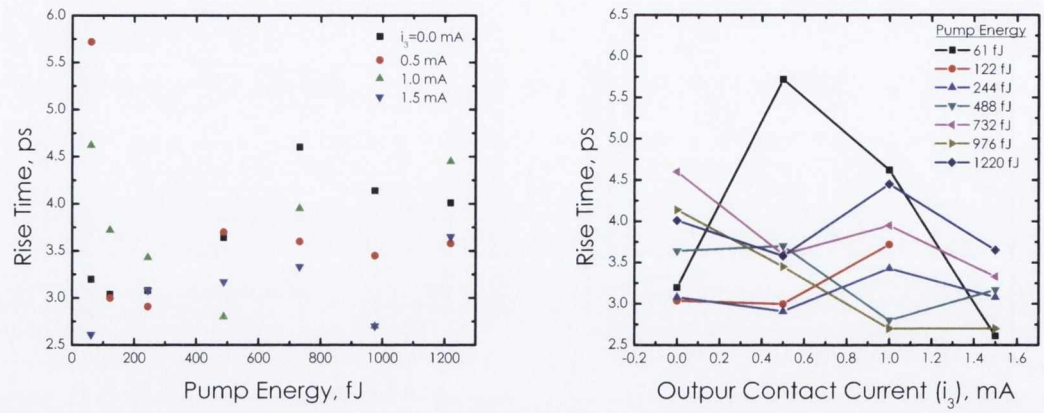

(a) (b)

Figure 6.25: Rise time of maximum absorption due to optical pumping at low applied current (i_3), as a function of (a) pump energy and (b) applied current. The pump energies are 61, 122, 244, 488, 732, 976 & 1220 fJ

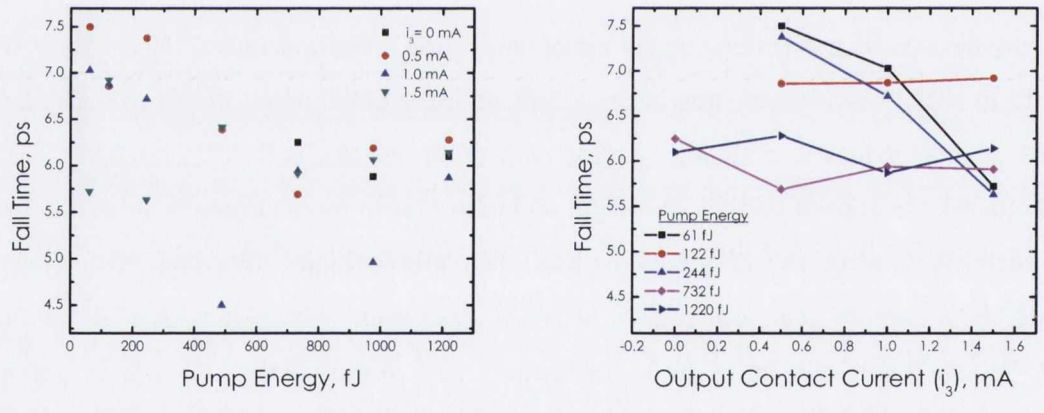

(a) (b)

Figure 6.26: Fall time of the induced gain down to the maximum compression point, as a function of (a) pump energy and (b) applied current. The applied pump currents are varied from 0-1.5mA. The pump energies are 61, 122, 244, 488, 732, 976 & 1220 fJ.

The fall time as a function of pump power is again quite stable, but does decrease slightly from 7ps to 6ps on average. At i_3=1.5mA, the time is approximately 6ps across all pump powers. As before these features are linked to the length of the device. Finally there is a fast recovery of this gain too, before the slow recovery of the device back to the original unsaturated level takes place. This fast component is plotted in Figure 6.27.

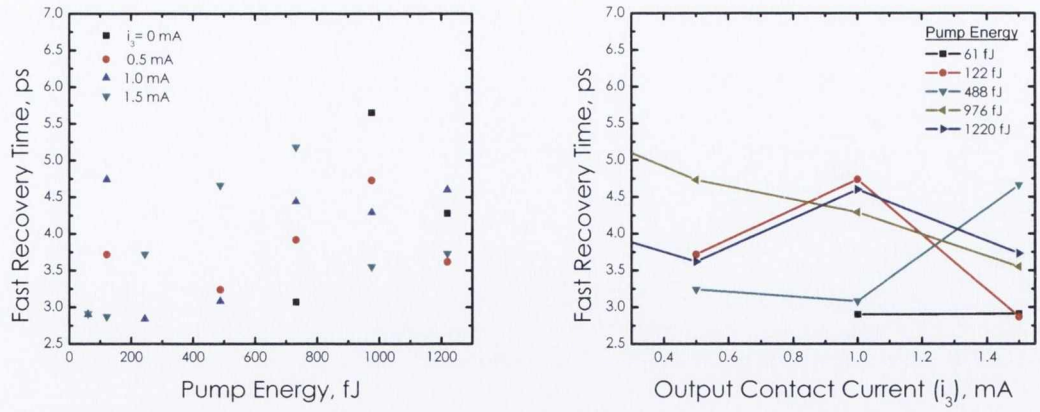

(a) **(b)**

Figure 6.27: Fast recovery time of the compressed gain as a function of (a) pump energy for i_3=0,0.5,1.0 & 1.5mA, and (b) pump current for pump powers of 61, 122, 488, 976 & 1220 fJ.

The fast recovery, due to intraband processes, dominated in this case by carrier heating, is quite noisy but largely set in a 4ps range. The extraction of this data proved difficult due to the low magnitude compressions (not shown). The interesting point about this recovery is that it opposes a slow decay back to the normalised baseline. The most promising bias condition in this case is for a value of i_3=1.5mA (the section is slightly smaller than i_1). Similar to the previous section there is a complete suppression of slow compression, once again demonstrating that a multi-contact SOA is capable of controlling the relative gain dynamics. However in this case there is also an additional component of maximum absorption.

6.4.2 Discussion

As a result of varying the output contact current, additional features manifested on the transmission decays. In particular, a sharp absorption by the pump pulse at very low biases, lead to an increased gain transient, which was them compressed, and subsequently recovered over a two stage process. Whereas the variation in probe facet presented a clearer picture with regards to gain switching (compression followed by a fast recovery) this scheme is more complex. Firstly, the gain is much higher as a result of the pump pulse increasing the gain of the output section. In general, for functional duties, gain must be appreciable, preserving a good SNR where possible. In addition, much like varying the input contact could directly control the recovery process, varying the output section has a similar effect. At a bias of 1.5mA, all slow recovery processes

are suppressed. It is possible that this bias configuration, with contra-propagation, can also be used functionally, at speeds not seen in a single contact bulk SOA. Again, this represents a preliminary study on a prototype structure, and much future work is planned. In particular, modelling and systems based tests to ascertain if the potential for application can be fulfilled.

6.5 Conclusions

The carrier density dependent gain dynamics have been investigated through contra-propagation pump-probe studies, with 2.5ps resolution. Initially, the transient behaviour for a total injected bias of 150mA, with different carrier density profiles was examined. This complimented the steady-state characterisation of Chapter 5. It was found that in all cases the noise controlled profiles produced lower interband and intraband compressions, relative to the Standard profile. This was somewhat expected, based on the reduced gain of these profiles under continuous wave injection. The timescales associated with the compression mechanisms were found to depend on the implemented carrier profile at low pump energies. However at higher pulse energies, the values levelled off. The intraband response was very closely matched across all three profiles, although the High P_{sat} configuration was slightly slower at 6ps. The limiting factor for use in functional optical duties is the slow recovery time. Due to the increased level of ASE in the Standard case the interband recovery was more than 100ps quicker than the noise controlled profiles with their reduced ASE levels.

The chapter went on to examine the facet dependent dynamics, when the remaining sections were held at a constant bias. At low bias values the MCSOA can be modified to work as an SOA-Absorber combination, or vice versa. This began in section 6.3 where the input facet was varied from the absorption regime through to gain. The experiment was repeated in section 6.4 for the reverse configuration, where the output facet was varied. As the pump-probe technique used was counter propagation the relative position of the pump to the varied facet had a significant outcome on the induced transients.

It was found that in both cases, there was an applied current that acted to suppress any slow gain recovery, with potential implications for optical processing, specifically in this case gain switching. For variation of the input probe current, a total compression and full recovery resulted, occurring in approximately 11ps, at the expense of the total gain magnitude. For the reciprocal of this configuration, where the pump facet acts as an absorber, a similar effect was

obtained around the transparency bias of that section. In this case, the rapid recovery was accompanied by an additional increase in gain to very high values (in comparison).

This work has unambiguously shown that control of the carrier density in a multi-section SOA can directly control the dynamic response of the SOA. It is possible, with both future modelling and experimental work, that these features be harnessed for various fast optical processing configurations. Limitations in total gain can easily be improved upon in future, refined devices. With comprehensive modelling it is believed that the effects presented here, can be harnessed in a positive way, and improvements in overall performance achieved.

References

[1] M. N. Ngo, G. Girault, M. Gay, L. Bramerie, J.-C. Simon, R. Brenot, F. Lelarge, and G.-H. Duan, "Suppression of slow gain recovery in ultralong quantum-dash semiconductor optical amplifier emitting at 1.55μm," *Optics Communications*, vol. 284, pp. 4910–4913, Sept. 2011.

[2] F. Girardin, G. Guekos, and A. Houbavlis, "Gain recovery of bulk semiconductor optical amplifiers," *Photonics Technology Letters, IEEE*, vol. 10, no. 6, pp. 784–786, 1998.

[3] X. Li, M. J. Adams, D. Alexandropoulos, I. F. Lealman, "Gain recovery in semiconductor optical ampliers," *Optics Communications*, vol. 281, pp. 3466–3470, 2008.

[4] L. Occhi, Y. Ito, H. Kawaguchi, L. Schares, J. Eckner, and G. Guekos, "Intraband gain dynamics in bulk semiconductor optical amplifiers: Measurements and simulations," *IEEE Journal of Quantum Electronics*, vol. 38, no. 1, pp. 54–60, 2002.

[5] K. L. Hall, E. R. Thoen, E. P. Ippen, *Nonlinearities in Active Media*. Academic Press, 1999.

[6] S. Jagdeep, *Ultrafast Spectroscopy of Semiconductors & Semiconductor Nanostructures*. Springer, 1996.

[7] C. S. Cleary, M. J. Power, S. Schneider, R. P. Webb, and R. J. Manning, "Fast gain recovery rates with strong wavelength dependence in a non-linear SOA.," *Optics express*, vol. 18, pp. 25726–37, Dec. 2010.

[8] J. M. P. Borri, S. Scaffetti, "Measurement and calculation of the critical pulsewidth for gain saturation in semiconductor optical amplifiers," *Optics Communications*, no. 99, pp. 51–55, 1999.

[9] K. L. Hall, G. Lenz, E. P. Ippen, and G. Raybon, "Heterodyne pump-probe technique for time-domain studies of optical nonlinearities in waveguides," *Optics letters*, vol. 17, p. 874, June 1992.

[10] H. Soto, D. Erasme, and G. Guekos, "Cross-polarization modulation in semiconductor optical amplifiers," *IEEE Photonics Technology Letters*, vol. 11, no. 8, pp. 970–972, 1999.

[11] S. Philippe, A. L. Bradley, B. Kennedy, F. Surre, and P. Landais, "Experimental Investigation of Polarization Effects in Semiconductor Optical Amplifiers and Implications for All-Optical Switching," *Journal of Lightwave Technology*, vol. 26, no. 16, pp. 2977–2985, 2008.

[12] P. Borri, W. Langbein, J. Hvam, F. Heinrichsdorff, M.-H. Mao, and D. Bimberg, "Spectral hole-burning and carrier-heating dynamics in InGaAs quantum-dot amplifiers," *IEEE Journal of Selected Topics in Quantum Electronics*, vol. 6, no. 3, pp. 544–551, 2000.

[13] J. Mark and J. Mork, "Subpicosecond gain dynamics in InGaAsP optical amplifiers: Experiment and theory," *Applied Physics Letters*, vol. 61, no. 19, pp. 2281–2283, 1992.

[14] H. Dorren, D. Lenstra, M. Hill, and G.-D. Khoe, "Nonlinear polarization rotation in semiconductor optical amplifiers: theory and application to all-optical flip-flop memories," *IEEE Journal of Quantum Electronics*, vol. 39, pp. 141–148, Jan. 2003.

[15] R.J. Manning, A. Antonopoulos, R. Le Roux and A.E. Kelly, "Experimental measurement of nonlinear polarisation rotation in semiconductor optical amplifiers," *Electronics Letters*, vol. 37, no. 4, pp. 229–231, 2001.

[16] J. C. S. F. Ginovart, "Gain dynamics studies of a semiconductor optical amplifier," *J. Opt. A: Appl. Opt.*, vol. 4, pp. 283–287, 2002.

[17] J. Leuthold, R. Bonk, T. Vallaitis, A. Marculescu, W. Freude, C. Meuer, D. Bimberg, R. Brenot, and F. Lelarge, "Linear and nonlinear semiconductor optical amplifiers," in *Optical FIbre Communications*, pp. 2–5, 2010.

[18] Y. Yi, H. Lirong, X. Meng, T. Peng, and H. Dexiu, "Enhancement of gain recovery rate and cross-gain modulation bandwidth using a two-electrode quantum-dot semiconductor optical amplifier," *J. Opt. Soc. Am. B*, vol. 27, no. 11, 2010.

[19] A. Poustie, "Light Up All-Optical Signal Processing," *Photonics Spectra*, no. August, 2007.

[20] T. P. Hessler, M.-a. Dupertuis, B. Deveaud, J.-Y. Emery, and B. Dagens, "Optical speedup at transparency of the gain recovery in semiconductor optical amplifiers," *Applied Physics Letters*, vol. 81, no. 17, p. 3119, 2002.

[21] R. Giller, R. J. Manning, G. Talli, R. P. Webb, and M. J. Adams, "Analysis of the dimensional dependence of semiconductor optical amplifier recovery speeds.," *Optics express*, vol. 15, pp. 1773–82, Feb. 2007.

[22] J. Mø rk and T. W. Berg, "The Dynamics of Semiconductor Optical Amplifiers," *Optics & Photonics News*, pp. 42–48, 2003.

[23] J.-N. Fehr, M.-a. Dupertuis, T. Hessler, L. Kappei, D. Marti, F. Salleras, M. Nomura, B. Deveaud, J.-Y. Emery, and B. Dagens, "Hot phonons and Auger related carrier heating in semiconductor optical amplifiers," *IEEE Journal of Quantum Electronics*, vol. 38, pp. 674–681, June 2002.

[24] B. N. Gomatam, A. P. DeFonzo, "Theory of hot carrier effects on nonlinear gain in GaAs-GaAlAs lasers and amplifiers," *IEEE Journal of Quantum Electronics*, vol. 26, no. October, pp. 1689–1704, 1990.

[25] T. Houbavlis, K. E. Zoiros, M. Kalyvas, G. Theophilopoulos, C. Bintjas, S. Member, K. Yiannopoulos, N. Pleros, K. Vlachos, H. Avramopoulos, L. Schares, L. Occhi, G. Guekos, J. R. Taylor, S. Hansmann, and W. Miller, "All-optical signal processing and applications within the Esprit Project DO _ ALL," *Journal of Lightwave Technology*, vol. 23, no. 2, pp. 781–801, 2005.

[26] G. Talli, S. Member, and M. J. Adams, "Gain dynamics of semiconductor optical amplifiers and three-wavelength devices," *IEEE Journal of Quantum Electronics*, vol. 39, no. 10, pp. 1305–1313, 2003.

[27] R. J. Manning, "High speed all-optical signal processing using semiconductor optical amplifiers," *International Conference of Transparent Optical Networks (ICTON)*, pp. 161–164, 2006.

[28] D. A. Reid, A. M. Clarke, S. Member, X. Yang, R. Maher, R. P. Webb, R. J. Manning, and L. P. Barry, "Characterization of a Turbo-Switch SOA wavelength converter using spectrographic pulse measurement," *IEEE Journal of Selected Topics in Quantum Electronics*, vol. 14, no. 3, pp. 841–848, 2008.

7

Multi Contact SOA: Design Development

A primary limitation of the prototype MCSOA is carrier leakage between neighbouring contacts. As the MCSOA previously characterised in Chapters 5 & 6 represents a 1st generation component, there is a natural progression towards refinement at the next design phase. In an attempt to enhance the device performance, and provide as much information as possible for the second stage of development, post processing of the device is presented. Adjacent contact isolation is increased through Focussed Ion Beam (FIB) etching of the InP region between contacts, in order to gain greater control over the carrier profiles. The subsequent iterative change in steady state performance was measured experimentally and will be discussed under conditions of injection and non-injection.

7.1 Adjacent Carrier Leakage

As the MCSOA is a 1st generation prototype, there are aspects of the design which require development for the optimisation of future generations. For example, it is possible that future devices would benefit from the characteristics that a quantum dot based gain media would provide (Chapter 2), coupled with the versatility of the multi-contact structure. This of course is impossible to test experimentally without fabrication of a redesigned chip. However, one feature which may be investigated before this point is carrier leakage across adjacent contacts.

In order to sustain the proposed carrier density profile, adequate isolation between adjacent contacts is required. If this criterion is not adhered to, carrier spreading may occur resulting in a broadening of the desired carrier profile. The consequence of this being that the optimum Low NF carrier density profile may not be reached. At the very least it adds a degree of uncertainty to the proposed experimental pump conditions, in that it is impossible to say with confidence what the resultant carrier density in any one section will be. The idea is illustrated qualitatively in Figure 7.1.

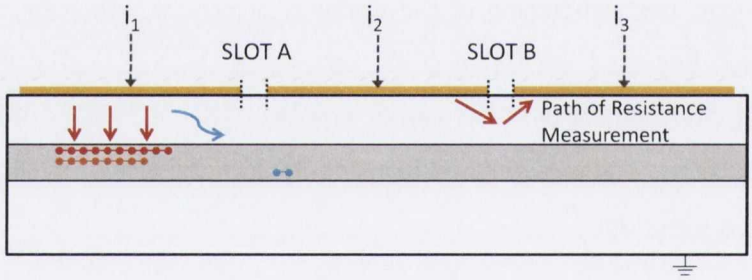

Figure 7.1: Qualitative demonstration of carrier leakage between adjacent contacts at Slot A, resulting in a broadening of proposed carrier density profile. Red is the desired carrier density, orange is the resultant carrier density, and blue represents the carriers lost. Also shown at Slot B is the resistance measurement path.

Observing sections 1 and 2, an injected current results in an expected carrier density, governed by Equation 4.16. This is represented in the diagram in red. However, if some of these carriers are lost to the adjacent section, due to poor isolation, then the actual carrier density value will be less than expected, shown by the orange dots. The difference in carrier density may be lost to this adjacent section, given by the blue dots. In this idealised scenario, carriers lost to the neighbouring section my not contribute to the gain. In order to initially quantify the level of leakage that may occur the resistance is measured between contacts 1 & 2 (Slot A) and 2 & 3 (Slot B). The path of measurement, when using a multimeter directly across the adjacent contacts, is different to that experienced by the current path which results in the creation of

carriers in the active region (shown at Slot B). This means that resistance measurements are used as a guide in quantifying any leakage, rather than an absolute measurement of leakage that occurs.

This chapter seeks to address the improvement of longitudinal carrier density control by attempting to augment the resistance between contacts, through the etching of deeper isolation slots directly into the top p-type cladding. The chosen method relies on Focused Ion Beam (FIB) milling, now described.

7.2 Improving Carrier Density Control

The technique used to process the device in this chapter, described below, was not the only possible choice. Ion implantation, proton implantation or in situ doping could all have been used, however in general represent techniques more suitably used during growth. The technique chosen for this work, Focused Ion Beam (FIB) etching, was more suitable as an after the fact test option, as the device had already been fully processed and mounted. It should be noted that the device investigated in this chapter is different to the MCSOA of Chapters 4 & 5, but of the same design and from the same wafer. It was decided not to use the previously characterised device due to the risky nature of the etching process.

7.2.1 Focused Ion Beam Etching

Focused Ion Beam (FIB) systems operate in a similar fashion to a scanning electron microscope (SEM) with the key difference that, rather than a beam of electrons, FIB utilises a direct-write focused beam of heavy ions (e.g. 30keV Ga^+ ions). The finely focused beam can sputter atoms or structurally modify the surface atoms at a vacuum-target interface to produce altered surface topographies [1]. Low beam currents can be used for imaging. The system is fundamentally designed for nanofabrication via controlled localized ion milling or ion assisted deposition, which can be simultaneously monitored with the SEM column, making it an ideal candidate for material removal with sub-micron precision [2, 3, 4]. FIB is unique in that patterns can be produced in virtually any material, unlike other nano-lithography methods which are limited to patterning resist materials. Unfortunately, the process is relatively slow. For most materials, the removal rate for a 30keV gallium ion is around 110 atoms per incident ion, corresponding to a machining rate of around $0.11\mu m^3$ per nC of incident ions.

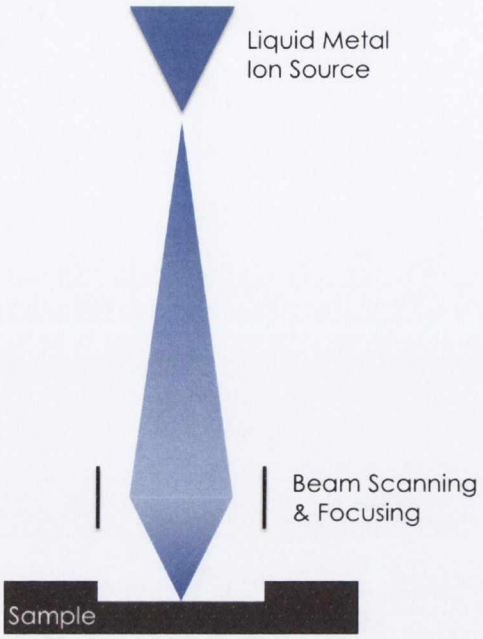

Figure 7.2: Simplified schematic of the focused ion beam system. The ion beam (usually gallium) is generated from a liquid metal source (LMIS) and the Ga^+ ions are focused down the FIB column on to the substrate. For focused ion beam chemical vapor deposition (FIBCVD), provision is usually made for a gas nozzle assembly next to the sample so as to provide a flow of gas molecules to the sample surface during irradiation

Lithography using ion beams has several unique characteristics, primarily due to the physical nature of the ion (at least three orders of magnitude heavier than the electron). For slow heavy ions (e.g., 30keV Ga^+), the interaction process is that of altering the surface structure of a material, modifying surface chemistry, and removing atoms from the surface through sputtering. In contrast, the primary interaction of fast lighter ions (e.g., 100 keV[3] MeV protons) is that of deep penetration into the material, with a minimal amount of surface disruption. For both light and heavy ions, diffraction effects are not an issue (the wavelength of a 100keV proton is around 104 nm) [5]. A simplified schematic of a FIB device is shown in Figure 7.2.

As the image shows, the gallium (Ga^+) ion primary beam hits the sample surface and sputters a small amount of material, which subsequently leaves the surface as either secondary ions or neutral atoms. The primary beam also produces secondary electrons. As the beam scans the sample surface, the signal from the sputtered ions or secondary electrons is collected to form an image. At low primary beam currents, very little material is sputtered, but surface modification does occur, and so great care is taken to maintain distance from the SOA facets in the following work.

If the sample is non-conductive, a low energy electron flood gun can be used to provide charge

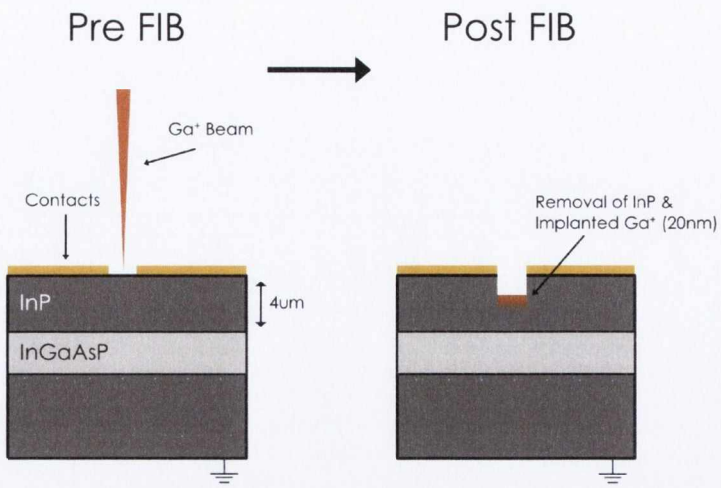

Figure 7.3: Schematic of a single etch stage (the first), where the device on the left is the unmodified MCSOA, and that on the right is the MCSOA with a modified slot. Shown is the focussed Ga^{+} beam, the MCSOA structure with active layer depth and the small implanted region (≈20nm) directly underneath the target area (not to scale).

neutralization [6, 3]. This option was not available at the time of milling. In this manner, by imaging with positive secondary ions using the positive primary ion beam, even highly insulating samples may be imaged and milled without a conducting surface coating, as would be required in a SEM. It was determined to be risky, when considering the facets of the device, and so would not have been used. As such, surface charging proved a significant feature of this work, and affected greatly the level of both lateral and depth control, and will be discussed below.

7.2.2 Etching the Isolation Slots

Milling was undertaken directly into the InP region between adjacent contacts, corresponding to the isolation slots. Each of Slot A & B were etched over 3 successive iterations, incrementally increasing the slot depth each time. Identical optical characterisation as before is performed at each point in the process to assess any change in performance, which will be presented in a following section. Initially, and after each etching step, the slot depths are measured using the SEM column (angle resolved). A detailed description of the entire FIB process, from an experimental point of view, can be found in [6, 3]. The realised depths, as will be described, differed from the proposed steps of 500nm per etching stage. The process for one milling iteration is shown schematically in Figure 7.3.

A feasibility test was undertaken on a sacrificial device from the same wafer, to confirm the structural dimensions. Figure 7.4 provides low magnification SEM images of the chip surface

(a), including an image of Slot A (b) and Slot B (c). Annotated is the slot region, which is approximately 10μm wide, and covers the full extent of the contact width. The images were cross sectioned using the FIB, and imaged with the partner SEM. They characterised both the depth of the current slots (limited to the gold contact depths at approximately 200nm), and the 4μm distance to the active layer - information of vital importance in realising the limits of this technique. Etching too far will lead to detrimental effects on the travelling mode. These images are shown in Figure 7.5.

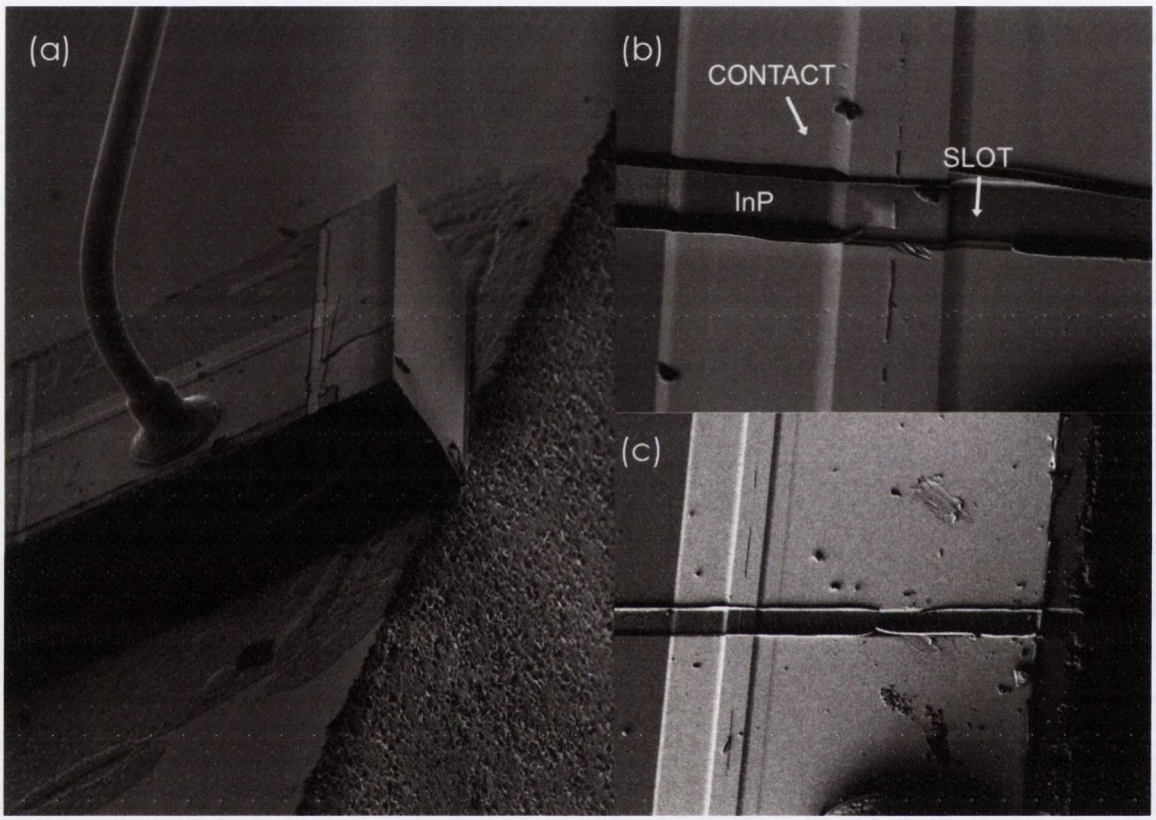

Figure 7.4: Low magnification SEM images of the sacrificial MCSOA chip (a), and Slot A and Slot B in (b) and (c). The 10μm wide isolation slots are clearly visible, extending over the whole width of the chip.

One of the negatives associated with using a FIB in this way, and which contributes significantly to the difficulty in performing the mill, is the presence of surface charge as a result of the beam interaction with insulating material on the target structure. This results in drift, where a movement of the sample in the two dimensional pattern plane can occur at any time during the process. This results in variation and potentially catastrophic misalignment of the designated milling area. It is of particular concern with the MCSOA, as significant misalignment could result in irreparable damage to a facet or electrode contact.

Due to the limitations imposed by the chip submount and large experimental mount (including remnants of heat sink compound) beam drift was prevalent, and occurred at almost every stage

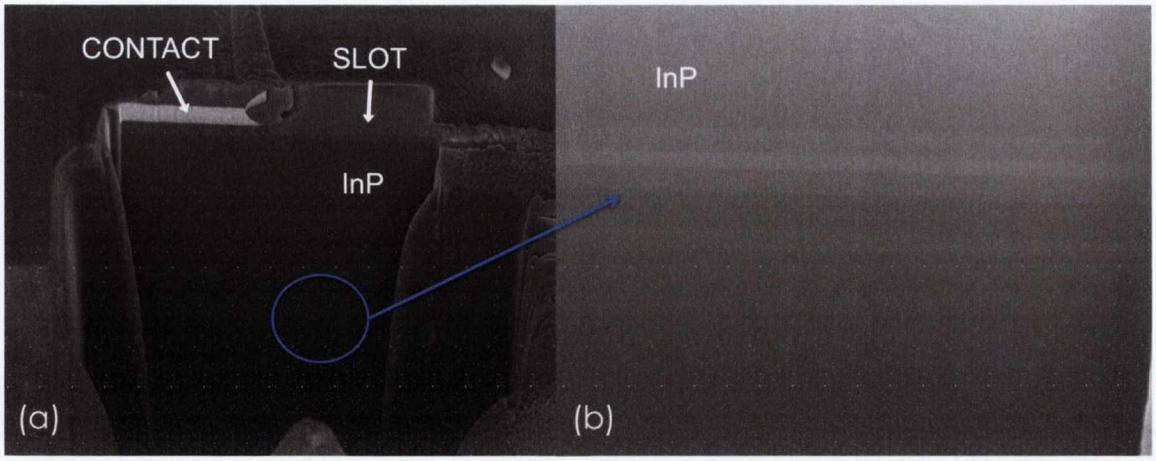

Figure 7.5: Higher magnification SEM images of cross sections cut out using the FIB. The images is taken side on (i.e. the propagation axis runs from left to right). Shown in (a) is the contact and slot interface, a 4μm deep InP cladding layer, which sits on the active region, which is shown under high magnification in (b), to be comprised of a separate confinement heterostructure (SCH).

of the etching. Before proceeding to remove InP, material (dose) tests must be performed to estimate the level of material removed as a function of time. It is important to note that dose testing is generally a routine process, but not in this case. The dose tests this time act to estimate the level of drift only, and account for this effect through the choice of pattern area. The consequent etching processes varied in their success, in some cases behaving as directed in both lateral width and milling depth, and the opposite to this where overall depth varies as a function of position. The result is an inconsistent depth profile at the slots, and further evidence in support of ion implantation or improved contact design. As can be seen in the sample SEM images of Figure 7.5, the width and depth both fall prey to high levels of drift during the milling processes.

Representative images of the slots after the first etching iteration are shown in the composite image in Figure 7.6 below. Due to the high levels of drift, the etching area was restricted to a 100μm^2 region, directly over the active strip. This was thought to be enough for an improvement in isolation, as the structure likely contains various current confining layers either side of the stripe, not resolvable in the SEM images [7, 8, 9].

Finally the depths in each of Slot A and Slot B into the top p-layer over all milling iterations, are plotted in Figure 7.7, relative to the baseline. The active layer is shown at the bottom of the graph, approximately 4μm deep. The stages of the process are numbered 0-3, where 0 represents the unmodified structure with original slots; 1, 2 & 3 the subsequent attempts at removing material. The baseline at 0nm is also shown. As is evident from the graph, uniform

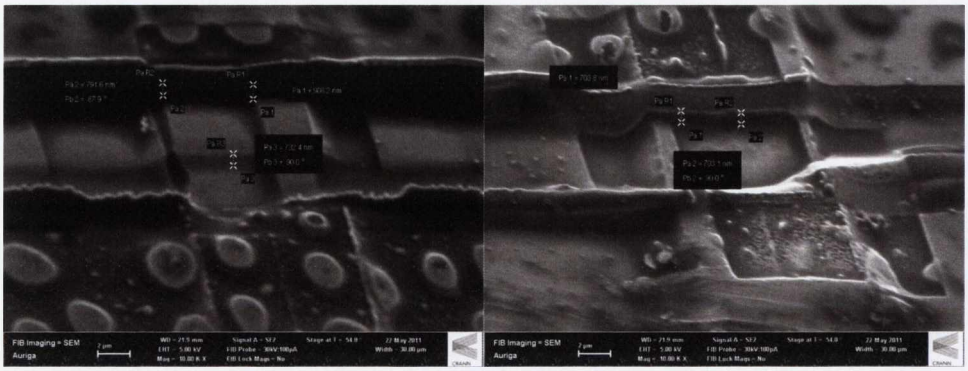

(a) (b)

Figure 7.6: Representative images of Slots A & B after the first FIB based etching. Multiple platforms can be seen, owing to the difficulties imposed by an unsteady beam column. In future iterations this was accounted for with more success.

depth was not achieved when comparing both slots. That Slot B always proved to induce less drift is presumably linked to the lower level of surface charge in this region. This explains the more controlled increase in depth each time. Slot A on the other hand was more difficult to process, and so no further modification took place between stages 1 & 2. This problem was remedied for the final iteration. The reason why Slot A ultimately reaches greater depths even with a larger degree of drift is a consequence of the drift itself: Where Slot B was etched with much more control, constant overlapping at Slot A produced deeper slots.

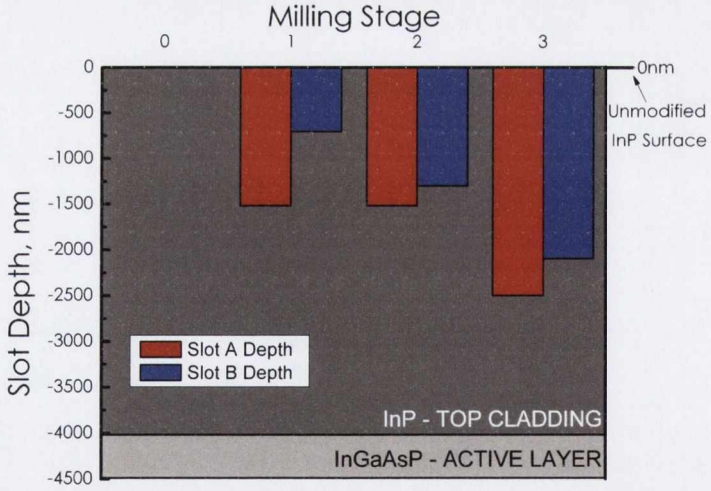

Figure 7.7: Etched depth into the top InP layer given relative to the baseline of 0nm. The dark grey represents the InP layer, and the light grey region is the InGaAsP active layer.

As a final note, the effective depth is not simply the base level minus the material removed. In

addition to this, there is an estimated 20nm of implanted Ga^+ ions (not shown) that have the ability to affect the electrical and optical properties of the structure, although it is not thought to contribute in a significant way. The ultimate depths reached are still significantly far from the waveguide that it is thought little interference with the travelling mode will occur. This idea is presented in the next section, with the aid of a transfer matrix based model.

7.2.3 Confinement & Mode Transmission

The confinement factor, defined in Chapter 2 and given by Equation 2.18, is the ability of the waveguide to contain the injected light. Where the confinement is high, the mode is tightly held in the waveguide region. When this value is quite low (<0.1), as with some quantum well and dot structures in particular, the mode tail will further protrude into the surrounding InP-cladding layers. If the InP is removed to great enough depths, the mode tail may interact with the high contrast InP/air interfaces. This effect is harnessed in DFB lasers, where the induced reflection through interaction with a periodic index contrast provides the wavelength selective feedback required for single mode operation. In an SOA reflections have a negative impact on operation, causing gain modulation. The generation of reflections within the cavity is not an effect that is thought to be of primary concern in this process. Of more importance is an increase in waveguide loss.

Basic modelling was undertaken (with our collaborators) to ascertain the extent of induced reflection and losses from a single milled passive slot, where the depth is varied from 0nm (the baseline) to -4000nm (the surface of the active layer). The model is based on The Scattering Matrix Method (SMM), and details of same can be found in [10]. The waveguide core layer is extended to a thickness of 0.5μm based on two 200nm thick SCH layers and a 100nm thick active layer, as seen in Figure 7.3.

Figure 7.8 plots the simulated normalised field amplitude as a function of transverse direction (depth from surface), for the unmodified structure and the idealised case where the etch removes material almost all the way down to the top of the active layer (3μm). The simulation however is taken for all depths down to the surface of the active layer.

The blue line is the field amplitude, the red dashed line the refractive index. The majority of the mode is contained within or close to the confining active layer. Once the material is removed the mode interacts with the InP/air interface, leading to a change in the field amplitude function.

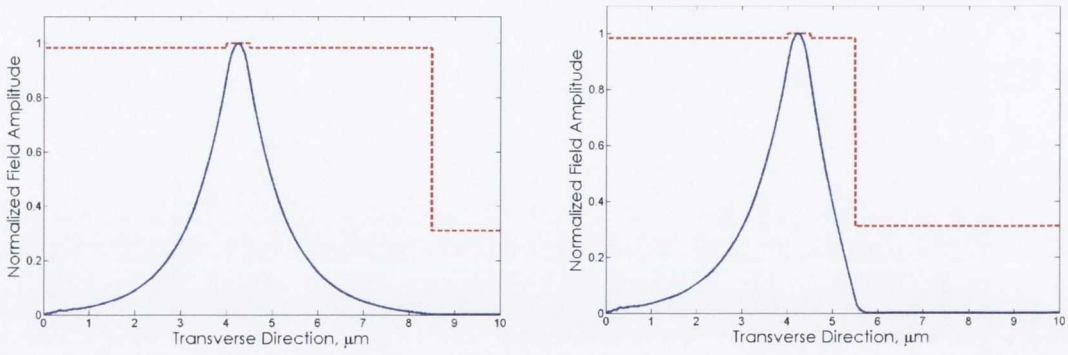

(a) **(b)**

Figure 7.8: Simulated normalised field amplitude, showing tail overlap with cladding layers (a) Pre-FIB (b) Post-FIB, 4000nm depth (this depth was not achieved experimentally).The dashed red line represents the refractive index.

This represents the absolute limit of milling depth, where the effect on the travelling mode is purely negative.

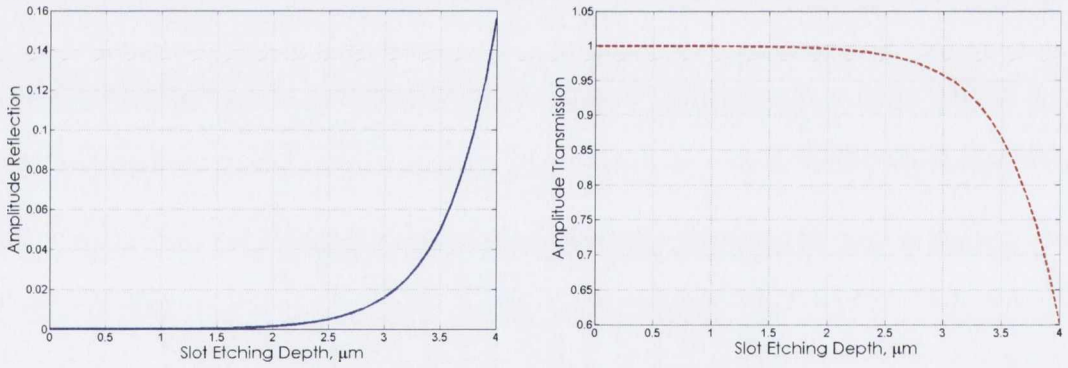

(a) **(b)**

Figure 7.9: The change in (a) Amplitude reflection and (b) transmission as a function of increasing slot depth from 0nm to 4000nm, for a single slot.

Figure 7.9 illustrates that the sacrifice in terms of increased reflection from a single slot is minimal, and as will be seen in the experimental data does not contribute significantly. For the etching depth of 3μm, the refractive index of the guided modes in the waveguide and the slot region are estimated to be 3.181 and 3.179, respectively. The calculated reflection and transmission from the etched slot are about 0.016 and 0.96, respectively, showing very little effect on the travelling mode. Further to this, there is a decrease in transmission predicted, of about 4% at the maximum experimental depth reached of 2500nm, which occurs at only a

single slot. The minimum depth of Slot B is 2100nm, meaning that the effect is even less severe in this case.

7.3 Iterative Characterisation

7.3.1 Contact Size Non-Uniformity

The optical characterisation is undertaken in exactly the same way as before, with a modification to the pumping arrangement necessary to accommodate the non-uniformity of section sizes of this device. The weighting for the new current distributions were based on the percentage difference in applied current for the Low Noise case of the device previously characterised, assuming the same level of conversion efficiency as the diode is materially and structurally identical aside from the section sizes. The physical size of the contacts was taken into account. For instance, where as before the Standard profile was given by 50,50,50mA, it is now given by 59,58,33mA, whilst the Low Noise profile is given by 92,43,17mA. Two images of the device are shown in Figure 7.10, an optical image in (a) and a low magnification SEM image (in the FIB chamber) in (b). The disparity in section size is visible in both images.

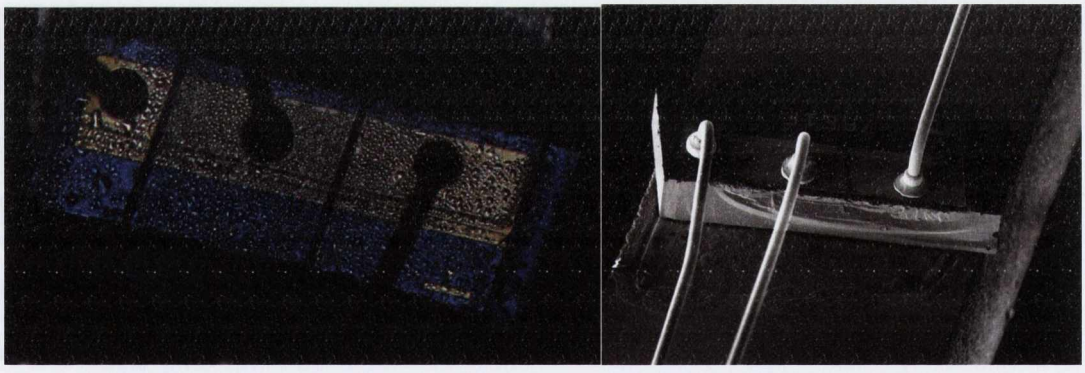

(a) **(b)**

Figure 7.10: (a) Optical microscope image of MCSOA, showing non-uniform contact regions and ball-bonded wires. (b) Low Magnification SEM image of sacrificial MCSOA before any material etching.

7.3.2 Resistance Measurements

To ascertain the level of increased isolation over the various FIB stages, the resistance is measured directly across the slots. Figure 7.11 plots the measured resistance as a function of

increased depth for both Slot A and Slot B. As shown in Figure 7.11, this does not necessarily quantify the level of leakage, but acts as a guide to the potential for carrier drift from one section to the next. The measurement is made directly by probing the contacts.

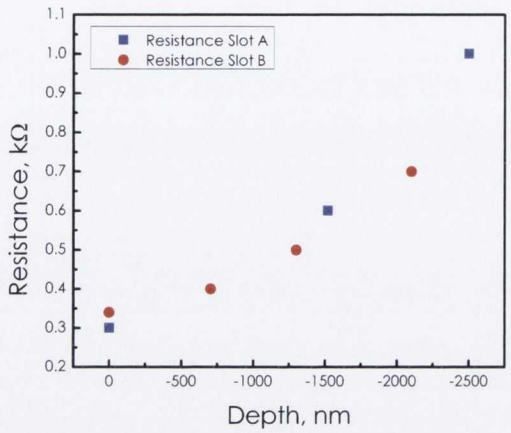

Figure 7.11: Measured resistance across isolation Slot A (blue) & Slot B (red), as a function of increased slot depth. These values are measured by probing the contacts directly with a multimeter.

The measured resistance increases non-linearly with increasing slot depth. In general integrated photonic components maintain values of at least 1kΩs regarded as sufficient in preventing any substantial loss of current between sections [11, 12]. This is achieved by the final attempt at improving slot A, where a value of 1kΩ is achieved for a material depth of -2500nm. It was not possible to continue the FIB process after this point, however from the simulations a decrease in transmission of 5% will occur beyond 3μm. By incorporating deeper slots at the growth level it is thought, based on this data, that an improved level of contact isolation will be achieved. An alternative approach, for the reasons discussed would be ion implantation, which would likely yield better results, at the expense of more complex fabrication [13, 14]. In addition to an increase in slot depth, the distance between the slots was also inadvertently widened, as a result of drift. This will also contribute to an increase in measured resistance. An additional result of this is a potential reduction in gain in the region directly below the slot, the effect of which may manifest under continuous wave injection. It should be noted that this only occurred at the first etching stage. After this, the effect of drift was contained within the slot region.

7.3.3 ASE Power & Spectral Measurements

7.12a plots the absolute ASE power collected with an integrating sphere power meter, emitted

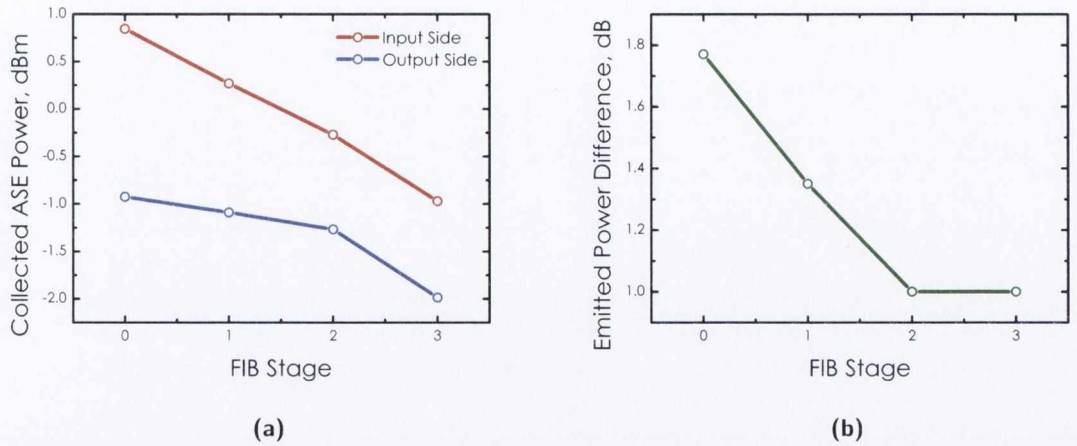

Figure 7.12: (a) Measured emitted ASE power collected at both the input and output of the device as a function of etching stage, for the Standard profile (b) The consequent relative power difference.

from both the input and output sides of the device, for the Standard profile current injection, as a function of FIB processing step. Figure 7.12b is the resulting emitted power difference.

With the increased resistance seen above, it is expected that, bar any facet effects, the asymmetrical power behaviour of the Standard profile would converge towards symmetrical, assuming it is asymmetrical due to leakage. This pattern occurs until the final stage where no further improvement is seen, although the value achieved is a respectable 1dB. It is thought that this trend towards equalisation of emitted power is due to an improvement in isolation, and so a reduction in current lost to the neighbouring section. It is difficult to say with certainty that this is the reason for this change, but it is the most obvious parameter that is changed in a significant way that is quantifiable. An alternative explanation, relates to an increase in non-radiative recombination rate at the surface and defect sites created by the FIB. This is a reasonable assumption considering the problems with drift and the non-uniform depths which results.

The measured ASE power for the situation where the input section is held at 90mA similar to section 5.3, and the middle and output sections are varied from 0-90mA, is given in Figure 7.13. Firstly, the clearest indication that the FIB process has modified device behaviour is seen in the maximum output power observed at 90, 90, 25mA. This peak power drops from $1000\mu W$ to $\sim 820\mu W$. The decrease in power occurs to some degree over all injected currents, however the trend is most clear in this peak power region. As stated above the possible cause of this reduction in power is an increase in non-radiative transitions, specifically relating to surface and defect recombination. This is coupled with the evidence from simulation which suggests little effect on the travelling mode at the depths reached. However as the resistance is clearly

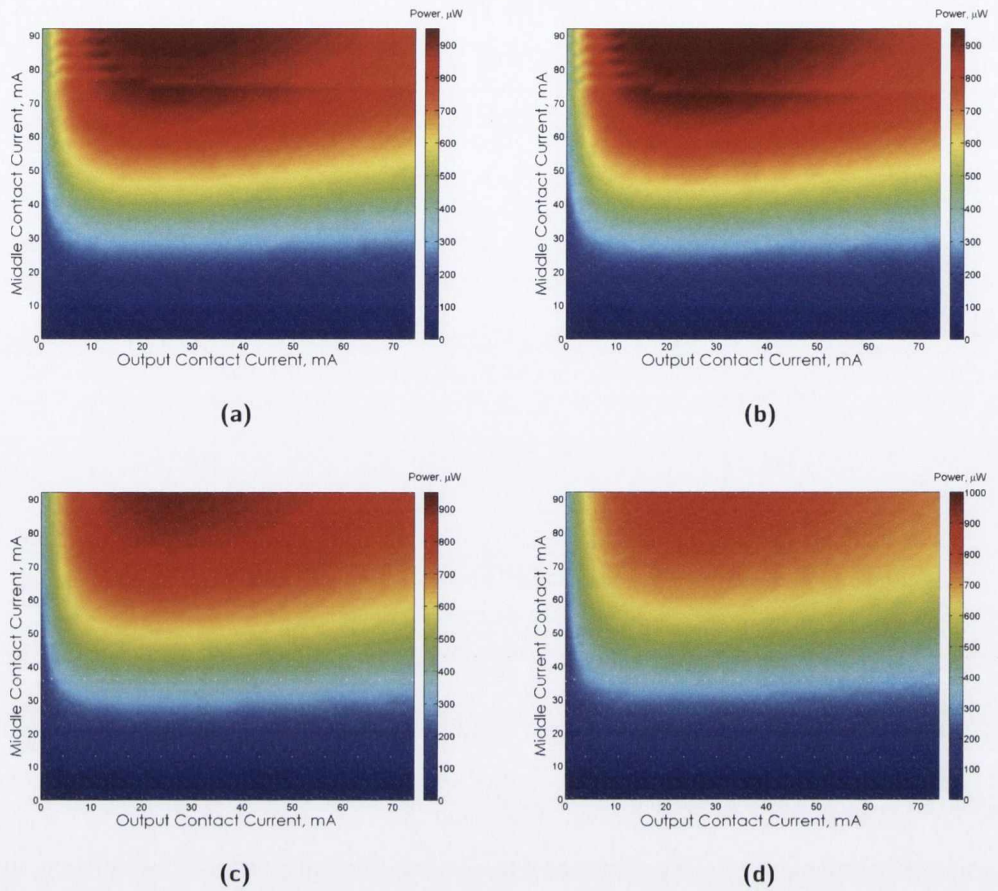

Figure 7.13: Colour maps, collected at the output of the MCSOA with an integrating sphere and power meter for the (a) Pre FIB (b) FIB 1 (c) FIB 2 (d) FIB 3 cases. The input contact is held at 90mA, and i_2 and i_3 are varied through the Low Noise profile, to 90,90,90mA.

increased, the improvement in carrier density control that this results in likely contributes to this trend.

To corroborate this although not easily identifiable, a greater range of power change is seen with each FIB step for increasing values for i_2 (middle contact) and i_3 (output contact) insinuating further control of the carrier density in each section. This is clearest across all i_3 values, where i_2 falls in the range of 40mA to 70mA. The ripple in power where the middle contact is greater than i_2=75mA, and the output current is less than i_3=20mA, are related to large fluctuations in voltage across the input contact. The voltage data for i_1 when i_2=0,10,50,90mA, are given below in Figure 7.14.

The fluctuations in voltage across the section are seemingly quenched with an increase in resistance, for slot A. In addition, at input biases in the range 0-20mA, the divergence is seen to decrease, particularly for the pair of low i_2 values and high i_2 values separately. These features

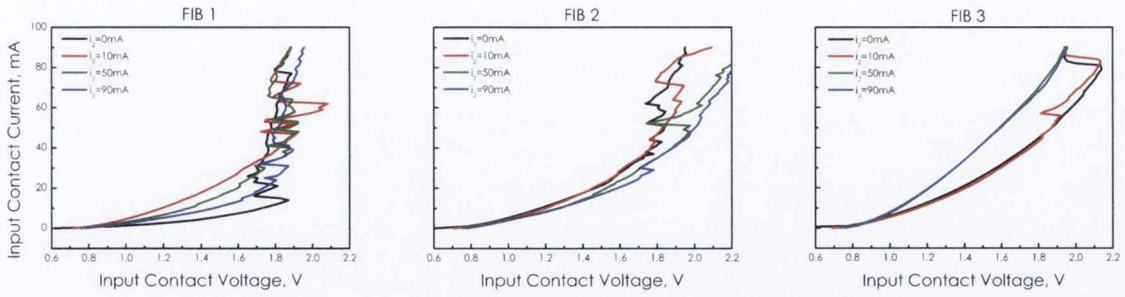

Figure 7.14: Input contact current (i_1) as a function of voltage (V_1), for the four cases were i_2=0,10,50,90mA, recorded after each FIB step.

are not present to this degree for other contacts (not shown). Also evident in this plot is the change in I–V maxima post FIB 2. This effect may also be tied to the direction of carrier leakage, as this will occur mostly from high to low current regions. When the value of i_2 is high enough, current leakage across the section is less prevalent. This would help to explain the i_2 dependence of these fluctuations.

The polarisation resolved ASE spectra with the Standard profile applied are given by Figure 7.15. Plots (a) and (b) were recorded at the output of the MCSOA using an optical spectrum analyser and shown for FIB 1 and FIB-3, at 2nm resolution bandwidth, respectively. Plots (c) and (d) are the same data with a resolution of 0.06nm.

Looking first at the data taken with 2nm resolution in Figure 7.15 (a) and (b), the chief observable difference is a narrower ASE bandwidth after the final milling stage. It is possible that this decrease in gain off the peak wavelength resulted in the reduction of the integrated output power seen in the LI data. The ASE ripples are not resolvable at this resolution. In Figure 7.15 (c) and (d) the equivalent data centred about the peak bandwidth is given for a resolution bandwidth of 0.06nm, representing the limit of the optical spectrum analyser. Ripples are clearly visible in these plots, the most striking feature being the change in modulation depth, with a reduced level seen after FIB-3, consistent with a reduction in gain. The mechanism responsible for this seems to affect both polarisation modes similarly.

7.3.4 Continuous Wave Injection

The continuous wave characterisation described in Chapter 4 & 5 is used for the iterative steady state characterisation of the etched MCSOA. This was done for after each of the three FIB

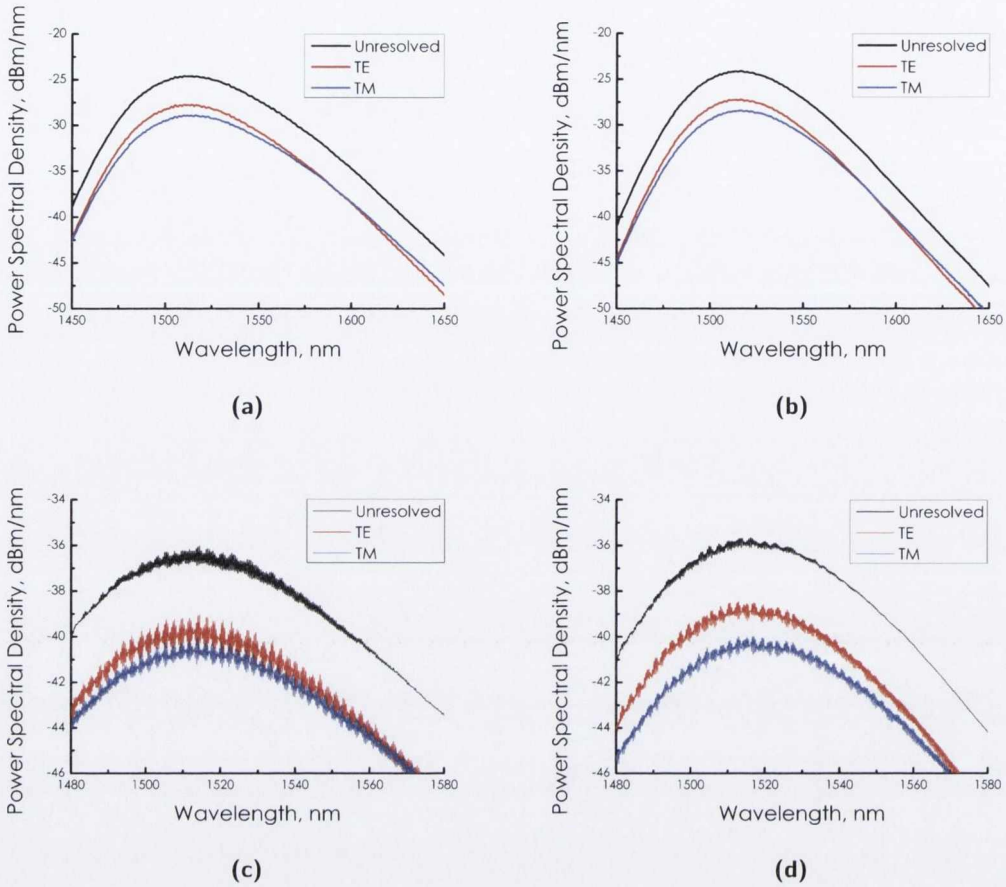

Figure 7.15: Polarisation Resolved ASE spectra collected on the output of the MCSOA at a resolution of 2nm for (a) FIB-1 and (b) FIB-2, and a resolution of 0.06nm for (c) FIB-1 and (d) FIB-3.

processes, and the initial characterisation of the unmodified MCSOA. The injected signal is in the small signal regime for all plots, with a signal power of -15dBm after input losses, and injected along the TE and TM eigenmodes. The objective of this, from a development point of view, is to show a greater level of control over the carrier density with each FIB step, and to achieve a greater improvement in NF over the Standard profile. With that, the following data plots the modification to the gain and NF for the Standard and Low Noise carrier profiles.

Standard Current Profile - Gain

Figure 7.16 plots the TE gain as a function of wavelength for the Standard profile pump scheme, over successive FIB iterations. As stated above, the importance of polarisation resolved data for these experiments relates to the fact that etching takes place in the TM direction. Although, the LI data suggests only a small effect for the TM case relative to the TE, the extent that this affects the polarisation dependent gain & NF might differ.

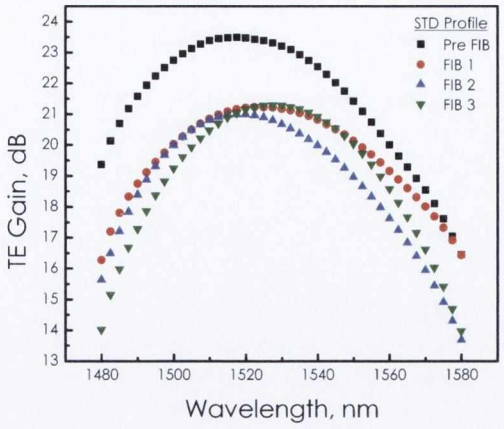

Figure 7.16: Wavelength dependent gain of the Standard pumping profile over successive etching iterations for a small-signal injected along the transverse electric (TE) eigen mode.

The most striking feature of the plot is the initial drop in gain from 23.5dB at 1518nm before any material is removed, to approximately 21dB at red-shifted wavelengths for the post FIB scenarios. It was noticed, that due to the aforementioned drift which plagued this process, a small amount of gold was removed from the contacts. This occurred after FIB-1 only. The possibility exists that this effective widening of the slot region produces a localised reduction in gain in this region, resulting in this initial drop in gain. As the drift was contained within the slot region over subsequent FIB iterations, the gain after this point does not drop off as sharply. It should be noted that material debris remained on one of the facets after stage two of the etching process, and this is likely the cause of the break in trend of both peak wavelength shift, and 3dB bandwidth. It will not be presented after this section. The spectral influence over successive iterations has also shown to be of importance, mirroring the ASE spectra presented. The corresponding gain for a TM signal is shown in Figure 7.17

The TM gain for the Standard profile, behaves similarly to the TE case in terms of slight red shift Post FIB-1, and also with regards to the stray behaviour of post FIB-2 data. The peak TM gain is 23.1dB at 1519nm. Again, a significant drop in gain occurs after the first etching stage. As was seen previously where the ASE output levels were similarly reduced, it was thought solely due to an increase in non-radiative recombinations. However, the effect was to a much lesser degree than 2dB, and so acts as only a partial explanation for the difference, again adding support to the localised reduction of gain between the contacts. Finally, as this data is taken for the Standard profile, improving the carrier density may have little effect on the gain and NF. For the Low Noise profile, where the gradient in carrier density between adjacent contacts is large,

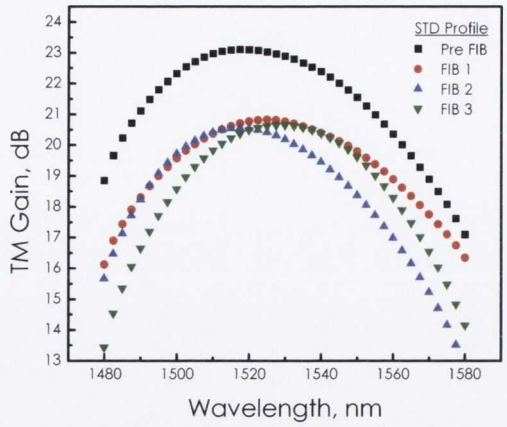

Figure 7.17: Wavelength dependent gain of the Standard pumping profile over successive etching iterations for a small-signal injected along the transverse magnetic (TM) eigen mode.

the effect should be more substantial. Figure 7.18 plots the polarisation dependent change in the peak gain wavelength as a consequence of the etching procedure.There is a trend of red shifting of over 10nm along each eigen mode. The difference in peak wavelength of the TE and TM modes is maintained at 1nm over all stages, within the error of the measurement. It is possible that the peak shift to lower energy is associated with an increase in defect and surface state recombination [8], as these would generally manifest at lower wavelengths.

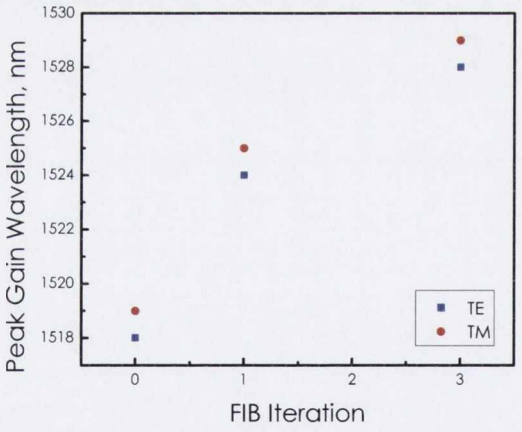

Figure 7.18: Peak small-signal gain wavelength for both TE & TM injected polarisations plotted for each etching stage.

Finally the change in polarisation dependent gain (PDG) is given by Figure 7.19 and seen to increase. The % of TE & TM co-polarised ASE (not shown), does not vary with the FIB stage, presenting an unusual situation where there is a change in polarisation dependent gain, and also in the polarisation resolved ASE spectra. However the relative change in measured ASE power

for both modes is the same as the total unresolved power change. The difference in PDG is quite low, with a total increase from pre FIB to the final iteration of 0.35dB.

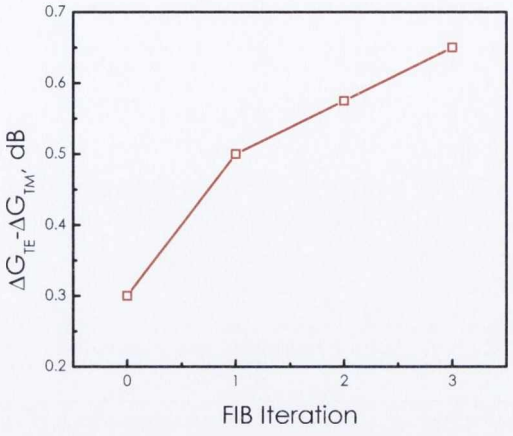

Figure 7.19: Change in polarisation dependent gain difference with each etching step.

Standard Current Profile - Noise Figure

The noise figure corresponding to the gain curves above are given in Figure 7.20 and Figure 7.21. It must be noted that any decrease in NF after FIB-1, occurs where the gain level is largely unchanged, signifying a direct influence on the ASE, which was seen previously in the LI data.

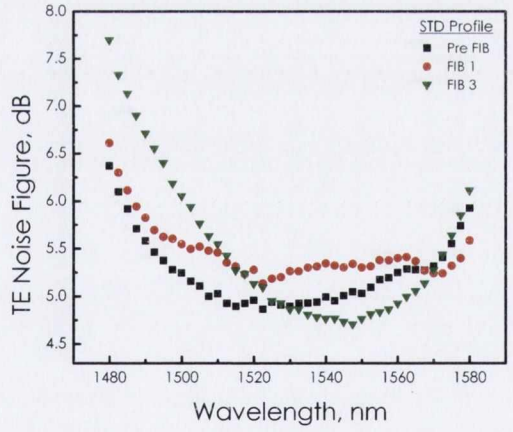

Figure 7.20: Wavelength dependent noise figure of the Standard pumping profile over successive etching iterations for a small-signal injected along the transverse electric (TE) eigen mode

Looking first at the TE NF for the Standard bias configuration (the blue data, post FIB-2, has been removed) it is clear that there is little trend in the NF reduction, as the effect of the first stage of milling is to increase the NF, corresponding to the drop in gain. However by the end of the third stage, the NF has decreased slightly, by 0.4dB, albeit at a much shifted wavelength

to lower energy. This occurs with a sacrifice to useable bandwidth, mirroring the change in gain performance,and the ASE. The minimum measured NF after the final stage of etching is 4.75dB at 1547nm, representing a substantial shift in NF minima.

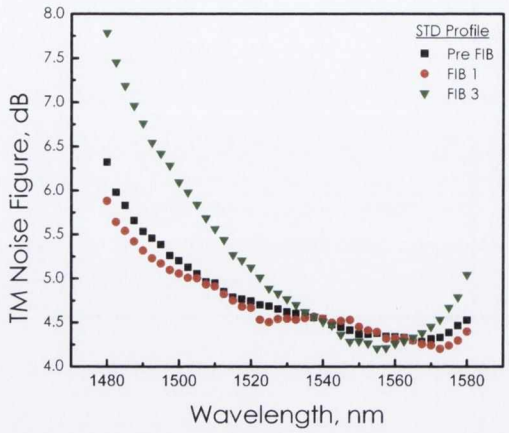

Figure 7.21: Wavelength dependent noise figure of the Standard pumping profile over successive etching iterations for a small-signal injected along the transverse magnetic (TM) eigen mode

The TM NF data on the other hand shows a relative lack of change in NF in the region of peak performance, with the pre FIB, first and third FIB stages contained within 0.2dB from 1535 to 1565nm. This is a positive result in that improving the carrier control over the standard profile, should not yield a large change in NF. The same sacrifice to bandwidth is seen in this data after the final stage of etching. A large increase in NF occurs at lower wavelengths, with an increase in NF of over 1.0dB in the range of 1480nm1500nm, reflecting the larger change in TM gain on the blue side.

Low Noise Current Profile - Gain

The Low Noise profile is now discussed. In this case any improvement in control is hoped to lead to a reduced NF, negating the effects of carrier leakage. Figure 7.22 plots the gain for the Low Noise bias configuration, along the TE axis, for the same injected signal power as before. The pre FIB and FIB-1 gain levels are almost identical with a 0.1dB difference, with values of 20dB and 19.9dB respectively at 1530nm. At Post FIB-3 the difference in gain levels relative to the other stages decreases by a further 0.2dB, and a small shift to longer wavelength.

The TM gain data is given in Figure 7.23. The modification of the gain in this case is similarly small for Post FIB-1, relative to the Pre FIB conditions, however, there is a larger effect on the gain compared with that experienced by the TE data. Specifically, a decrease in gain of 0.9dB to 18.9dB at shifted peak of 1535nm. As was the case before, the decrease in gain is more

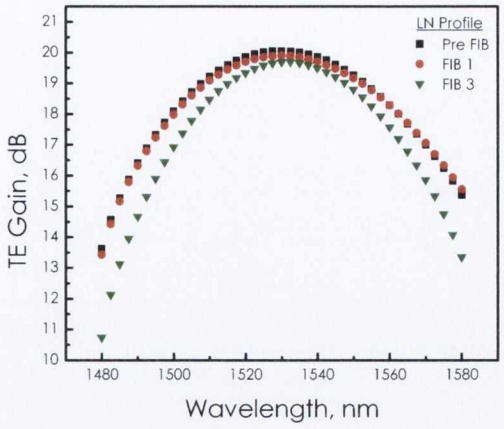

Figure 7.22: Wavelength dependent gain of the Low Noise pumping profile over successive etching iterations for a small-signal injected along the transverse electric (TE) eigen mode

significant at lower wavelengths.

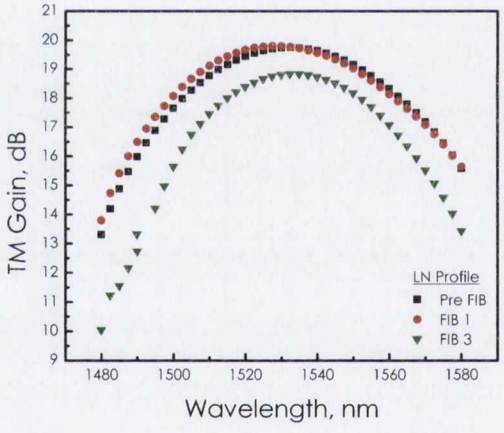

Figure 7.23: Wavelength dependent gain of the Low Noise pumping profile over successive etching iterations for a small-signal injected along the transverse magnetic (TM) eigen mode

The resultant shift in peak wavelengths and gain bandwidth are shown in Figure 7.24. As opposed to the standard case, there is much less of a peak shift for either TE or TM. The TE case shifts by only 2nm over the 4 FIB stages, where as he TM deviates by a maximum of 4nm. It is also noted that by the end of FIB-3 the peak gain wavelengths have are close to the pre-FIB values.

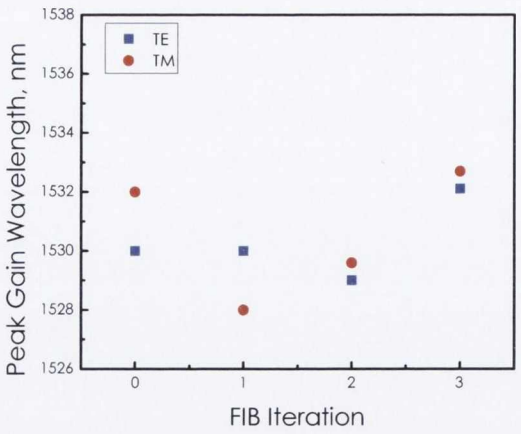

Figure 7.24: Peak small-signal gain wavelength for both TE & TM injected polarisations plotted for each etching stage.

Low Noise Current Profile - Noise Figure

The TE NF for the Low Noise Profile is given by Figure 7.25. Successive improvement in NF is achieved, with a change from 5.34dB to 5.16dB at 1550nm, after the first milling stage. Then excluding the second stage, and looking at the final attempt, a further improvement of 0.29dB to 4.87dB is achieved. This results in a total NF improvement at 1550nm of 0.47dB, at a constant injected bias. This wavelength corresponds to the largest range of NF improvement for the TE mode. Due to the bandwidth decrease post FIB 3, the improvement is limited at longer wavelengths. At higher energies no improvement is observed. In fact with each iteration the NF worsens. These slight improvements occur even as the gain is held reasonably constant after each etch, and indeed for the best NF obtained the gain has decreased by its maximum amount. From this data it is clear that for the small improvement in NF around the wavelength of NF minima, a greater sacrifice is made to NF performance at lower wavelengths. The FIB technique is far from ideal in this situation and is used only to investigate if changes of the contact isolation benefit the NF control, which it does. At the fabrication level, where control of the slot dimensions is of significantly better resolution, better performance across all wavelengths would likely be achieved.

The TM NF is given by Figure 7.26. Due to the larger sacrifice in gain resulting from FIB-3, the NF fails to decrease beyond the improvements achieved by FIB-1. This result however proved significant, giving an improvement in NF of 0.3dB at 1530nm, and 0.5dB at 1550nm.

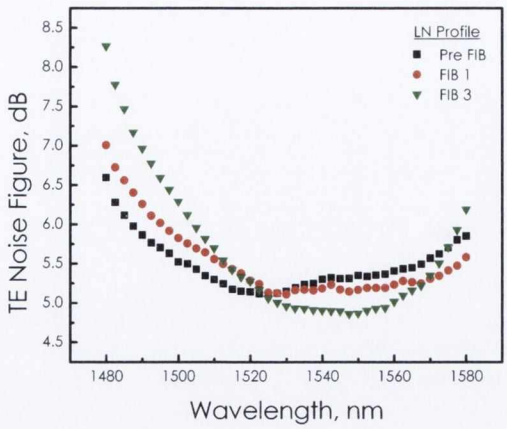

Figure 7.25: Iterative NF across all FIB stages for the Low Noise current configuration for injection along the TE mode.

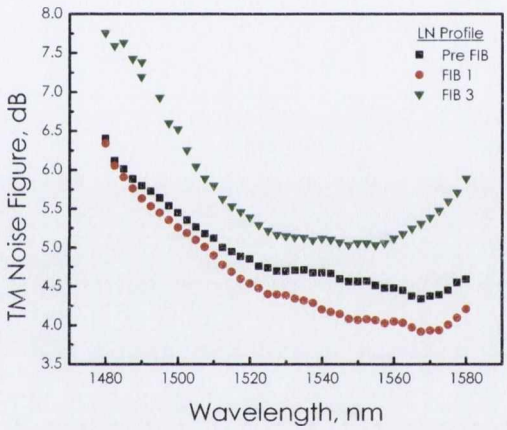

Figure 7.26: Iterative NF across all FIB stages for the Low Noise current configuration for injection along the TM eigen mode.

The onset of improvement in TM NF occurs at higher energies, and is stable over a larger bandwidth. The initial deviation from the Pre FIB data occurs at 1488nm, with a difference of 0.1dB. This opens up to nearly 0.5dB over a range of 1534nm to the limits of the ECL at 1580nm.

7.4 Comparison

To summarise the relative achievements of this post-processing of the MCSOA, the NF is plotted for all the stages of the characterisation (bar FIB-2) for the Standard (solid shapes) and Low

Noise Profiles (hollow shapes). The data is given separately for each of the two polarisation eigen modes. The TE noise figure is plotted in Figure 7.27.

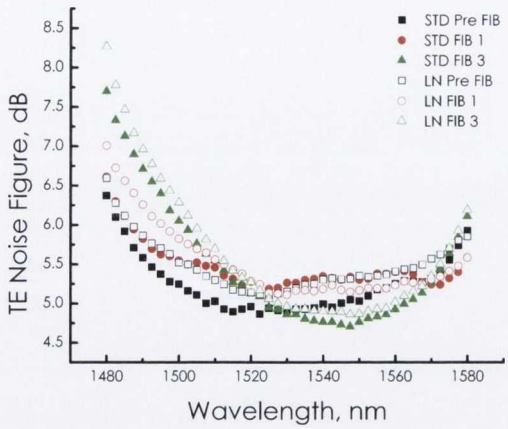

Figure 7.27: TE noise figure as a function of wavelength over all the mill iterations

The previous plots showed the wavelength dependent change in NF as a function of FIB step for a given profile. In this plot any improvement in NF when the Low Noise current profile is applied can be seen relative to the Standard profile. In this case the improvement is non-existent except with the exception of FIB-1 where the Low NF set up is marginally better, however around the peak wavelengths the differences are negligible. On top of this, in the only instance where the NF is improved over the Pre FIB Standard data, the Standard NF at the same stage for etching has also improved, negating any changes. The TM data is given by Figure 7.28.

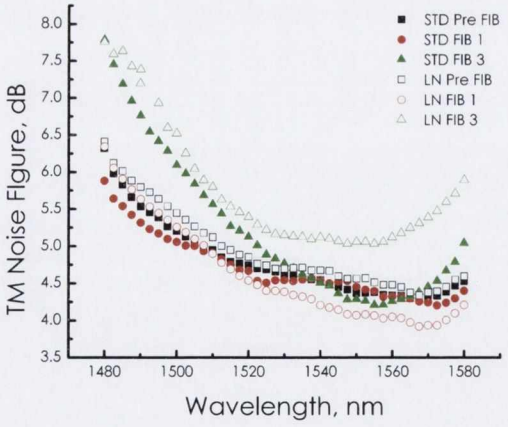

Figure 7.28: TM noise figure as a function of wavelength over all the mill iterations, for the Standard and Low Noise profiles

Whereas the TE data showed some incremental improvement in NF for the Low Noise profile,

the TM data below, yields a positive result relative to the baseline NF of the Standard profile Pre FIB. The solid data representing the Standard profile is relatively constant, bar the change in bandwidth seen previously. The initial NF performance under Low Noise conditions was actually slightly worse than the Standard case. However after the first FIB etch, the NF decreased by nearly 0.5dB, relative to both the Pre and FIB-1 Standard profile. After this, as a result of possibly etching too deeply, the NF increased again beyond the original value. This was even more prevalent off the peak wavelength.

7.5 Conclusions

This chapter explored the idea of reducing the level of current leakage between adjacent sections, by selectively etching material from the isolation region between neighbouring contacts. The chosen technique for achieving this was Focused Ion Beam (FIB) milling, due to its versatility and accuracy for post processing in this way. Although regarded as a slow process, lacking the rapidity of fabrication for cost effective mass production of components compared with conventional mask lithography, for developmental work it proved ideal on paper. In reality, due to limitations of how the MCSOA chips are mounted the process proved difficult, with accuracy of the milling region greatly affected by surface charging and consequent drift of the sample.

A sacrificial MCSOA was probed using the FIB and accompanying SEM, to determine the layer structure and depths from the surface. With this knowledge the characterised MCSOA was processed a total of three times, and characterised in the steady state at each point, including an initial characterisation before any etching. The planned milling depth per etch was 500nm, however for the reasons outlined this was rarely adhered to, instead producing a non-uniform depth profile. In addition to this, during the first FIB stage, some of the gold contact was accidentally removed, leading to an effective widening of isolation Slot A. The final depths reached are 2500nm and 2100nm for Slot A and Slot B, respectively. The top of the active layer is 4000nm from the surface. The resistance, measured directly between contacts, was found to increase from 300Ω to 1kΩ at Slot A, and 340Ω to 740Ω at Slot B.

The experimental consequence of this was first examined, as before, through the LI and ASE data. As a result of the increased isolation, and possibly other factors, the undesired asymmetrical output of the Standard profile converged over each step. The original power difference was thought to be a product of current leakage between sections, ultimately creating a non-uniform

current profile and output power. With the introduction of increased isolation, this effect was seen to be reduced. However, the unplanned increase in slot width may also have contributed to this. The final relative power difference was 1dB, an improvement of over 0.8dB from the Pre FIB data. When looking at the ASE spectra for the Standard profile, the peak power changed only slightly, however the bandwidth decreased with each iteration, contributing to the total power reduction observed.

The characterisation of the MCSOA under injection of a small signal, mirrored this change in bandwidth. Initially, as a result of the first FIB stage, the gain in both the TE and TM modes dropped by nearly 2dB for the Standard profile, where the total system gain is more susceptible to the widening of the Slot A region. However, under the Low NF configuration the gain is largely set by the input section, and so if there is a localised reduction in a small region underneath Slot A, it would have less of an effect on the gain. This is exactly what was seen, where the iterative reduction in peak gain over each FIB step is quite low. The bandwidth however was affected similarly as before. The non-uniform surface topography resulting from the poor etch, which could be construed as damage, is also potentially responsible for an increase in both surface and defect state recombination. The effect of this would be to reduce the total carrier density along the length of the device. With this in mind, a small improvement in TM NF of 0.5dB was still observed relative to the unperturbed device with an injected Standard current profile. This change is believed to be a product of the isolation change and represents an excellent outcome.

The aim of this chapter was to apply a post processing technique to investigate one of many design characteristics of the prototype which will need to be refined in future generations of the MCSOA concept. Physically little can be done to the device beyond this work to tweak performance and validate the concept more fully than in Chapter 5. Although the attempt at augmenting the ability of the MCSOA to control the carrier profile was difficult and not fully accountable for any improvements, a NF reduction was observed, which we believe to be directly related to the increased isolation. In fact the main outcome of this chapter was that although not unequivocal, further control of the carrier density profile is desirable. Future design concepts will take this into account at the modelling level, using this information, along with different gain media models and internal structures to help improve overall performance and control.

References

[1] F. Watt, A. A. Bettiol, J. Kan, E. J. Teo, and M. B. H. Breese, "Ion beam lithography and nanofabrication: A review," *International Journal of Nanoscience*, vol. 4, no. 3, pp. 269–286, 2005.

[2] C. Faulkner, *Focused Ion Beam patterning of planar magnetic nanowires*. PhD thesis, Trinity College Dublin, 2006.

[3] N. Yao, *Handbook of Microscopy for Nanotechnology: Focused Ion Beam SystemA Multifunctional Tool For Nanotechnology*. No. figure 1, Springer, 2005.

[4] D. Petit, C. C. Faulkner, S. Johnstone, D. Wood, and R. P. Cowburn, "Nanometer scale patterning using focused ion beam milling," *Review of Scientific Instruments*, vol. 76, no. 2, p. 026105, 2005.

[5] S. N. Bhavsar, S. Aravindan, and P. V. Rao, "A critical review on microtools fabrication by focused ion beam (FIB) technology," in *Proceedings of the World Congress on Engineering, Volume II*, vol. II, 2009.

[6] L. A. Giannuzzi, *Introduction to Focussed Ion Beams: Instrumentation, Theory, Techniques and Practice*. Springer, 2005.

[7] J. Buus, *Tunabe Laser Diodes & Related Optical Sources*.

[8] L. A. Coldren, S. W. Corzine, *Diode Lasers and Photonic Integrated Circuits*.

[9] M. J. Connolly, *Semiconductor Optical Amplifiers*. Kluwer Academic Publishers, Boston, 2010.

[10] Q. Y. Lu, W. H. Guo, R. Phelan, D. Byrne, J. F. Donegan, P. Lambkin, and B. Corbett, "Analysis of slot characteristics in slotted single-mode semiconductor lasers using the 2-D scattering matrix method," *Photonics Technology Letters, IEEE*, vol. 18, no. 24, pp. 2605–2607, 2006.

[11] J. P. Engelstaedter, B. Roycroft, and B. Corbett, "Laser and detector using integrated reflector for photonic integration," *Electronics Letters*, vol. 44, no. 17, pp. 3–4, 2008.

[12] Q. Lu, W. Guo, M. Nawrocka, A. Abdullaev, C. Daunt, J. O'Callaghan, M. Lynch, V. Weldon, F. Peters, and J. F. Donegan, "Single mode lasers based on slots suitable for photonic integration.," *Optics express*, vol. 19, pp. B140–5, Dec. 2011.

[13] G. Lifante, *Integrated Photonics Fundamentals*. No. March, Wiley, 2003.

[14] S. Charbonneau, E. Koteles, P. Poole, J. He, G. Aers, J. Haysom, M. Buchanan, Y. Feng, A. Delage, F. Yang, M. Davies, R. Goldberg, P. Piva, and I. Mitchell, "Photonic integrated circuits fabricated using ion implantation," *IEEE Journal of Selected Topics in Quantum Electronics*, vol. 4, no. 4, pp. 772–793, 1998.

8

Conclusions & Future Work

This thesis was concerned with the reduction of the noise figure (NF) of semiconductor optical amplifiers. A specific concept was proposed to reduce the NF of SOAs based on modification of the longitudinal carrier density profile, to a particular distribution. The technique was described conceptually relative to a Standard profile of the same total carrier density, before detailing two very different designs for achieving the low NF condition. Through characterisation of these SOAs, proof of principle was achieved as direct control of NF was demonstrated. In addition to this it was shown that a corollary of the NF technique allows for the improvement in saturation power by reversing the optimum NF conditions. A summary of the results is now given for each structure.

8.1 Lateral Cavity SOA

The first of two designs presented was based on the implementation of a lateral lasing cavity transverse to a portion of a multi-quantum well active length. Resonance was provided by InP/air Distributed Bragg Reflectors (DBR), etched directly into the cladding region outside the active width. It was shown through simulation that upon reaching threshold the lateral laser clamps the output carrier density, establishing the conditions for a reduced NF. It was also demonstrated that the manifestation of the lasing function is a change in slope of the output photon density, and indeed that the optimum conditions occur for a mirror length of ~60% of the active length. The direct affect on the carrier density profile upon initialisation of lasing was shown relative to the expected carrier density in a device with no lateral cavity, and of the same physical dimensions.

A number of chips were fabricated for experimental characterization. Of these, five emitting devices with different mirror types and positions were characterised, one of which had no lateral cavity representing the ideal control device. The LCSOAs were investigated initially under the conditions of no injection, where the ASE spectra and absolute power were collected to illustrate the effective reduction and asymmetry in ASE power produced. This acted as a good indicator of the noise performance under injection of a continuous wave signal. Indeed, this ASE-LI characterisation proved valuable in determining the success of the clamping mechanism on the spontaneous amplified noise source.

The small-signal gain and NF performance was established for the most promising of the LCSOAs and the control device. Although from the same wafer, and physically identical with the exception of the absence of a lateral cavity, a direct comparison between the chips was difficult due to differing gains. By injecting in a forward propagation direction, the Low Noise profile was accessed while reversing this then acted as a proof of concept, producing an increased NF. An improvement over the reverse propagation injection of 2.55dB was accompanied by a small shift in peak wavelength, representing the effect of the non-uniform carrier profile. This result directly corroborates the concept proposed, however comparison of the effectiveness with literature is difficult. This is because previous work has demonstrated an improvement in NF with an equivalent Standard carrier density profile in the same SOA, something the LCSOA is not capable of. The LCSOA device cannot establish a Standard profile, but rather compares between a low and higher NF at the same total current density, depending on which facet the light is injected into.

The carrier modification effect on the saturation performance of the device was also determined. The 3dB saturation output power for forward injection is 2.75dBm, and 4.33dBm for reverse injection. When injecting into the output side of the device (reverse propagation) it was found to increase by 1.58dB, as expected based on the discussion of Chapter 3. This improvement represents a significant contribution to the area of SOA development, specifically power saturation improvement, complimenting other methods demonstrated in the literature [1, 2, 3]. The improved saturation performance when the LCSOA is operated in reverse propagation may be ideal for application as a booster amplifier.

The nature and complexity of the LCSOA from a fabrication and simulation point of view was also addressed. There were a number of key issues highlighted that greatly affect future design iterations. It was discussed that from a growth perspective, the dimensions of the DBRs may lead to non-ideal fabrication. The dry-etch process used to remove the InP material to create the air trenches, is state of the art. However, this was the primary attempt at creating these structures and some problems resulted. Furthermore, operating constraints of the mirrors means that the trenches themselves require an excellent degree of surface uniformity, a criteria that may not have been met in the LCSOA chips grown. This last point may have been localised to specific points in the mirrors as the width is long, at 450μm, making it more difficult to sustain the etching process. These points represent possible reasons that all the chips did not operate as intended, and are speculative. Future work will investigate how critically variations in mirror reflectivity affect the device performance. This will also include the scenario where gold may leak into the slots during growth. With additions to the modelling of the LCSOA, including the implementation of a more appropriate gain model to fully represent the multi-QW active region and the effects of wideband ASE, an improvement in the design of future iterations and further control of the NF can be achieved.

8.2 Multi Contact SOA

Noise figure control based on the same concept described, was also achieved by using a bulk multi-contact SOA (MCSOA). In this case it was shown that carrier density control is achieved more directly and with great versatility, and where no gain-clamping takes place in the MCSOA.

8.2.1 Steady State

The steady-state performance of the device was initially observed through a modified version of the LCSOA simulation, taking the multi contact nature of the MCSOA into account. In this case the reverse propagation (High P_{sat}) equivalent was achieved by changing the applied current to the opposite profile. It was shown that a gain sacrifice exists between the Low Noise and High P_{sat} conditions, and that of the homogenous Standard SOA profile. This is an expected result as the gain available in the low carrier density regions of the device is reduced. However the simulated improvement in NF between the Low NF profile and that of the Standard profile is 0.8dB. The difference between the two noise controlled profiles is 2.3dB at 1590nm, increasing to ~4dB at lower wavelengths, showing substantial control with this technique. The simulated carrier density profile dependent power saturation was equally impressive, with an increase in P_{sat} at the peak wavelength, to a maximum value of 12.6dBm. This equates to a 1.6dB improvement over the control case and a 4.45dB increase relative to the Low Noise profile. This represents an important distinction in the relative level of control achievable between the NF and saturation power. More specifically, the data presents a qualitative look at the sensitivity to carrier density profile, the outcome being that the saturation power is highly sensitive to the modification, where as the NF is much less so.

Experimentally, the steady-state performance for the MCSOA was first observed in a similar fashion to the LCSOA, by observing changes in the light output. In this case, the behaviour as a function of individual sections was acquired before looking at the device working at the three current profiles used to test the concept. The LI data provided good evidence for the carrier density effect, and subsequent behaviour under injection. In particular, the ASE spectra collected for the three current profiles exhibited a clear level of control of the ASE, both in magnitude and spectrally.

The proof of concept for this design was demonstrated by continuous wave injection. As predicted by simulation a gain difference occurs between the Standard profile and the noise controlled profiles, which had a further contact size related discrepancy between each other of 0.7dB. The difference in NF of the High P_sat case over the low noise case is approximately 2dB, which showed directly the clear effect due to the bias current distribution, but 0.75dB less than the simulated difference. Intrinsic NF values compare very well with those found in the literature for bulk structures [4, 5]. The improvement relative to the Standard profile at the same current density, was found to be minimal, in disagreement with the predicted result. It

is believed the reason for this was related to carrier leakage between sections, which was not taken into account in the simulations.

The relation between the CW NF characterisation and a more practical figure of merit, the bit error ratio (BER), was also investigated. Under non-saturated injection, the BER was tested at two wavelengths, the peak gain wavelength 1565nm, and an off peak wavelength of 1550nm. The low noise configuration displays a better sensitivity over the High P_{sat} as expected, with a power penalty of 1.21dB for the High P_{sat} configuration, at 1565nm. However, the Low NF profile, sacrifices a power penalty when compared with the Standard profile, with the single contact distribution performing better. This minimal contrast in NF in both the steady state and BER data, was addressed by post processing of the slot region, in an attempt to reduce the level of carrier leakage.

8.2.2 MCSOA Development

A reduction in current leakage between adjacent contacts was achieved by successive Focused Ion Beam (FIB) etching steps, removing InP material locally from within the isolation slot regions. The function of the FIB and the process undertaken was described. The ultimate depths reached were approximately 3000nm, from the surface of the p-type layer. It was shown that with each progression of slot depth the resistance measured between adjacent contacts was increased. The maximum value achieved in the end was 1kΩ, a 700Ω improvement from its starting value of 0.3kΩ. It is believed, based on the literature, that 1kΩ will provide sufficient isolation. By then assessing the steady-state change in performance as the resistance was increased it was possible to quantify the effect. The characterisation technique was identical to before, where firstly non-injection based measurements were taken, followed by injection of a continuous wave.

The LI data revealed an overall reduction in ASE power produced for all bias distributions. The measured spectra also showed the effect of reduced gain, manifesting as a reduction in the residual ripple depth. However, these data also positively showed a reduction in the power deficit that existed between light measured at the input and output sides, respectively, under Standard pumping, representing an improvement of 0.8dB. This original asymmetry was thought to be related to carrier leakage. It is believed that this effect could have been improved upon more substantially, however the milling process became unusable at times, leading to either poor etching confidence, or no increase in depth. This latter point was visible between FIB-1 and

FIB-2 at one of the slots, as due to surface charge milling was impossible.

The gain and NF spectral dependence was then determined under continuous wave injection, using the previous techniques. Although it was shown that a reduction in gain occurred relative to the pre-FIB conditions, it was seen that when comparing the NF of the Pre-FIB Standard profile, and that of the Low NF profile post FIB1, a reduction in NF of 0.5dB was achieved, to a minimum attained value of 4dB at a red shifted wavelength for a TM polarised signal. This is an excellent and highly positive result, despite the small decrease in gain which generally acts counter to NF reduction. This data from a design point of view is very valuable. TE polarised improvements did not occur to the same extent, also requiring deeper etches to see a small improvement.

The simulated NF reduction relative to the Standard profile was never achieved in the MCSOA experimentally. Of course the simulation represents an ideality, and does not factor in a number of important elements, that have been identified in the course of this study. The most significant of these is carrier diffusion between sections. The natural progression of device refinement is multiple iterations of the simultion, design, fabrication and experimental characterisation. However, limiting this process to as few steps as possible is a valid goal. The FIB etching provided this opportunity, and with very positive results. However, this is not to say that FIB processing is the preferred solution. In fact, based on the troubles endured with sample drift and time taken, FIBing does not represent the best method for improved isolation at the growth level. Instead, ion and proton implantation, which have been used widely in multi-section lasers and integrated photonics, are likely the greatest candidates for this role. It is believed that through improved simulation, improved design, and as a consequence better isolation between contacts, NF control can be significantly bettered.

Additional design features may also benefit the concept, and will also require comprehensive simulation. The first is the number of contacts. The three section MCSOA detailed here proved ideal due to its short length. However, as longer devices are required this may need to be compensated for by using additional contacts. This furthers the case for a single source/resistor network based injection scheme, as the cost will undoubtedly grow with the number of sources required. The size of these contacts will also require additional work, especially in terms of the dynamic performance seen. In that case there was a sacrifice made to overall gain, however by improving the chip gain and minimising the absorbing section used to suppress the interband recovery, better performance may be obtained, discussed below.

With all of this in mind, future simulation, and the concept of NF reduction, may benefit well from alternative gain media, specifically quantum dots (QD). The benefits of QD gain media have been well documented in the literature and discussed previously, but it is still a fledgling area of SOA research. Their quasi three-level system is naturally lower in noise than the two-level bulk structure, in effect more akin to the Erbium doped fibre amplifier (EDFA). Future work in this regard will be computationally intensive, requiring both analysis of the additional length generally required by the low confinement QD gain medium, and the consequent effect of this on electrode number. From a dynamic point of view this is especially interesting as QDSOAs have already displayed very impressive recovery rates. The combination of the two techniques may lead to further improvements in this regard.

8.2.3 Gain Dynamics

The MCSOA gain dynamics were investigated using a contra-propagation pump-probe technique for two injected current schemes. The first part of the work was concerned with observing any changes in dynamic behaviour for the three bias configurations discussed, at a constant injected bias. The data was analysed in terms of both the relative contribution of interband and intraband gain compressions, and their associated timescales. The gain compressions were found to be reduced across all pump powers for the Low Noise and High P_{sat} cases, relative to the Standard profile. This was an expected result due to the reduced gain observed for these two profiles. The profile dependent timescales presented typical behaviour at high pump powers, however at low pump powers an effect directly related to the local carrier density at the output was observed. In this case the effect of the pump was altered by this carrier density difference. The result was a difference in fall time experienced by the gain compression. This results in a much longer fall time for the Low Noise profile, due to its lesser carrier density at the output, followed by the Standard case and the High P_{sat} case, respectively. The intraband recovery follows a similar pattern, with the exception at high powers that the High P_{sat} profile experiences slower times than the other two profiles. The final, and in many ways most important compression and timescale combination, is related to the interband recovery, and represents a limitation of the MCSOA as a functional component. The slow compressions were again found to follow a typical trend, with the greater magnitude experienced by the Standard profile. However, when looking at the time constant associated with this process, the carrier profile dependence manifests as a 100ps recovery difference between the Standard profile and the other two distributions. This is a direct result of the reduction of ASE by the non-uniform profiles [6, 7], and is an important

result which may need to be taken into consideration depending on the application and the appropriate carrier profile.

As the multi-contact nature of the MCSOA allows for variation of the pump and probe facet currents, the effect of the complete variation of this from 0mA-90mA was investigated, as it was expected to be able to instigate atypical features on the decays. This data was taken for a variation in i_{tot}, another important distinction from the previous described results. The experiment looked at the effect of both pump and probe facet-bias variation, each in turn.

It was found that applied currents below 3mA produced interesting transients as a result of the carrier density in the output section being below or around transparency. As a result, a strong absorption peak was observed before decay and recovery as the effect of the other sections took over. At higher biases than 5mA the decays approached a typical form. However at low biases, for both facets, it was shown that the relative importance of intraband and interband recovery can be controlled precisely, which may have a significant impact on potential application.

For pump facet current variation, the effect of the pump at low carrier densities was to produce a sharp local peak in gain, optically induced, followed by a typical gain recovery. However in this case the interband process was a slow relaxation. As the carrier density approached transparency for the section, the complete suppression of slow recovery was achieved. The entire process then, of bleaching and total recovery to an unsaturated level, occurred via three stages: An absorption time of ~5ps, a total compression of 6ps and a final fast recovery back to the unsaturated gain of 4ps. Further work is required to understand the potential applications of this behaviour. Recently, Tian et al [8]. have demonstrated simulation of a 2 section SOA under injection of a co-linear 10ps pump and CW probe. In this case the output section is pumped to a greater extent to counteract patterning effects due to the gain recovery process. This represents a different cross gain modulation setup to that described here, leading to the observation of different transients. We have found that around the transparency current of the output section, the slow recovery has been completely suppressed due to dynamic gain compensation of this section, similar to Zhou et al [9] but with a single SOA, and with no additional filtering required.

In the opposite case to this, where the bias of the section at the probe input was varied, the potential switch capabilities are more clear cut. When the input facet bias was held near the transparency current of that section, the gain recovery may be limited to just intraband processes. Following a maximum gain compression of 6dB, a full recovery back to the baseline occurs over approximately ~5ps. Full recovery rates in bulk materials have not been demon-

strated at these speeds. Other work has achieved extremely good recovery, such as the Turbo-Switch [10]; two-colour set-ups, where the pump acts near the transparency wavelength [11]; polarization based switching demonstrated by Philippe et al. in bulk SOAs; and more recently in bulk SOAs with two sections by Zhou [9]. It must be noted though that unlike these other methods, the fast recovery comes at a cost to gain, and therefore the SNR, which may impact specific application [10]. It is thought that by improving the gain of the remaining sections, by any of the number of techniques described previously, the SNR can be preserved. Future work in this regard will rely heavily on computational investigations of the ultrafast gain and phase dynamics, for a variety of gain media and device geometries (including the number and relative size of the contacts), in addition to a collinear XGM configuration.

References

[1] J. Klamkin, J. J. Plant, M. Sheehan, W. Loh, S. M. Madison, and P. W. Juodawlkis, "High-output saturation power variable confinement slab coupled optical waveguide amplifier," in *Optical FIbre Communications*, vol. 1, pp. 10–12, 2011.

[2] M. Yoshino and K. Inoue, "Improvement of saturation output power in a semiconductor laser amplifier through pumping light injection," *IEEE Photonics Technology Letters*, vol. 8, no. 1, pp. 58–59, 1996.

[3] M. Babaei, S. Somayeh Hosseini, S. Mirza Kuchaki, "Improving gain and saturation output power in single quantum well semiconductor optical amplifiers by injection current," *World Applied Sciences Journal*, vol. 10, no. 3, pp. 342–347, 2010.

[4] S. S. Saini, J. Bowser, R. Enck, V. Luciani, P. J. S. Heim, M. Dagenais, "A Semiconductor Optical Amplifier with high saturation power, low noise figure and low polarization dependent gain over the C-band," in *Lasers and Electro-Optics Society (LEOS)*, pp. 102–103, 2004.

[5] M. J. Connolly, *Semiconductor Optical Amplifiers*. Kluwer Academic Publishers, Boston, 2010.

[6] R. Lennox, K. Carney, R. Maldonado-Basilio, S. Philippe, a. L. Bradley, and P. Landais, "Impact of bias current distribution on the noise figure and power saturation of a multi-contact semiconductor optical amplifier," *Optics letters*, vol. 36, pp. 2521–3, July 2011.

[7] J. C. S. F. Ginovart, "Gain dynamics studies of a semiconductor optical amplifier," *J. Opt. A: Appl. Opt.*, vol. 4, pp. 283–287, 2002.

[8] P. Tian, L. Huang, W. Hong, and D. Huang, "Pattern effect reduction in all-optical wavelength conversion using a two-electrode semiconductor optical amplifier," *Applied Optics*, vol. 49, no. 26, pp. 5005–5012, 2010.

[9] E. Zhou, F. Ohman, C. Cheng, X. Zhang, W. Hong, J. Mø rk, and D. Huang, "Reduction of patterning effects in SOA based wavelength converters by combining cross-gain and cross-absorption modulation.," *Optics express*, vol. 16, pp. 21522–21528, Dec. 2008.

[10] R. J. Manning, R. Giller, X. Yang, R. P. Webb, and D. Cotter, "SOAs for all-optical switching techniques for increasing the speed," in *International Conference of Transparent Optical Networks (ICTON)*, vol. 00, pp. 239–242, 2007.

[11] C. S. Cleary, M. J. Power, S. Schneider, R. P. Webb, and R. J. Manning, "Fast gain recovery rates with strong wavelength dependence in a non-linear SOA.," *Optics express*, vol. 18, pp. 25726–37, Dec. 2010.

A

Steady-State Multi-Section Program

The segmented steady state model used to simulate the continuous wave performance of the SOAs used in this thesis was written and developed in Dublin City University, by F. Surre. Additional modifications necessitated by multi-contact modelling were undertaken by Carney & Lennox [1] . The model itself is based on that of Connolly [2] and Durhuus [3]. The flowchart of the simulation is given by Figure A.1. Initially, the SOA paramters are input and an arbitrary carrier density value is chosen. From this the signal and ASE fields are calculated. The rate equation is solved such that the change in carrier density is a minimum. This begins the iterative process until convergence is reached. From this value of carrier density all output parameters are calculated.

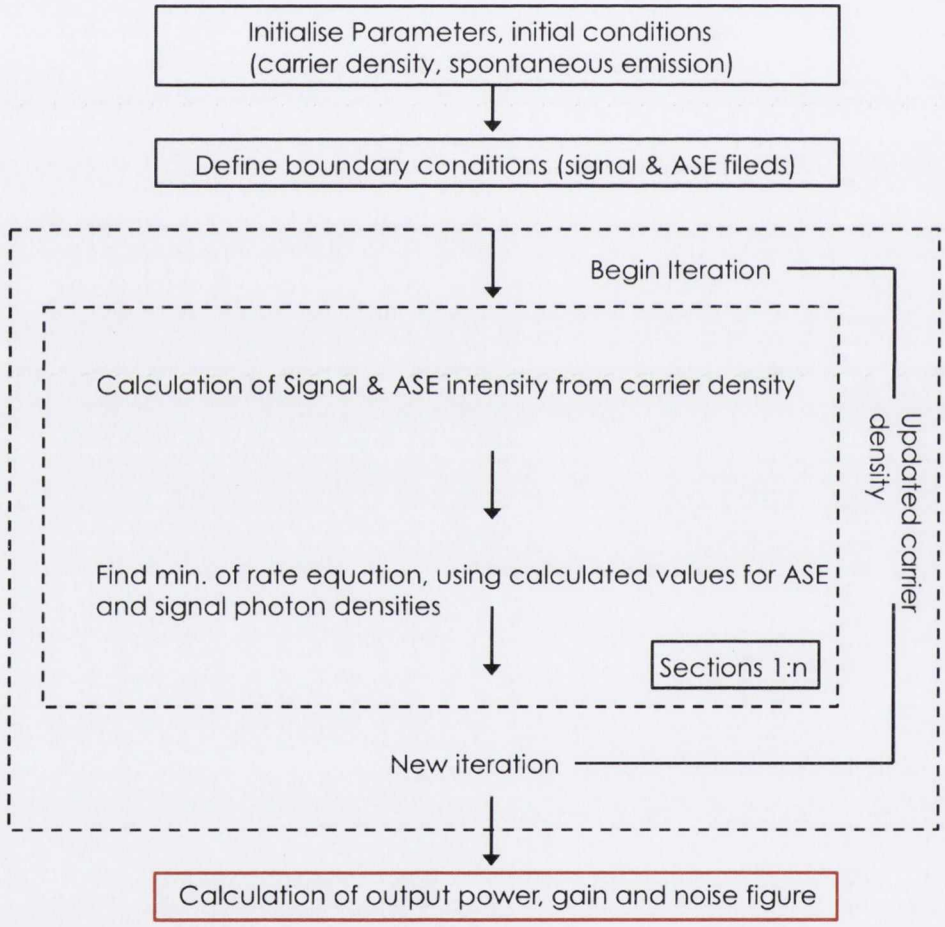

Figure A.1: Flow diagram of the iterative segmented-simulation of gain and NF calculation

References

[1] R. Lennox, K. Carney, R. Maldonado-Basilio, S. Philippe, a. L. Bradley, and P. Landais, "Impact of bias current distribution on the noise figure and power saturation of a multicontact semiconductor optical amplifier," *Optics letters*, vol. 36, pp. 2521–3, July 2011.

[2] M. J. Connelly, "Wideband semiconductor optical amplifier steady-state numerical model," *IEEE Journal of Quantum Electronics*, vol. 37, no. 3, pp. 439–447, 2001.

[3] T. Durhuus, B. Mikkelsen, and K. Stubkjaer, "Detailed dynamic model for semiconductor optical amplifiers and their crosstalk and intermodulation distortion," *Journal of Lightwave Technology*, vol. 10, no. 8, pp. 1056–1065, 1992.